



Geological and geophysical characterization of accretionary and collisional systems : the Central Asian Orogenic Belt and the Bohemian Massif

Alexandra Guy

► To cite this version:

Alexandra Guy. Geological and geophysical characterization of accretionary and collisional systems : the Central Asian Orogenic Belt and the Bohemian Massif. Earth Sciences. Université de Strasbourg, 2012. English. NNT : 2012STRAH005 . tel-00827691

HAL Id: tel-00827691

<https://theses.hal.science/tel-00827691>

Submitted on 29 May 2013

HAL is a multi-disciplinary open access archive for the deposit and dissemination of scientific research documents, whether they are published or not. The documents may come from teaching and research institutions in France or abroad, or from public or private research centers.

L'archive ouverte pluridisciplinaire **HAL**, est destinée au dépôt et à la diffusion de documents scientifiques de niveau recherche, publiés ou non, émanant des établissements d'enseignement et de recherche français ou étrangers, des laboratoires publics ou privés.

ÉCOLE DOCTORALE Sciences de la Terre, de l'Univers et de l'Environnement (ED 413)

Institut de Physique du Globe de Strasbourg (UMR 7516)

Université de Strasbourg

THÈSE

présentée pour l'obtention du grade de

Docteur de l'université de Strasbourg

Discipline/spécialité : Sciences de la Terre - Géologie/Géophysique

par

Alexandra GUY

**Caractérisation géologique et géophysique de
système d'accrétion et de collision :
application à la ceinture orogénique d'Asie
centrale et au Massif de Bohême.**

Soutenue publiquement le 14 décembre 2012, devant la Commission d'Examen :

Prof. Carole PETIT
Prof. Wen Jiao XIAO
Prof. Gianreto MANATSCHAL
Dr. Thierry BAUDIN
M. Jean-Marc MIEHE
DR. ZDENĚK VENERA
Prof. Karel SCHULMANN

Université de Nice
Chinese Academy of Sciences
Université de Strasbourg
BRGM
AREVA Mines
Czech Geological Survey
Université de Strasbourg

Rapporteur externe
Rapporteur externe
Rapporteur interne
Examineur
Examineur
Invité
Directeur de thèse

A ma grand-mère,
A mon grand-père,
Cette femme et cet homme de la terre

To my grandmother,
To my grandfather,
This woman and this man devoted to the earth

*Choisissez une étoile,
ne la quittez pas des yeux.
Elle vous fera avancer loin,
sans fatigue et sans peine.*

Alexandra David-Néel
Exploratrice Française

*Je ne pense pas qu'il faille sans arrêt essayer
de justifier la recherche par des applications.
Je pense que la recherche en elle-même, basée sur la curiosité,
est un honneur de la civilisation et de la culture.*

Serge Haroche
Prix Nobel de Physique 2012

Sommaire

Introduction	11
Chapter I:	
Introduction to orogenic systems - Geology of the Central Asian Orogenic Belt	17
Chapter II:	
Late Palaeozoic-Mesozoic tectonic evolution of the Trans-Altai and South Gobi Zones (oceanic vs. continental domains) in southern Mongolia based on structural and geochronological data	33
Chapter III:	
Gravity and magnetic features combined with geological constraints in southern Mongolia: Revision of terrane boundaries	77
Chapter IV:	
Crustal structure of southern Mongolia inferred from geophysical forward modelling along four transects	145
Chapter V:	
Geophysical model of the Variscan orogenic root (Bohemian Massif): implications for modern collisional orogens	195
Conclusion	225
Bibliographie	229
Remerciements	253
Liste des Figures	257
Liste des Tables	261
Tables des matières	263

Avant-Propos

A la question, souvent posée, qu'est-ce qu'un thésard ? Je réponds par la simple définition : un thésard est un apprenti chercheur au sens littéral du terme.

Et le travail de thèse, de recherche de manière générale, n'est pas forcément un travail mené en solitaire, c'est surtout un travail d'équipe. Il passe ainsi par l'entraide entre les thésards et l'intégration au sein de l'équipe de l'unité de recherche, sans oublier bien sûr les interactions avec le directeur de thèse, pour aboutir à la publication scientifique, l'école de rigueur pour un chercheur en devenir. Bien qu'ayant une place primordiale dans la carrière d'un chercheur, la rédaction scientifique est loin de devoir être ses seules compétences. Ainsi j'ai pu découvrir pendant ces années de formation qu'un bon chercheur n'est pas seulement un bon scientifique, mais aussi un fin stratège, un très bon administrateur pour pouvoir être capable de se mouvoir dans les méandres administratifs, omniprésents dans la recherche (le négliger serait pêcher par orgueil), un bon comptable, sans oublier d'être un bon communicant sachant promouvoir ses idées, sa méthode, sa recherche.

Pour mon travail de thèse, j'ai eu la chance de faire une mission de terrain en Mongolie dans le désert de Gobi. J'admets, et cela n'a rien de scientifique, être tombée amoureuse de ce pays ainsi que de toute la région de l'Asie centrale en général. Je n'ai qu'un seul regret, c'est de ne pas avoir pu y retourner de manière plus assidue et régulière. Les dédales du travail d'un chercheur sont parfois semés de bien des embûches ; mais je n'ai pas dit mon dernier mot ! Car j'espère pouvoir encore travailler sur cette partie du globe.

Ce travail de recherche a pu être réalisé dans un premier temps grâce au soutien financier du consortium Européen C2C (« crust to core ») financé par le programme de la commission européenne « Marie Curie Research Training networks ». Le relais a ensuite été pris par la société AREVA, où j'ai eu la chance de collaborer dans le groupe AREVA Mines, puis par le CGS (Czech Geological Survey) à Prague.

L'opportunité m'a été donnée de travailler avec de nombreux spécialistes. M. Munsch et J-B. Edel (Université de Strasbourg) ont été de précieux conseils pour la modélisation géophysique. Les données structurales de terrain en Mongolie ont été acquises en collaboration avec P. Hasalová (Université de Monash, Australie) et O. Lexa (Université Charles, Prague) et les résultats des datations ont été possibles grâce au concours de N. Clauer (CNRS-Université de Strasbourg), R. Seltnann et R. Armstrong (Museum d'histoire naturelle, Londres).

Le manuscrit est divisé en cinq chapitres dont les quatre premiers présentent principalement une étude géologique et géophysique de la ceinture orogénique d'Asie centrale. Le dernier chapitre porte sur la modélisation 3D du Massif de Bohême. J'ai ainsi essayé de suivre une progression linéaire en évitant la juxtaposition d'articles qui aurait entraîné des répétitions.

Enfin, il est à préciser que certains travaux et résultats préliminaires effectués durant ma thèse ne sont pas présentés dans ce manuscrit. Il s'agit de la modélisation numérique de la formation des diapirs de granulite felsique effectuée en étroite collaboration avec P. Maierová et O. Lexa (Université Charles, Prague) lors de mes séjours à Prague à l'automne 2009 et 2010, ainsi que de l'étude structurale de la partie Chinoise des Altaïdes (5 semaines de terrain) effectué en collaboration avec J. Zhang (Université de Hong-Kong). J'espère poursuivre ces collaborations et ces travaux engagés au-delà de ma thèse afin de faire fructifier ces investissements scientifiques.

Introduction

Subduction of oceanic and continental lithosphere at convergent margins is one of the major consequences of plate tectonic (e.g. McKenzie and Parker, 1967; Le Pichon, 1968; Moore, 1973; Spence, 1987) and plays an important role in mountain building (Dewey and Bird, 1970). The net crustal growth of the continental crust is mostly due to the magmatic activity and the continental construction is related to the tectonic accretion of crustal fragments at subduction zones (Hawkesworth et al., 2010; Safonova et al., 2011). The accretion of microcontinents, oceanic crust and plateaux along convergent margins has made the accretionary orogens the primary sites of formation of the continental crust for the last 3 billion years (Dhuime et al., 2012). Classically, the accretionary orogens are considered as a distinct class of long lived orogenic systems in contrast to short lived collisional orogenic systems (Cawood et al, 2009). However, the collision between two continental plates at the end of a Wilson Cycle is no more recognized as a distinct type of orogen but likely as the logical end of an accretionary orogen (Schulmann and Paterson, 2011). These authors pointed out that the transition from net crustal growth and continental construction, characteristic for accretionary orogens, to collisional processes remains poorly constrained. These complex mechanisms can be characterized by a multidisciplinary approach to study the crustal architecture.

Palaeozoic mountain ranges represent eroded parts of ancient orogens and expose nearly complete sections of the orogenic crust. Therefore, they represent key areas for the study of tectonic processes occurring within the internal parts of mountain belts during orogeny. The deep crustal section of these orogens studied by means of geophysics allows correlating structure of orogenic belts with modern orogens when structural and geochronological data are lacking.

In the present work, detailed structural data combined with lithostratigraphical reconstructions are used to constrain the succession of deformation events, while magmatic petrology documents the generation and evolution of deep crust using geochemical data (Collins et al., 2011). In addition, the kinematics and time scales of these deformation phases are evaluated with U-Pb zircon dating of plutonic intrusions and K-Ar geochronology of low-grade rocks. Finally, the gravity and magnetic potential fields provide new insights on the main structures at different crustal levels. The combination of structural geology, geochronology and petrology with gravity and magnetic potential fields provides an effective tool to constrain and model the structure of the orogenic crust. Moreover, the identified orogenic architectures should be compared with those recognized in ancient or present-day accretionary or collisional orogens. This thesis tries to reconstruct the structures of orogenic crust in two Palaeozoic orogens: the Central Asian Orogenic Belt (southern Mongolia) and the Bohemian Massif (eastern Europe)

and define their tectonic evolution using plate tectonic paradigm valid for modern orogenic systems.

In southern Mongolia, the correlation between geological and potential field data is carried out by the creation of a geological map at the 1:500 000 scale and the processing of gravity and magnetic maps. This combination of geological and potential field data also represents a novel approach since the two observations were never jointly explored in the Central Asian Orogenic Belt (CAOB). The main result of this study is the review of the terrane boundaries suggesting that the quasi-exclusive use of terrane concept cannot be an objective method of regional tectonic analysis of the Mongolian basement units.

In the Bohemian Massif, the extensive work which has been carried out for more than a century represents a strong basis for modelling purposes. There, the geological and geophysical data were combined to produce a new 3D gravity model of the Bohemian Massif. The model chiefly suggests that the growth of the continental crust in the easter branch of the Variscan Europe is due to a relamination of low density felsic as a result of continental subduction. Thanks to the gravity model, the shape and extent of this felsic lower crustal portion can be precisely constrained.

Chapter I:

Introduction to orogenic systems
Geology of the Central Asian Orogenic Belt

Chapter I:

Introduction to orogenic systems Geology of the Central Asian Orogenic Belt

Orogeny is the geodynamical process leading to the deformation of the lithosphere and the formation of mountain belts as a result of tectonic plate motion. The growth of orogenic belts can be characterized by a succession of different tectonic phases such as crustal thickening or thinning. The orogens comprise thick sequences of sedimentary, volcanic and volcanoclastic material, acid and basic basement rocks and sometimes slices of oceanic crust and mantle. These sequences are deformed and metamorphosed to varying degrees and intruded by plutonic rocks of various compositions. Orogenic cycles do not only reflect tectonic processes, but also correspond to a given time span as exemplified by the Variscan (Late Palaeozoic), Caledonian (Early Palaeozoic), Alpine (Late Mesozoic-Cenozoic) orogenic systems.

Previous authors considered that orogenic systems are the consequence of a collision between two continental plates at the end of the Wilson cycle (Wilson, 1966; Dewey and Bird, 1970; Dewey and Burke, 1974). However, several orogens do not display any evidence for continental collision as for example the circum Pacific orogenic belts. Accordingly, the different types of orogens were classified into three categories: collisional, accretionary and intra-continental orogens. Collisional orogens result from the collision of continental fragments, accretionary orogens exhibit complex assemblages of continental/oceanic crustal material, and intra-continental orogens correspond to systems located relatively far (>1000 km) from active plate margins. This chapter will detail the distinguishing features of collisional and accretionary orogens, present a brief definition of accretionary orogens and finally give an overview of the geology of the Central Asian Orogenic Belt.

1. Collisional vs. accretionary orogens

1.1. Distinguishing features

Collisional and accretionary orogenic cycles have occurred from Early Proterozoic times until present. Both orogens form along oceanic subduction zones but preserve distinguishing features (Table 1). A collisional orogen rather presents a linear architecture perpendicular to the direction of convergence (Cawood et al., 2009) with a low quantity of juvenile material (Maruyama and Parkinson, 2000; Chardon et al., 2009) and large domains of high pressure and high temperature (HP-HT) metamorphic rocks. On the other hand an accretionary orogen forms crustal belts without any preferred orientation and contains a large amount of juvenile material with only scarce HP-HT domains (Maruyama and Parkinson, 2000). A collisional orogen is usually composed of continental crust formed before the collision (Cawood et al., 2009) and displays foreland flexural basins (Maruyama and Parkinson, 2000), whereas an accretionary orogen contains complete sequences of accretionary prisms with large volcanoclastic basins. The differences between these two orogenic types also extend into the deep mantle. A collisional orogen has a stiff upper mantle with a relatively cold asthenosphere and a mantle decoupled from the crust along the Moho (Chardon et al., 2009) while the mantle of an accretionary orogen is rather weak and hot in its upper part. Nevertheless, it has been recently proposed that an accretionary orogen can be the precursor of a collisional orogenic cycle and not a distinct type of orogen (Schulmann and Paterson, 2011).

Table 1: Summary of the main differences between collisional and accretionary orogens.

<i>Collisional Orogens</i>	<i>Accretionary Orogens</i>	<i>ref.</i>
Linear and long structures perpendicular to the convergence direction	Variable global structure	Cawood et al., 2009
Pre-collisional continental crust involved in the orogen	Accretionary prisms	Cawood et al., 2009
Little juvenile material	Abundant juvenile material over a long period	Maruyama et al., 2000 and Chardon et al., 2009
Large units of HP-HT rocks	Small and scarce HP-HT units	Maruyama et al., 2000
Foreland flexural basins	Large volcanoclastic basins	Maruyama et al., 2000
High topography	Low topography	Chardon et al., 2009
Stiff upper mantle with cold asthenosphere and decoupling at the Moho	Weak and hot upper mantle	Chardon et al., 2009

1.2. Location of contemporaneous collisional vs. accretionary orogens

Nowadays, the collisional fronts are mainly located along the border of the Eurasian plate (Fig. 1) and are controlled by the relative motion of the African, Arabian and Indian plates towards the north-north-east. They form a wide orogenic belt which stretches from the Alps in Europe up to the Himalayas in Asia, and which is called the Alpine-Himalayan orogen. The accretionary processes mainly occur in the western, southwestern and northern parts of the Pacific plate where different types of subduction zones (Japan, Mariannes, Andes), magmatic arcs, ocean ridges and continental fragments are involved (Fig. 1).

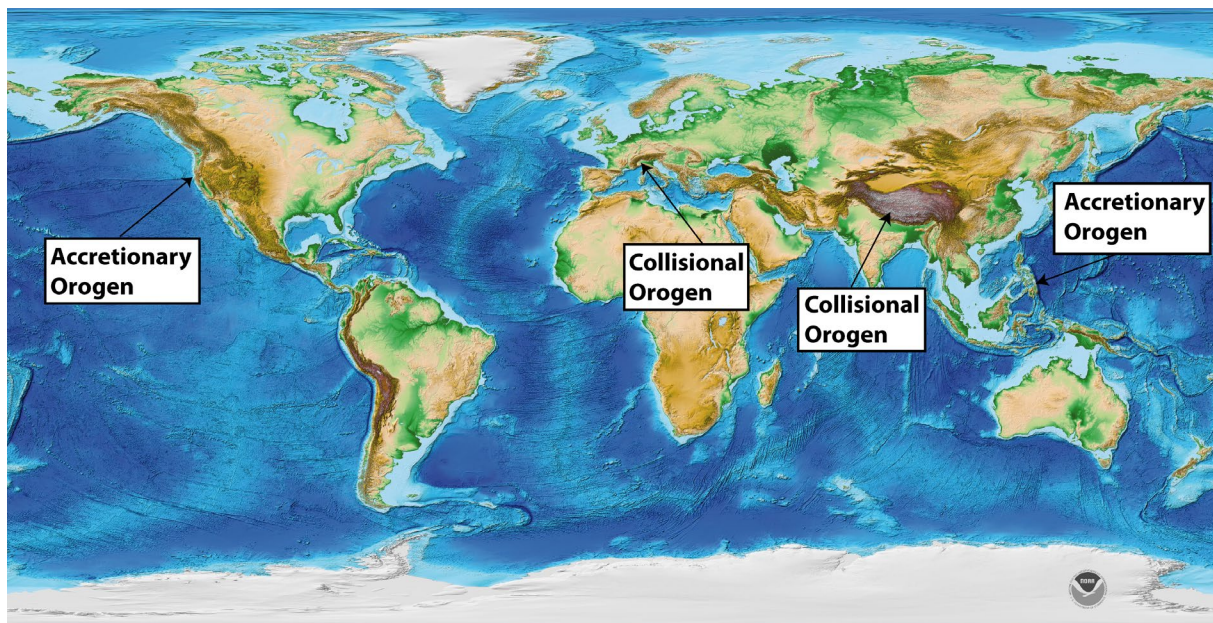


Figure 1: Distribution of present-day collisional and accretionary orogens (Relief map from NOAA, ETOPO1).

1.3. Definition of an accretionary orogen

At present, crustal growth is directly linked with the activity of subduction zones (Hawkesworth et al., 2010) and accretionary orogens are the primary sites of formation of the recent continental crust (Jahn et al., 2004). An accretionary orogen is composed of accretionary wedges containing not only material accreted from the downgoing plate and eroded from the upper plate, but also allochthonous parts such as island arcs, back-arc basins, dismembered ophiolites, oceanic plateau and/or old continental blocks. As a result of accretion, they also show post-accretionary granitic rocks, exhumed high- or ultra high pressure metamorphic rocks and clastic sedimentary basins (Cawood et al., 2009). An accretionary orogen usually has a long evolutionary history that spans a hundreds of millions years, but with distinct tectono-thermal pulses correlated with the tectonic plate motions.

The type of the collision depends on the nature of the subducting and overriding plates (Collins, 2002a). In order to amalgamate all the different materials which compose an accretionary orogen, different types of collisions can occur along the subduction zones: forearc/continental margin, forearc/continental fragment, island arc/continental margin, island arc/continental fragment, island arc/island arc, or continental/continental. Moreover, the roll-back or the roll-forth of the subducted plate and the associated behavior of the overriding plate are essential in the accretionary processes. The roll-back or the roll-forth phases cannot be continuous throughout the history of an accretionary orogen. Therefore, Cawood et al. (2009) introduced the concept of advancing and retreating accretionary orogens (Fig. 2). An advancing orogen develops where the overriding plate moves faster than the subducting plate retreats. It results in compression of the overriding plate. A retreating orogen undergoes an extension because the slab roll-back is faster than the advancing overriding plate. The result is an extension of the overriding plate and a formation of a back-arc basin. Lister et al. (2001) suggested that an accretionary orogen can have several cycles of advancing and retreating phases.

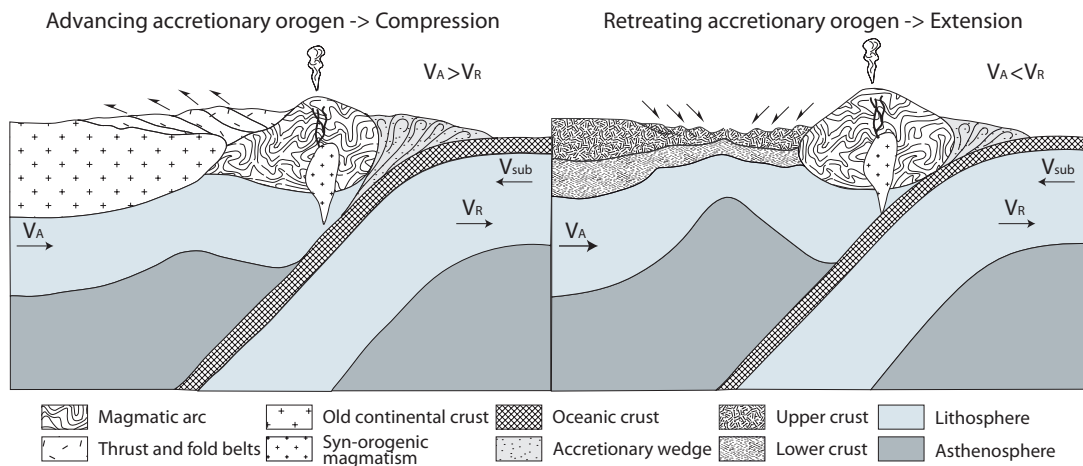


Figure 2: Advancing and retreating accretionary orogens (modified after Cawood and Buchan, 2007). (a) The velocity of the overriding plate (V_A) is greater than the velocity of the slab retreat (V_R) for the subducting plate (V_{sub}), hence the occurrence of compression in the overriding plate and the formation of fold and thrust complexes; (b) the velocity of the slab retreat is greater than the velocity of the overriding plate, hence the occurrence of extension in the overriding plate and the formation of a back arc basin.

Oblique convergence can also play an important role in the amalgamation of material and thus, in the development of an accretionary orogen. For example, oblique convergence has been proposed for the origin of the Cenozoic northwestern Cordillera in North America (Johnston 2001; Colpron and Nelson, 2006) or the present-day orogenic belts located along the southeastern (Hall, 2009; Spakman and Hall, 2010) and southwestern (Oncken et al., 2006) parts of the Pacific plate margin where the subduction zones and oceanic ridges are at a high angle to the continental plate margins.

1.4. Crustal growth and continent construction

The crustal formation is defined by the ratio between the newly-formed crustal material and the reworked and recycled older crust. Two processes of crustal formation are distinguished: (1) crustal growth which corresponds to the addition of juvenile material such as granitoids generated above subduction zones, and (2) continental construction which represents the lateral accretion of various crustal fragments.

Crustal growth is directly linked with the subduction processes and results from the production of granitoids in magmatic arcs (e.g. Rudnick, 1995). Subduction zones initially generate basic magmas which need to evolve to more acid melts in order to be incorporated into the former crust and not to be recycled into the mantle. The incorporation of these large volumes of magmas can occur via: (1) incorporation into the accretionary wedge because of the rollback of the slab and the retreat of the subduction zone (Collins, 2002a); (2) incorporation into the accretionary wedge because of the tectonic switch between roll-back and roll-forth of the slab (Collins, 2002b); (3) incorporation in the continental crust because of the re-melting of old continental crust in Andean type margins (Oncken et al., 2006).

Continental construction is the amalgamation of crustal fragments like microcontinents, continental margin material, oceanic crust or oceanic plateaus. The following continental construction processes can be distinguished: (1) horizontal accretion of continental blocks, oceanic plateaus and magmatic arcs transported towards the continental margin by the subducting plate (Cawood et al., 2009; Johnston, 2001); (2) obduction of ophiolites over the continental crust; (3) generation of anorogenic granites due to crustal reheating during the above-mentioned processes (Jahn, 2004; Kovalenko et al. 2004). Continental construction is usually accompanied by a switch in tectonic plate motion which is probably linked with a superplume activity in the mantle (Vaughan and Scarrow, 2003). Mantle dynamics play a major role in the formation of oceanic lithosphere formation on one side of the plate, and in the subduction of this lithosphere in the opposite side. Therefore, the acceleration of crustal growth and the peak activity of lateral accretion of crustal fragments can probably be driven by the activity of the mantle.

2. The Central Asian Orogenic Belt (CAOB)

2.1. Global setting of the CAOB

The Central Asian Orogenic Belt is an accretionary orogen which extends from the Ural Mountains to the west up to eastern Mongolia across Kazakhstan, northwestern China and Siberia (Fig. 3). Suess (1901) was the first to recognize that the crust of the Asian continent grew at the periphery of the Siberian cratonic nucleus and used the term *Altaids* to characterize this orogenic cycle. The *Altaids* are also termed the Central Asian Orogenic Belt (CAOB) by Windley et al. (2007).

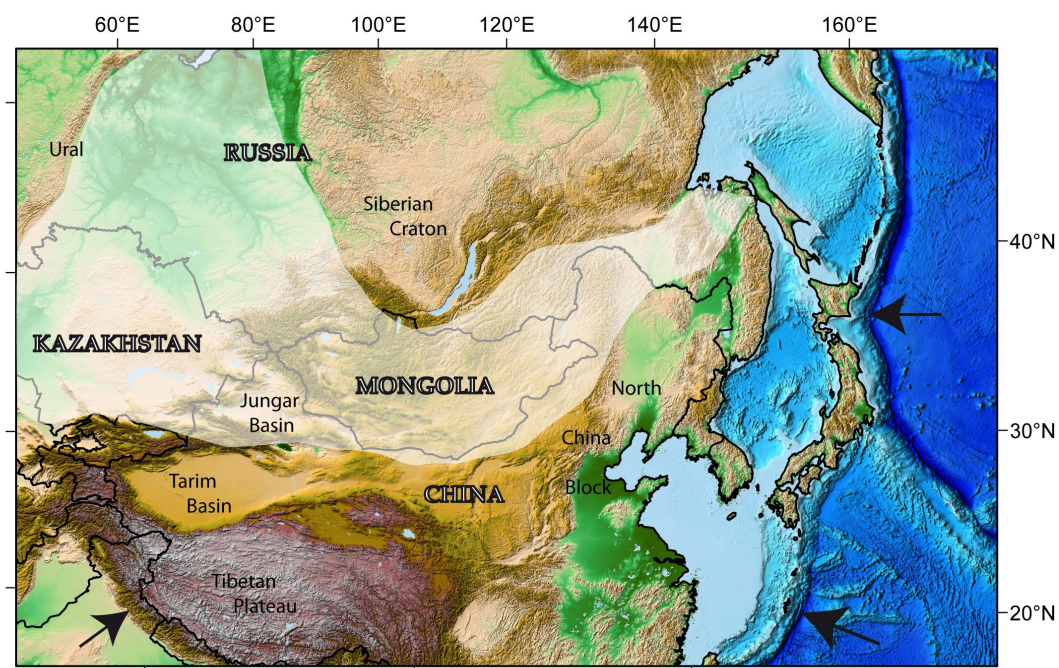


Figure 3: Relief map of central Asia (from NOAA, ETOPO1, <http://www.ngdc.noaa.gov/mgg/global/relief/>). The location of the CAOB is represented by the white area. Black arrows represent relative plate motions from the Eurasia plate referential.

The CAOB is one of the largest accretionary orogens on Earth. It represents almost one third of the total volume of the Asian continent. This accretionary system formed from the Mesoproterozoic to the Permian (Kröner et al., 2010) by the amalgamation of continental blocks of Grenvillian to Archean age (Rojas-Agramonte et al., 2011), accretionary prisms, magmatic arcs and backs-arcs of Ordovician and Devonian age (Badarch et al., 2002; Kröner et al., 2010), ophiolites, and post-accretionary granitic intrusions. It is proposed that this mosaic of crustal segments was built by complex and successive accretionary mechanisms during the Palaeozoic followed by a Mesozoic collisional phase. Since the Cenozoic, it has been evolving as an intracontinental orogen.

In the CAO, two geological domains separated by a major fault called the Main Mongolian Lineament (MML) are distinguished (Zonenshain, 1973): the northern and southern parts are called the Caledonian and Hercynian domains, respectively. These two domains also correspond to two periods of major continental growth in the CAO: (1) the late Proterozoic to early Palaeozoic period, when the Palaeo-Asian Ocean I (PAO I) was closed and late Proterozoic ophiolites accreted to the Precambrian continental basement, and (2) the late Palaeozoic to Mesozoic period, when the Solonker suture formed during the closure of the Palaeo-Asian Ocean II (PAO II).

2.2. Lithotectonic zonation of the CAO

The CAO is traditionally divided into several lithotectonic units based on the lithological successions of sedimentary and volcanic sequences. These units are often bounded by strike-slip faults and therefore were interpreted as “terrane” (Badarch et al., 2002). Alternatively, the units were characterized by their lithological and structural features and were defined as lithotectonic zones (Zonenshain et al., 1975). The latter approach was reintroduced by Kröner et al. (2010) who took into account the main lithological differences and evolutionary trends, U-Pb zircon geochronology of the main Mongolian zones, and detailed structural analysis of the individual units. According to Kröner et al. (2010), the classical lithotectonic zonation can be defined as an alternation of E-W trending continental domains, passive margin sequences and oceanic fragments. The figure 4 (next page) shows an attempt to reconstruct and summarize the different units of the CAO. This synthesis is the combination of numerous pioneering works (Şengör and Natal'in, 1996; Parfenov et al., 2001; Badarch et al., 2002; Parfenov et al., 2003; Xiao et al., 2004; Kuzmichev et al., 2005; Volkova and Sklyarov, 2007; Xiao et al., 2008; De Boisgrollier et al., 2009; Kröner et al., 2010; Windley et al., 2007). The units are distinguished according to their tectonic and lithological characteristics and their ages of formation. The distribution of the accretionary wedges, island arcs, passive and active continental margins, basins, oceanic units, cratons and basement blocks is accompanied by the sutures (more or less well-constrained) and the approximate location of major magmatic arcs. The study area of this thesis is located to the south of Mongolia where alternations of continental basement blocks, oceanic domains, passive and active margin sequences, and island arcs are present (Fig. 5).

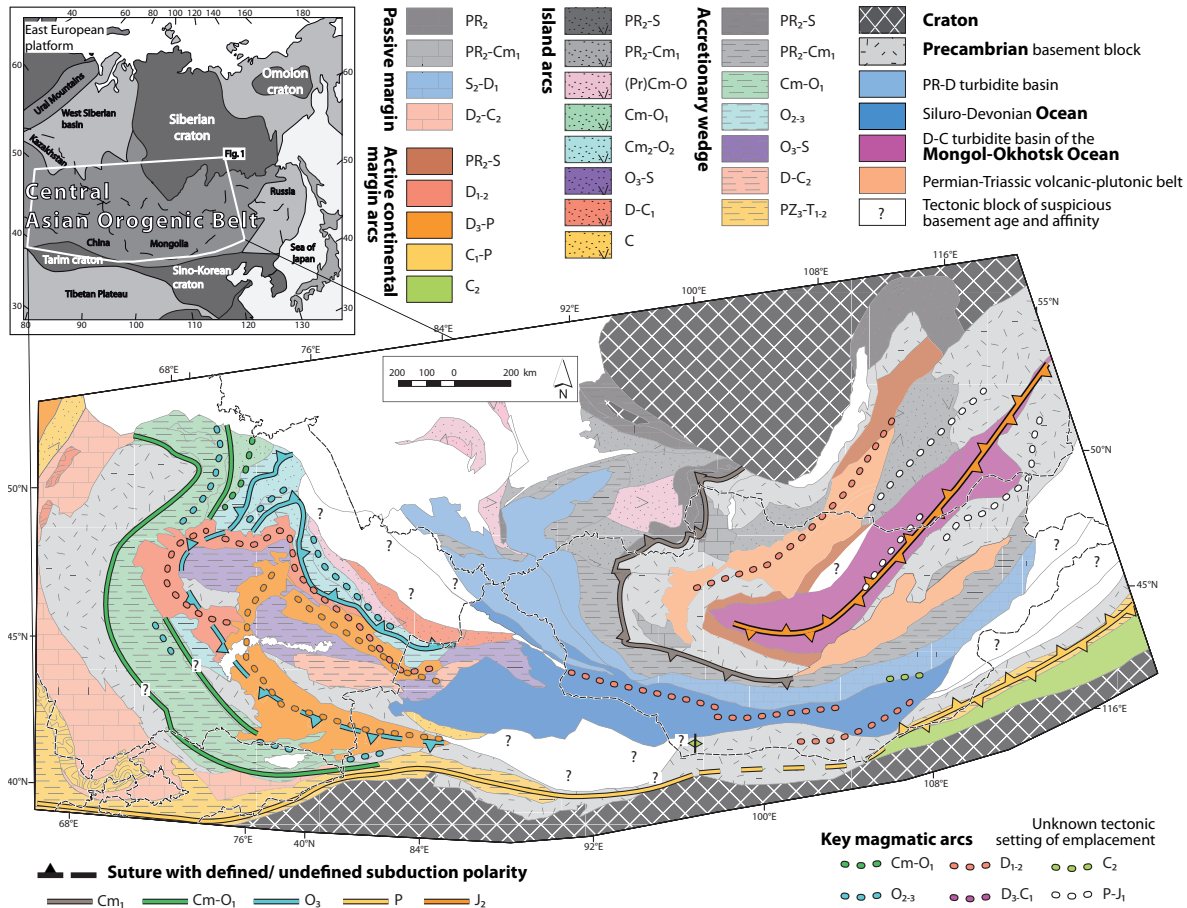


Figure 4: Simplified lithotectonic map of the CAOB showing the distribution of the continental and oceanic domains, alternating with island arcs, cratons and sutures (modified after Şengör and Natal'in, 1996; Parfenov et al., 2001; Badarch et al., 2002; Parfenov et al., 2003; Xiao et al., 2004; Kuzmichev et al., 2005; Volkova and Sklyarov, 2007; Xiao et al., 2008; De Boissgrolier et al., 2009; Kröner et al., 2010; Windley et al., 2007). The inset shows the location of the CAOB in the frame of Asia.

The individual zones in Mongolia are characterized by the presence of Precambrian to Carboniferous arc-type granitoids and volcanic rocks and HP rocks indicating the presence of suture zones (Štípská et al., 2010; Qu et al., 2011). To the north of Mongolia occurs the Grenvillian to Archean basement of the Dzabkhan and Baydrag microcontinents (Kozakov et al., 2007) covered by late Proterozoic and early Cambrian passive margin sequences (Rojas Agramonte et al., 2011). The basement is overthrust, from the south, by an early Cambrian accretionary wedge consisting of eclogites, peridotite-bearing mélanges and ophiolites collectively termed as the Lake Zone. This unit is limited to the south by a major strike-slip fault named the Main Mongolian Lineament (Tomurtogoo, 1997a, 1997b) which separates the northern region affected essentially by Cambrian-Ordovician tectonic and metamorphic events from the southern Gobi-Altai Zone which underwent a Devonian-Carboniferous tectono-metamorphic overprint. The Gobi Altai Zone is interpreted as a Silurian-Devonian passive margin developed on a late Cambrian substratum and intruded by a Devonian-Carboniferous

Japan-type magmatic arc. The Trans-Altai fault zone (equivalent of the Erquis fault zone in China) marks the boundary between the Gobi-Altai Zone and the southern Trans-Altai Zone. The latter generally consists of an ultramafic basement covered by late Silurian cherts, early Devonian volcanic rocks and late Devonian to Carboniferous volcanoclastic sediments (Ruzhentsev et al., 1992; Badarch et al., 2002). This large tectonic zone was interpreted as a collage of Devonian-Carboniferous oceanic arcs, back arcs and ophiolites (Lamb and Badarch, 1997; 2001). The Trans-Altai Zone is separated from the southern South Gobi Zone by the E-W striking Gobi-Tianshan fault (Ruzhentsev, 2001). The South Gobi Zone is considered as a continental domain of predominantly Grenvillian age (Rojas-Agramonte et al., 2011) covered by Ordovician and Silurian clastic sequences and Devonian to Carboniferous volcanoclastic and volcanic rocks.

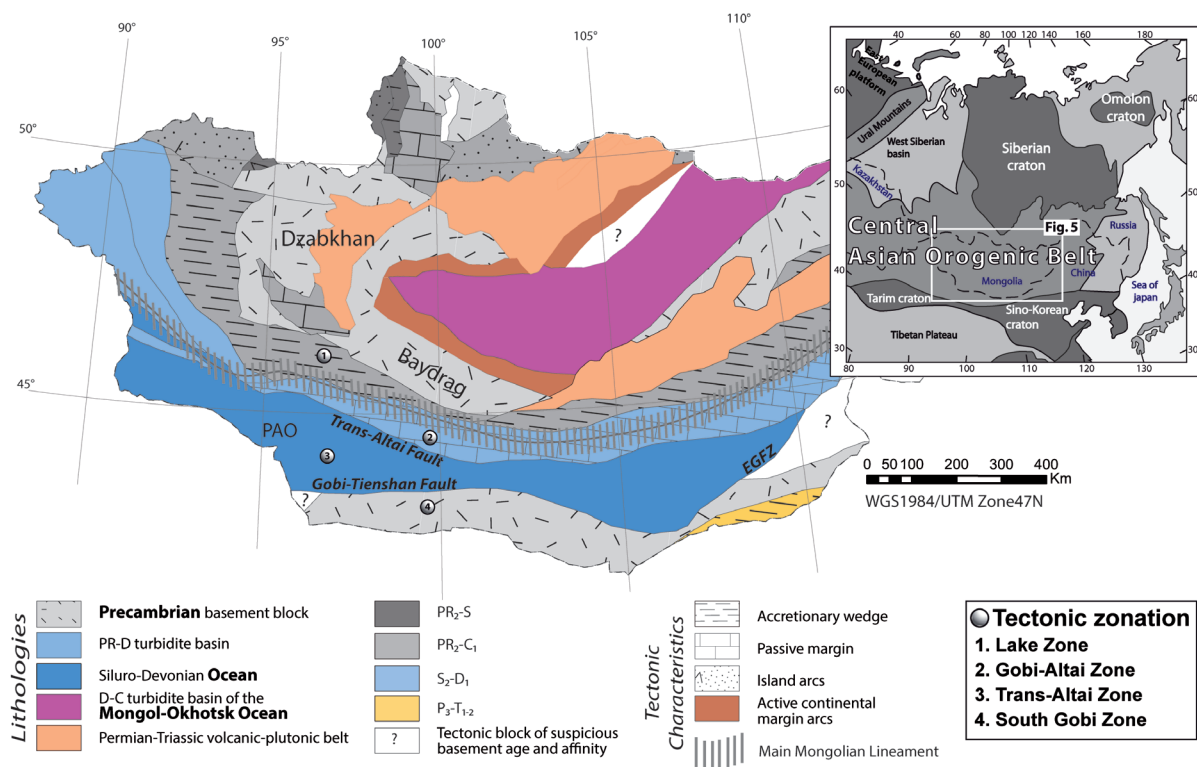


Figure 5: Main lithotectonic units of the Central Asian Orogenic Belt in Mongolia. The inset displays the location of Mongolia in the whole CAOB surrounded by cratons and in the frame of the Asian continent. Black rectangle shows the Ömnögovı Province. PR: Proterozoic; S: Silurian; D: Devonian; C: Carboniferous; P: Permian; T: Trias; J: Jurassic. EGFZ: East Gobi fault zone.

2.3. Tectonic evolution of the CAO

The Lake Zone is composed of the so-called Dzabkhan microcontinent with Precambrian basement rocks. The oldest tectonic event affecting the Lake Zone is a Lower Cambrian thrusting of an eclogitic mélangé and ophiolites over the Dzabkhan microcontinent (Stipska et al., 2010). In Ordovician-Silurian times, the stretching of the Dzabkhan microcontinent (Zonenshain, 1973; Zorin et al., 1993) favored the formation of a carbonate shelf on a proximal margin located to the south of the Lake Zone in present-day coordinates (Fig. 6). This passive margin sequence, which forms the Gobi Altai Zone, developed during the late Silurian and the early Devonian. Farther to the south, the Trans-Altai Zone shows evidence for the contemporaneous exhumation of lithospheric mantle in areas corresponding to a distal passive margin environment (Ruzhentsev and Pospelov, 1992; Ruzhentsev, 2001), thereby attesting for the progressive formation of oceanic crust during the early Devonian, i.e. for the opening of the Palaeo-Asian Ocean II. The Gobi Altai Zone experienced syn-convergent emplacement of arc magmas within the continental crust due to the activity of a subduction zone during the Devonian and Carboniferous. In the Trans-Altai Zone, ophiolitic nappes were thrust over Devonian sediments probably during late Devonian to early Carboniferous (Zonenshain et al., 1975). Both the Lake Zone and the Gobi Altai Zone show the existence of a thermal event leading to graben formations, bimodal volcanism and the partial melting of the crust during the Permian.

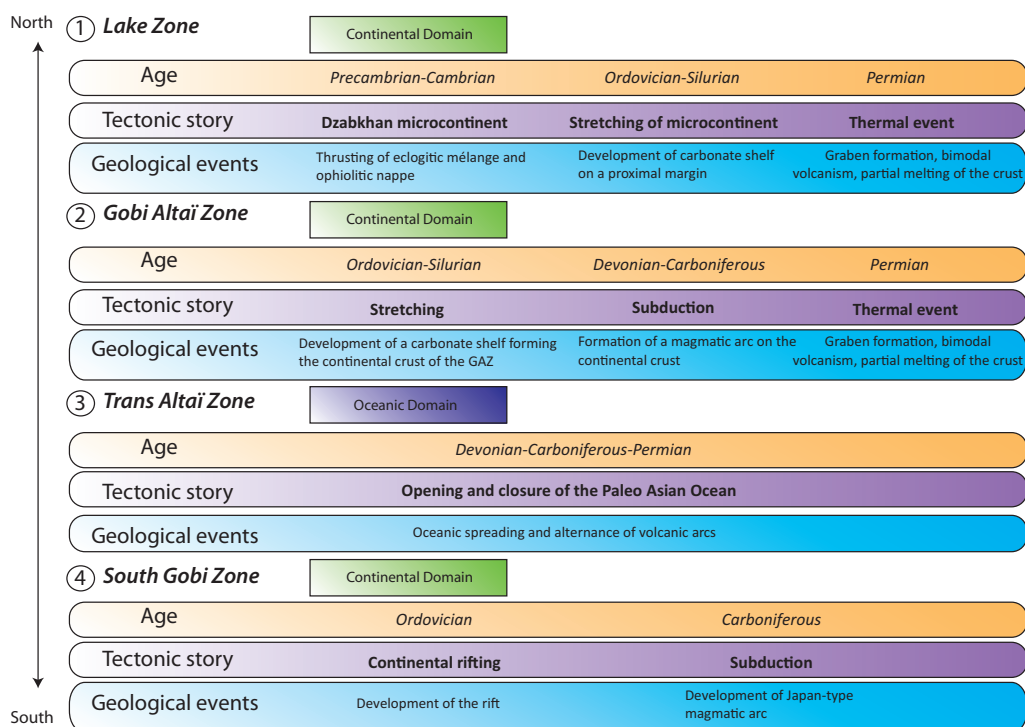


Figure 6: Outline of tectonic and geological events of the four lithotectonic zones in southern Mongolia (after Lehmann et al., 2010).

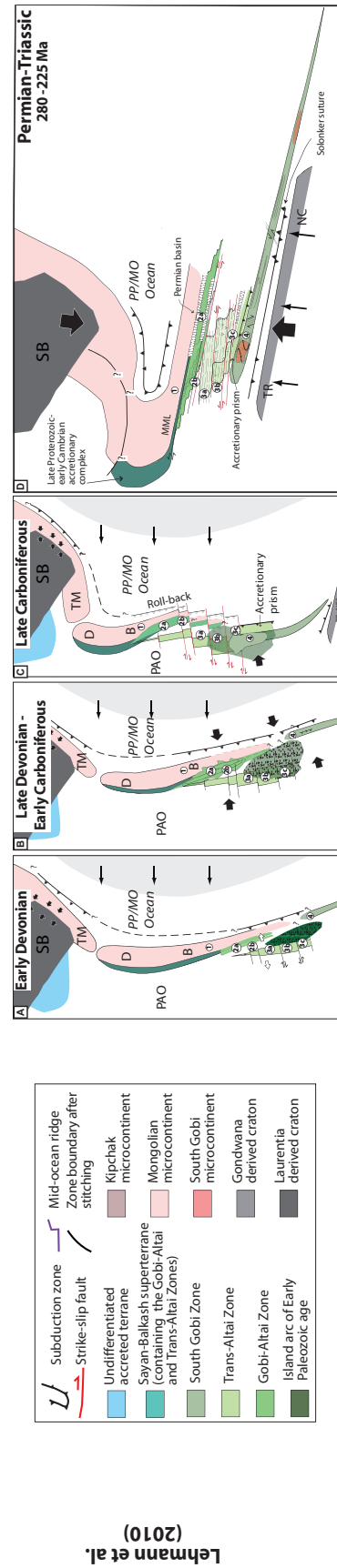
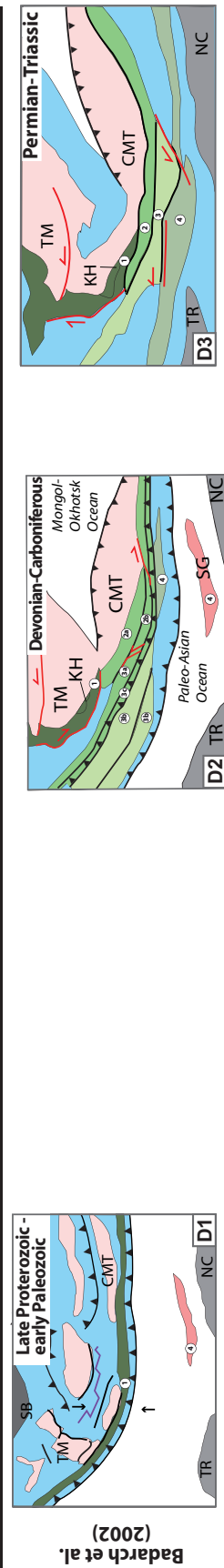
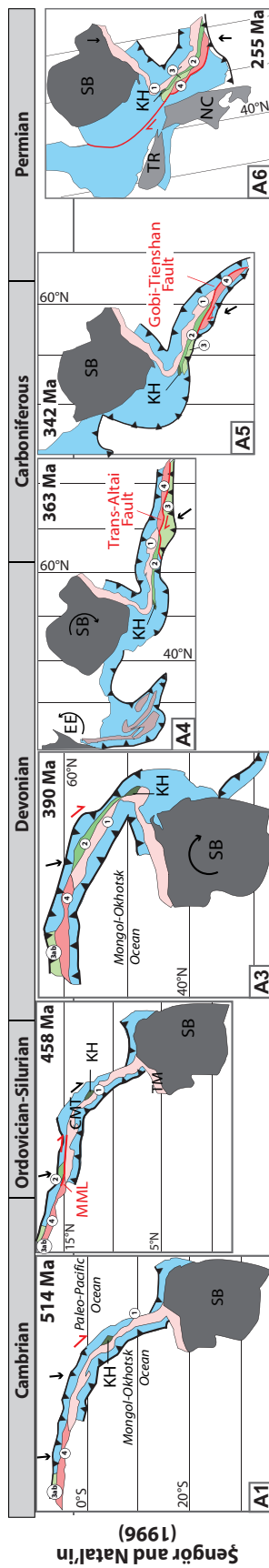
In contrast, the tectonic evolution of the South Gobi Zone is less documented and its relationships with the other lithotectonic zones remains poorly understood. The South Gobi Zone shows a thin-skinned tectonic deformation pattern with Ordovician and Devonian rocks being thrust onto Carboniferous sediments. In places, the South Gobi Zone also reveals the development of a Carboniferous Japan-type magmatic arc during subduction and E-W shortening. The major deformation phase affecting all the lithotectonic zones corresponds to a N-S compression event which reflects a convergent episode driven by the clockwise rotation of the Siberian craton combined with the north-directed motion of the North China and Tarim cratons from the late Permian to the Mesozoic.

2.4. Existing geodynamic model for the CAO

Three different models dealing with the tectonic evolution of the CAO (Fig. 7) have been proposed so far: (1) the strike-slip duplication followed by the oroclinal bending of a giant magmatic arc called the Kipchak-Tuva-Mongol arc (Şengör et al., 1993; Şengör and Natal'in, 1996); (2) the successive lateral accretions of oceanic and continental terranes to the Siberian craton (Badarch et al., 2002; Windley et al., 2007), and (3) a two-stage evolution involving an initial “Pacific” type accretion during the Devonian-Carboniferous followed by the “Tethyan” type oroclinal bending and collisional shortening from Permian to Jurassic (Lehmann et al., 2010; Schulmann and Paterson, 2011).

The first model is based on the oroclinal bending of a single and giant arc (Fig. 7). It involves an oblique and steady-state subduction zone inducing right lateral strike-slip movements parallel to the arc combined with a second subduction zone with an opposite polarity. The two subduction zones can explain the important amount of accretionary wedge materials which is present in the CAO. The clockwise rotation of the Siberian craton accompanied by the northward drift of the North China and Tarim cratons are the driving forces of the oroclinal bending. Yakubchuk et al. (2005) and Zorin (1999) also used this model as a base to interpret the evolution of the CAO.

The second model implies the existence of exotic terranes and multi-subduction systems like in the southwestern Pacific (Fig. 7). The model supposes a succession of opening and closure of small oceanic basins and the development of a new southward subduction zone leading to the generation of the Gobi-Altai and Trans-Altai Zones. The strike-slip movements affecting the whole CAO are explained by the northward drift of the North China and the Tarim cratons.



- Legend:**
- Subduction zone**
 - Strike-slip fault**
 - Mid-ocean ridge**
 - Zone boundary after stitching**
 - Undifferentiated accreted terrane**
 - Sayan-Balkhash superterrane (containing the Gobi-Altai and Trans-Altai Zones)**
 - South Gobi Zone**
 - Trans-Altai Zone**
 - Gobi-Altai Zone**
 - Island arc of Early Paleozoic age**
 - Kipchak microcontinent**
 - Mongolian microcontinent**
 - South Gobi microcontinent**
 - Gondwana derived craton**
 - Laurentia derived craton**
- Tectonic zonation**
- Lake Zone**
 - Gobi-Altai Zone**
 - Gobi-Altai Subzone
 - Mandalovoo Subzone
 - Trans-Altai Zone**
 - Khuvinkharin Subzone
 - Edrengin Subzone
 - Dzolen Subzone
 - South Gobi Zone**
- Other abbreviations:**
- B:** Baydrag
 - CMT:** Central Mongolian Terrane
 - D:** Dzabkhan
 - EE:** East European Craton
 - KA:** Kazakhstan terrane collage
 - KH:** Khantaihir ophiolite complex
 - MO:** Mongol-Okhotsk
 - NC:** North China Craton
 - PAO:** Paleo-Asian Ocean
 - PP:** Paleo-Pacific
 - SB:** Siberian Craton
 - SBT:** Sayan-Balkhash turbiditic Superterrane
 - SG:** South Gobi Microcontinent
 - TM:** Tuva-Mongol block
 - TR:** Tarim Craton

The third model suggests that an initial E–W directed shortening event led to crustal imbrications associated with a Pacific type (Fig. 7). The second N–S directed shortening was responsible for a re-folding of all previous structures into upright E–W trending folds with major E–W striking cleavage fronts connected to continental collision (Kröner et al., 2010).

However, none of these models take into account the role of the late Carboniferous to Permian calc-alkaline to alkaline magmatism which hallmarks the transition from subduction to collision. Moreover, these models suffer many contradictions and uncertainties, and do not solve the problem of orthogonal deformation phases which are widely observed in the CAOBS especially regarding the switch of the deformation from Devonian to Carboniferous E–W shortening to Permian to Jurassic N–S shortening (Lehmann et al., 2010).

Therefore, the remaining questions that need to be addressed in this work involve: (1) the tectonic segmentation of the CAOBS into terranes; (2) the parameters of lateral and vertical construction of the crust of this orogenic system; and (3) the origin and correlation of geological events such as the intrusion of ultramafic and granitic rocks or the exhumation of deep-seated rocks.

Chapter II:

Late Palaeozoic-Mesozoic tectonic evolution of the Trans-Altai and South Gobi Zones (oceanic vs. continental domains) in southern Mongolia based on structural and geochronological data

Chapter II:

Late Palaeozoic-Mesozoic tectonic evolution of the Trans-Altai and South Gobi Zones (oceanic vs. continental domains) in southern Mongolia based on structural and geochronological data

The study area is located in southern Mongolia in the so-called Ömnögovi province that is set astride two critical lithotectonic domains. We investigated the interactions between the South Gobi Zone that is assumed to be mainly a continental domain, and the Trans-Altai Zone that is considered to be an Early Palaeozoic oceanic domain belonging to the Paleo Asian Ocean. Several time of closure of the Palaeo-Asian Ocean have been proposed: (1) early Cambrian for its western part (Kovalenko et al., 2004; Kruk et al., 2011; Glorie et al., 2011); and for its eastern part, (2) Devonian to early Carboniferous (Zonenshain et al., 1975; Zorin et al., 1993; Sengör and Natal'in, 1996; Yakubchuk et al., 2005); (3) Carboniferous to early Permian (Zonenshain et al., 1990; Parfenov et al., 1995; Charvet et al., 2007; Li, 2006; Hegner et al., 2010); (4) late Permian-early Triassic (Chen et al., 2009a; Safonova et al., 2009; Xiao et al., 2009a, 2009b). The study area is therefore a matter of debate and is critical for understanding of Central Asian Orogenic Belt (CAOB) accretionary processes.

1. Geological setting of the Trans-Altai and the South Gobi Zones

1.1. Geology of Ömnögovi Province

The study area is located in the Ömnögovi province that covers the Trans-Altai Zone to the north and the South Gobi Zone to the south (Fig. 1). The South Gobi Zone contains Neoproterozoic basement associated with various Palaeozoic and Mesozoic, marine and non-marine, sedimentary units alternating with episodic Devonian-Carboniferous volcanic sequences. In contrast, the Trans-Altai Zone is dominated by late Silurian ultramafic rocks and cherts covered by a thick basaltic and andesitic volcanic sequence of early Devonian age (Helo et al., 2006). Late Palaeozoic and Mesozoic syn- and post-tectonic granites intruded both lithotectonic zones marking important stages in the orogenic cycle (Fig. 1). The regional distribution of late Carboniferous bimodal volcanic and magmatic associations marking the boundary between the South Gobi and Trans-Altai zones led Kovalenko et al. (2006) and

Kozlovsky et al. (2006) to introduce the term Gobi Tianshan rift zone related to north–dipping subduction zone activity. It is this magmatism and its tectonic setting that are examined and discussed in this study.

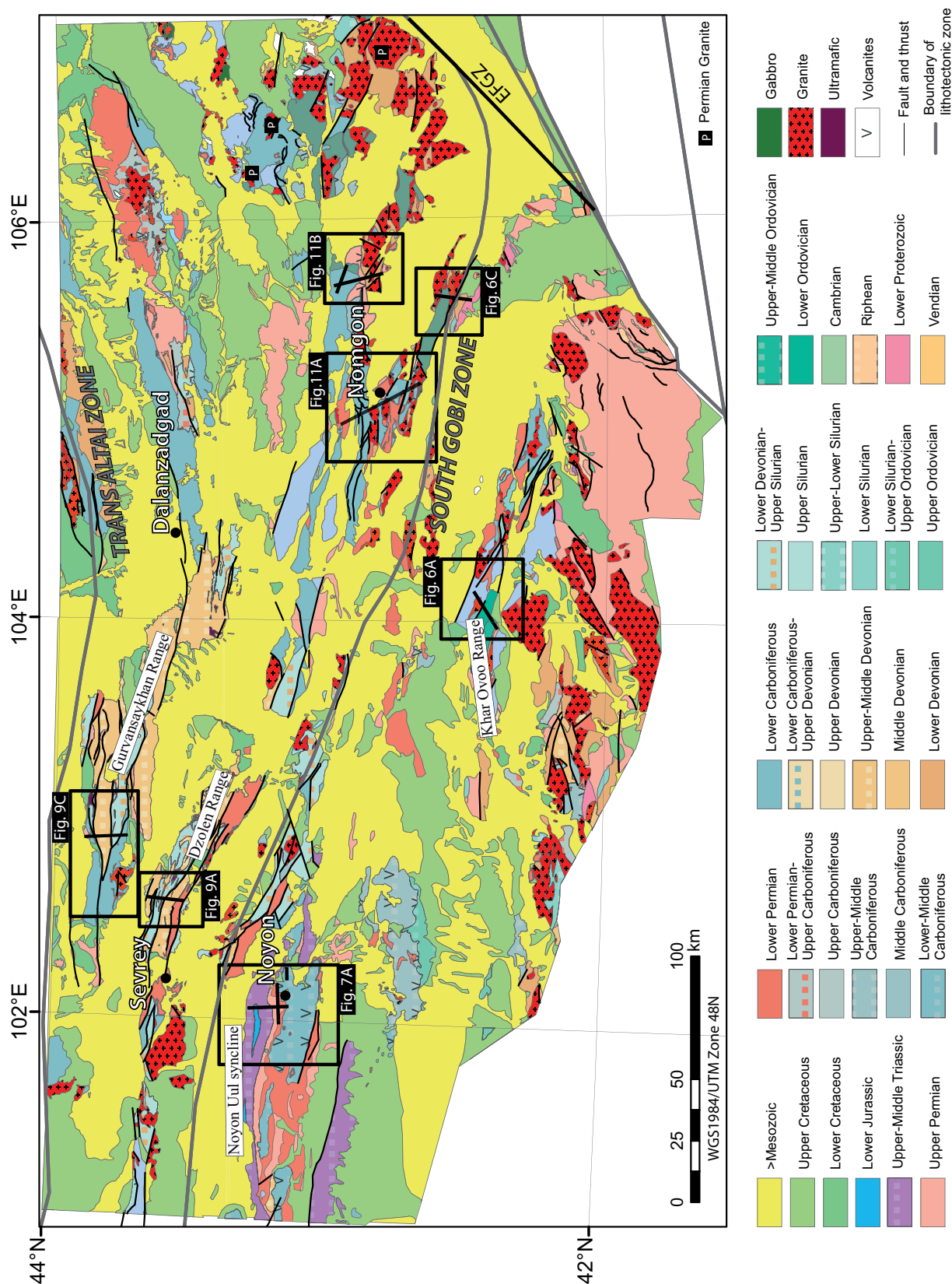
1.2. Lithostratigraphy of the South Gobi Zone in the Ömnögovi Province

Rocks of the South Gobi Zone are exposed in the southernmost part of the CAOBS and range from Neoproterozoic (outcrops located to the east of the South Gobi Zone) to Permian in age (west of the South Gobi Zone). The variably metamorphosed rocks are well exposed in ridges that are juxtaposed against young intermontane basins filled with Mesozoic and Cenozoic sediments (Fig. 1).

1.2.1. Central part of the South Gobi Zone

For this area we adapted the nomenclature and lithostratigraphic sections from the geological map report of Damdinjav and Delgersaikhan (1996-98, report N°5307) combined with our own observations (Fig. 2a). In the Khar Ovoo Range, the succession starts with the low-grade Ordovician Tömörtyn formation (Markova, 1975) represented by fossiliferous carbonates intercalated with a series of sandstones, siltstones and limestones, conformably overlain by Upper Ordovician siliceous clastic rocks, sandstones and micaschists. Locally, the Ordovician sequences are overlain by shales assigned to the early Silurian dated by fossiliferous carbonates. The scarce Lower to Middle Devonian sediments unconformably overlie the Ordovician-Silurian sequences and consist mainly of marbles and other calc-silicate rocks intercalated with rhyolitic and andesitic rocks. Locally, the Silurian and Devonian sequences may occur directly above Proterozoic basement. The Lower Palaeozoic rocks are subsequently unconformably overlain by Middle to Upper Carboniferous volcanic rocks represented by andesites intercalated with rhyolite to rhyodacite lava flows, tuffs and other products of sub-aerial volcanism. Rare Middle to Upper Permian volcanic rocks were also reported (Damdinjav and Delgersaikhan, 1996-98, report N°5307).

Figure 1: Geological map of the Ömnögovi province (synthesis of at least 25 geological maps of 1:200 000). This area is divided in two lithotectonic units (grey thick curves). The rectangles depict the study areas and the black lines the locations of the structural cross-sections.



1.2.2. Western part of the South Gobi Zone

The lithostratigraphy of the Noyon Uul Mesozoic syncline and its surrounding Palaeozoic rocks (Fig. 2b) was previously studied by Lamb and Badarch (1997, 2001), Hendrix et al. (1996) and Damdinjav and Delgersaikhan (1996-98). The Lower to Middle Carboniferous sequence of Tost Uul formation (Lamb and Badarch, 1997) consists of argillites overlain by volcanoclastic sandstones, tuff, andesite-basaltic tuff and porphyritic lava flows (Lamb and Badarch, 2001). These rocks are unconformably overlain by the Lower Permian conglomerates and volcanoclastic sandstones, progressively evolving into siliceous sediments and unconformably covered by Middle to Upper Permian formations displaying meandering fluvial deposits (Hendrix et al., 1996). The overlying Noyon Uul syncline strata consist of Lower and Upper Triassic and Lower Jurassic syntectonic fluvial facies that originated as a foreland basin during collision taking place some 100 km farther south in Inner Mongolia of China.

1.3. *Lithostratigraphy of the Trans-Altai Zone in the Ömnögovi province*

The Palaeozoic rocks of the Trans-Altai Zone, ranging from Silurian to Permian in age, are exposed in ridges that are juxtaposed against young intermontane basins filled with Mesozoic and Cenozoic sediments (Fig. 1). We compiled the lithologies from the western part of the Trans-Altai Zone close to Sevrey village and in the east close to Nomgon village (Fig. 1) in two representative lithostratigraphic successions (Fig. 2c and d).

1.3.1. Eastern part of the Trans-Altai Zone

The oldest rocks of the Nomgon area are represented by a small outcrop of presumably early Silurian age, overlain by early Devonian andesitic volcanic rocks and tuffs (Fig. 2c) followed by siliceous sediments of middle to late Devonian age. The early Carboniferous sequence is represented by andesite volcanic rocks and their tuffs in the lowermost part of the

Figure 2: Stratigraphic columns for the South Gobi Zone and the Trans-Altai Zone, and the associated legend. a) Khar Ovoo Range; b) Noyon Uul syncline; c) Nomgon district; d) Sevrey district.



sequence and basaltic rocks in the uppermost part. The Middle to Upper Carboniferous Murgotsog formation consists of intercalations of siliceous sediments and sandstones, followed by andesite volcanic rocks and their tuffs, together with sandstones and siliceous sediments. This thick Carboniferous sequence is conformably overlain by the Lower Permian Togoot Khar formation composed of trachyte volcanic rocks intercalated with basaltic rocks. The Middle to Upper Permian Deliin Shand formation consists of conglomerates evolving progressively into sandstones with siliceous sedimentary intercalations.

1.3.2. Western part of the Trans-Altai Zone

To the west of the Trans-Altai Zone, the area of the Sevrey district (Fig. 2) reveals the most complete lithostratigraphic section (Togtokh et al., 1986, mapping report N°3912,). The rocks range from late Silurian to late Permian in age. The lowermost part of the Upper Silurian-Lower Devonian assemblage begins with a thin layer of fossiliferous ophicalcite, followed by andesite and basaltic rocks intercalated with shales, sandstones, tuffs and volcanoclastic sandstones. An unconformity is located in the middle of the formation that highlights the transition from mainly volcanic rocks to terrigenous mainly shaly sedimentary deposits. This sequence is conformably overlain by a Lower to Middle Devonian massive diabase alternating with basaltic lava breccia and a sheeted dike complex ~ 2500 m thick, indicating the formation of a juvenile intra-oceanic arc of early Devonian age (Helo et al., 2006). These rocks are conformably overlain by a Middle to Upper Devonian transgressive formation, imbricated with clastic sediments consisting of siltstones, sandstones, jasper, conglomeratic assemblage, phyllites and argillites, volcanoclastic sandstones. The Lower Carboniferous strata that conformably overlie the Devonian formation consist of the lowermost part of fossiliferous limestones, overlain by intercalated siltstone, sandstone and siliceous sediments. On the Carboniferous is a ~ 1700 m thick mainly volcanic Lower Permian formation, overlain by the Middle to Upper Permian rocks. The east of the Trans-Altai Zone in the Nomgon district (Fig. 2c) displays presumably the entire Carboniferous succession represented by a ~ 3000 m thick mostly volcanic sequence, whereas the western Trans-Altai Zone displays only the Lower Carboniferous sequence consisting of an almost 3000 m thick sedimentary rocks.

2. Carboniferous and Permian intermediate to felsic intrusive magmatism

The magmatic rocks of the study area are dominated by granitoid magmatism of late Paleozoic age (Carboniferous to Permian) as shown in figure 3. In total, new geochemical data of 69 samples are presented (Table 1) that were collected in 2006 during the Altaids geotraverse study of the Natural History Museum London (Seltmann et al., 2008). 69 samples are petrologically and geochemically characterized here from which 13 samples were selected for age dating by SHRIMP U-Pb zircon geochronology.

In order to assess whether compositional variation of these intrusive units was a result of heterogeneities of the basement across the study area, the samples were grouped according to their geographic distribution and age. Four geographic zones can be distinguished that in the following text we name the NW zone, the Khongor zone; the SW zone and the Eastern zone (Fig. 3). These zones were derived from the mapped distribution of intrusive rocks and were then further refined/split using the new geochronological data. Whereas this process was relatively

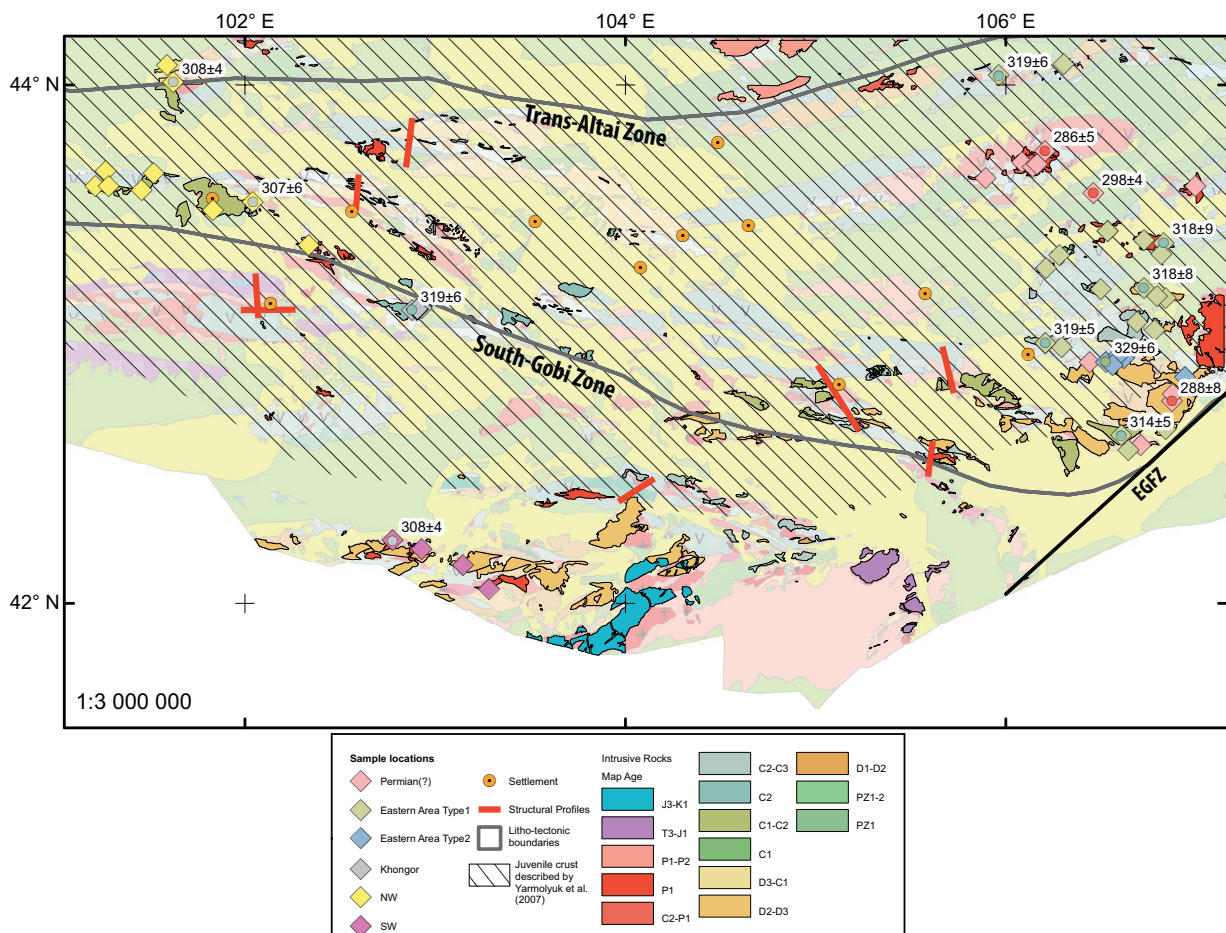


Figure 3: Main massifs of magmatic rocks and geochronological ages superposed on a geological map.

Table 1: Trace elements of 69 sample rocks.

SAMPLE	T1-190	T1-192	T1-222	T1-227	T1-228	T1-229	T1-234	T1-235	T1-236	T1-237	T1-238	T1-239	T1-240	T1-301	T1-302	T1-303	T1-304
Rock Type	granite, catclastic	granite	granite, aplitic	alkali-redspar granite, aplitic	qtz catclastic	granodiorite, monzonitic	granite	granite, catclastic	granodiorite, monzonitic	gabbro, trachyoid	tonalite	qtz monzonite (altered rock)	andesite-dacite (altered rock)	quartz diorite	granite porphyry	granite, subophyritic	andesite-dacite, (altered rock)
Fe ⁺ class																	
MAFI class																	
ASI class																	
SiO ₂	67.29	72.54	75.56	63.64	70.53	70.81	70.95	70.05	58.76	63.86	68.70	68.70	56.47	68.20	71.05	66.85	64.14
TiO ₂	0.70	0.38	0.20	0.56	0.25	0.32	0.37	0.37	0.78	0.54	0.54	0.40	0.40	0.46	0.40	0.51	0.47
Al ₂ O ₃	14.12	14.11	13.11	16.68	14.68	16.17	14.55	14.41	16.21	15.93	15.62	15.62	17.14	15.02	14.98	15.63	14.72
Fe ₂ O ₃	4.66	2.46	1.42	5.12	1.76	3.12	2.75	3.08	2.92	7.87	4.16	2.74	7.22	3.55	2.96	4.09	4.61
MnO	0.08	0.04	0.03	0.10	0.03	0.06	0.05	0.05	0.16	0.07	0.07	0.06	0.12	0.09	0.07	0.03	0.04
MgO	1.20	0.78	0.14	2.68	0.47	0.83	0.70	1.32	3.85	2.08	1.08	1.08	3.88	1.64	1.06	2.26	2.52
CaO	3.10	2.15	0.35	5.34	1.96	2.30	2.99	2.46	6.19	4.15	2.70	4.15	6.82	2.70	3.08	1.35	3.10
Na ₂ O	3.46	3.80	4.44	3.44	3.64	4.15	3.53	4.23	3.66	3.97	4.79	3.73	4.29	4.37	4.29	6.08	6.03
K ₂ O	3.08	3.80	4.99	1.83	4.38	4.91	4.10	2.43	1.15	3.25	2.85	2.85	1.76	2.71	2.94	0.93	0.61
P ₂ O ₅	0.25	0.08	0.03	0.20	0.08	0.13	0.10	0.10	0.28	0.18	0.14	0.14	0.25	0.14	0.12	0.21	0.19
LOI @ 1000°C	1.03	0.69	0.50	1.88	0.87	0.75	1.10	1.16	1.93	1.20	1.00	1.00	1.58	1.48	0.37	2.40	3.89
Total	98.96	100.83	100.76	101.47	98.66	100.85	100.97	100.97	100.82	99.39	99.95	100.09	99.95	100.36	101.33	100.33	100.32
Ag	0.00	0.04	0.09	0.03	0.08	0.04	0.00	0.00	0.02	0.03	0.03	0.07	0.16	0.11	0.05	0.15	0.03
As	0.71	1.59	4.57	0.56	0.13	0.00	0.58	0.61	1.78	4.55	0.18	0.18	0.12	3.34	0.37	4.15	1.18
B	0.00	0.00	0.00	0.00	0.00	0.00	0.00	0.00	0.00	0.00	0.00	0.00	0.00	6.41	0.00	0.00	0.00
Be	0.32	0.31	1.30	0.24	0.37	0.60	0.17	0.16	0.15	0.12	0.35	0.35	0.23	0.46	0.19	0.38	0.45
Ba	492.30	520.50	255.00	408.10	983.20	1060.10	1143.10	446.50	485.90	473.90	643.90	740.10	414.70	694.20	699.80	662.90	815.20
Ce	96.48	47.17	59.68	42.26	80.51	86.64	78.43	22.98	23.52	27.42	32.74	39.87	32.40	33.29	37.63	29.23	31.81
Cr	7.25	0.00	7.37	18.50	0.00	0.00	40.65	28.42	36.46	54.63	34.04	23.19	74.87	0.00	0.00	85.16	110.24
Ga	21.13	16.93	18.09	18.23	18.03	19.82	16.57	15.03	16.20	20.80	18.58	18.14	19.20	18.03	16.20	21.44	18.04
Hf	7.45	3.66	7.02	2.36	3.85	6.88	5.61	2.84	3.56	2.97	3.42	3.79	3.35	4.41	4.72	2.67	2.83
Nb	12.44	7.82	13.12	4.58	11.41	11.27	6.70	2.87	2.95	3.03	3.93	5.66	4.80	3.69	3.90	2.89	3.56
Rb	122.05	143.42	101.18	45.26	167.34	196.15	81.68	38.07	37.37	20.98	64.24	63.47	34.43	72.11	79.09	19.26	13.15
Sc	9.90	7.07	2.95	12.45	3.06	5.32	5.47	5.85	6.25	21.55	11.59	4.92	20.74	9.28	7.20	7.06	7.54
Sn	3.92	1.82	3.10	0.00	3.11	9.12	1.29	0.00	0.00	1.31	1.11	1.14	1.24	1.36	0.00	1.75	1.91
Sr	227.06	182.04	286.62	489.85	355.35	241.50	286.55	404.09	367.96	580.06	436.26	355.45	613.68	508.84	309.33	712.13	544.98
Ta	0.75	0.79	1.25	0.44	0.93	0.87	0.72	0.23	0.17	0.17	0.39	0.51	0.37	0.33	0.39	0.22	0.24
Th	16.40	13.42	9.36	6.95	18.83	15.62	12.00	3.28	2.61	1.83	9.61	5.24	2.98	5.88	6.72	2.37	2.46
U	1.73	3.99	3.51	1.37	2.19	3.43	2.30	0.66	0.87	0.62	1.37	1.94	0.91	2.00	1.69	1.57	0.96
V	45.34	33.24	0.00	91.13	21.25	30.21	28.43	55.25	57.19	167.42	106.83	54.11	165.00	61.49	47.02	72.03	75.15
W	0.00	0.53	0.79	0.00	0.00	0.91	0.60	0.00	0.00	0.00	0.00	0.00	0.00	0.54	0.00	0.00	0.00
Y	30.71	23.26	24.81	11.98	13.44	29.16	20.97	10.00	9.44	23.77	11.93	12.06	21.00	15.44	15.31	8.19	8.30
Zr	255.71	131.67	256.36	88.45	152.49	247.68	198.90	89.89	117.67	97.79	114.91	143.31	117.49	156.52	183.72	84.60	93.60
Cs	10.01	3.42	1.12	1.62	2.73	5.48	0.67	0.31	0.26	0.40	0.94	0.72	0.89	2.15	2.19	1.61	1.30
La	43.96	23.56	29.81	22.09	42.86	42.52	40.72	10.84	11.24	10.85	16.41	20.75	14.59	16.38	18.84	14.20	15.54
Ce	96.48	47.17	59.68	42.26	80.51	86.64	78.43	22.98	23.52	27.42	32.74	39.87	32.40	33.29	37.63	29.23	31.81
Pr	11.83	5.14	6.45	4.51	8.59	9.78	8.72	2.94	2.84	3.89	3.94	4.27	4.52	3.92	4.28	3.52	3.87
Nd	46.84	18.86	23.37	16.34	30.14	35.37	31.92	12.71	11.27	18.61	15.17	15.44	19.40	14.45	15.94	14.58	16.64
Sm	8.63	3.77	4.20	2.78	4.72	6.18	5.52	2.17	2.24	4.40	3.27	2.89	2.94	2.73	2.73	2.46	3.10
Eu	1.78	0.86	0.32	0.92	0.93	1.55	0.89	0.66	1.14	0.94	1.46	0.94	1.46	0.91	0.70	0.83	1.18
Gd	7.52	3.79	3.80	2.71	3.99	5.47	4.50	1.94	1.97	4.05	2.40	2.51	4.34	2.62	2.52	2.35	2.23
Tb	1.13	0.64	0.68	0.40	0.54	0.99	0.69	0.30	0.25	0.70	0.42	0.34	0.75	0.46	0.41	0.33	0.33
Dy	5.65	3.56	4.08	2.13	2.57	4.98	3.81	1.69	1.63	4.11	2.15	2.01	3.79	2.60	2.67	1.64	1.63
Ho	1.08	0.66	0.80	0.43	0.50	1.04	0.70	0.34	0.27	0.85	0.39	0.39	0.82	0.51	0.50	0.30	0.28
Er	3.28	2.36	2.59	1.24	1.34	2.94	2.31	0.92	0.92	2.53	1.23	1.21	2.31	1.78	1.55	0.78	0.85
Tm	0.43	0.38	0.44	0.17	0.20	0.42	0.35	0.16	0.14	0.36	0.16	0.22	0.34	0.24	0.25	0.10	0.12
Yb	3.02	2.60	3.34	1.25	1.29	3.11	2.57	1.14	1.09	2.55	1.58	1.38	2.42	1.86	2.03	0.74	0.73
Lu	0.45	0.40	0.47	0.19	0.16	0.44	0.17	0.09	0.39	0.19	0.21	0.21	0.34	0.29	0.31	0.00	0.13
Eu/Eu*	0.67	0.69	0.24	1.01	0.65	0.81	0.54	0.86	0.96	0.82	1.02	1.06	1.01	1.03	0.81	1.04	1.36
M	1.77	1.64	1.66	1.78	1.65	1.55	1.64	1.60	1.60	2.07	1.96	1.67	2.27	1.65	1.68	1.37	1.80

Table 1. continued

T1-305	T1-306	T1-307	T1-308	T1-309	T1-310	T1-311	T1-312	T1-313	T1-314	T1-315	T1-317	T1-318	T1-319	T2-013	T2-014	T2-015	T2-016
trachyandesite- dacite	granite porphyry, microgranular	granite porphyry, microgranular	granite porphyry, (altered rock)	granite porphyry, (altered rock)	trachyandesite basalte	trachydacite- andesite	trachyandesite- basalte	granite porphyry (altered rock)	granite porphyry trachyandesite- basalte	Magnesian Peralumino	granite porphyry	granite porphyry microgranular	andesite	andesite-basalt K-feldspathic	leucogranite	granodiorite, pegmatoid	quartz syenite- diortite
43,15357 102,92788	43,15364 102,92776	43,15376 102,92770	43,15386 102,92755	43,15419 102,92380	43,15042 102,92810	43,14707 102,92989	43,14500 102,90700	43,14500 102,90700	43,14500 102,90700	43,14500 102,90700	43,14500 102,90700	43,14500 102,90700	43,14500 102,90700	42,88406 106,94015	42,81718 106,87604	42,78765 106,87275	42,67943 106,84014
Magnesian ALKALI-CALCIC Metaluminous	Magnesian ALKALI-CALCIC Metaluminous	Magnesian ALKALI-CALCIC Metaluminous	Magnesian ALKALI-CALCIC Metaluminous	Magnesian ALKALI-CALCIC Metaluminous	Magnesian ALKALI-CALCIC Metaluminous	Magnesian ALKALI-CALCIC Metaluminous	Magnesian ALKALI-CALCIC Metaluminous	Magnesian ALKALI-CALCIC Metaluminous	Magnesian ALKALI-CALCIC Metaluminous	Magnesian ALKALI-CALCIC Metaluminous	Magnesian ALKALI-CALCIC Metaluminous	Magnesian ALKALI-CALCIC Metaluminous	Magnesian ALKALI-CALCIC Metaluminous	Magnesian ALKALI-CALCIC Metaluminous	Magnesian ALKALI-CALCIC Metaluminous	Magnesian ALKALI-CALCIC Metaluminous	Magnesian ALKALI-CALCIC Metaluminous
64.04	65.82	63.75	64.10	57.40	60.91	58.68	64.92	55.59	62.57	69.03	64.32	58.26	58.29	73.89	66.04	68.11	71.58
0.63	0.64	0.66	0.66	0.74	0.74	0.73	0.54	0.76	0.61	0.40	0.56	0.78	0.64	0.14	0.66	0.72	0.42
14.89	15.09	15.13	14.91	15.16	14.99	14.90	15.49	14.89	14.74	15.26	15.14	14.25	14.46	14.17	15.36	15.76	14.98
4.38	4.53	4.99	4.88	5.51	5.50	5.84	4.29	5.98	4.37	3.15	3.99	6.22	5.94	1.33	3.16	3.44	2.43
0.08	0.08	0.10	0.08	0.07	0.08	0.07	0.06	0.10	0.07	0.06	0.05	0.13	0.09	0.08	0.09	0.09	0.06
2.41	2.37	2.84	2.68	4.08	4.14	4.71	2.65	4.80	3.00	1.36	2.85	5.23	4.33	0.32	0.88	1.06	0.80
2.49	2.50	3.10	3.17	4.35	3.98	3.28	2.31	4.76	3.50	1.85	2.36	4.18	4.74	1.20	2.19	2.48	2.14
4.78	4.52	4.27	4.48	5.90	5.65	4.82	4.84	5.89	4.73	4.96	4.83	4.55	5.30	4.38	4.67	4.64	4.51
3.17	3.42	3.40	2.88	1.45	0.64	1.29	1.76	1.12	2.45	2.94	1.88	0.49	0.68	3.81	4.18	4.10	3.69
0.18	0.24	0.26	0.25	0.35	0.27	0.27	0.23	0.35	0.24	0.12	0.22	0.27	0.25	0.07	0.20	0.21	0.11
2.59	1.88	2.54	1.93	5.12	4.42	4.67	3.35	4.90	3.29	1.26	3.56	5.85	5.65	0.67	0.67	0.51	0.91
99.63	101.09	101.06	100.03	100.13	101.33	99.25	100.43	99.14	99.58	100.38	99.75	100.22	100.36	100.07	98.10	101.13	101.62
0.14	0.10	0.09	0.13	0.09	0.06	0.06	0.05	0.08	0.06	0.03	0.11	0.09	0.08	0.03	0.05	0.06	0.02
2.09	2.67	2.21	2.10	5.11	2.66	3.98	1.12	7.05	1.47	1.17	1.92	0.32	1.48	0.89	3.08	2.42	0.88
0.00	0.00	0.00	0.00	0.00	0.00	0.00	0.00	0.00	0.00	6.22	0.00	0.00	0.00	0.00	0.00	0.00	0.00
0.62	0.90	0.74	0.71	0.45	0.62	0.62	0.53	0.62	0.49	0.60	0.48	0.44	0.56	0.27	0.68	0.58	0.29
625.30	692.70	685.30	484.50	781.70	477.20	165.30	633.80	747.50	668.70	676.80	508.50	747.30	357.70	830.22	867.45	819.34	895.08
44.75	46.58	47.93	46.79	49.95	36.14	37.71	22.45	49.37	33.09	31.53	24.36	33.48	32.80	29.79	72.95	71.23	41.87
93.33	93.13	102.70	104.80	141.45	202.77	171.92	102.81	175.36	142.24	0.00	102.64	291.34	315.14	0.00	0.00	0.00	0.00
18.00	19.44	19.37	18.85	18.95	18.16	17.32	20.25	19.12	18.82	14.15	19.76	18.08	18.71	15.54	20.25	20.06	16.58
4.52	4.64	4.46	4.46	2.76	3.43	2.77	3.06	2.58	2.81	3.29	2.65	2.88	2.78	3.20	7.72	8.10	5.47
5.90	6.26	6.26	6.38	3.25	3.94	3.86	3.44	3.26	4.15	3.28	3.46	3.89	3.43	6.19	12.06	13.47	7.60
62.89	69.52	67.06	46.30	27.04	12.08	23.83	27.43	14.38	43.27	70.85	37.19	11.25	12.37	95.24	106.20	106.52	55.46
10.37	10.67	10.82	11.11	12.72	12.56	13.69	8.83	13.80	9.64	7.94	8.42	15.09	15.21	2.78	8.68	8.79	2.35
1.89	1.05	1.74	1.51	0.00	1.25	0.00	1.05	0.00	1.23	0.00	0.00	1.16	0.00	0.00	4.39	2.38	1.14
415.33	587.13	575.70	565.14	697.11	554.38	457.97	444.79	446.63	703.41	378.61	1254.95	362.04	676.76	183.08	332.54	336.59	536.12
0.49	0.54	0.51	0.55	0.30	0.30	0.31	0.24	0.24	0.34	0.30	0.25	0.33	0.30	0.64	0.95	1.18	0.58
5.81	6.39	6.24	6.40	4.02	3.55	3.59	2.50	3.56	3.97	5.82	2.64	3.42	3.21	4.70	7.86	8.32	4.33
1.93	2.00	2.07	2.34	1.37	1.16	1.12	0.83	1.22	1.35	1.70	1.08	1.02	0.93	0.89	2.02	2.23	1.02
85.40	87.66	105.41	92.61	125.37	120.54	127.42	84.93	132.90	96.29	54.59	85.23	142.70	125.97	8.51	51.42	58.17	35.66
0.51	0.67	0.61	0.00	0.00	0.00	0.00	0.00	0.00	0.00	0.00	0.00	0.00	0.00	1.66	1.98	1.76	0.97
15.45	15.38	16.09	15.23	10.39	10.53	10.86	8.79	10.57	9.32	14.47	8.64	12.06	10.86	15.77	30.35	30.96	15.42
157.87	164.50	174.03	169.66	97.23	109.71	97.97	95.97	92.15	104.17	120.11	101.98	105.60	89.53	74.46	242.61	254.48	182.46
1.91	1.74	1.70	1.51	1.05	1.46	2.85	2.76	0.44	0.92	2.22	1.89	2.03	1.54	1.71	3.02	2.74	0.40
21.70	22.52	22.83	22.75	22.75	17.36	17.96	10.46	22.90	15.82	16.07	10.99	15.12	14.97	15.81	36.41	35.44	19.87
44.75	46.58	47.93	46.79	49.95	36.14	37.71	22.45	49.37	33.09	31.53	24.36	33.48	32.80	29.79	72.95	71.23	41.87
5.43	5.66	5.70	5.63	6.41	4.74	4.79	3.01	6.22	4.19	3.80	3.04	4.25	4.24	3.53	8.91	8.55	4.93
21.78	23.52	23.06	23.06	25.76	19.16	19.46	12.36	26.03	17.31	14.58	13.47	18.42	17.05	12.94	33.02	32.45	18.50
4.37	4.83	4.46	4.72	4.60	3.86	3.51	2.29	4.95	2.95	0.72	2.66	3.43	3.63	2.80	6.31	6.52	3.74
1.04	1.22	1.14	1.08	1.63	1.17	1.00	0.87	1.45	1.01	0.75	0.79	1.20	1.04	0.66	1.59	1.48	1.14
3.96	3.88	3.78	3.53	3.25	2.63	2.74	2.01	3.29	2.52	2.46	2.33	2.97	2.81	2.34	5.61	5.54	2.88
0.55	0.54	0.55	0.55	0.39	0.39	0.45	0.30	0.48	0.38	0.42	0.32	0.46	0.46	0.38	0.85	0.81	0.44
2.68	2.76	2.98	2.79	2.01	1.89	2.10	1.58	2.01	1.60	2.34	1.58	2.03	2.27	2.21	5.06	5.02	2.54
0.53	0.52	0.57	0.54	0.40	0.36	0.38	0.30	0.37	0.31	0.46	0.32	0.41	0.41	0.49	1.02	1.01	0.51
1.55	1.62	1.58	1.52	0.97	1.15	1.08	0.90	1.11	0.88	1.57	0.96	1.41	1.26	1.48	2.97	2.97	1.47
0.25	0.23	0.24	0.25	0.15	0.15	0.17	0.13	0.14	0.10	0.23	0.14	0.21	0.19	0.22	0.44	0.46	0.24
1.72	1.44	1.69	1.63	0.92	1.06	1.29	0.90	1.11	0.92	1.78	0.88	1.30	1.17	1.79	3.16	3.41	1.58
0.26	0.26	0.29	0.23	0.15	0.18	0.18	0.15	0.14	0.15	0.28	0.14	0.19	0.17	0.26	0.49	0.49	0.23
0.76	0.80	0.90	0.81	1.28	1.12	0.98	1.23	1.09	1.12	0.85	0.97	1.14	0.99	0.78	0.81	0.75	1.05
1.89	1.81	1.94	1.91	2.35	1.97	1.87	1.53	2.50	2.02	1.59	1.61	1.96	2.25	1.53	1.87	1.80	1.66

Table 1. continued

T2-017	T2-018	T2-019	T2-020	T2-021	T2-022	T2-023	T2-024	T2-025	T2-026	T2-027	T2-028	T2-029	T2-037	T2-038	T2-039	T2-040	T2-041
granite, subophyritic	granite-porphyr., leucocratic	granite, cataclastic	andesite-dacite, tufflava	andesite-dacite, bitite-hornblende	andesite-dacite, tufflava	granite, graphic	andesite-dacite, tufflava	granite-porphyr.	granite, medium/ coarse-grained	granite-porphyr. graphic	granite-porphyr. granodiorite-porphyr.	granite	quartz diorite-porphyr.	granite, cataclastic	granite, cataclastic	granite-porphyr.	granodiorite
42,62012	42,59894	42,65558	42,99889	42,95615	42,92774	42,93870	42,94198	42,92432	42,93870	42,93870	42,99863	43,01488	43,01442	43,35671	43,09260	43,18798	43,19285
106,70946	106,64425	106,60705	106,67123	106,61936	106,56072	106,52432	106,52432	106,52432	106,44021	106,29236	106,20730	106,20822	106,81622	106,78275	106,68878	106,83927	106,79260
314 ± 5						329 ± 6						319 ± 5					
Ferroan	Ferroan	Ferroan	Magnesian	Magnesian	Magnesian	Magnesian	Magnesian	Magnesian	Ferroan	Magnesian	Magnesian	Magnesian	Magnesian	Magnesian	Magnesian	Magnesian	Magnesian
ALKALIC	ALKALIC	ALKALIC	ALKALIC	ALKALIC	ALKALIC	ALKALIC	ALKALIC	ALKALIC	ALKALIC	ALKALIC	ALKALIC	ALKALIC	ALKALIC	ALKALIC	ALKALIC	ALKALIC	ALKALIC
Peraluminous	Peraluminous	Peraluminous	Peraluminous	Peraluminous	Peraluminous	Peraluminous	Peraluminous	Peraluminous	Peraluminous	Peraluminous	Peraluminous	Peraluminous	Peraluminous	Peraluminous	Peraluminous	Metamorphic	Metamorphic
71,41	72,23	72,15	64,81	69,51	67,95	75,36	71,91	71,91	71,91	64,57	77,50	60,99	72,23	73,30	74,06	68,93	65,63
0,31	0,21	0,35	0,33	0,33	0,33	0,33	0,33	0,33	0,33	0,33	0,33	0,33	0,33	0,33	0,33	0,33	0,33
14,27	13,81	14,20	15,80	14,50	15,34	13,23	14,15	14,15	14,15	16,27	13,00	15,90	14,17	13,98	13,30	16,21	15,89
1,46	1,84	2,37	3,71	1,90	3,01	1,39	1,81	1,81	1,81	4,21	0,77	5,42	1,95	1,86	0,94	3,57	3,38
0,03	0,07	0,04	0,06	0,05	0,08	0,05	0,04	0,04	0,04	0,09	0,16	0,08	0,06	0,07	0,03	0,08	0,08
0,22	0,35	0,39	0,42	0,43	0,43	0,27	0,20	0,20	0,20	1,44	0,45	2,53	0,49	0,49	0,27	1,23	1,13
0,76	2,80	1,41	2,67	1,58	2,40	0,74	0,61	0,61	0,61	3,86	0,68	4,51	1,26	1,35	0,97	2,58	2,56
4,31	3,94	3,42	4,13	4,13	4,21	4,18	4,61	4,61	4,61	4,70	3,93	3,99	4,26	4,02	3,57	4,11	4,06
5,23	3,39	4,06	2,98	3,85	3,49	4,20	4,20	4,20	4,20	1,84	2,19	2,19	3,99	3,99	4,67	4,54	4,43
0,03	0,04	0,08	0,19	0,05	0,12	0,02	0,03	0,03	0,03	0,20	0,04	0,26	0,06	0,05	0,03	0,12	0,15
0,45	0,86	0,84	0,97	2,28	1,36	1,04	0,75	1,04	0,75	1,06	0,50	1,86	0,71	0,70	0,45	1,08	0,91
98,49	99,34	99,18	98,06	98,62	99,25	100,66	98,87	98,87	98,87	98,64	100,97	98,58	99,37	100,04	98,43	102,96	98,73
0,06	0,03	0,04	0,06	0,03	0,03	0,03	0,06	0,06	0,06	0,03	0,13	0,13	0,02	0,04	0,03	0,02	0,02
1,02	3,28	0,57	3,39	0,63	1,61	2,47	1,13	1,13	1,13	0,86	0,77	1,35	3,96	1,64	0,89	0,84	1,28
0,00	0,00	0,00	0,00	0,00	0,00	0,00	0,00	0,00	0,00	0,00	0,00	0,00	0,00	0,00	0,00	0,00	0,00
0,27	0,58	0,18	0,54	0,43	0,39	0,64	1,11	1,11	1,11	0,13	0,22	0,15	0,34	0,34	0,27	0,44	0,37
692,06	627,29	610,73	676,68	963,67	688,04	613,38	564,00	536,17	488,65	521,96	488,65	521,96	546,07	596,43	531,96	1185,89	882,73
60,87	51,07	60,47	44,27	44,67	41,06	44,77	59,27	29,44	29,44	34,52	34,52	34,52	46,10	47,53	38,46	48,01	50,13
0,00	0,00	0,00	0,00	0,00	0,00	0,00	0,00	0,00	0,00	0,00	0,00	0,00	0,00	0,00	0,00	0,00	0,00
18,52	15,63	18,41	14,30	17,96	14,95	15,65	18,40	19,02	15,41	15,82	15,82	21,03	15,81	15,82	14,73	17,98	16,58
8,39	11,41	5,75	6,06	6,13	4,85	5,18	8,32	3,88	3,88	4,17	4,17	4,17	4,92	4,37	2,60	7,61	6,91
12,61	11,41	9,67	7,24	7,24	5,77	8,02	10,55	2,99	2,99	6,49	6,49	9,46	10,28	8,49	5,79	6,46	6,65
145,63	76,19	73,36	73,36	73,32	79,32	101,40	99,93	31,83	132,14	43,76	43,76	43,76	102,68	98,07	98,81	145,63	126,39
3,76	3,24	3,86	3,61	4,04	5,31	3,89	4,33	8,97	12,05	10,82	10,82	10,82	4,61	4,61	2,44	8,52	9,12
2,42	2,04	2,21	1,67	1,60	1,23	2,48	3,74	0,00	0,00	1,84	1,84	1,84	1,50	2,43	0,00	1,87	1,60
93,44	304,51	185,74	163,43	372,43	164,91	386,31	61,66	388,82	61,66	106,17	106,17	651,13	148,32	179,42	146,45	389,61	339,36
1,24	1,03	1,32	0,73	0,52	0,63	0,62	0,95	0,21	0,95	0,21	0,70	0,69	1,20	0,87	0,71	0,58	0,58
13,06	11,12	19,74	7,67	5,32	7,32	6,77	7,14	2,77	7,14	2,77	7,43	3,36	10,28	7,78	8,94	7,85	8,93
3,85	2,27	3,64	1,38	1,52	1,30	1,31	1,66	0,65	1,66	0,65	1,25	0,83	1,62	1,71	1,29	2,24	1,70
13,46	20,28	18,70	16,11	56,49	37,43	9,25	8,07	57,29	8,31	57,29	8,31	11,580	18,66	19,09	9,00	64,77	61,23
1,93	1,14	0,73	1,13	1,03	0,78	1,30	1,01	0,76	1,01	0,76	0,54	0,84	0,71	1,82	0,79	0,77	0,00
26,09	19,04	19,51	25,79	28,46	17,46	27,50	33,87	19,72	33,87	19,72	9,64	16,27	24,78	21,86	15,73	21,95	24,44
257,00	115,66	148,17	247,84	175,10	163,60	137,89	271,74	110,41	271,74	110,41	59,70	120,84	141,67	133,43	69,85	256,22	229,07
2,43	0,53	4,34	0,85	1,41	1,29	0,94	1,45	0,59	1,45	0,59	2,02	0,92	1,17	1,05	0,64	2,81	2,02
30,79	27,71	32,84	25,87	21,61	21,42	20,86	28,32	15,42	28,32	15,42	18,33	16,66	23,44	22,54	20,51	23,78	24,27
60,87	51,07	60,47	50,34	44,27	41,06	44,77	59,27	29,44	59,27	29,44	34,52	34,52	46,10	47,53	38,46	48,01	50,13
7,03	5,50	6,72	6,18	5,71	4,64	5,03	7,02	3,59	7,02	3,59	3,79	4,62	5,15	4,96	4,19	5,88	6,07
24,43	19,07	22,98	22,27	23,64	16,69	18,79	25,11	14,30	25,11	14,30	12,47	17,96	18,24	16,74	13,92	21,89	23,45
4,74	3,57	4,41	4,41	3,71	3,30	3,78	5,36	3,14	5,36	3,14	2,52	3,71	3,67	3,19	2,61	4,57	4,96
0,85	0,85	0,68	0,93	0,91	0,42	0,42	0,60	0,92	0,60	0,92	0,92	1,17	0,54	0,57	0,51	1,04	0,97
3,91	3,14	3,45	3,81	3,49	2,90	3,41	4,97	3,27	4,97	3,27	1,98	3,19	3,60	3,25	2,11	3,95	4,10
0,61	0,48	0,50	0,63	0,72	0,43	0,62	0,78	0,47	0,78	0,47	0,29	0,48	0,58	0,52	0,33	0,56	0,60
3,94	2,65	3,03	3,92	4,37	2,41	3,98	5,02	2,84	5,02	2,84	1,42	2,88	3,68	3,30	2,30	3,54	3,85
0,86	0,60	0,62	0,83	0,69	0,57	0,91	1,08	0,65	1,08	0,65	0,33	0,55	0,77	0,69	0,47	0,74	0,77
2,55	1,83	1,76	2,63	2,82	1,66	2,71	3,44	1,93	3,44	1,93	0,93	1,60	2,52	2,16	1,56	2,22	2,42
0,39	0,33	0,29	0,41	0,37	0,27	0,44	0,57	0,31	0,57	0,31	0,14	0,22	0,42	0,37	0,26	0,33	0,38
3,10	2,33	3,14	3,30	2,99	2,21	3,71	4,12	2,37	4,12	2,37	1,12	1,56	2,66	2,30	2,13	2,58	2,90
0,47	0,36	0,29	0,53	0,44	0,34	0,57	0,63	0,34	0,63	0,34	0,18	0,26	0,52	0,40	0,34	0,40	0,45
0,60	0,66	0,53	0,69	0,77	0,89	0,36	0,35	0,87	0,35	0,87	0,44	1,03	0,45	0,54	0,66	0,74	0,66
1,71	1,72	1,60	1,62	1,62	1,67	1,55	1,62	1,55	1,62	1,55	1,48	1,94	1,58	1,56	1,59	1,73	1,83

Table 1. continued

T2-042	T2-043	T2-044	T2-046	T2-047	T2-048	T2-049	T2-051	T2-052	T2-053	T2-054	T2-055	T2-056	T2-057	T2-058	T2-062	T2-063
granodiorite	granodiorite-porphyr.	diorite-porphyr.	granite	granite-porphyr.	quartz monzonite, porphyritic	granite-porphyr., fine-grained	dacite	trachyandesite	dolomite (diabase)	trachydacite	granite	granite, aplite	granite, pegmatoid	granite-porphyr., fine-grained	quartz diorite	diorite-porphyr.
43,22535	43,22120	43,30053	43,39882	43,40945	43,58871	43,61678	43,35083	43,44314	43,44309	43,64580	43,70757	43,69031	43,69890	43,75012	44,03664	44,07967
106,72453	106,49757	106,21064	106,82894	106,72592	106,46056	106,99681	106,27999	106,53340	106,53326	105,89285	106,08504	106,13983	106,16353	106,20575	105,96225	106,30324
318 ± 8			318 ± 9		298 ± 4									286 ± 5	319 ± 6	
Magnesian	Magnesian	Magnesian	Magnesian	Magnesian	Magnesian	Magnesian	Ferroan	Magnesian	Magnesian	Magnesian	Magnesian	Ferroan	Ferroan	Ferroan	Magnesian	Magnesian
ALKALIC	ALKALIC	ALKALIC	ALKALIC	ALKALIC	ALKALIC	ALKALIC	ALKALIC	ALKALIC	ALKALIC	ALKALIC	ALKALIC	ALKALIC	ALKALIC	ALKALIC	ALKALIC	ALKALIC
Peraluminous	Peraluminous	Peraluminous	Peraluminous	Peraluminous	Peraluminous	Peraluminous	Peraluminous	Peraluminous	Peraluminous	Peraluminous	Peraluminous	Peraluminous	Peraluminous	Peraluminous	Peraluminous	Peraluminous
69.34	66.45	57.97	68.32	74.08	68.93	69.22	63.09	65.25	59.86	66.90	73.85	71.88	69.72	73.69	64.59	61.41
0.41	0.62	0.39	0.39	0.39	0.38	0.27	0.90	0.55	0.95	0.54	0.19	0.29	0.37	0.18	0.18	0.63
15.21	14.71	16.56	15.77	13.74	14.60	14.72	14.66	16.36	15.83	16.40	14.63	14.06	14.70	13.70	15.96	15.64
2.41	5.23	8.44	3.29	1.20	3.44	2.42	5.61	3.61	5.91	2.46	1.45	1.49	1.95	1.35	4.16	3.83
0.07	0.09	0.14	0.05	0.02	0.05	0.05	0.13	0.06	0.11	0.08	0.03	0.03	0.05	0.02	0.03	0.09
0.60	2.01	3.59	1.30	0.39	0.79	0.86	1.38	1.61	4.36	0.63	0.28	0.24	0.30	0.19	2.58	2.39
1.30	3.93	7.46	2.82	1.07	1.66	1.84	4.03	3.31	6.17	0.98	0.95	0.95	0.61	0.72	3.82	3.95
4.48	3.47	3.45	4.33	4.16	4.59	3.31	4.52	4.42	3.77	5.15	4.09	4.28	4.80	4.15	4.09	4.10
5.00	3.21	1.15	3.14	4.03	4.39	4.62	1.34	2.88	2.28	5.40	5.24	4.51	4.53	4.80	3.52	2.84
0.08	0.13	0.19	0.08	0.04	0.05	0.08	0.30	0.12	0.33	0.10	0.05	0.05	0.05	0.00	0.19	0.26
0.77	1.35	1.10	1.53	0.50	0.85	1.18	0.58	1.58	2.42	0.73	0.48	0.53	0.58	0.54	1.30	1.01
99.68	101.22	101.04	101.02	99.43	99.74	98.57	96.56	99.74	101.98	99.38	101.25	98.31	97.66	99.34	100.76	96.15
0.08	0.04	0.05	0.03	0.03	0.03	0.04	0.05	0.09	0.11	0.05	0.04	0.05	0.04	0.26	0.03	0.07
1.95	1.71	0.64	4.15	1.40	5.33	8.16	3.07	1.52	3.71	2.80	1.17	1.86	1.60	3.44	1.97	8.33
0.00	0.00	0.00	0.00	0.00	6.91	6.29	0.00	0.00	0.00	0.00	0.00	0.00	0.00	0.00	6.77	0.00
0.92	0.28	0.14	0.30	0.17	1.20	0.69	0.00	0.34	0.31	0.43	0.34	0.42	0.75	0.62	0.40	0.39
671.29	676.09	352.65	748.69	806.90	822.67	847.76	447.59	824.04	740.46	1008.55	347.94	732.33	744.77	592.41	888.61	968.08
62.42	38.79	18.88	29.61	38.64	67.84	51.05	21.90	30.81	48.67	98.80	50.83	39.30	57.29	46.57	49.14	45.65
0.00	0.00	0.00	0.00	0.00	0.00	0.00	0.00	11.91	195.11	0.00	0.00	0.00	0.00	0.00	135.76	61.03
18.13	16.86	18.34	17.38	14.25	23.31	16.91	18.08	18.74	21.27	21.12	17.31	17.50	19.49	16.22	19.04	18.11
9.48	6.90	3.15	3.76	3.67	7.93	4.71	3.33	3.32	4.23	12.14	4.90	6.19	9.09	6.13	4.42	3.69
8.93	3.95	2.32	2.71	6.31	7.42	5.52	7.96	4.26	7.96	9.79	8.17	7.37	10.72	7.82	7.08	7.48
148.39	86.23	26.39	68.60	78.72	108.11	155.36	18.80	44.25	33.22	61.86	115.77	102.83	106.33	116.66	93.87	47.79
7.05	17.35	27.53	7.30	2.25	7.44	5.23	20.17	7.19	17.05	7.76	3.73	3.28	5.18	3.43	10.44	9.19
2.01	1.44	1.30	0.00	4.47	2.58	1.42	1.20	0.00	1.15	0.00	2.10	1.86	2.68	2.15	1.50	1.19
166.19	300.56	376.87	480.25	256.73	205.49	260.32	379.63	745.04	1355.54	254.36	146.45	166.99	149.02	105.38	839.81	128.108
0.75	0.36	0.22	0.26	0.69	0.70	0.61	0.15	0.40	0.58	0.71	0.91	0.80	0.91	0.93	0.63	0.60
12.09	6.61	2.04	4.85	6.52	9.30	11.05	1.61	2.84	2.71	6.68	9.22	7.03	8.27	8.54	12.24	6.18
3.04	1.13	0.54	1.57	1.12	2.23	1.38	0.39	0.98	0.90	1.86	1.43	1.41	2.32	1.63	2.04	1.34
29.00	110.40	257.70	70.54	16.40	28.93	29.81	69.00	81.89	197.30	31.04	14.03	12.37	11.85	10.56	88.25	111.50
0.97	0.61	0.00	0.96	0.00	1.38	1.72	0.51	0.59	0.52	0.85	0.58	0.90	1.18	0.67	0.70	0.58
32.46	34.96	23.83	8.97	8.52	40.99	15.10	31.79	9.74	13.70	28.64	20.58	17.62	28.41	22.47	15.28	11.01
283.85	196.03	79.94	136.25	119.70	297.66	161.40	108.23	126.19	146.93	515.77	142.41	226.28	377.65	186.98	143.32	126.25
5.34	1.33	0.46	1.21	0.87	1.43	5.01	0.72	0.57	0.27	0.54	1.98	2.29	1.45	2.26	1.23	1.25
30.56	17.86	8.37	16.38	21.25	32.31	16.38	9.36	16.05	23.25	49.56	26.83	18.82	27.48	24.46	25.69	24.21
62.42	38.79	18.88	29.61	38.64	67.84	51.05	21.90	30.81	48.67	98.80	50.83	39.30	57.29	46.57	49.14	45.65
7.49	5.25	2.73	3.35	4.32	8.77	5.87	3.39	3.60	6.20	11.62	5.60	4.31	6.60	5.40	5.65	5.68
29.27	22.31	11.90	14.44	14.44	33.40	20.93	15.71	12.91	24.96	42.07	20.09	14.71	23.35	19.41	20.92	22.20
5.98	5.35	2.06	3.35	2.23	7.28	3.77	4.29	2.48	4.60	6.98	3.76	2.91	4.44	3.71	4.11	4.09
0.98	0.94	1.00	0.63	0.46	1.45	0.73	1.39	0.76	1.29	1.62	0.47	0.71	0.88	0.56	1.10	1.05
5.40	5.13	3.72	1.62	1.73	6.95	3.19	5.03	2.15	3.43	6.15	3.37	2.83	4.21	3.46	3.50	2.89
0.77	0.87	0.63	0.24	0.25	1.08	0.44	0.80	0.25	0.50	0.84	0.49	0.71	0.71	0.56	0.44	0.39
4.88	5.32	3.81	1.40	1.26	6.87	2.60	5.36	1.63	2.67	4.89	3.17	2.86	4.42	3.38	2.67	2.06
1.06	1.17	0.81	0.32	0.27	1.33	0.51	1.09	0.32	0.50	0.98	0.66	0.59	0.91	0.72	0.53	0.39
3.31	3.30	2.44	0.89	0.85	4.19	1.58	3.34	1.00	1.32	2.89	2.06	1.85	2.86	2.28	1.43	1.19
0.52	0.52	0.37	0.15	0.14	0.69	0.24	0.48	0.15	0.20	0.44	0.34	0.22	0.44	0.34	0.22	0.16
3.88	3.75	2.74	1.12	1.03	4.73	1.65	3.53	1.04	1.29	3.34	2.54	2.16	3.28	2.82	1.74	1.00
0.58	0.57	0.38	0.18	0.15	0.66	0.26	0.48	0.15	0.19	0.52	0.38	0.34	0.53	0.40	0.26	0.15
0.53	0.55	0.86	1.06	0.72	0.62	1.64	0.91	1.00	0.99	0.75	1.61	0.76	0.62	0.47	0.88	0.93
1.74	1.90	2.26	1.65	1.55	1.81	1.64	1.88	1.73	2.29	1.78	1.61	1.63	1.64	1.62	1.93	1.98

straightforward in the western sector, the Eastern sector has experienced repeated magmatism since the Upper Devonian (Wainwright et al., 2011) and was thus grouped as the Eastern zone, with three age-based subgroups: 329 Ma, 319–314 Ma, and 298–288 Ma respectively. The western sector was divided into the NW and SW zones both of which were dated at ~307 Ma and the Khongor Complex (319 Ma).

2.1. Petrology and geochemistry of granitic rocks

All samples discussed are of intermediate to felsic composition and have a range of TiO_2 from 0.12–0.99 wt.%. Each group demonstrates a normal negative correlation of SiO_2 vs TiO_2 space (Fig. 4A).

In accordance with the geochemical classification of Frost et al. (2001), the majority of samples are Magnesian in nature (Fig. 4B) and plot in the alkali-calcic field on a SiO_2 vs MALI diagram (Fig. 4C). Outlying points for some of the “Carboniferous” samples can be variably attributed to post-emplacement hydrothermal alteration (sericitization of feldspars and regional epidotization) and weathering affects. The only grouping which consistently contains samples within the Ferroan field (Fig. 4B) and the alkalic field (Fig. 4C) is the Permian group from the Eastern sector. This group is also characterized by high SiO_2 values (66.89–73.85 wt.%) and straddles both the Ferroan/Magnesian and alkalic/alkali-calcic field boundaries (Fig. 4B and C).

All studied samples have an ASI (Alumina Saturation Index) value of less than 1.1, classifying them as metaluminous to weakly peraluminous (Shand, 1943) which corresponds to I-type values of Chappell & White (1974) (Fig. 4D). Therefore, in accordance with the schema of Frost et al. (2001), the majority of samples examined can be classified as Metaluminous Magnesian Alkali-Calcic granitoids and roughly corresponding to the I-type class of Chappell & White (1974). The granitoids of the Permian group occupy the same geochemical space in the plot B and C in figure 4, as was demonstrated by Frost et al. (2001) for “A-type” granitoids.

The trace element diagram of Pierce et al. (1984) was used to determine a geotectonic setting for the examined granitoids. In the Nb+Y vs Rb space (Fig. 4E inset) all samples plot in the Volcanic Arc Granitoid (VAG) field of Pierce et al. (1984). The data distribution spread for all samples converges towards the triple point of the VAG - Within-Plate (WPG) - Syn-Collisional fields (Pierce et al., 1984). This is particularly the case of the Permian group.

A plot of Nb+Y vs Zr (ppm)/M (defined in Watson & Harrison, 1983) splits the samples further, with the Permian group showing significantly higher Nb+Y vs Zr (ppm)/M values

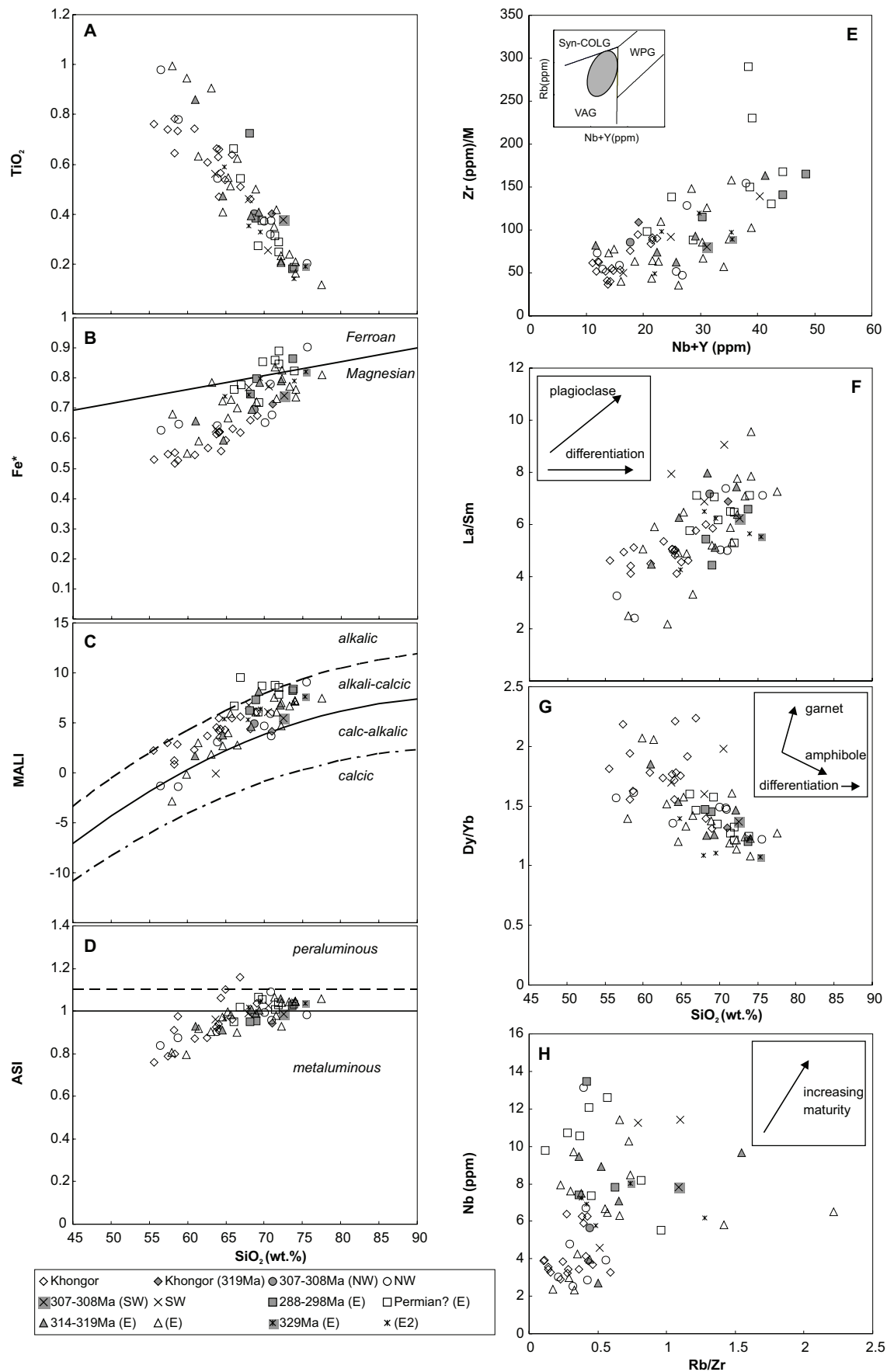


Figure 4: Plots of SiO_2 vs. TiO_2 (A), SiO_2 vs. Fe^* (B), SiO_2 vs. MALI (C), SiO_2 vs. ASI (D), $\text{Nb}+\text{Y}$ vs Zr (ppm)/M (E), SiO_2 vs. La/Sm (F), SiO_2 vs Dy/Yb (G) for samples of intrusive units which are of intermediate to acidic composition.

(ranging from 88.26 to 290), which is consistent with major element chemistry of "A-type" granitoids in figure 4B and C (Frost et al., 2001; Loiselle & Wones, 1979). Notably a small number of samples from the eastern and western Carboniferous groups also have elevated Nb+Y vs Zr (ppm)/M values. When the Nb+Y vs Zr (ppm)/M is high, there is a corresponding negative Eu anomaly suggesting that the crystallization of feldspar-plagioclase is in part responsible for the "highly fractionated" signature observed (Table 1).

The effect of plagioclase can be described further in the SiO₂ vs La/Sm space (Fig. 4F). Samples from the Khongor group and the Eastern 319-314 Ma group show the largest variation in SiO₂ vs La/Sm with strong positive correlation (Fig. 4F). Samples from the southwestern group have a higher average La/Sm value than those of the northwestern group despite a broadly similar SiO₂ distribution (Fig. 4F). The cluster of Permian samples is also suggestive of a significant role of plagioclase in their fractionation history.

The heavy REE distribution is described by the plot SiO₂ vs Dy/Yb (Fig. 4G). This shows that the Khongor samples have a strongly positive correlation, suggesting that garnet was an important phase during their evolution. The samples from the southwestern group display no clear correlation, which may also be indicative of the role of garnet, whereas all other groups have a negative correlation suggesting that either clinopyroxene or amphibole were the crucial phases.

The plot of Rb/Zr vs Nb (ppm) shows an overall positive correlation trend (Fig. 4H). The granitoids of the Permian group have the highest average values in this space consistent with their generally more evolved nature, whereas the Khongor group shows the least evolved signature. The eastern 319-314 Ma group shows the greatest variation with an overall positive correlation.

2.2. U-Pb zircon geochronology

Zircons were separated at St. Petersburg University, and magmatic grains were dated on the SHRIMP II of the Center of Isotopic Research, VSEGEI, St-Petersburg, Russia, after spot selection on cathodoluminescence images. Analytical procedures are detailed in Seltnann et al. (2011).

Sample locations are listed in Table 1 and shown in figure 3, the U-Th-Pb SHRIMP data for magmatic zircons in Table 2, and for two selected sample suites, two concordia are plotted on figure 6. In total 13 samples of granitoids were analysed (Table 2, Fig. 3). Representative

of the full dataset, figure 5 illustrates two characteristic samples of the Carboniferous suite and two characteristic samples of the Permian suite for which the Concordia analytical results are described below. All analyzed grains are magmatic and none contains inherited cores.

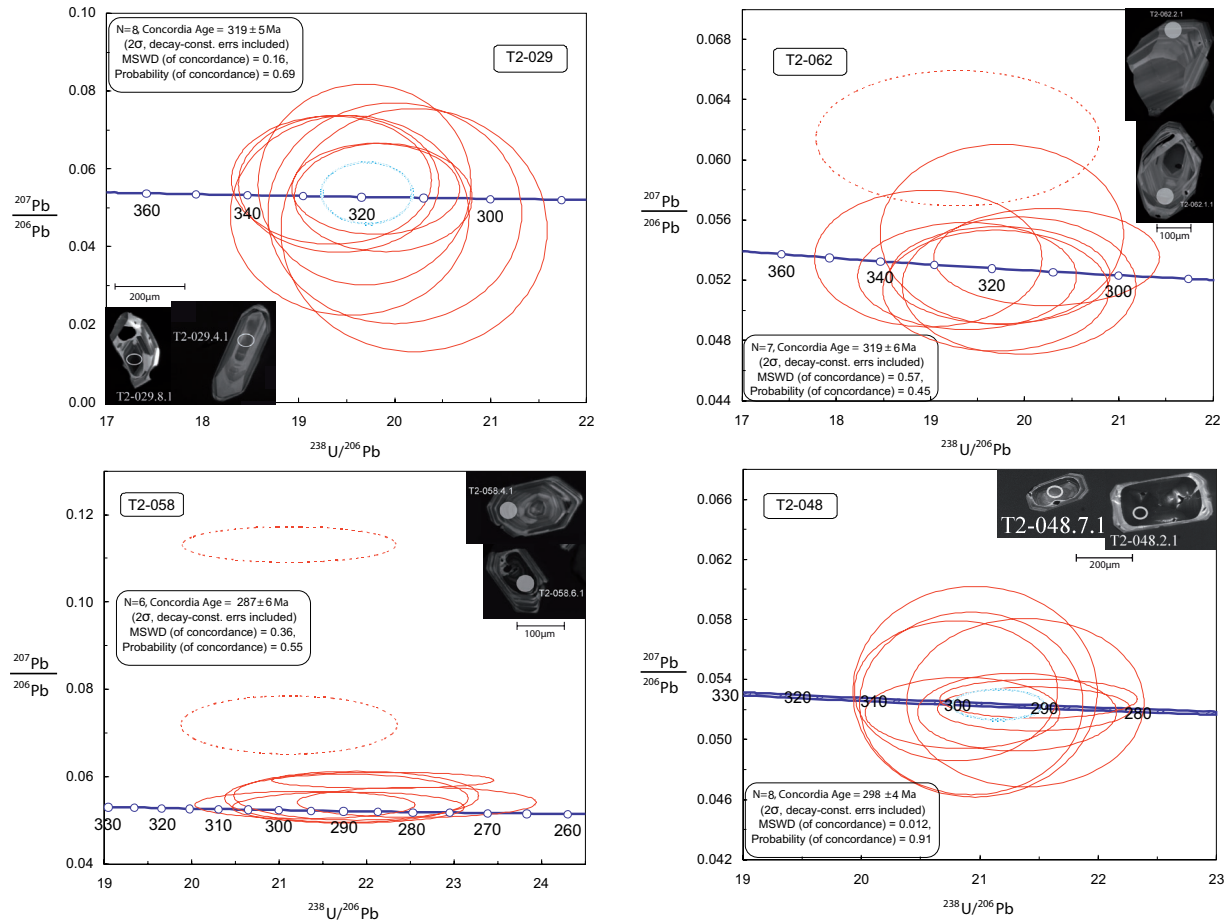


Figure 5: U-Pb Concordia diagrams. Red ellipsoids denote data used for Concordia age calculations. Error ellipses are 2σ .

Sample T2-029: Eight spots were analysed in eight zircon grains. The spots were located in both inner and outer parts of the grains. All 8 analyses plot on concordia as a tight cluster and yield a $^{206}\text{Pb}/^{238}\text{U}$ concordia age of 319.3 ± 5.0 Ma (MSWD = 0.16) which is a preferred crystallization age of sample T2-029.

Sample T2-062: On CL images the zircon grains are characterized by stubby or elongate shapes with distinct facets and oscillatory and sector zoning. Eight spots were analysed on eight zircon grains. The spots were located in both inner and outer parts of the grains. Seven out of eight analyses plot on concordia as a relatively tight cluster and yield a $^{206}\text{Pb}/^{238}\text{U}$ concordia age of 319 ± 6 Ma (MSWD = 0.57) which is a preferred crystallization age of sample T2-062.

Sample T2-058: On CL images the zircon grains are characterized by strongly elongate prismatic shapes with distinct facets and oscillatory zoning. Eight spots were analysed on eight

Table 2: U-Pb analytical data and calculated ages.

Sample- spot # ^a	Concentrations			Isotope ratios ^c								Age (Ma)					
	U	Th	Th/U	²⁰⁶ Pb ⁺	f206 ^b	²⁰⁷ Pb ⁺	±1σ	²⁰⁷ Pb ⁺	±1σ	²⁰⁶ Pb ⁺	±1σ	err. ^d	²⁰⁶ Pb ⁺	±1σ	²⁰⁷ Pb ⁺	±1σ	Disc. ^e
	ppm	ppm		ppm	%	²⁰⁶ Pb ⁺	%	²³⁵ U	%	²³⁸ U	%	corr.	²³⁸ U		²⁰⁶ Pb	%	
Sample T1-190																	
T1-190.1.1	742	234	0.33	32.6	0.71	0.0449	10.7	0.314266	10.7	0.0508	1.0	.092	319.1	3.1	-61	261	-119
T1-190.2.1	692	206	0.31	28.6	0.64	0.0478	10.9	0.315204	11.0	0.0478	1.1	.098	301.2	3.2	89	259	-70
T1-190.3.1	741	268	0.37	30.5	0.10	0.0496	3.4	0.327952	3.5	0.0479	0.9	.242	301.8	2.5	178	80	-41
T1-190.4.1	502	150	0.31	21.6	0.34	0.0494	6.5	0.339843	6.6	0.0499	1.0	.158	314.2	3.2	165	151	-48
T1-190.5.1	317	117	0.38	12.1	0.10	0.0562	4.8	0.342946	5.0	0.0443	1.5	.306	279.3	4.2	459	106	64
T1-190.6.1	321	154	0.49	13.4	--	0.0576	5.1	0.385599	5.2	0.0486	1.3	.243	305.8	3.8	513	112	68
T1-190.7.1	537	156	0.30	22.7	--	0.0527	3.7	0.357839	3.9	0.0492	1.0	.256	309.9	3.0	316	85	2
T1-190.8.1	686	224	0.34	29.3	0.22	0.0521	4.5	0.356605	4.6	0.0497	0.9	.191	312.5	2.7	288	103	-8
Sample T1-192																	
T1-192.1.1	265	199	0.78	12.2	0.45	0.0492	8.9	0.363	9	0.0535	1.5	.165	336	4.9	158	210	-53
T1-192.2.1	166	75	0.46	7.13	0.00	0.0504	6.4	0.347	6.7	0.04996	1.8	.273	314.3	5.6	215	150	-32
T1-192.3.1	221	117	0.55	9.59	0.54	0.0537	7.6	0.372	8.2	0.0502	3	.374	315.8	9.4	358	170	13
T1-192.4.1	281	162	0.59	11.5	0.19	0.0525	5.6	0.345	5.8	0.04773	1.6	.282	300.5	4.8	306	130	2
T1-192.5.1	359	368	1.06	15.1	1.12	0.0436	13	0.291	13	0.04839	1.4	.107	304.6	4.2	-134	330	-144
T1-192.6.1	216	117	0.56	9.15	1.40	0.0484	15	0.325	15	0.0487	2.1	.135	306.4	6.2	120	360	-61
T1-192.7.1	264	154	0.60	11.6	0.74	0.0489	13	0.343	13	0.05078	1.6	.120	319.3	5	145	310	-55
T1-192.8.1	217	128	0.61	8.9	0.00	0.0557	6.4	0.368	6.6	0.04782	1.6	.251	301.1	4.8	442	140	47
Sample T1-239																	
T1-239.1.1	476	689	1.49	20.4	0.00	0.0515	5.6	0.354	5.8	0.04991	1.6	.282	314.0	5	263	130	-16
T1-239.2.1	227	178	0.81	9.8	2.23	0.046	27	0.307	27	0.0487	2.5	.094	306.7	7.5	-22	640	-107
T1-239.3.1	82	50	0.63	3.3	0.00	0.0576	14	0.375	14	0.0472	3.5	.250	298.0	10	514	300	73
T1-239.4.1	151	93	0.64	6.4	0.00	0.0619	16	0.429	16	0.0503	2.9	.183	316.1	9.1	672	340	113
T1-239.5.1	74	36	0.51	2.8	0.00	0.072	17	0.432	18	0.0434	4.7	.266	274.0	13	991	350	262
T1-239.6.1	153	121	0.81	6.2	0.97	0.0586	13	0.374	13	0.0463	2.7	.208	291.8	7.7	552	280	89
T1-239.7.1	30	17	0.60	1.3	0.00	0.094	17	0.64	18	0.0497	5.8	.322	312.0	18	1502	320	381
T1-239.8.1	255	325	1.32	10.8	1.34	0.0446	18	0.299	19	0.0486	2.5	.132	305.8	7.3	-79	450	-126
Sample T1-302																	
T1-302_1.1	100	61	0.62	4.39	--	0.0728	11	0.522	12	0.052	2.7	.231	326.7	8.6	1009	230	209
T1-302_2.1	132	83	0.65	5.67	0.57	0.0564	7.4	0.387	7.8	0.0497	2.5	.313	312.7	7.5	468	160	50
T1-302_3.1	171	130	0.78	7.42	0.35	0.0521	6.3	0.363	6.8	0.0504	2.4	.358	317.1	7.5	292	140	-8
T1-302_4.1	406	407	1.04	15	0.29	0.0594	5.2	0.352	5.7	0.04296	2.3	.396	271.1	6	581	110	114
T1-302_5.1	109	66	0.63	4.93	1.63	0.0422	14	0.301	15	0.0517	2.5	.176	325	8.1	-214	360	-166
T1-302_6.1	179	136	0.79	7.78	0.72	0.0468	9.8	0.325	10	0.0503	2.4	.237	316.1	7.4	41	240	-87
T1-302_7.1	46	50	1.12	18	--	0.1609	2.7	10.17	3.6	0.458	2.4	.656	2432	48	2465	46	1
T1-302_8.1	131	83	0.66	5.81	1.41	0.0451	20	0.316	20	0.0509	2.6	.133	320	8.2	-51	480	-116
Sample T2-015																	
T2-015.1.1	153	104	0.70	5.94	0.60	0.0454	11	0.281	12	0.0449	3.5	.297	283.2	9.7	-32	270	-111
T2-015.2.1	237	239	1.04	9.35	0.13	0.052	3.5	0.329	4.9	0.0458	3.4	.699	288.9	9.6	287	80	-1
T2-015.3.1	153	109	0.74	6.04	0.26	0.0505	5.4	0.319	6.4	0.0458	3.5	.547	288.6	9.9	218	120	-24
T2-015.4.1	215	168	0.81	8.45	0.17	0.0511	3.6	0.322	5	0.0458	3.5	.694	288.4	9.7	243	83	-16
T2-015.5.1	172	125	0.75	6.69	0.23	0.0516	4	0.321	5.3	0.0451	3.5	.655	284.2	9.6	268	91	-6
T2-015.6.1	156	107	0.71	6.29	0.00	0.0552	3.3	0.358	4.8	0.047	3.5	.719	296	10	422	75	43
Sample T2-019																	
T2-019.1.1	1107	969	0.90	48.4	1.37	0.0531	4.8	0.367	5.2	0.05016	1.9	.374	315.5	5.9	332	110	5
T2-019.2.1	469	367	0.81	20.3	1.96	0.0504	9.9	0.343	10	0.0494	2	.201	310.8	6.2	214	230	-31
T2-019.3.1	1990	1099	0.57	86.1	3.60	0.0526	5.6	0.352	5.9	0.04853	1.9	.323	305.5	5.7	310	130	1
T2-019.4.1	249	160	0.66	11.4	0.77	0.0547	5.8	0.399	6.3	0.0529	2.4	.378	332.6	7.7	399	130	20
T2-019.5.1	322	309	0.99	13.8	2.97	0.0565	10	0.377	11	0.0484	2.1	.198	304.4	6.2	471	230	55
T2-019.6.1	412	328	0.82	18	0.42	0.0522	3.9	0.365	4.3	0.05074	1.9	.450	319.1	6.1	295	88	-8
T2-019.7.1	650	480	0.76	28.4	1.59	0.0495	7.4	0.342	7.6	0.0501	1.9	.255	315.1	6	172	170	-45
Sample T2-025																	
T2-025.1.1	187	69	0.38	8.35	0.20	0.0539	4	0.386	4.7	0.0519	2.5	.531	326.4	7.9	367	90	13
T2-025.2.1	207	78	0.39	9.49	0.89	0.0503	7.8	0.368	8.2	0.053	2.5	.301	332.9	8	210	180	-37
T2-025.3.1	180	37	0.21	8.02	0.17	0.0527	3.8	0.376	4.5	0.0518	2.5	.542	325.7	7.8	315	87	-3
T2-025.4.1	87	50	0.59	3.78	0.40	0.0539	7	0.374	7.5	0.0503	2.6	.346	316.3	8	369	160	17
T2-025.5.1	205	81	0.41	9.42	0.25	0.0536	3.4	0.395	4.1	0.0534	2.4	.582	335.6	7.9	353	76	5
T2-025.6.1	191	108	0.59	8.67	0.34	0.0534	3.6	0.388	4.3	0.0527	2.4	.561	330.9	7.8	346	81	5
T2-025.7.1	292	129	0.46	13.4	0.37	0.0545	5.2	0.399	5.8	0.0531	2.4	.417	333.5	7.8	394	120	18
T2-025.8.1	218	95	0.45	9.9	0.52	0.052	4.2	0.376	4.8	0.0525	2.4	.503	330	7.8	284	95	-14
Sample T2-029																	
T2-029.1.1	91	80	0.90	4.09	1.11	0.0563	13	0.399	13	0.0515	2.2	.167	323.4	7	462	280	43
T2-029.2.1	91	72	0.81	4.09	0.72	0.057	11	0.407	12	0.0517	2.2	.185	325.1	7	492	250	51
T2-029.3.1	56	43	0.80	2.51	2.06	0.048	22	0.339	22	0.0512	2.6	.121	321.7	8	102	510	-68
T2-029.4.1	64	51	0.82	2.84	2.71	0.049	24	0.335	24	0.05	2.7	.110	314.5	8	128	570	-59
T2-029.5.1	137	123	0.93	6.0	1.24	0.0526	10	0.365	11	0.0503	1.9	.184	316.3	6	312	240	-1
T2-029.6.1	116	98	0.87	5.15	1.67	0.056	19	0.392	19	0.0508	2.3	.119	319.7	7	449	420	40
T2-029.7.1	53	35	0.69	2.34	3.55	0.044	29	0.302	29	0.0495	2.8	.098	311.2	9	-96	710	-131
T2-029.8.1	177	177	1.03	7.77	1.08	0.0549	8.7	0.382	8.9	0.0505	1.8	.207	317.6	6	407	200	28

Table 2. continued

Sample T2-042																	
T2-042.1.1	288	141	0.51	12.7	0.04	0.0521	2.5	0.369	4.2	0.0514	3.4	,809	323	11	289	56	-10
T2-042.2.1	263	184	0.72	11.6	0.34	0.0585	4.9	0.413	5.9	0.0512	3.4	,575	322	11	550	110	71
T2-042.3.1	1632	2954	1.87	69.7	0.65	0.0516	2.4	0.351	4.1	0.0494	3.3	,807	311	10	266	56	-14
T2-042.4.1	149	89	0.61	6.6	0.58	0.0508	8.1	0.358	8.8	0.0511	3.5	,396	321	11	234	190	-27
T2-042.5.1	381	199	0.54	17.2	0.62	0.0511	5.8	0.367	6.7	0.052	3.4	,506	327	11	247	130	-25
T2-042.6.1	120	48	0.41	5.2	0.15	0.0501	4.7	0.347	5.9	0.0503	3.6	,600	316	11	199	110	-37
T2-042.7.1	262	184	0.73	11.2	0.75	0.0587	6	0.399	6.9	0.0493	3.5	,499	310	10	556	130	79
Sample T2-046																	
T2-046.1.1	72	27	0.38	3.14	0.23	0.0502	6.4	0.35	7.3	0.0506	3.6	,492	318	11	204	150	-36
T2-046.2.1	117	49	0.43	5.31	0.98	0.045	13	0.323	14	0.0521	3.5	,260	327	11	-58	320	-118
T2-046.3.1	114	46	0.41	5.07	0.03	0.0537	5.8	0.382	6.8	0.0516	3.5	,515	324	11	357	130	10
T2-046.4.1	90	37	0.43	3.94	0.15	0.0501	5	0.351	6.1	0.0508	3.5	,581	320	11	200	110	-37
T2-046.5.1	101	40	0.41	4.32	0.25	0.0503	5.2	0.345	6.3	0.0498	3.5	,558	313	11	207	120	-34
T2-046.6.1	158	139	0.91	4.98	0.13	0.0512	5.2	0.258	6.3	0.0366	3.6	,567	231.7	8	249	120	7
T2-046.7.1	70	26	0.39	2.74	1.70	0.043	23	0.267	24	0.0451	3.8	,162	284	11	-173	580	-161
T2-046.8.1	138	82	0.61	5.98	0.69	0.0499	9.5	0.344	10	0.05	3.6	,349	315	11	190	220	-40
Sample T2-048																	
T2-048.5.1	1303	1547	1.23	52.1	—	0.0527	1.0	0.3381	1.9	0.0465	1.6	,844	293.1	5	317	23	8
T2-048.2.1	1875	2549	1.40	75.1	0.07	0.0520	1.1	0.3344	1.9	0.0466	1.6	,805	293.7	4	287	26	-2
T2-048.4.1	136	66	0.50	5.5	0.53	0.0525	4.4	0.3382	4.8	0.0468	1.9	,402	294.6	6	305	99	4
T2-048.6.2	574	516	0.93	23.1	0.10	0.0518	2.0	0.3352	2.6	0.0469	1.6	,619	295.6	5	277	47	-6
T2-048.1.1	105	62	0.61	4.3	0.27	0.0532	5.4	0.3499	5.8	0.0477	2.0	,349	300.5	6	337	122	12
T2-048.7.1	175	76	0.45	7.1	—	0.0524	4.7	0.3453	5.1	0.0478	1.8	,362	300.9	5	303	108	1
T2-048.3.1	667	459	0.71	27.5	0.09	0.0518	1.9	0.3423	2.5	0.0480	1.6	,653	302.0	5	276	43	-9
T2-048.6.1	420	357	0.88	17.4	0.26	0.0532	3.6	0.3529	4.0	0.0481	1.7	,426	302.7	5	339	81	12
Sample T2-058																	
T2-058.1.1	96	35	0.38	3.78	0.58	0.0504	10	0.317	11	0.0457	2.7	,253	287.8	8	212	240	-26
T2-058.2.1	965	63	0.07	37.4	0.65	0.054	3.4	0.333	4.1	0.0448	2.3	,570	282.3	7	369	76	31
T2-058.3.1	279	148	0.55	11.2	0.31	0.0511	5.5	0.329	6	0.0468	2.4	,408	294.9	7	243	130	-18
T2-058.4.1	91	42	0.47	3.56	0.21	0.054	5.2	0.339	5.8	0.0456	2.6	,450	287.5	7	369	120	28
T2-058.5.1	221	89	0.42	8.7	0.81	0.0464	9	0.291	9.3	0.0455	2.5	,272	286.9	7	17	220	-94
T2-058.6.1	450	217	0.50	18.3	6.54	0.0613	11	0.373	11	0.0442	2.5	,231	278.8	7	649	230	133
T2-058.7.1	306	139	0.47	12.5	2.50	0.0518	14	0.33	14	0.0462	2.5	,182	290.8	7	276	310	-5
T2-058.8.1	229	82	0.37	8.71	0.35	0.0513	5.3	0.312	5.8	0.0441	2.5	,428	278.4	7	252	120	-9
Sample T2-062																	
T2-062.1.1	72	33	0.47	3.13	0.82	0.0484	12	0.335	12	0.0502	2.8	,229	315.7	9	119	280	-62
T2-062.2.1	88	50	0.58	3.8	0.28	0.0494	5.9	0.341	6.4	0.05	2.6	,398	314.6	8	166	140	-47
T2-062.3.1	185	110	0.61	7.85	0.05	0.0532	2.6	0.362	3.5	0.0494	2.4	,685	310.8	7	336	58	8
T2-062.4.1	87	51	0.61	3.93	0.45	0.0498	8.1	0.36	8.5	0.0525	2.6	,310	329.6	9	187	190	-43
T2-062.5.1	174	93	0.55	7.73	0.53	0.0572	4.6	0.407	5.6	0.0516	3.2	,569	324	10	500	100	54
T2-062.6.1	144	89	0.64	6.37	0.29	0.05	5.3	0.354	5.8	0.0514	2.5	,421	323.3	8	194	120	-40
T2-062.7.1	173	90	0.53	7.54	0.00	0.0523	2.5	0.366	3.5	0.0507	2.4	,694	318.6	8	300	57	-6
T2-062.8.1	114	59	0.53	4.96	0.04	0.051	3.3	0.357	4.1	0.0508	2.5	,604	319.2	7.7	240	76	-25

^a the last two digits denote number of grain and number of analytical spot within the grain

^b f206 denotes 100*(common ²⁰⁶Pb)/(total measured ²⁰⁶Pb)

^c corrected for ²⁰⁴Pb

^d Error correlation ²⁰⁷Pb/²³⁵U - ²⁰⁶Pb/²³⁸U.

^e Disc. % denotes 100*((1 - (age²⁰⁶Pb/²³⁸U)) / (age²⁰⁷Pb/²⁰⁶Pb))

zircon grains. The spots were located in both inner and outer parts of the grains. Six out of eight plot on concordia as a relatively tight cluster and yield a ²⁰⁶Pb/²³⁸U concordia age of 287 ± 6 Ma (MSWD = 0.36) which is a preferred crystallization age of sample T2-058.

Sample T2-048: On CL images the zircon grains are characterized by stubby and slightly elongate prismatic shapes with distinct facets and oscillatory zoning. Eight spots were analysed on seven zircon grains. The spots were located in both inner and outer parts of the grains. All eight analyses plot on concordia as a tight cluster and yield a ²⁰⁶Pb/²³⁸U concordia age of 298 ± 4 Ma (MSWD = 0.012) which is the preferred crystallization age of sample T2-048.

3. New observations of structural geology and tectonic evolution of the South Gobi and Trans-Altai Zones

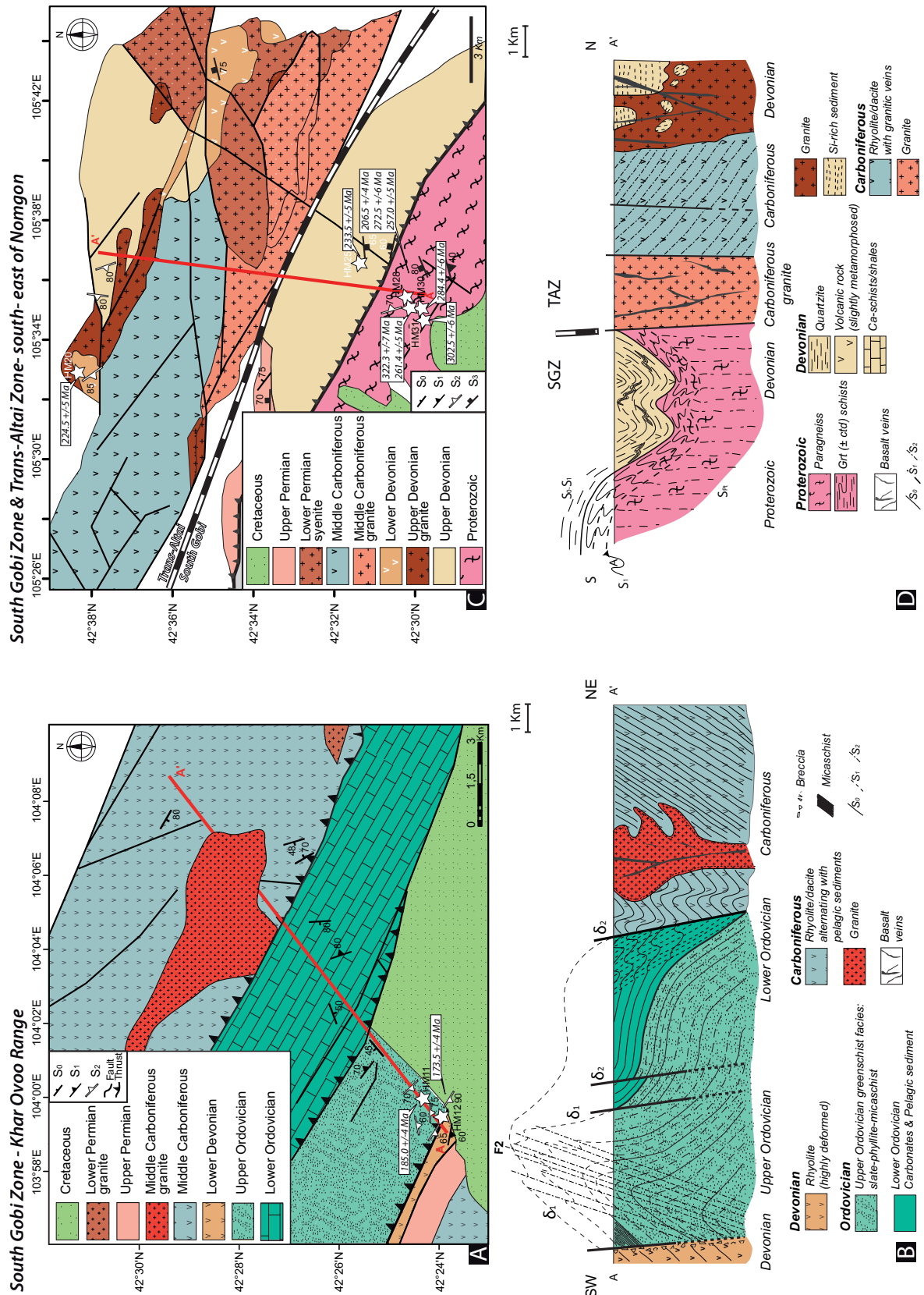
3.1. The South Gobi Zone

Two cross-sections, accross the Khar Ovoo Range located 120 km to the south of Dalanzadgad and the Noyon Uul syncline in the north (Fig. 1), show structural styles of the South Gobi Zone at different crustal levels.

3.1.1. Structural geology of the Khar Ovoo Range

This cross-section consists of Carboniferous volcanic rocks and granites to the north, a sequence of Lower to Upper Ordovician rocks in the middle, and Devonian carbonates with volcanic rock intercalations to the south (Fig. 6A).

The Carboniferous volcanic rocks are intruded by undeformed late Carboniferous granite and show a well-developed, variably dipping flow fabric. These rocks are juxtaposed against Ordovician sediments along a late fault contact (Fig. 6B). The dip of the bedding of the Lower Ordovician sediments is variable but generally steep near the contact with the Carboniferous volcanic rocks. The structurally higher Lower Ordovician sequences are affected by small-scale upright folds with E–W trending hinges, accompanied by fracture cleavage. Towards the footwall, the shales gradually pass into Upper Ordovician slates, phyllites and micaschists in the Upper Ordovician with well-defined bedding parallel to schistosity, marked by preferred orientation of muscovite and quartz ribbons and the development of isoclinal syn-schistose folds. The metamorphic schistosity is folded along E–W trending upright folds with axial planes dipping steeply to the south (Fig. 8 – HM11a). This late post-metamorphic folding is represented either by kink bands and chevron folds of small dimensions (Fig. 8 – HM11b) or by large 100-meter scale folds (Fig. 6B) associated with the development of spaced and crenulation cleavage. Farther south occurs a narrow strip of highly deformed low-grade Devonian rocks marked by growth of tiny sericite crystals on foliation planes affected by a subvertical, E–W trending cleavage.



3.1.2. Structural geology across the Noyon Uul Syncline

Three different cross-sections that cover the Noyon syncline as well as surrounding rocks were studied (Fig. 7A). The A-A' structural section (Fig. 7B) starts in the south in the Lower Carboniferous volcanic sequences that are followed by Lower to Upper Permian volcanoclastic rocks and finally by Triassic and Jurassic clastic sequences of the Noyon Uul syncline. The Lower Carboniferous and the Permian sequences to the south are deformed by large-scale, open N-S trending, upright folds with sub-horizontal hinges as shown in the C-C' cross-section (Fig. 7B) and photograph HM54 (Fig. 8). The limbs of these large folds were affected by subsequent N-S shortening that produced metre-scale E-W trending upright folds with subhorizontal hinges (Fig. 7B, A-A' cross-section). The asymmetrical folding is accompanied by the formation of north-vergent thrusts (Fig. 8 photograph HM89b). This combined structural pattern of N-S upright folds refolded by E-W upright folding can be further depicted from the map pattern of the Carboniferous volcanic strata south east of the Noyon Uul syncline (Fig. 7A). The structural data collected here reveal the presence of a basin-like structure, slightly elongated in an E-W direction (Fig. 7B, B-B' cross-section). The results of the N-S compression are most pronounced in the Triassic and Jurassic clastic rocks that are folded by the large-scale E-W trending upright Noyon Uul syncline (Fig. 7B, A-A' cross-section). The higher amplitude of the Noyon Uul syncline compared to the low amplitude of folds affecting the Carboniferous and Permian Palaeozoic rocks may be explained due to the occurrence of syn-sedimentary fold (Hendrix et al., 1996).

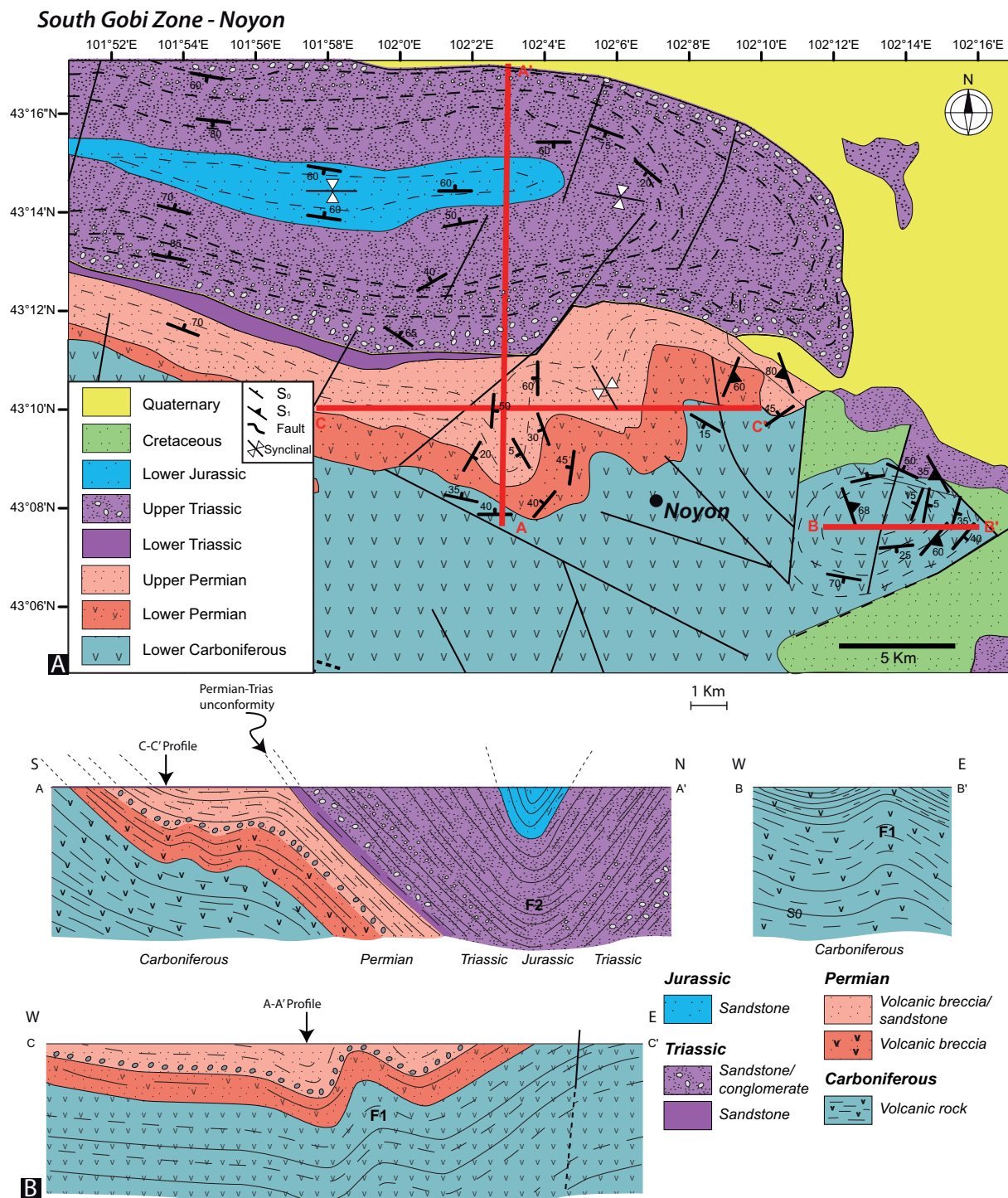
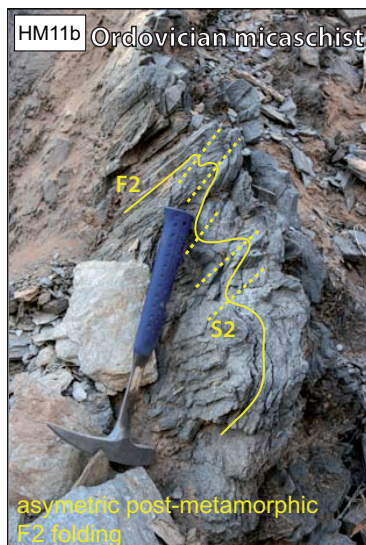
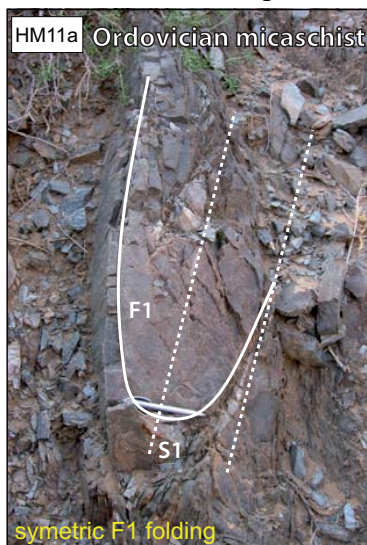
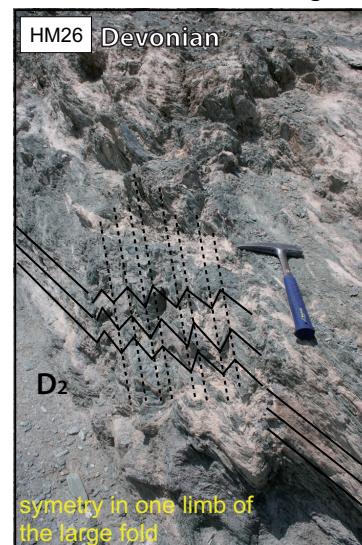


Figure 7: A. Structural map of the Noyon Uul syncline area. Structural trends indicate extrapolations of major orientations of structural foliations measured in the field. The red lines are the locations of the cross-sections. B. Interpretative structural cross-sections.

Profile Khar Ovoo range :



Profile South-east of Nomgon:



Profile Noyon:

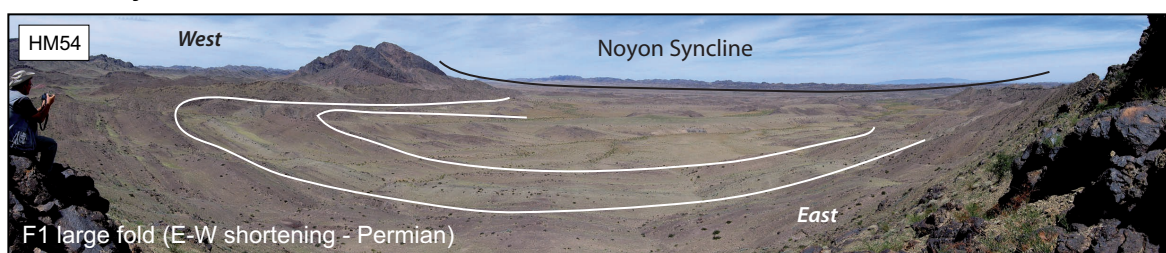


Figure 8: Field photographs showing structural features observed in the South Gobi Zone. (HM 11a) Ordovician micaschist folded symmetrically in the area of the Khar Ovoo Range; (HM11b) Ordovician micaschist with asymmetric post metamorphic F2 folding in the area of the Khar Ovoo Range; (HM26) Devonian kinkbands in one limb of a larger fold to the south-east of Nomgon; (HM54) Permian volcaniclastic F1 large fold with N-S hinge trending in Noyon area; (HM89b) Duplex and F2 Upper Permian sandstone with E-W hinges trending in Noyon area.

3.2. The Trans-Altai Zone

Four N–S trending sections that crosscut the Gurvansaykhan terrane (Badarch et al., 2002) of the Trans-Altai Zone were investigated.

3.2.1. Structural geology east and north-east of the Sevrey village

The Sevrey range is characterized by Upper Silurian volcano-sedimentary rocks containing elongated fragments of mantle rocks (Fig. 10, HM76) and forms an ESE–WNW trending belt thrust over the Upper Devonian pelagic sediments to the south (Fig. 9A and B). The Upper Silurian and Lower Devonian oceanic rocks reveal a greenschist–facies schistosity that has reworked the siliceous Upper Silurian-Lower Devonian metasediments, serpentized peridotite and opicalcites (Fig. 9B). These rocks were subsequently folded into tight E–W upright folds associated with the development of an intense crenulation cleavage. The Upper Devonian sediments and volcanic rocks to the south and north display large-scale, open, E–W trending folds without an axial planar cleavage. To the south, a belt of Permian basalts and tuffs, locally intruded by dykes of Permian granite, displays steep bedding dipping to the NE (Fig. 9B).

The Gurvansaykhan Range (Fig. 1) differs from the Sevrey Range by the presence of an important Lower Carboniferous volcano-sedimentary sequence (Fig. 10, HM119 and Fig. 9C) rimming the E–W trending belt of Upper Silurian and Lower Carboniferous rocks (Fig. 9D). The Upper Silurian rocks display a greenschist–facies metamorphic schistosity that was affected by regional E–W trending folding associated with a steep spaced cleavage forming a fan structure. The Upper Devonian volcanic rocks display a strong and steep spaced cleavage crosscutting bedding surfaces at various angles, attesting that the Upper Devonian is deformed by a large scale E–W trending fold (Fig. 9D). Bedding of the Lower Carboniferous sediments is also folded into E–W trending folds of various scales (Fig. 10, HM119).

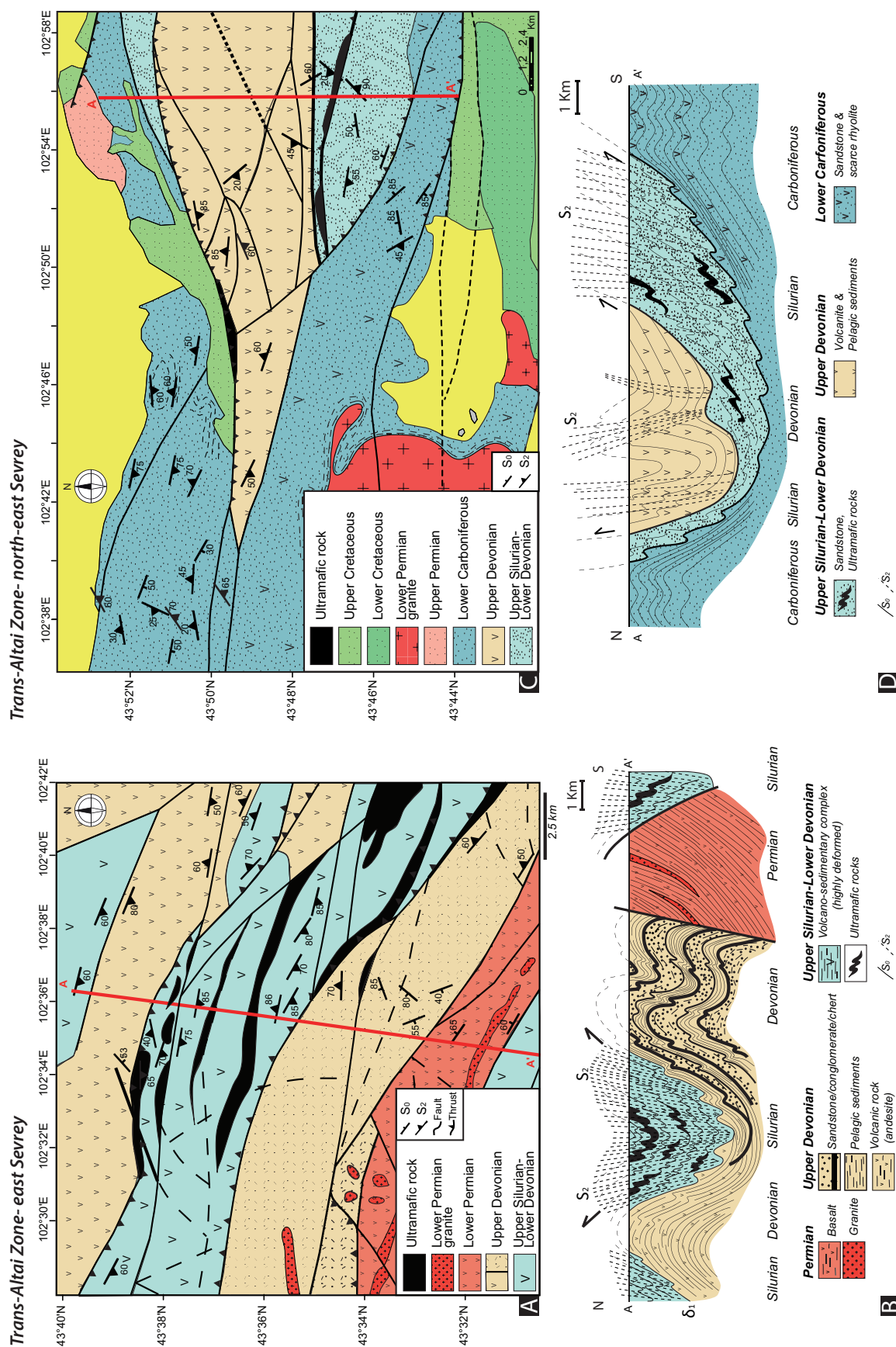


Figure 9: A. Structural map of the area located to the east of the Sevrey village. Structural trends indicate extrapolations of major orientations of structural foliations measured in the field. The red line is the location of the cross-section. B. Interpretative structural cross-sections. C. Structural map of the area located to the north east of the Sevrey village. The red line is the location of the cross-section. D. Interpretative structural cross-sections.

3.2.2. Structural geology of the Nomgon district

The Lower Silurian volcano-sedimentary rocks west of Nomgon village are gently folded into upright NNW–SSE trending folds and separated from Lower Carboniferous sequences by a steep fault farther to the north (Fig. 11A). The Lower Carboniferous graywackes and shales are marked by repetition of sedimentary packages along west-vergent thrust surfaces, suggesting an E–W imbrication and N–S folding of the entire sequence. The imbricated thrust pile is refolded by E–W trending upright folds in a large-scale synform located in the eastern part of the studied area. The Lower Permian rocks in the northern part of the section reveal the presence of a steep E–W trending cleavage, consistent with a general N–S shortening event.

The region east of Nomgon village exposes Permian rocks in the south showing a steep E–W dipping spaced cleavage (Fig. 11B and C). The Permian rocks are juxtaposed against the Devonian volcanic suite that shows well-developed NW or SE dipping spaced cleavages associated with late kink-bands and E–W trending upright folds developed in the volcanic tuffs (Fig. 10, HM36). In some places, these volcanic rocks are intruded by Carboniferous granite that contains xenoliths of undeformed Devonian volcanic rocks (Fig. 11B). Farther north occur Lower Permian volcanic rocks and tuffs that reveal no signs of ductile deformation. The Middle and Lower Carboniferous volcanic rocks were affected by at least two phases of folding. The older medium to large-scale, N–S trending folds with moderately to steeply south dipping axial planes were refolded by E–W trending folds of similar wavelength and amplitude, and moderate to steeply dipping axial planes to the south (Fig. 11C, cross-sections A-A' and B-B'). The early, open to tight N–S trending folds have rounded hinges and are associated with locally developed spaced cleavage (Fig. 11C, cross-section B-B'). In contrast, the late E–W trending folds show typical buckle forms, and the hinges are cut by numerous quartz veins (Fig. 10, HM144).

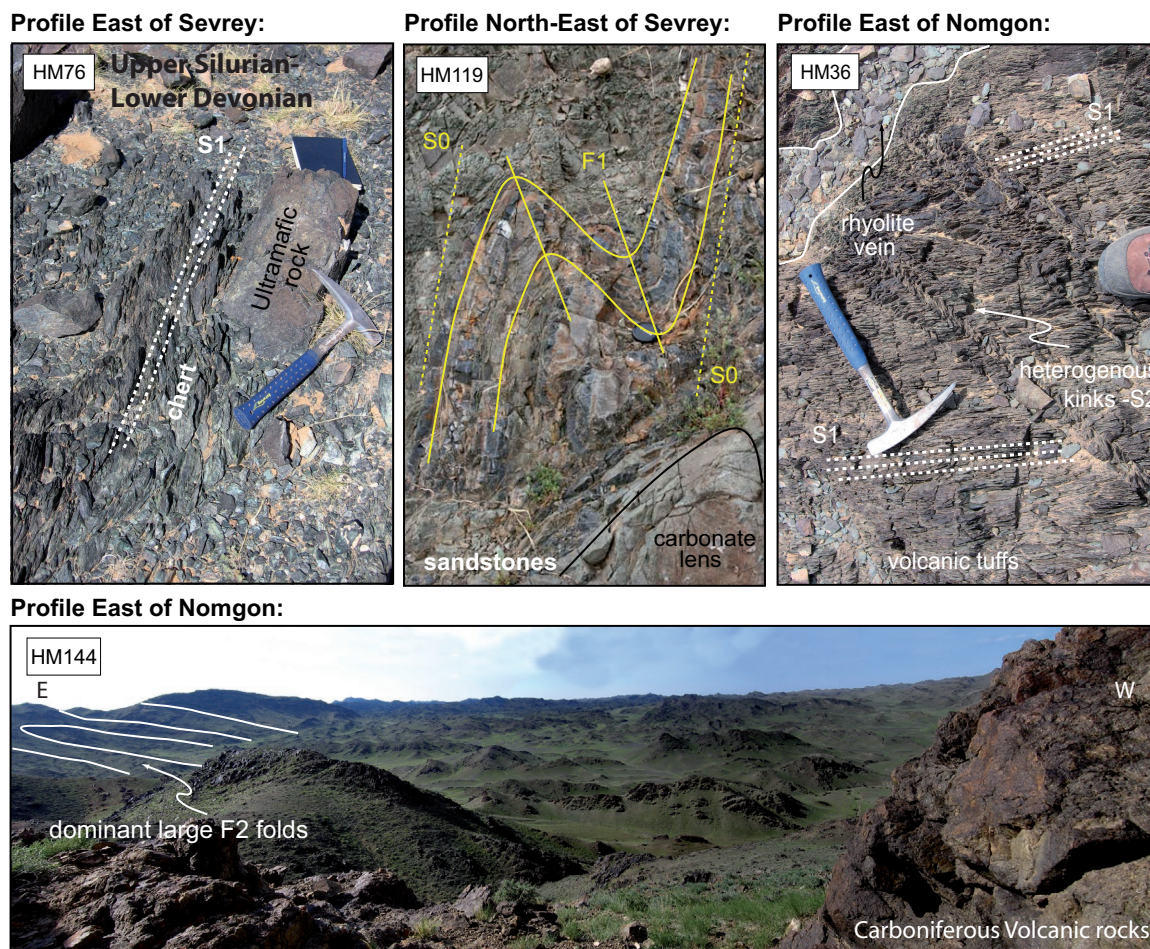


Figure 10: Field photographs showing structural features observed in the Trans-Altai Zone. (HM76) Upper Silurian-Lower Devonian chert intercalated with lenses of ultramafic rocks to the east of the Sevrey village; (HM 119) Lower Carboniferous sandstones intercalated with carbonate lens showing F1 folding to the north-east of the Sevrey village; (HM 36) Devonian volcanic tuff S2 kinkbands intruded by rhyolitic veins to the east of Nomgon; (HM144) Overview of large F2 folds with N-S hinges trending in Carboniferous volcanics, to the east of Nomgon.

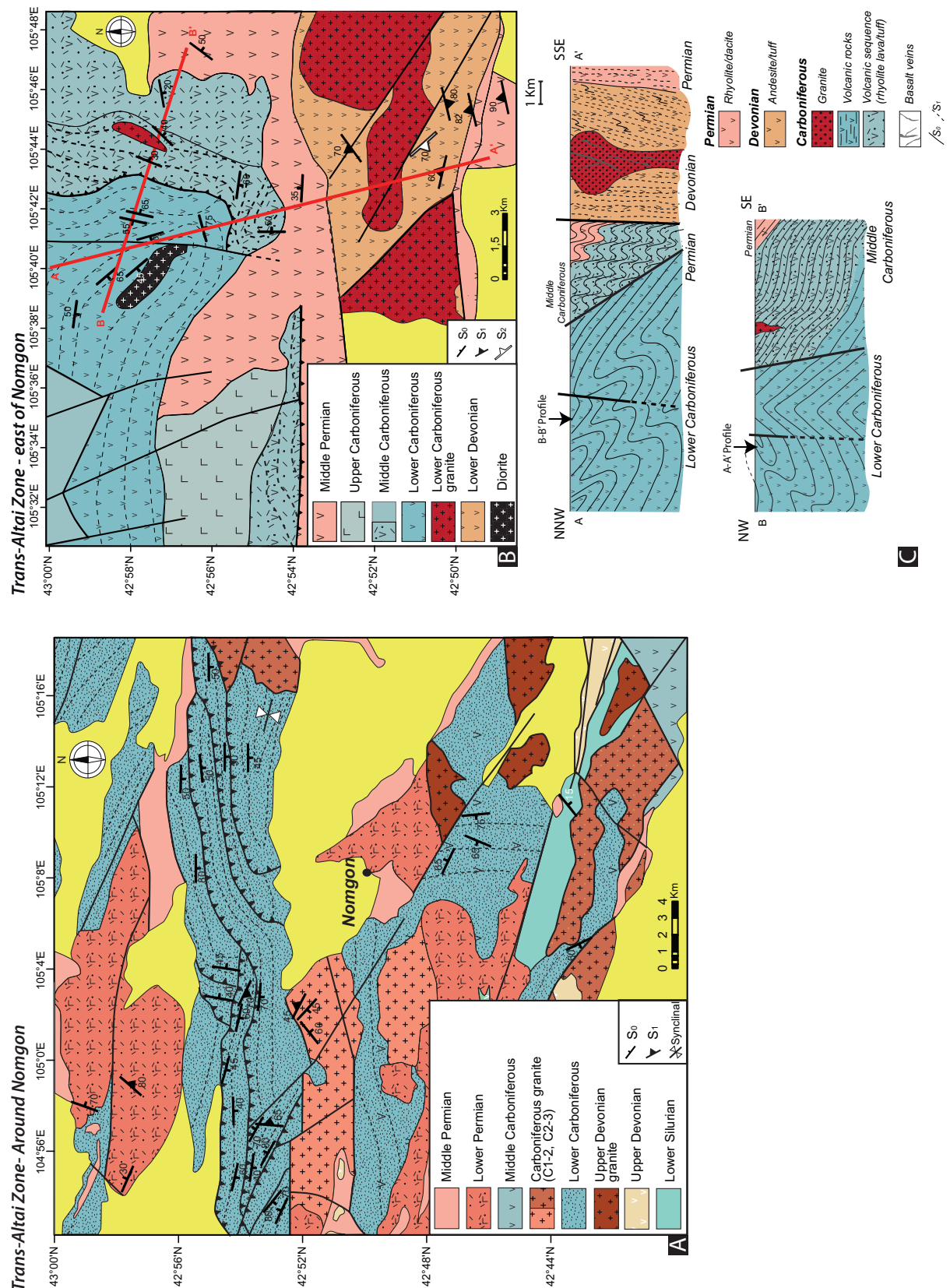


Figure 11: A. Structural map of the area located around the Nomgon village. Structural trends indicate extrapolations of major orientations of structural foliations measured in the field. B. Structural map of the area located to the east of the Nomgon village. The red lines are the location of the cross-sections. C. Interpretative structural cross-sections.

3.3. The South-Gobi/Trans-Altai transition

The regional trend of lithologies suggests that this section crosses the boundary between the South Gobi and the Trans-Altai zones (Fig. 1 and Fig. 6C). However, no important fault zone is observed that can be correlated with the Gobi-Tianshan fault zone farther to the west (Lehmann et al., 2010). The southern part of the section (Fig. 6C) consists of a Proterozoic basement inlier in tectonic contact with Devonian and Silurian cover (Fig. 6C), whereas the northern part of the section is marked by the presence of Devonian and Carboniferous granitoids, Devonian metasediments and volcanic rocks typical of the Trans-Altai Zone.

Structural observations show that the rocks of the Proterozoic basement reveal the most complex structural patterns characterized by dispersed and NW–SE trending metamorphic fabrics. In several places, this metamorphic fabric is refolded by meter-scale N–S trending, close to isoclinal folds with axial planes moderately dipping towards the west or east. All these structures were refolded by open upright E–W trending folds. The adjacent Devonian slates reveal a complete transposition of bedding into a new metamorphic schistosity (Fig. 6D) that is further refolded by several hundred meters wavelength E–W trending upright folds with sub-horizontal hinges and by numerous small-scale kink bands and chevron folds (Fig. 8, HM26).

The northern (Trans-Altai Zone) part of the section consists of Carboniferous granitoids and volcanic rocks (Fig. 6C). These volcanic rocks show isoclinal folds and elongated volcanoclastic rocks probably related to lava and ignimbrite flows. The isotropic Carboniferous granite is cut by a set of N–S trending tensional joints resulting from a N–S oriented compressive stress and an E–W horizontal extension. This is compatible with the orientation of late E–W trending folds that were measured in the adjacent metasediments of presumed Devonian age. The Devonian slates occur in form of stoped blocks within supposedly Devonian granodiorite (precise age uncertain) that shows a well-developed steep N–S trending magmatic fabric defined by alignment of mafic enclaves and preferred orientation of plagioclase and hornblende. In contrast, the Carboniferous granites (precise age unknown) and volcanic rocks (Fig. 6D) do not reveal the N–S trending emplacement fabrics (Bouchez et al., 1997). Finally, farther to the west occur Devonian volcanic rocks that are not represented in the cross-section. These rocks have been affected by an early, steep, N–S trending schistosity that was refolded by later, post-metamorphic, upright E–W trending folds.

4. K-Ar dating of low grade fabrics

4.1. Analytical procedure

After removal of altered parts, fresh sample fragments were gently crushed and the powders were dropped into de-ionized water to separate the $<2\ \mu\text{m}$ size fraction by gravity, following Stokes law. This size fraction $<2\ \mu\text{m}$ was X-rayed (XRD) to check if the mineral composition is only illite. Then, illite was dated by the K-Ar method. The XRD determinations were made on smear slides of air-dried, ethylene-glycolated and heated specimens of each $<2\ \mu\text{m}$ fraction. The illite crystallinity index was controlled by measuring the Full Width at Half Maximum (FWHM) of the (001) illite peak. This index allows rapid evaluation of the illite crystallization degree (Kübler and Goy-Eggenberger, 2001) with limits of the FWHM set at 0.55 for the limit between the diagenetic and anchimetamorphic domains, and at 0.25 for the limit between the sub-greenschist and anchimetamorphic domains.

The K-Ar dating procedure was similar to that described by Bonhomme et al. (1975). Potassium was measured by atomic absorption with an overall reproducibility of ca. 1.5 %. For Ar analysis, the samples were pre-heated under vacuum at 100°C for about 12 hours to reduce the amount of atmospheric Ar adsorbed on the mineral surfaces during sample preparation and handling. Ar extractions were controlled by analysis of the international GL-O and LP6 standards and the $^{40}\text{Ar}/^{36}\text{Ar}$ ratio of atmospheric Ar. The K content was 6.55% and that of the radiogenic ^{40}Ar 1.1246×10^{-9} mol/g for one measurement of the GL-O standard, and 8.37% and 1.9068×10^{-9} mol/g also for one measurement of the standard LP6 during the study. The $^{40}\text{Ar}/^{36}\text{Ar}$ ratio of the atmospheric Ar was measured at 295.9 ± 0.1 (2σ) in two independent measurements. These data being close to the theoretical values, there was no need for data corrections. The decay constants recommended by Steiger and Jäger (1977) were used for the age calculations, and the overall error of the K-Ar age determinations was evaluated to be better than 2%.

4.2. Results

The K-Ar method is a geochronological method applied to date very low grade metamorphic events or age of formation of clay minerals related to fault rocks like cataclasites or gouges. By dating ultrafine grained fractions of illites or white micas the method allows to determine the age of deformation events in very low grade metasediments and hydrothermal activity of fault zones. Eleven samples were collected at two locations and dated to support the timing of the structural events described above. The Upper Ordovician micaschist HM 11B and the Devonian siltstone HM 12 that reveal strongly developed E-W trending spaced cleavage

were collected at the Khar Ovoo Range (Fig. 6A). The nine other samples come from SE of the village of Nomgon and were taken on both sides of the structural limit between the Trans-Altai and South Gobi zones (Fig. 6C). They consist of: 1) a Devonian greenschist-facies metavolcanic rocks HM 20B affected by strong low-grade deformation within the Trans-Altai Zone, 2) Devonian slates HM 25A from the South Gobi Zone bordering the Trans-Altai Zone, and 3) a variety of Proterozoic rocks from the South Gobi Zone basement including strongly retrograded paragneisses HM 8B2 and HM 28B3, and the greenschist-facies rocks HM 28A from the contact between basement and Devonian cover. In addition, samples were taken from the structurally deepest part of the South Gobi Zone basement revealing isoclinally refolded chloritoid micaschists HM 29A and HM 29B, amphibolite HM 30 and metabasite HM 31B (Fig. 6C).

The X-ray diffraction study shows that illite is the dominant mineral component (100 to 36%) of most of the extracted <2 µm size fractions, except for amphibolite HM 30 (Table 3). The other mineral is chlorite (6 to 90%), except for the two Proterozoic paragneisses HM 28 B2 and HM 28B3, and the Upper Devonian micaschist HM 11B. Kaolinite was detected in the claystone HM 25A, the paragneiss HM 28B2 and the chloritoid HM 29B. Its occurrence in the two strongly metamorphosed samples HM 28B2 and HM 29B suggests an overprint by a greenschist-facies metamorphism. The Full Width at Half Maximum (FWHM) values of the illite crystallinity are clearly indicating epimetamorphic conditions (limit at 0.25 at the anchimetamorphic domain). Most values are below and suggest metamorphic crystallization temperatures at least above 250°C (Clauer and Chaudhuri, 1998).

Table 3: XRD mineralogical data of the studied <2 m fractions.

Sample ID	Stratigraphy	Lithofacies	illite (%)	chlorite (%)	kaolinite (%)	Acc. Min.	FWHM
HM 11B	U. Ordovician	micaschist	100			Qz, Fth	0.21
HM 12	Devonian	siltstone	94	6		Sm	0.30
HM 25A	Devonian	claystone	51	44	5	Qz, Fth	0.18
HM 20B	Devonian	volcanite	56	44		Qz, 2Fth, Cal	0.19
HM28A	Proterozoic	greenschist	36	64		Qz, 2Fth, Cal	0.30
HM28B2	Proterozoic	paragneiss	94		6	Qz, Fth	0.20
HM28B3	Proterozoic	paragneiss	100			Qz, Fth	0.20
HM 29A	Proterozoic	chloritoid	49	51		Fth	0.20
HM 29B	Proterozoic	chloritoid	49	47	4	Qz, Fth, Cal	0.20
HM 30	Proterozoic	amphibolite	10	90		Fth	0.40
HM 31B	Proterozoic	nd	nd	nd	nd	nd	nd

Acc. Min. stands for accessory minerals, for FWHM see text

The overall quality of the Ar extractions can be evaluated from the percentage of radiogenic ^{40}Ar extracted from different size fractions that is systematically higher than 87 % of the total amount of measured ^{40}Ar (Table 4). The limited set of eleven K-Ar data for $<2\ \mu\text{m}$ size fractions provides K-Ar ages ranging from 173.5 ± 3.6 to 322.3 ± 6.6 Ma. The fractions of the two stratigraphically host rock Ordovician and Devonian from the Khar Ovoo Range site yielded the youngest K-Ar ages at 180 ± 5 Ma. The samples collected near Nomgon village contain $<2\ \mu\text{m}$ fractions whose K-Ar ages range from about 206.6 ± 4.1 Ma for the Proterozoic greenschist HM 28A, Triassic ages of 220 ± 5 and 230 ± 5 Ma for the two Devonian rocks HM 20 and HM 25A, respectively and Palaeozoic ages from ~ 260 Ma to ~ 322 Ma for the $<2\ \mu\text{m}$ size fraction of the basement rocks HM 31, HM 30 and HM 29, HM 28.

Table 4: Results of the K-Ar dating.

Sample ID	Stratigraphy	K (%)	rad. ^{40}Ar (%)	rad. ^{40}Ar (mol/g $\times 10^{-9}$)	Age (Ma) ($\pm 2\sigma$)
HM 11B	U. Ordovician	6.13	92.82	2.0712	185.0 (3.8)
HM 12	Devonian	4.16	87.88	1.3139	173.5 (3.6)
HM 25A	Devonian	2.18	91.46	0.9423	233.5 (4.7)
HM 20B	Devonian	3.34	89.02	1.3847	224.5 (4.5)
HM 28A	Proterozoic	3.39	87.49	1.2872	206.6 (4.1)
HM 28B2	Proterozoic	4.28	91.86	2.1840	272.5 (5.5)
HM 28B3	Proterozoic	4.97	91.48	2.3813	257.0 (5.1)
HM 29A	Proterozoic	4.07	94.40	2.4912	322.3 (6.6)
HM 29B	Proterozoic	3.88	88.33	1.8926	261.4 (5.4)
HM 30	Proterozoic	1.20	87.99	0.6411	284.4 (5.9)
HM 31B	Proterozoic	2.08	90.36	1.1881	302.5 (6.1)

Whatever the type, the stratigraphic age and the metamorphic grade of the selected host rocks, the K-Ar ages of their $<2\ \mu\text{m}$ clay mineral size fractions are within the timing of the Palaeozoic greenschist-facies shearing, from about 322 to 260 Ma, and the timing of Mesozoic deformation from 240 to 170 Ma. On the basis of this preliminary set of K-Ar ages on mica-type $<2\ \mu\text{m}$ fractions, the Palaeozoic greenschist-facies shearing D1 appears to be the major deformational event in the region since the Proterozoic period. Also, no specific age trend relates to the degree of crystallization or recrystallization of the mica-type minerals that were dated. In addition, there is a correlation between E-W folding in the Khar Ovoo Palaeozoic samples and the K-Ar ages of about 180 ± 5 Ma, and the samples collected near the Nomgon village and the mean age of 230 ± 5 Ma for the analyzed $<2\ \mu\text{m}$ fractions. Overall, there is not a distinct difference between K-Ar ages of Trans-Altai and South Gobi zone lithologies. The observed trend in the South Gobi zone is consistent with progressive younging of K-Ar ages towards the supposed Trans-Altai/South Gobi zone boundary where it becomes early Triassic.

5. Discussion

5.1. Tectono-sedimentary and volcanic setting of the Trans-Altai Zone and South Gobi Zone

The South Gobi Zone is characterized by the presence of passive margin type Ordovician to Silurian siliciclastic sediments and carbonates, followed by volcanic arc activity represented by early Devonian andesitic volcanism (Fig. 12). The eastern part of the South Gobi Zone was emerged from the late Devonian until the early Carboniferous whereas the late Carboniferous is marked by a continental shelf setting. The continental regime was dominant from the Permian to Jurassic. The western part of the South Gobi Zone shows the upper crustal part of the volcanic and sedimentary early Carboniferous edifice passing to the Lower Permian to Jurassic clastic sequences. In contrast, the Upper-Silurian to Lower-Devonian succession of Trans-Altai Zone reveals exhumation of the lithospheric mantle in a distal passive margin setting characterized by the development of ophticalcites and siliceous sediments, followed by andesitic and basaltic volcanism interpreted as having resulted from a volcanic arc developed on oceanic crust (Lamb and Badarch, 2001; Helo et al., 2006; Rippington et al., 2008). The Upper Devonian volcanoclastic succession suggests the development of an intra-oceanic basin (back arc or fore arc) in which both the clastic and volcanic arc-derived products were deposited (Lamb and Badarch, 1997). The clastic Lower Carboniferous flyschoid sequences are interpreted as foreland basin sediments (Badarch et al., 2002). The important sub-aerial to marine volcanic activity in the Nomgon area is a typical feature of the entire Trans-Altai Zone and was interpreted in terms of a volcanic arc (Lamb and Badarch, 2001).

In conclusion, the South Gobi Zone represents a continental shelf environment beginning in the late Silurian until the late Carboniferous, followed by continental synorogenic sedimentation in the Permian. In contrast, the Trans Altai Zone represents an oceanic environment during the entire Devonian, passing into a flyschoid sedimentation associated with an arc-type volcanism during the Carboniferous.

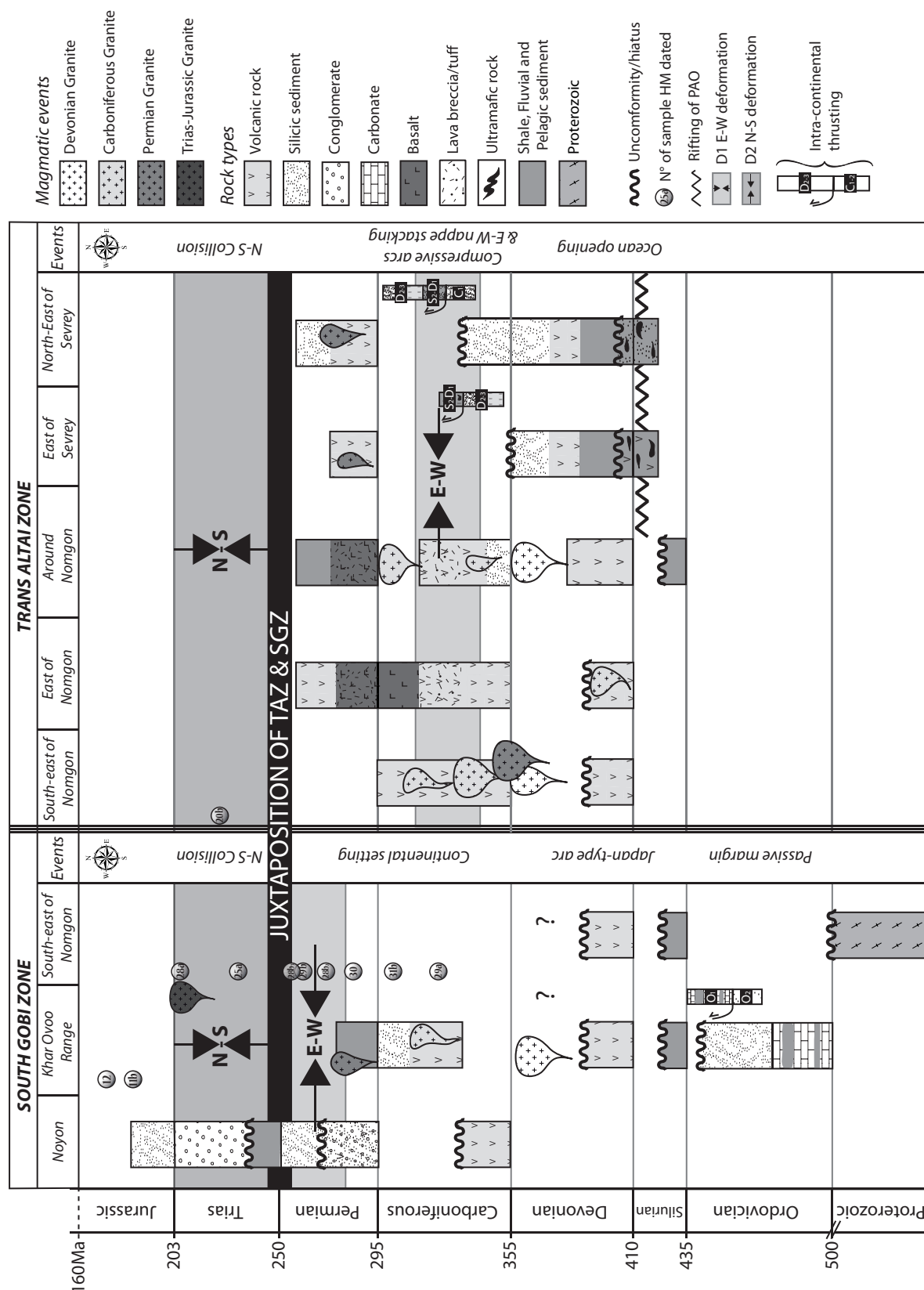


Figure 12: Summary of the lithostratigraphy (simplified stratigraphic columns according to the present review and the references therein) combined with the tectonic events in the South Mongolia region including the K-Ar and the U-Pb datation.

5.2. Kinematic regimes of D1 and D2 deformations

Structural evidence in the Khar Ovoo cross-section (South Gobi Zone) indicates synmetamorphic thrusting of Lower Ordovician over Upper Ordovician rocks. Similarly, the southeastern Nomgon area (eastern South Gobi Zone) displays a synmetamorphic décollement of Devonian metasediments over the presumed Proterozoic basement. Unfortunately, the structural observations do not allow determining the kinematics and orientation of the thrust tectonics due to intensive late refolding. The only area providing a clear indication for D1 kinematics is the Noyon region, where the earliest N–S folds are present. The general picture that emerges suggests that the upper crustal level reveals open upright folding related to E–W compression, which may correspond to deeper crustal, synmetamorphic, E–W directed thrusting. The latter suggestion agrees with the N–S orientation of the metamorphic fabrics and syntectonic intrusion of granitoids in the Gobi Tianshan plutonic complex farther west where Lehmann et al. (2010) confirmed a synmetamorphic crustal E–W shortening tectonic regime.

The geometry of the Palaeozoic rocks in the Sevrey district can be interpreted in terms of shallow dipping thrusting of Upper Silurian-Lower Devonian and Upper Devonian sequences over the Lower Carboniferous clastic and volcanic rocks or thrusting of Upper Silurian rocks over Upper Devonian strata. This thrusting produced sub-horizontal nappe structures, but the sense of shearing cannot be determined because of the later intense refolding. In contrast, in the Nomgon area (eastern Trans-Altai Zone) the Devonian and Lower Carboniferous volcanic rocks have been affected by early N–S trending F1 folds and S1 cleavage developed during E–W compression (present coordinates). The E–W shortening model for D1 is further supported by a strong N–S striking steep magmatic fabric of assumed Devonian granodiorites and the Carboniferous volcanic rocks to the south-east of Nomgon. Therefore, we propose that this E–W directed folding is the shallow crustal expression of the synmetamorphic thrusting at deeper crustal levels and of syn-compressional emplacement of granodiorites. The second event is characterized by ubiquitous E–W trending upright folds and a sub-vertical cleavage, suggesting a generalized N–S shortening of the entire area.

The complex pattern in both South Gobi and Trans-Altai zones can be explained by two phases of deformation (Fig. 13). The D1 E–W shortening event was responsible for thrusting at deeper crustal levels. D1 thrusting in the South Gobi Zone is characterized by a thin-skinned tectonic model based on underthrusting of the basement, a detachment and imbrications of the cover tectonic sheets. In contrast, the D1 tectonic pattern of the Trans-Altai Zone is characteristic of a thick-skinned tectonic model implying imbrication of the oceanic basement-derived thrust sheets with the cover. The supracrustal Carboniferous cover of both units were affected

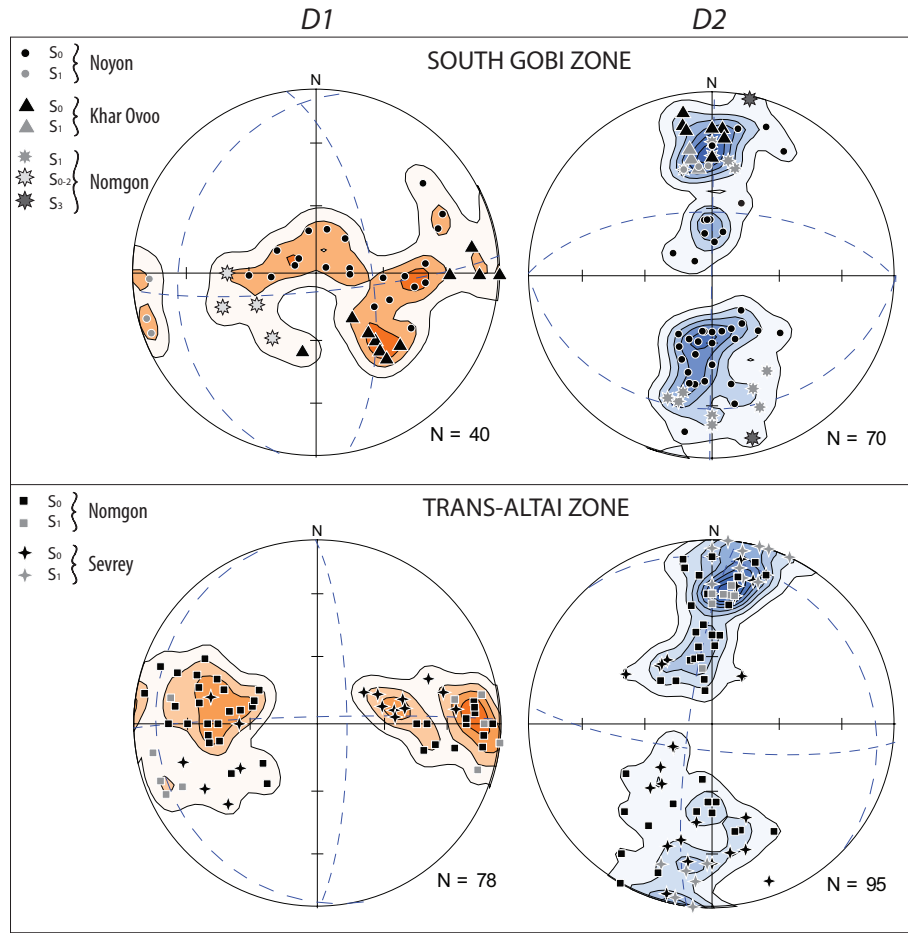


Figure 13: Stereograms representing the average poles of foliations and cleavages revealing the deformation phases in equal area lower hemisphere projection.

by gentle D1 upright N–S folding. This event was followed by the D2 E–W trending upright open folds resulting from a N–S shortening event heterogeneously affecting both the Trans-Altai and South Gobi units.

5.3. Timing of tectonic events

Although the South Gobi and Trans-Altai zones show the same succession of tectonic events, the deformation phases contrast in style and time. In the Trans-Altai Zone, the D1 E–W shortening event began in the middle Carboniferous as shown by the thrusting of the Upper Silurian-Lower Devonian oceanic floor over the Middle to Upper Devonian and Lower Carboniferous sequences (Yarmolyuk et al., 2007). These observations corroborate the relationship between the supposedly Devonian N–S foliated granodiorite and the undeformed Carboniferous granites (precise age unknown) in the southernmost Trans-Altai Zone, suggesting that emplacement of the former granitoid occurred during late Devonian to early Carboniferous E–W compression. An early Carboniferous age for the nappe stacking was already proposed

in the Trans-Altai Zone (Zonenshain, 1973), based on the presence of Lower Carboniferous sediments farther to the west and the Lower Carboniferous unconformity observed in the Sevrey region.

However, the structural data combined with K-Ar dating and the Middle Permian unconformity observed in the South Gobi Zone (the Noyon area) clearly suggest that E–W shortening is likely to have been of late Carboniferous to early Permian age. The timing of E–W shortening in the South Gobi Zone is confirmed by K-Ar ages of 322 – 290 Ma for a greenschist-facies fabric observed in the South Gobi Proterozoic basement, where two age peaks were determined at 320 – 300 Ma in the basement and 280 – 260 Ma in the Devonian cover. The former K-Ar age group matches remarkably well with the dating of the ~300 Ma syntectonic intrusion of the South Gobi magmatic arc (Lehmann et al., 2010) and E–W directed early Permian N–S folding in the Noyon area. The second age group reflects rejuvenation of early Permian fabrics by D2 deformation. Therefore, we propose that the South Gobi Zone continent was heterogeneously and possibly diachronously shortened in an E–W direction between late Carboniferous and the early Permian times.

The N–S shortening event most likely occurred between the Triassic and Middle Jurassic as shown by: (1) syntectonic deposits of Triassic and Lower Jurassic layers in the Noyon Uul syncline; and (2) E–W folding of Upper Permian volcanic rocks. These interpretations are further supported by K-Ar ages of 180 Ma for an E–W cleavage from the Khar Owoo range and 230 to 200 Ma K-Ar ages for E–W cleavage from the Trans-Altai-South Gobi zones tectonic boundary south of Nomgon. Triassic deformation of the Trans-Altai Zone was already reported by Zonenshain et al. (1985) and Lehmann et al. (2010) who observed folding of the Lower Triassic sediments. Late Permian to Triassic deformation was also very important in the Palaeozoic arc sequences to the south of the South Gobi continent and to the north of the North China craton (Xiao et al., 2009).

5.4. Interpretation of the Carboniferous to Permian magmatic evolution

As stated in previous sections, the geographic distribution of granitoids, combined with their petrology, geochemistry and ages, allows the clustering of distinctive domains that represent typical processes of magma generation (melting and fractionation mechanisms) and a specific crustal architecture (crustal thickness). A first order observation made from 1:200 000 scale state mapping is that the spatial density of exposed intrusive igneous rocks is greatest in the eastern zone approaching the East Gobi fault zone (Zuunbayan fault).

Most pre-Permian intrusions studied here are classified as Magnesian alkali-calcic metaluminous to weakly peraluminous granitoids (Frost et al., 2001) and plot within the volcanic arc granite field (Pierce et al., 1984). These characteristics bear a strong similarity to those in "I-type" granitoids of the Lachlan fold belt (Frost et al., 2001). Moreover, the REE characteristics are consistent with those observed from granitoids formed in a subduction setting. For the samples of Carboniferous age in all zones the distribution of data in the plots shown above is consistent with complex fractionation histories where the controlling mineralogy evolved from garnet and/or amphibole-dominated to plagioclase-dominated. This is reflected in some samples of Carboniferous age in the eastern zone with fractionated trace element characteristics that are spatially and temporally associated with apparently primitive granitoids (dated samples T2-019, T2-029, T2-042, T2-046, and T2-062, age range 314 ± 5 Ma– 319 ± 5 Ma).

In the western sector, the samples of the northwestern zone display significant differences in their REE systematics compared to those of the Khongor group and the southwestern zone. It can be seen in the plot SiO_2 vs Dy/Yb (Fig. 4) that the intrusions of the northwestern zone are dominated by amphibole and feldspar-plagioclase fractionation, whereas garnet had a strong influence on the fractionation process in the SW and Khongor zones. Moreover, there are indications that the crust was thickening from north to south i.e. from the Trans Altai Zone to the South Gobi Zone. It is entirely reasonable, and in line with consideration of the temporal differences between the Khongor group and the southwestern zone, that the observed geochemical trend is a reflection of the evolution of magmatic rocks in a more mature and thicker crustal section of the South Gobi Zone compared to the Trans Altai Zone in the northwest. This evident maturity reflects the presence of a more ancient crustal reservoir in the South Gobi Zone where the Neoproterozoic basement (~ 900 Ma) occurs (Yarmolyuk et al., 2007). In contrast, the dominance of amphibole in the magma source in the northwestern and eastern zones is consistent with a zone of isotopically juvenile crust coinciding spatially with the Trans-Altai Zone (Yarmolyuk et al., 2007; Dolgoplova et al., 2013). In considering these data and their spatial position, the Khongor group can be regarded as reflecting the transitional source at the South Gobi/Trans-Altai margin.

Granitoids of early Permian age were only found in the eastern zone of the study area. They are characterized by a highly fractionated and evolved chemical signature that indicates the role of plagioclase and apatite fractionation in their formation, and no samples of this age displayed any less evolved or less fractionated signatures as observed with the Carboniferous magmatism. In the Rb/Zr vs Nb (ppm) plot (Fig. 4), the Permian group consistently plots with high Nb values, which may be interpreted as having formed due to generation within thickened

arc crust (Brown et al., 1984). These characteristics are broadly consistent with those of the early Permian alkalic Khanbogd complex and the early Permian North Mandakh Granite, albeit less evolved (Kovalenko et al., 2006; Blight et al., 2010). It should be noted that all examined Permian intrusions are within 150 km of these magmatic bodies and lie on a SW–NE trending belt that is sub-parallel to the East Gobi Fault Zone (Figs. 1 and 3). While the late Carboniferous magmatism was related to E-W compressive regime (in the South-Gobi Zone), there is no evidence of either compressive or extensional regime related to emplacement of early Permian alkaline granites. The latter is likely driven by a distinct early Permian heating event related to post-collisional intrusive phase. It is suggested that in view of the whole rock geochemistry and geochronological data presented here, the assertions presented in the literature of an E–W trending belt of Permian alkaline (alkalic) magmatism (Yarmolyuk et al., 2008; Kovalenko et al., 2006) is actually a reflection of the presence of evolved and fractionated intrusions of the Carboniferous 314 – 319 Ma and 307 – 308 Ma alkali-calcic series. This idea is supported by Economos et al. (2012) who demonstrate clearly that the earliest Permian Atasbogd (Gobi-Tianshan Intrusive Complex) is a consequence of subduction and not “A-type” related rift magmatism (Yarmolyuk et al., 2008).

Conclusions and geodynamic model

Our study confirms that oceanic crust in the area of the Trans-Altai Zone was tectonically accreted during the late Devonian–early Carboniferous whereas the South Gobi Zone constituted stable continental crust for the entire tectonic evolution. The main feature of the E–W shortening event D1 in both the South Gobi and the Trans-Altai zones is a constant orientation of compressive fabrics responsible for crustal thickening in both units. The diachronous character of the D1 event also suggests that the two domains represented independent terranes during Devonian and Carboniferous. This implies that the Trans-Altai and South Gobi zones have to be separated by a discontinuity, probably a vertical fault zone with a horizontal displacement component of unknown age. In order to keep the orientation of the D1 fabrics constant in both domains during the fault displacement, it is necessary that the vertical fault does not rotate. However, the salient feature of a strike-slip fault is an internal or external rotation of blocks bounded by faults during global shortening (e.g. Dewey, 1989). In addition, if displaced by the strike-slip fault, the D1 fabrics in the adjacent Trans-Altai and South Gobi zones should be sheared and placed into parallelism to the fault boundary, which is not observed. The only vertical fault zone that could horizontally displace the crustal blocks without internal or external rotation is a transform fault (Wilson, 1965). We therefore assume

that the zone separating the Trans-Altai Zone from the South Gobi Zone was a palaeo-transform boundary with main activity peaks in the early Carboniferous and late Carboniferous to early Permian. This is indicated by the age of late Carboniferous magmatism which is associated to active shortening in South Gobi Zone and it is post tectonic in the Trans-Altai Zone. Figure 14 shows a possible tectonic scenario suggesting that the migration of deformation from north to south (Lehmann et al., 2010) and that the South Gobi Zone was pushed from west to east from about 300 Ma until 290 Ma. This scenario agrees with the K-Ar ages of the micaceous material from the Proterozoic basement and its Devonian cover away from the South Gobi-Trans-Altai zones contact zone which is related to greenschist-facies detachment of the Devonian cover. They thus correspond to cooling of the South Gobi Zone basement ~300 Ma related to the D1 event which matches with the age of syntectonic emplacement of the Atasbogd magmatic arc (Kröner et al., 2010; Economos et al., 2012) farther to the west as well as the early Permian E–W shortening reported from the Noyon area. The transform boundary was active during activity of N–S trending and west dipping pacific type subduction zone system (Schulmann and Paterson, 2011).

When approaching the South Gobi–Trans-Altai zones fault contact zone, the K-Ar ages become progressively younger, ranging from 260–233 Ma on the South Gobi Zone side to ~224 Ma on the Trans-Altai Zone side. These ages are linked to development of the vertical E–W striking D2 cleavage that resulted from the N–S shortening event. Therefore, we propose that the South Gobi–Trans-Altai zones contact zone did not operate as a vertical fault with a horizontal transport component during this time but was reactivated as a domain of frontal convergence. The D2 deformation probably lasted until the early Jurassic as documented by tectono-sedimentary data from the Noyon syncline and by K-Ar dating of the D2 cleavage in the Khar Ovoo range. To sum up, D2 N–S shortening was accommodated by heterogeneous deformation that was also diachronous across the entire orogenic system farther to the north (Lehmann et al., 2010) and to the south towards the North China craton (Xiao et al., 2009). The final phases of N–S shortening were probably accommodated by a system of strike-slip faults represented e.g. by the East Gobi Fault Zone farther east that was active as a sinistral fault during the late Triassic. The latter strike-slip fault displaced the South Gobi Zone farther to the NE by several hundred kilometers, thus underlining the importance of the late Permian – Triassic N–S shortening event.

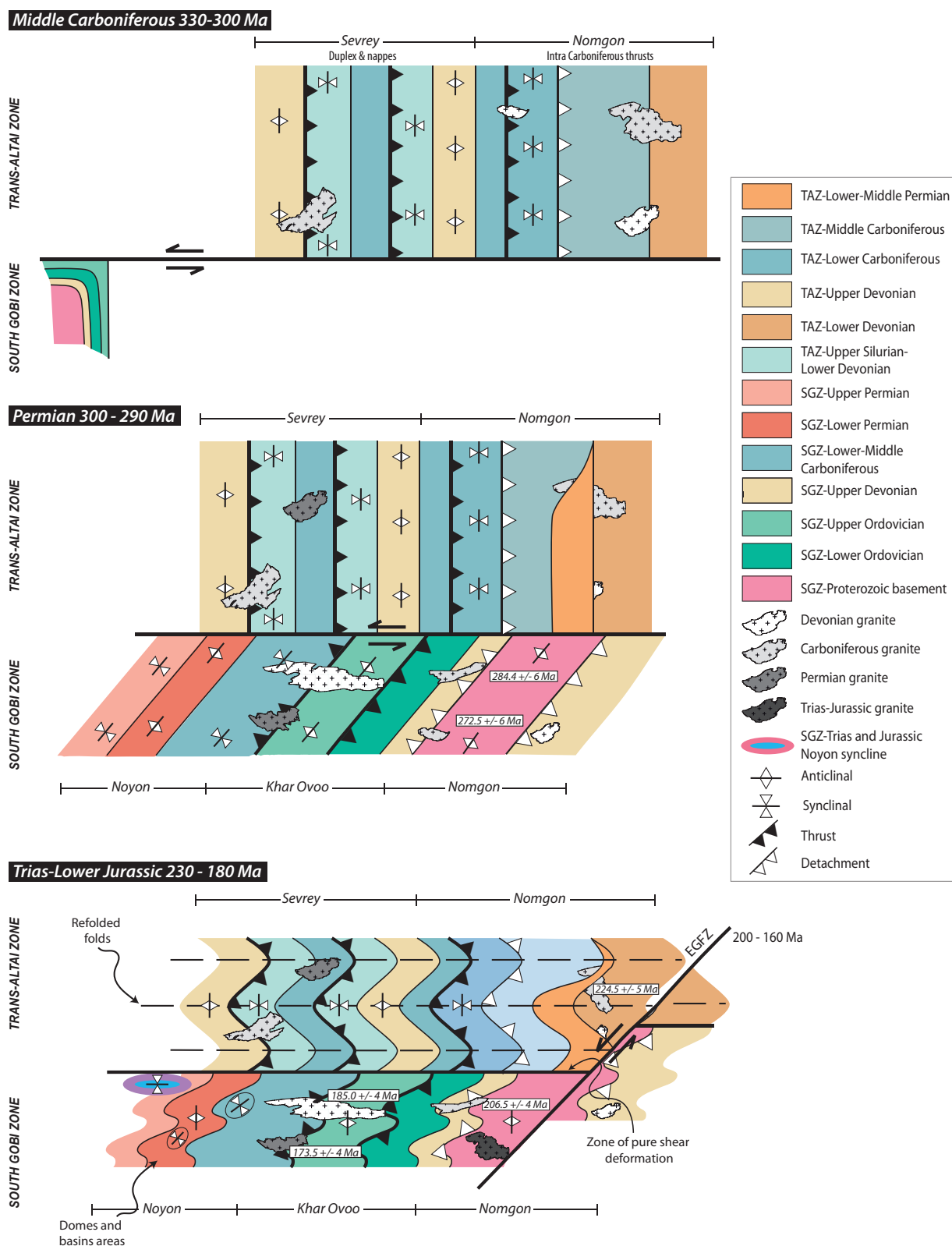


Figure 14: Scheme of the large scale tectonic evolution of the TAZ and the SGZ.

Kovalenko et al. (2006) and Yarmolyuk et al. (2008) suggested that the late Carboniferous to Permian was a period of an important bimodal magmatism developed along the Gobi Tianshan rift zone, parallel to the Trans-Altai–South Gobi zones contact. Other authors suggested that Permian magmatism was associated with the activity of major strike-slip faults in the Tien Shan area (e.g. Seltnann et al., 2011) while Economos et al. (2012) propose a subduction origin of early Permian plutonism in the west. This subduction system corresponds to an E–W trending north dipping Tethyan (Solonker) type subduction as proposed by Schulmann and Paterson (2011). From a synthesis of all field observations and new data, we show that E–W trending rift–type magmatism is not warranted. Instead, we propose a model that postulates episodic subduction processes which extended from the Devonian with E–W compression in the Trans-Altai, also evident from thrusting at Oyu Tolgoi (Wainwright et al., 2011; Hendrix et al., 1996), through to the late Carboniferous in the South Gobi Zone. Carboniferous subduction related magmatism was responsible for the voluminous granitoid emplacement in the late Carboniferous (300–305 Ma / 307–308 Ma, both syn-tectonic in South Gobi and post-tectonic in Trans-Altai) and indicates that a N–S trending subduction process dominated magmatic recycling of thickened (Grenvillian) continental crust (Rojas-Agramontes et al., 2011) in the south and early Cambrian juvenile crust in the north (Yarmolyuk et al., 2007; Dolgoplova et al., 2013). We concur with the model of a mature island arc basement in the region of the Trans-Altai Zone and thick continental crust in the South Gobi Zone that were recycled both during Carboniferous subduction and Permian post-subduction activity. Crust formation and growth was initially solely based on subduction and accretion processes, as evidence from hornblende fractionation, while the alkaline Permian granites have post-collisional features. This magmatic activity was followed by major plate reorganization manifested by the late Permian-Triassic N–S compression. The latter event is of a purely collisional character associated with final closure of the orogen in between Siberian and North Chinese cratons.

Chapter III:

Gravity and magnetic features combined with geological constraints in southern Mongolia: Revision of terrane boundaries

Chapter III:

Gravity and magnetic features combined with geological constraints in southern Mongolia: Revision of terrane boundaries

Introduction:

Terrane is by definition an area surrounded by steep shear zones/faults or sutures and characterized by rocks having a stratigraphy, petrology and/or paleogeography that is distinctly different from the neighboring crustal blocks or continents (Berg et al., 1972, 1978; Coney et al., 1980; Monger et al., 1982; Jones et al., 1983). The concept of terranes is often used to describe allochthonous or suspect tectonostratigraphic units observed in orogeny and implies that the orogenic belts consist of amalgamation of crustal fragments of various sizes and origins. The terrane analysis (Jones et al., 1983; Schermer et al., 1984) was a new methodology set up in the 1980s which established criteria to distinguish specific terranes and to reconstitute the relationships in time and space between all the other accreted blocks. Terrane boundaries are often deduced only by the juxtaposition of different lithologies which seem to have no correlation. This approach can lead to several ambiguities if it is not combined with other quantitative methods like geophysical surveys ranging from seismic to potential methods (e.g. Jones et al., 1977; Cady, 1989; Gray and Forster, 2004; Glen et al., 2007a; Burton, 2010). In the absence of seismic data, the gravity and magnetic anomaly maps can be a powerful tool to identify terrane boundaries because the terranes commonly reveal contrasting magnetic and gravity signatures. In the large scale terrane analysis, the gravity data commonly refer to crustal blocks with different densities (Edel and Weber, 1995; Guy et al., 2011) while the magnetic maps can provide information about the distribution of highly magnetic rocks like magmatic arcs (diorites, tonalites) and mafic volcanic rocks (andesites, basalts) and ophiolites (Edel and Schulmann, 2009). In addition, magnetic lineaments can reflect presence of shear and fault zones (e.g. Burton, 2010) associated with major fluid circulation. Both types of potential methods thus provide a different insight into terrane analysis and together with lithostratigraphic analysis present a powerful tool to study accretionary systems.

Lithostratigraphical, geochronological and structural studies (e.g. Zonenshain, 1973; Badarch et al., 2002; Windley et al., 2007; Kröner et al., 2010) show that the Central Asian Orogenic Belt is composed of contrasting lithotectonic domains. Based on these observations,

several authors came to the conclusion that the Central Asian Orogenic Belt is a mosaic of terranes that are defined as lithospheric/crustal blocks surrounded by steep fault zones and/or sutures (Badarch et al., 2002). As mentioned above, the fault/suture zones generally exhibit a characteristic and geophysical signature allowing characterizing them at the crustal scale thickness. In the Central Asian Orogenic Belt, potential field analysis and geophysical imageries of these terranes have never been explored although gravity and magnetic data exist. Therefore, the analysis of existing gravity and magnetic data combined with analysis of lithostratigraphy may help to better define terrane boundaries and justify or deny existing tectonic subdivisions.

This study is localized to southern Mongolia and presents a review and a synthesis of all the geological and geophysical data available for the area in order to characterize the compartmentalization into terranes of the Central Asian Orogenic Belt. Consequently, this synthesis identifies the criteria of the global processes of accretion at a scale of the southern part of the Central Asian Orogenic Belt. The structure and tectonic specification of the discrete tectonic units will be characterized in order to examine the similarities and differences between the various crustal units. These objectives are realized by means of the digitalization and the harmonization of the Russian and Mongolian 1:200 000 geological maps covering the area (Czech Geological Survey (CGS) collection) and creation of new map at 1:500 000 scale. The comparison of the 1:500 000 geological map with the analyzed gravimetric and magnetic grids enables the correlation between the tectonic boundaries and the trend of the gravity and magnetic signals. Therefore, these comparisons allow making the link between the geological structures deduced from geological and tectonic maps, and the potential method signal in order to better define heterogeneities of the accretionary system and to revise the model of terranes in the frame of the Central Asian Orogenic Belt.

1. Processing of a geological map of 1:500 000 scale and a GIS database

Although geological maps of 1:500 000 scale of Mongolia already exists, it is necessary to create a GIS geological database compiling the 1:200 000 geological maps available over the area of interest in order to overlap the geophysical data. This new map was produced by procedural steps presented in chart (Fig. 1) and constitutes a base which is able to include the last research results such as geochronology, geochemistry and Landsat images.

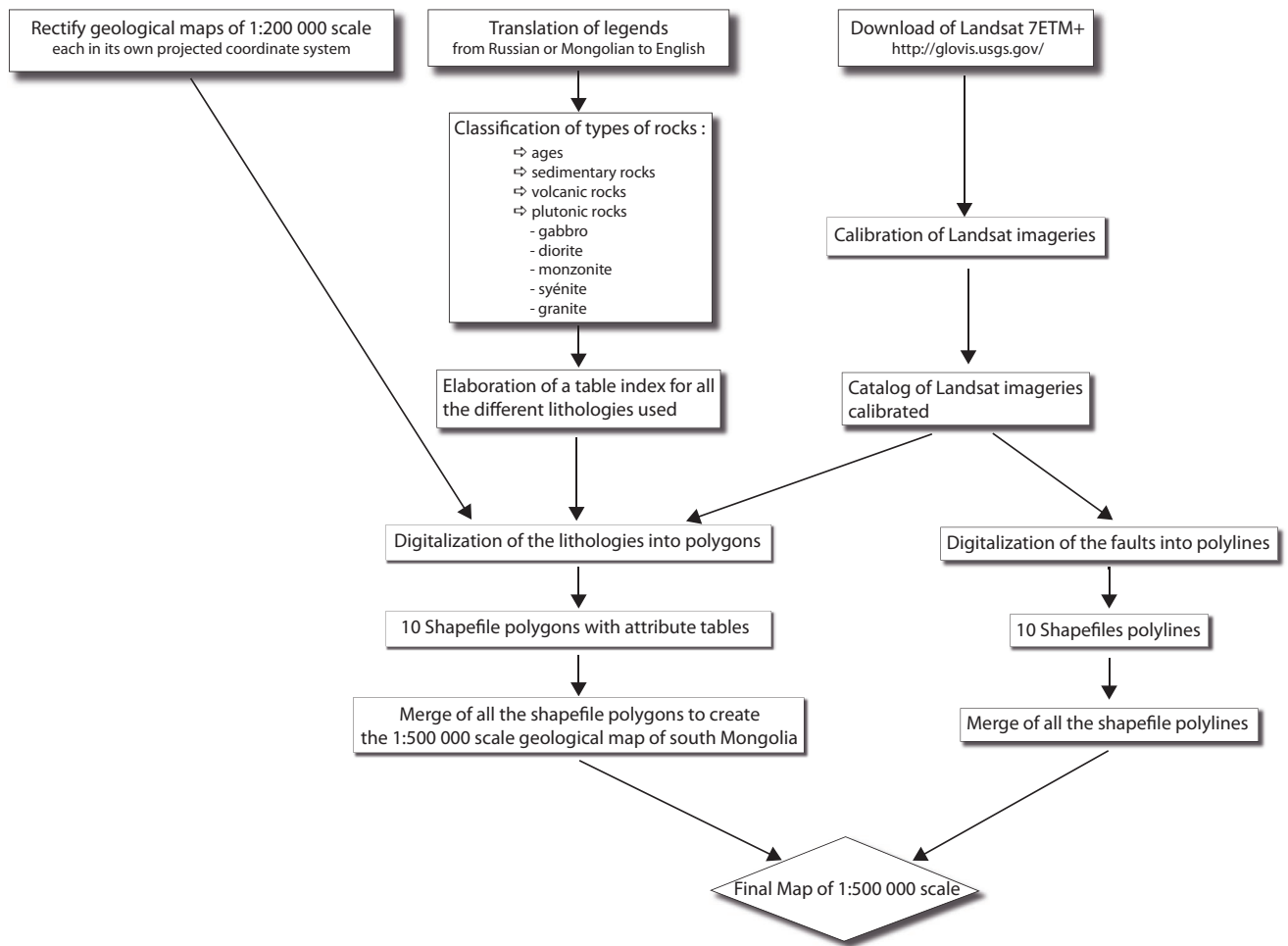


Figure 1: Workflow for geological mapping processes.

1.1. Harmonization of geological maps of 1:200 000 scale

1.1.1. Rectification of the 1:200 000 geological maps

More than fifty Russian and Mongolian geological maps of 1:200 000 scale were scanned and rectified (Fig. 2). One geological map of 1:500 000 scale was used to complete the gaps related to lack of five 1:200 000 scale maps in the west of the area. After rectification of each map in its original projected coordinate system (Projection: Gauss-Krueger; Datum: Pulkovo 1942, for most of the Russian maps), all maps were combined in one standard international system.

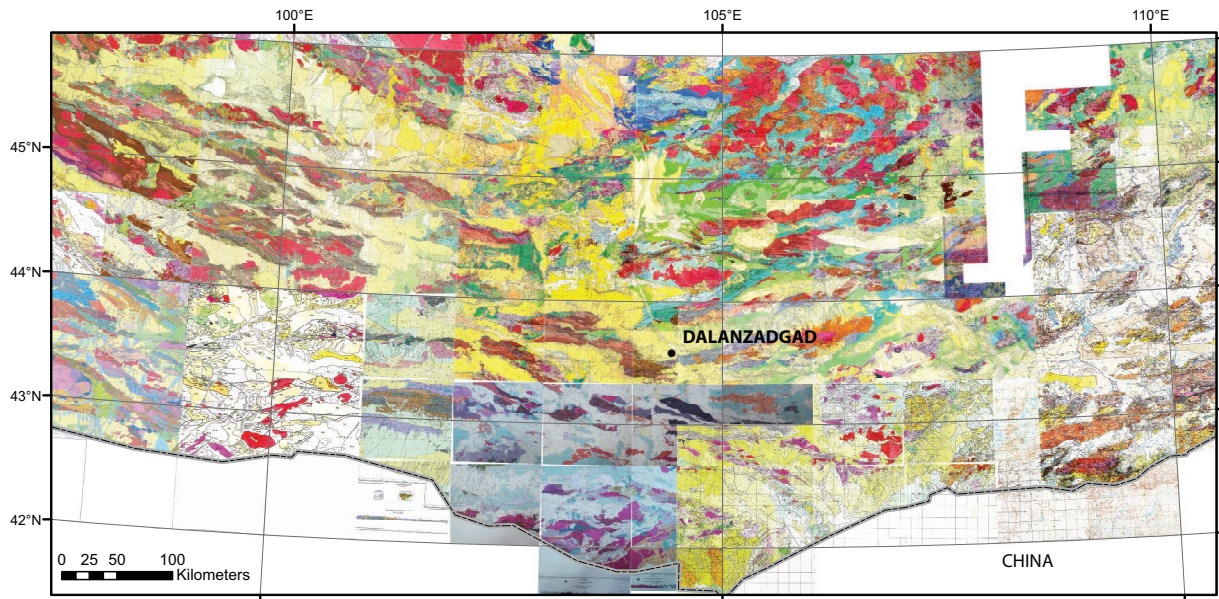


Figure 2: Geological maps scanned and rectified covering the south of Mongolia.

1.1.2. Harmonization of the map legends

The maps were scanned with their geological reports and legends, all in Russian language except one in Mongolian language. Therefore, after translation of the geological legends, they have been harmonized in order to define new lithological categories used for the digitalization in the 1:500 000 scale. For this purpose, the lithologies were classified according to their ages, the sedimentary rocks, volcanic rocks and plutonic protoliths (Fig. 1). For instance, the limestone, sandstone, carbonate and chert are put together under the category “sedimentary rocks”; the basaltic, andesitic, trachyte and rhyolitic rocks are under the category of “volcanic rocks”. However, the plutonic rocks are distinguished into the basic categories of: gabbro, diorite, monzonite, syenite and granite.

1.1.3. Catalog of Landsat images

As the area of the study is in an arid environment, the elaboration of a catalog of Landsat imageries (Fig. 3) can be helpful to update and complete the geological maps. Thus, a catalog of Landsat 7 Enhanced Thematic Mapper Plus (ETM+) imageries was elaborated. This catalog was used to have an overview on lithologies and geological structures, and to review the major faults over the whole south of Mongolia. Briefly, Landsat 7ETM+ consists in eight spectral bands, including a panchromatic and thermal band:

- Band 1 Visible (0.45 – 0.52 μm) 30 m spatial resolution
- Band 2 Visible (0.52 – 0.60 μm) 30 m
- Band 3 Visible (0.63 – 0.69 μm) 30 m
- Band 4 Near-Infrared (0.77 – 0.90 μm) 30 m spatial resolution
- Band 5 Near-Infrared (1.55 – 1.75 μm) 30 m
- Band 6 Thermal (10.40 – 12.50 μm) 60 m Low Gain / High Gain spatial resolution
- Band 7 Mid-Infrared (2.08 – 2.35 μm) 30 m spatial resolution
- Band 8 Panchromatic (0.52 – 0.90 μm) 15 m spatial resolution

Each Landsat image was downloaded on <http://glovis.usgs.gov/> and calibrated. Landsat data are provided in digital number and before processing, the images has to be converted into radiance or top-of-atmosphere reflectance (i.e. reflectance above the atmosphere).

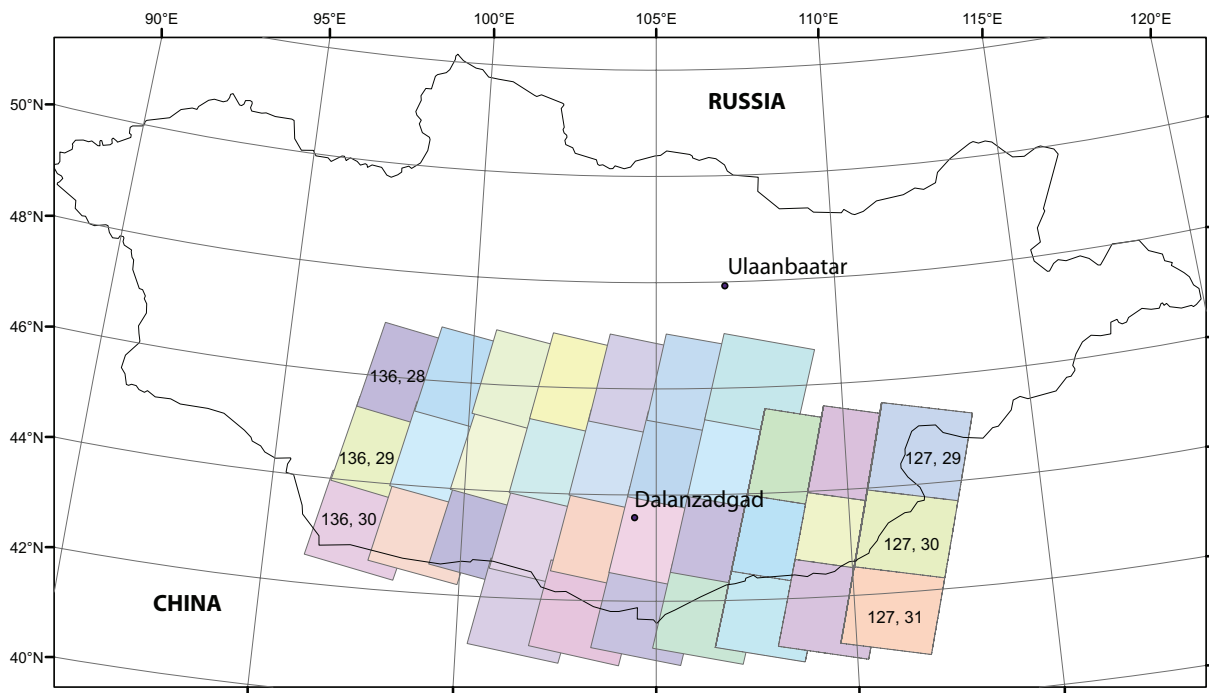


Figure 3: Catalog of Landsat imageries used to review the geological maps. The numbers in some squares are examples of the reference codes of the Landsat images (column: 136; row: 28).

1.2. Digitalization and topological rules

Each 1:200 000 scale map was digitalized in its own projected coordinate system into shapefile polygons linked to an attribute table where the ages and the geological characteristics of the lithologies are tagged. The digitalization of the maps was made at a constant view of 1:100 000 scale. In order to keep the most accurate spatial relationships between polygons, two topological rules were used during the digitalization step (Fig. 4): (1) no overlap, as two different lithologies do not exist at the same place and at the same time; (2) no gap, as obviously all surfaces have to be covered by a ground.

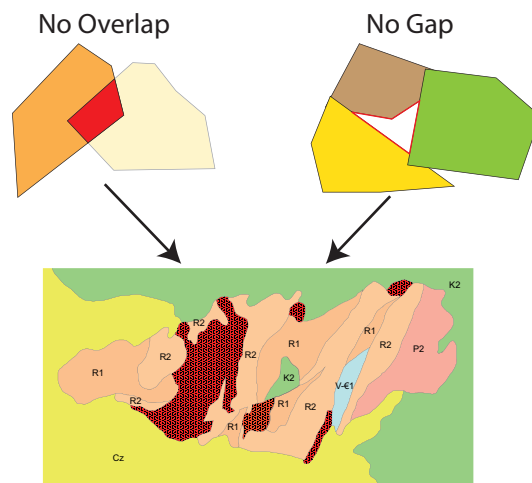


Figure 4: Basic topological rules to get a geological map with the accurate topology.

After digitizing all the geological maps in the appropriate coordinate system, the shapefile polygons obtained were merged in a unique standard international projected coordinate system to build the geological map of 1:500 000 scale over the south of Mongolia. The same processes are applied for the review of major fault systems (Fig. 1).

1.3. Geological map at 1:500 000 scale of southern Mongolia

The geological map (Fig. 5) is compiled according to the international standards and conventions of geological mapping. The final projected coordinate system is WGS 84 UTM Zone 48N, which is centered on the 105th meridian. The color codes of the geological units of the legend are the RGB codes according to the Commission for the geological map of the world (CGMW). The new geological and tectonic map is used as a key element for the comparisons of geological structure with the geophysical data.

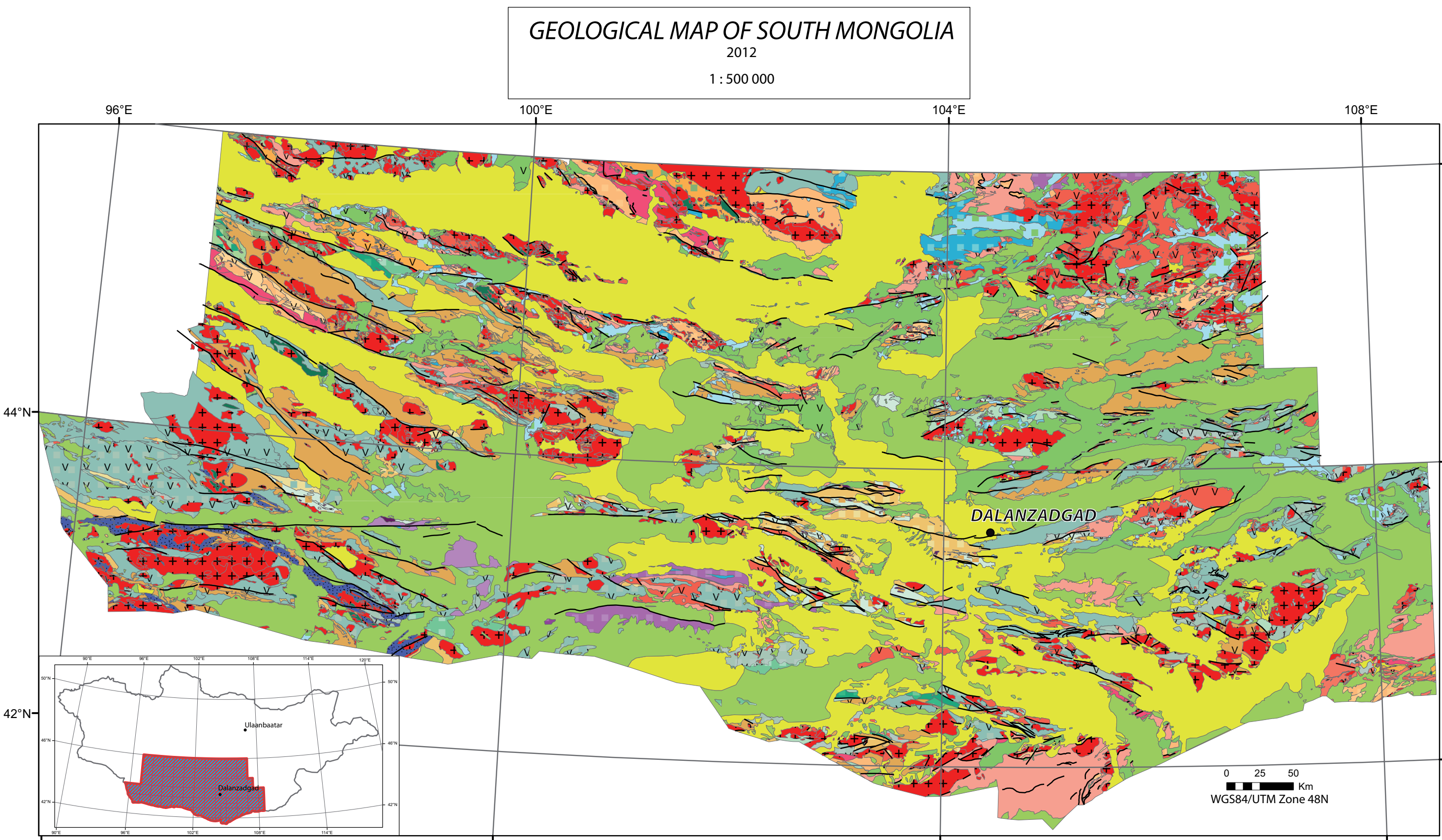


Figure 5: Geological map of 1:500 000 scale over the south of Mongolia and the corresponding legend (next page). The inset is the location of the area covered by the geological map

Lithologies

Mesozoic

- > Mesozoic
- Upper Cretaceous
- Upper Cretaceous Volcanite
- Lower Cretaceous
- Lower Cretaceous Volcanite
- Upper Jurassic-Lower Cretaceous
- Upper Jurassic-Lower Cretaceous Volcanite
- Upper Jurassic
- Upper Jurassic Volcanite
- Middle-Upper Jurassic
- Middle-Upper Jurassic Volcanite
- Lower-Middle Jurassic
- Lower-Middle Jurassic Volcanite
- Lower Jurassic
- Upper Trias-Lower Jurassic
- Upper Trias
- Middle-Upper Trias
- Lower-Middle Trias
- Lower Trias

Palaeozoic

- Upper Permian
- Upper Permian Volcanite
- Middle Permian
- Middle Permian Volcanite
- Lower Permian
- Lower Permian Volcanite
- Upper Carboniferous-Lower Permian
- Upper Carboniferous-Lower Permian Volcanite

- Middle-Upper Carboniferous
- Middle-Upper Carboniferous Volcanite
- Middle Carboniferous
- Middle Carboniferous Volcanite
- Lower-Middle Carboniferous
- Lower-Middle Carboniferous Volcanite
- Lower Carboniferous
- Lower Carboniferous Volcanite
- Upper Devonian-Lower Carboniferous
- Upper Devonian-Lower Carboniferous Volcanite
- Middle-Upper Devonian
- Middle Devonian
- Middle Devonian Volcanite
- Lower-Middle Devonian
- Lower-Middle Devonian Volcanite
- Lower Devonian
- Lower Devonian Volcanite
- Upper Silurian-Lower Devonian
- Upper Silurian-Lower Devonian Volcanite
- Upper Silurian
- Upper Silurian Volcanite
- Middle Silurian
- Middle Silurian Volcanite
- Lower Silurian
- Upper Ordovician-Lower Silurian
- Upper Ordovician
- Middle-Upper Ordovician
- Lower-Middle Ordovician
- Lower-Middle Ordovician Volcanite

- Lower Ordovician
- Upper Cambrian-Lower Ordovician
- Upper Cambrian-Lower Ordovician Volcanite
- Middle Cambrian
- Middle Cambrian Volcanite
- Lower-Middle Cambrian
- Lower-Middle Cambrian Volcanite
- Vendian-Lower-Cambrian
- Vendian-Lower-Cambrian Volcanite

Proterozoic

- Vendian
- Vendian Volcanite
- Upper Riphean Volcanite
- Middle-Upper Riphean
- Middle Riphean
- Lower-Middle Riphean
- Lower Riphean
- Lower Proterozoic
- Lower Proterozoic Volcanite

Archean

- Upper Archean
- Upper Palaeozoic
- Upper Palaeozoic Volcanite
- Lower Palaeozoic
- Mapped Metamorphic Basement
- Lower Proterozoic Granitoid
- Upper Palaeozoic Ultramafic rocks
- Upper Palaeozoic Gabbro

2. Geology and lithostratigraphy of the south of Mongolia

2.1. Distribution of major rock units

The Central Asian Orogenic Belt in the South of Mongolia is an assemblage of rocks ranging from early Proterozoic to late Cretaceous in age, adjacent to the North China and Tarim cratons to the south. A range of geotectonic interpretations have been proposed for Mongolian part of the Central Asian Orogenic Belt over the last two decades (Şengör and Natalin', 1996; Zorin, 1999; Badarch et al., 2002; Yakubchuk et al., 2005; Xiao et al., 2009; Lehmann et al., 2010) and the tectonic model is still discussed. This is in particular because the Central Asian Orogenic Belt was divided into several small geological units and these divisions depended on local lithological, structural and paleogeographical studies. The differences in terminology and in the position of terrane boundaries led Kröner et al. (2010) to synthesize the previous studies and to use the intermediate term "tectonic zone" to distinguish the following geological units: Lake zone for the northernmost unit, intermediate Gobi Altai Zone, and Trans Altai and South Gobi Zones for the southernmost units. The boundaries of the tectonic zones in the figure 6 constitute the synthesis of Kröner et al. (2010) based on lithostratigraphical, structural, geochronological and tectonic analyses. The names given to these units correspond to those introduced by Zaitsev et al. (1970), Zonenshain (1973), Markova (1975) and Ruzhentsev (2001).

The simple observation of the geological map reveals E–W trending elongated massifs of Palaeozoic rocks exposed in ridges that are juxtaposed against young intermontane basins filled with Mesozoic and Cenozoic sediments. These Palaeozoic belts were affected by the N–S Permo-Triassic shortening (Lamb et al. 2008; Lehmann et al., 2010) coupled with the oroclinal bending. However, while the present day E–W elongation of the tectonic zones resulting from the N–S compression between the Siberian craton and the North China-Tarim cratons is obvious, there is no clear evidence for a succession of subduction systems due to the lack of typical markers of sutures between the lithotectonic units. Following the Permo-Triassic compressional event, a NW–SE extension occurred from late Jurassic to early Cretaceous (Zorin, 1999; Ren et al, 2002; Meng, 2003; Darby et al., 2004; Lin and Wang, 2006) creating continental sedimentary basins (Watson et al., 1987; Trayna and Sladen, 1995; Allen et al., 1998; Khand et al., 2000; Ren et al., 2002; Meng et al., 2003). This extensive event affecting a large part of eastern Asia may be responsible for the disappearance of possible marker sutures. Finally, the Cenozoic compression (Cunningham et al., 2005) is the last tectonic event which remarkably reworked the Palaeozoic and Mesozoic structures of the Central Asian Orogenic Belt essentially by activity of large scale transcurrent faults. The restraining bends are in fact

responsible for the uplift of several mountain ranges while the releasing bends result in Cenozoic depressions (Cunningham, 2001, 2005; Cunningham et al., 2009).

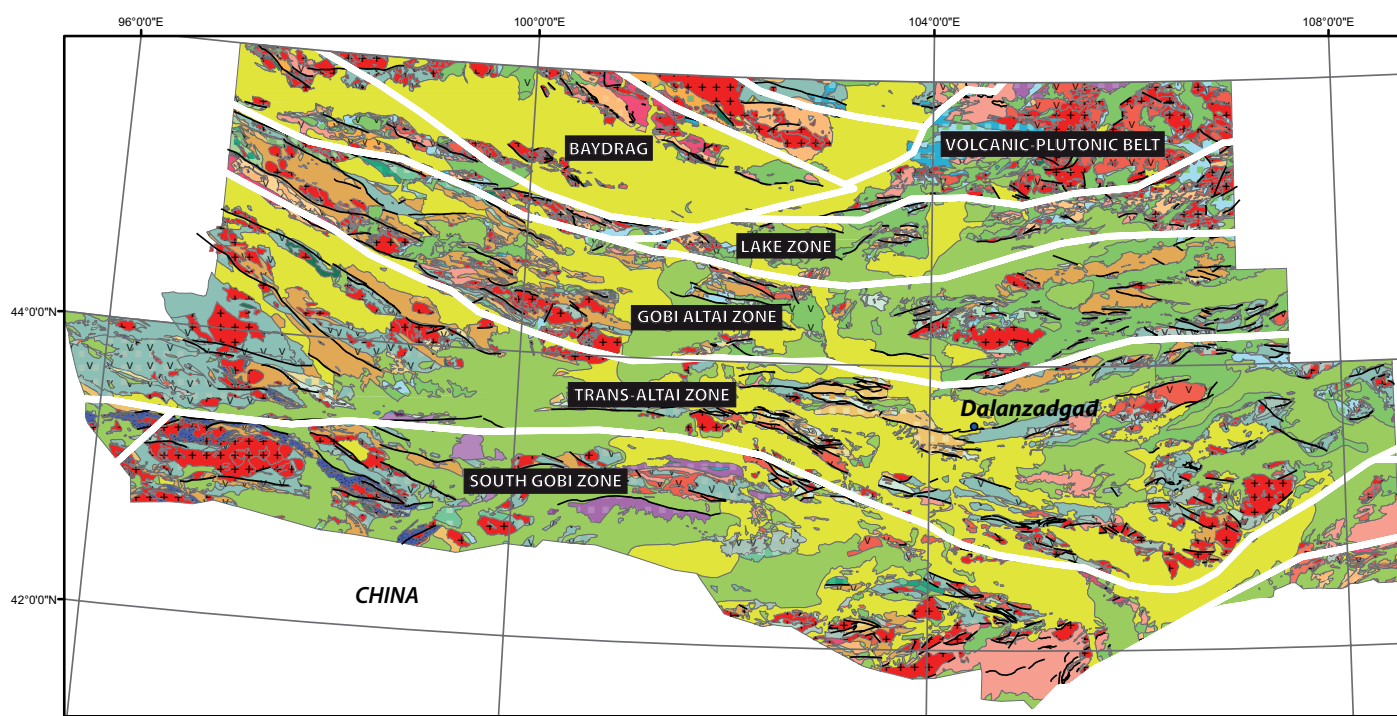


Figure 6: Geological map of the south of Mongolia with the lithotectonic zones superimposed.

2.2. Simplified lithostratigraphic characterization of the four tectonic zones

The lithologies were compiled and simplified for each tectonic zone in order to obtain one representative lithostratigraphic column from the west to the east. The lithostratigraphic columns are mainly modified from Kröner et al. (2010) and Guy et al. (submitted) and completed by the data from Russian geological map reports.

2.2.1. Lithostratigraphy of the Lake Zone

The rocks of the Lake Zone ranging from Proterozoic to Cretaceous age are exposed north of the Main Mongolian Lineament. The lithostratigraphy of the Lake Zone and its surrounding Palaeozoic rocks (Fig. 7) were previously studied by Markova (1975). The succession of the undifferentiated Proterozoic rocks starts with spillite diabase conformably overlain by an alternation of gneiss, schist and marble. These rocks are overlain by a typical succession of relics of an oceanic floor of Vendian age marked by the assemblage of serpentinite-peridotite, sheeted dike complexes, pillow lavas, breccia and associated tuff. These rocks are

conformably overlain by the Vendian to Lower Cambrian sequence mainly composed of marble intercalated with schist followed by weakly metamorphosed rock sequences represented by a succession of conglomerate, sandstone, siltstone and mudstone with breccia and volcanoclastic sediments from Lower to Middle Cambrian. An important unconformity is located between the Middle Cambrian and the Permian. During the 300 Ma of lack of deposition of sediments only, sporadic intrusions of Devonian and Carboniferous granitoids occurred. The Permian rocks are mainly composed of intercalations of breccia and associated tuff with dacite and rhyolite volcanic rocks. These Permian volcanoclastic sequences are unconformably overlain by Lower to Middle Jurassic basaltic and andesitic rocks followed by an alternation of conglomerates, sandstones, siltstones and mudstones up to the Upper Jurassic. Finally, the Upper Jurassic to the Lower Cretaceous consists of a succession of basaltic rocks, sandstones and mudstones.

2.2.2. Lithostratigraphy of the Gobi Altai Zone

The rocks of the Gobi Altai Zone are exposed in the south of the Lake Zone and range from Cambrian to Cretaceous (Fig. 7). The oldest rocks of the Gobi Altai Zone are represented by an alternation of schist and volcanoclastic sediments of presumably Lower-Middle Cambrian age, overlain by a thick intercalation of sandstone, siltstone and limestone ranging from Upper Cambrian to Middle Ordovician in age. An unconformity is located in the middle of the sequence and starts with the conglomerates followed by an alternation of sandstone, limestone and siliceous schist. This sequence is conformably overlain by Upper Silurian sedimentary rocks. The Lower Devonian part of the rock sequence is characterized by an alternation of conglomerates, sandstones and siltstones. The top of the Lower Devonian sequence displays pillow lavas with an alternation of sandstones and mudstones. These pillow lavas are unconformably overlain by Middle Devonian sedimentary sequences. The Lower Carboniferous strata that unconformably overlie the Devonian formation consist of intercalation of fine grained siliceous sediments. These sedimentary sequences are unconformably overlain by mainly volcanoclastic Lower Permian formations. The Lower Permian is conformably overlain by the Upper Permian sedimentary sequence mainly composed of intercalations of siltstone mudstone and argillite. The sedimentary Jurassic rocks unconformably overlain the Upper Palaeozoic sequences. The Jurassic rock sequences start by an alternation of conglomerates, sandstones, siltstones and mudstones from the Lower to Middle Jurassic followed by trachy-andesitic rocks from the Middle to Upper Jurassic. An alternation of sandstones and siltstones conformably overlay this volcanic sequence up to the Lower Cretaceous.

2.2.3. Lithostratigraphy of the Trans Altai zone

The rocks of the Trans-Altai Zone are exposed in the south of the Gobi Altai Zone. The rocks range from Silurian to Jurassic age (Fig. 7). The lowermost part starts with an Upper Silurian-Lower Devonian assemblage, which consists of ophiolite containing fossils, volcanic material composed of andesitic and basaltic volcanites intercalated with shales, sandstones, tuff and volcanoclastic sandstones. The unconformity points out the transition from mainly volcanites to shale dominated sedimentary deposits. Lower to Middle Devonian sequence conformably overlies these sequences with sedimentary deposits alternating with basaltic lava breccia. These rocks are conformably overlain by Middle to Upper Devonian sequence. This sequence contains mainly sedimentary material composed of siltstones, sandstones, jasper, conglomerates assemblage, phyllites and argillites, volcanoclastic sandstones. The Lower Carboniferous strata, which conformably overlain the Devonian sequence, consist in the lowermost part of thick pile of carbonates. These rock deposits are followed by important deposits of siltstones, sandstones and various siliceous sediments. The Middle to Upper Carboniferous sequence unconformably overlies the Lower Carboniferous sequences. These rocks are represented by andesitic rocks and their tuff in the lowermost part of the column, and basaltic rocks in the uppermost part. The Lower Permian conformably overlies the Carboniferous volcanic sequences beginning in the lowermost part by tuff and followed by andesite, basalt, trachyte and rhyolite volcanic rocks. The lowermost part of the Upper Permian consists of conglomerates evolving into stratified, conglomerate and sandstone, and ending by sandstones

2.2.4. Lithostratigraphy of the South Gobi Zone

Rocks of the South Gobi Zone are exposed in the southern most part of the Central Asian Orogenic Belt and are separated from the Trans-Altai Zone by the Gobi-Tianshan Fault Zone. The rocks are variably metamorphosed ranging from Neoproterozoic (outcrops located to the east of the South Gobi Zone) to Jurassic age (Fig. 7). The oldest rocks are represented by an assumed Neoproterozoic sequence containing metapelites, chlorite-schists and paragneisses unconformably overlain by Ordovician low grade metasediments. Then the Ordovician sequences are unconformably overlain mainly by micaceous schists and metabasalts assigned to the Lower Silurian. The Lower to Middle Devonian overlies unconformably the Ordovician-Silurian sequences and consists mainly of felsic tuff. The lithologies of the South Gobi Zone are typical for continental margin sedimentary rocks. The Middle to Upper Devonian conformably overlay the Lower Devonian being represented in the lowermost part by metavolcanoclastic

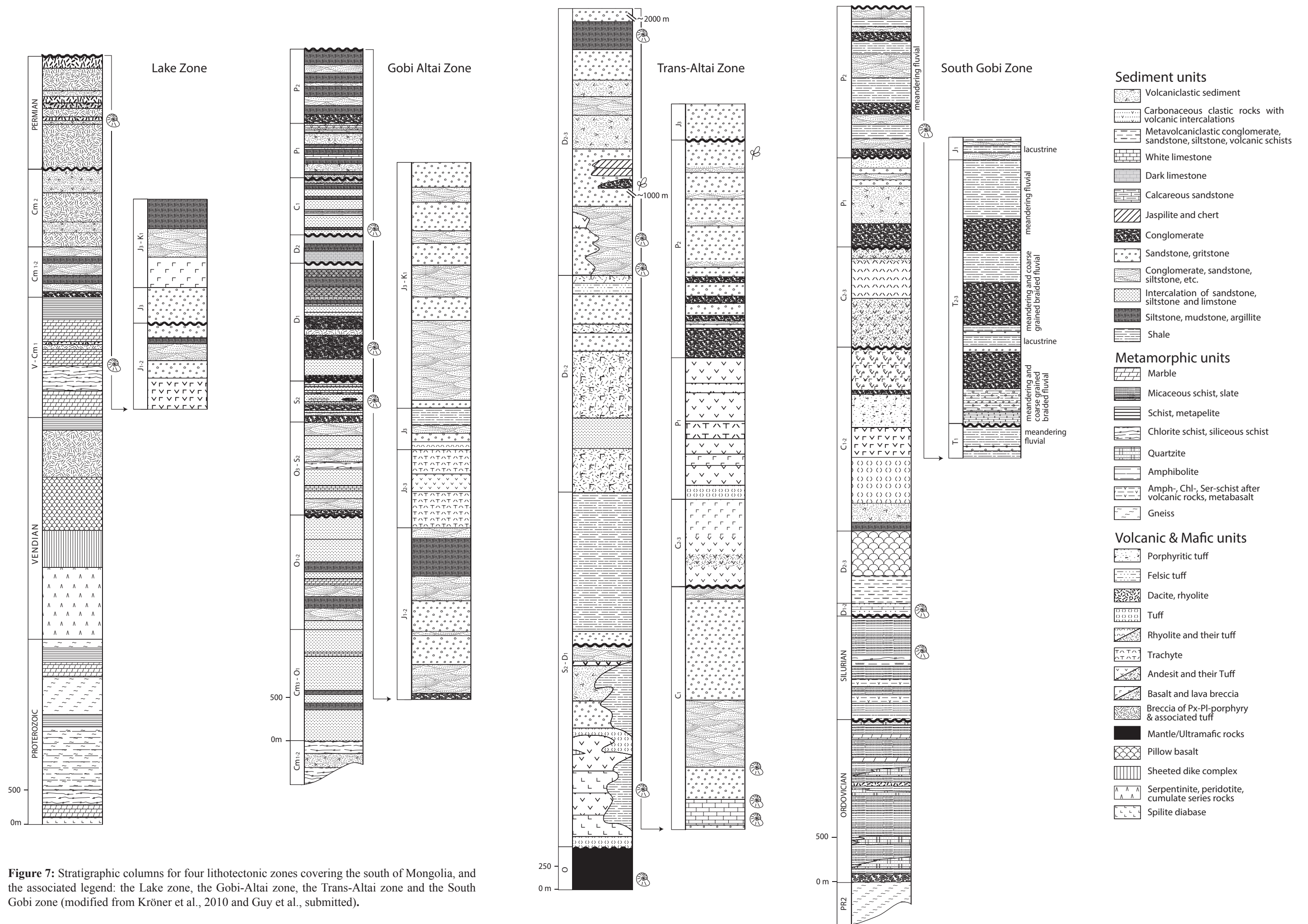


Figure 7: Stratigraphic columns for four lithotectonic zones covering the south of Mongolia, and the associated legend: the Lake zone, the Gobi-Altai zone, the Trans-Altai zone and the South Gobi zone (modified from Kröner et al., 2010 and Guy et al., submitted).

rocks followed by pillow lava sequence. The Lower to Middle Carboniferous sequence starts with argillite overlain by volcanoclastic sandstones, tuff, andesitic-basaltic tuff, porphyritic lava flows (Lamb and Badarch, 2001). These rocks are unconformably overlain by Middle to Upper Carboniferous alternation of andesitic tuff and rhyolitic rocks. Unconformable Lower Permian sequence is represented by an intercalation of conglomerates and volcanoclastic sandstones in the lowermost part to the intermediate part of the succession. The Lower Permian sequence progressively ends with dominantly siliceous sediments and sandstones compositions. Hendrix et al. (1996) assumed the existence of an unconformity between Lower Permian and Middle to Upper Permian probably because the Lower Permian is represented mainly by a typical continental arc deposit whereas the Upper Permian displays clearly meandering fluvial deposits. These Palaeozoic rocks are conformably overlain by Triassic fluvial laminated shales alternating with lacustrine sediments (Hendrix et al., 1996). Lower Jurassic lacustrine sequence is represented by thick laminated shales and siltstones.

3. Datasets

The compilation of geological data with geophysical data requires the collection of several datasets (Table 1) that have been gathered from different sources.

Table 1. Summary of the geophysical and topographical data

Data type	Data source	Native geographic resolution	Translated metric resolution	References
Gravity	DNSC08 free air gravity model	1' x 1'	~ 2 x 2 km	Andersen, O. B. from DTU Space
DEM	ETOPO 1	1' x 1'	~ 2 x 2 km	Amante and Eakins, 2009. NOAA
Magnetic	Compilations of airborne surveys	30" x 30"	~ 1 x 1 km	GETECH (Derek Fairhead)
		5' x 5'	~ 5 x 5 km	

3.1. Gravity data

The free air anomaly grid at 1'x1' resolution from the DNSC08 free air gravity model is provided by the Technical University of Denmark (Andersen and Knudsen, 2009) and covers whole Mongolia and surroundings (Fig. 8). The DNSC08 free air gravity model values over land have been derived as part of the development of EGM2008 by Nikos Pavlis from NGA (Pavlis et al., 2008). The EGM08 model combines high density topographic information with

airborne and terrestrial gravity. The values over land are interpolated using spline interpolation from available 5 or 15 minute mean anomalies from available gravity data (Andersen, personal communication). Therefore, EGM08 should contain all essential information available from the airborne and terrestrial gravity survey.

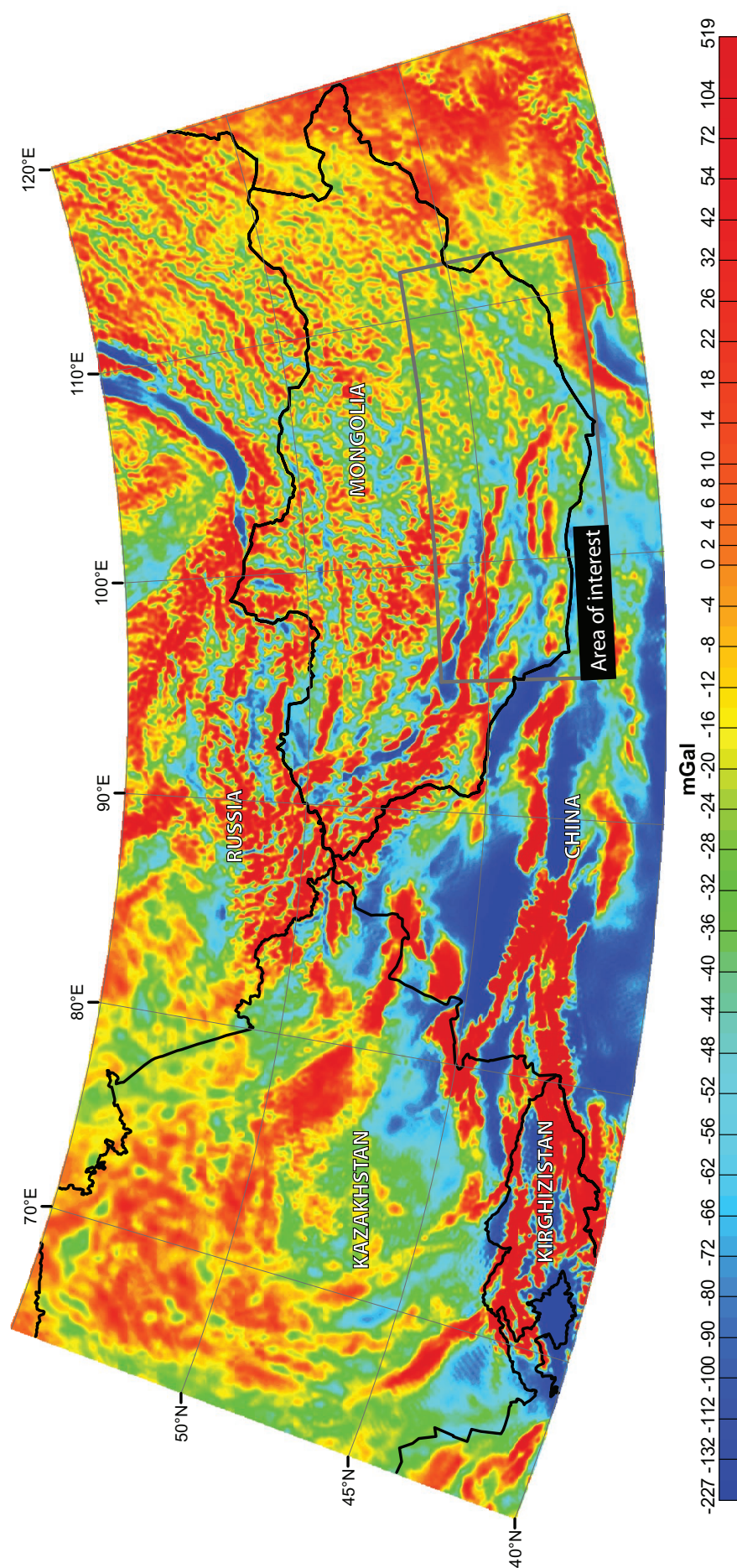
Taking into account the numerous origins of the different gravity data sets which compose the DNSC08 model, it is difficult to perform qualitative and quantitative evaluation of the free air anomaly values.

A digital elevation model is needed to correct gravity data from the topography effects and thus to process the Bouguer anomaly.

3.2. Digital Elevation Model (DEM)

The digital elevation model (DEM) used to process the Bouguer anomaly grid from the free air gravity data is the ETOPO1 (Amante and Eakins, 2009), which has the same resolution as the free air anomaly grid. Indeed, the cell size of this global bathymetric-topographic DEM is 1 arc-minute. ETOPO 1 contains the best available digital data from diverse global and regional digital datasets. These datasets were shifted to common horizontal and vertical datums, evaluated and edited before DEM generation. The data and DEM were quality checked, processed and gridded by Amante and Eakins (2009).

Figure 8: Free air anomaly grid of the CAO B provided by the technical University of Denmark. The black lines are the borders of the countries in Central Asia. The color scale is in equal area distribution.



3.3. Magnetic data

The two datasets of magnetic data presented here are available from Geophysical Exploration Technology (GETECH) in collaboration with the Mongolian Geological and Geophysical Exploration Company (MGGEC). The data were digitized from the isocontours of the maps concerning each survey (Fig. 9) and the data were reprocessed. Each individual magnetic grid has been integrated into a 1x1 km digital grid. The report of GETECH accompanying the data ensures that the maps were digitized either along NS or EW direction parallel to the original flight directions, and with line separation similar to the flight line separation in order to recapture as much original data as possible (although the original flight lines were apparently not marked on the contour maps at 1:200 000 scale). The second and coarser resolution (5'x5') data set comes from the resampling of the individual grids.

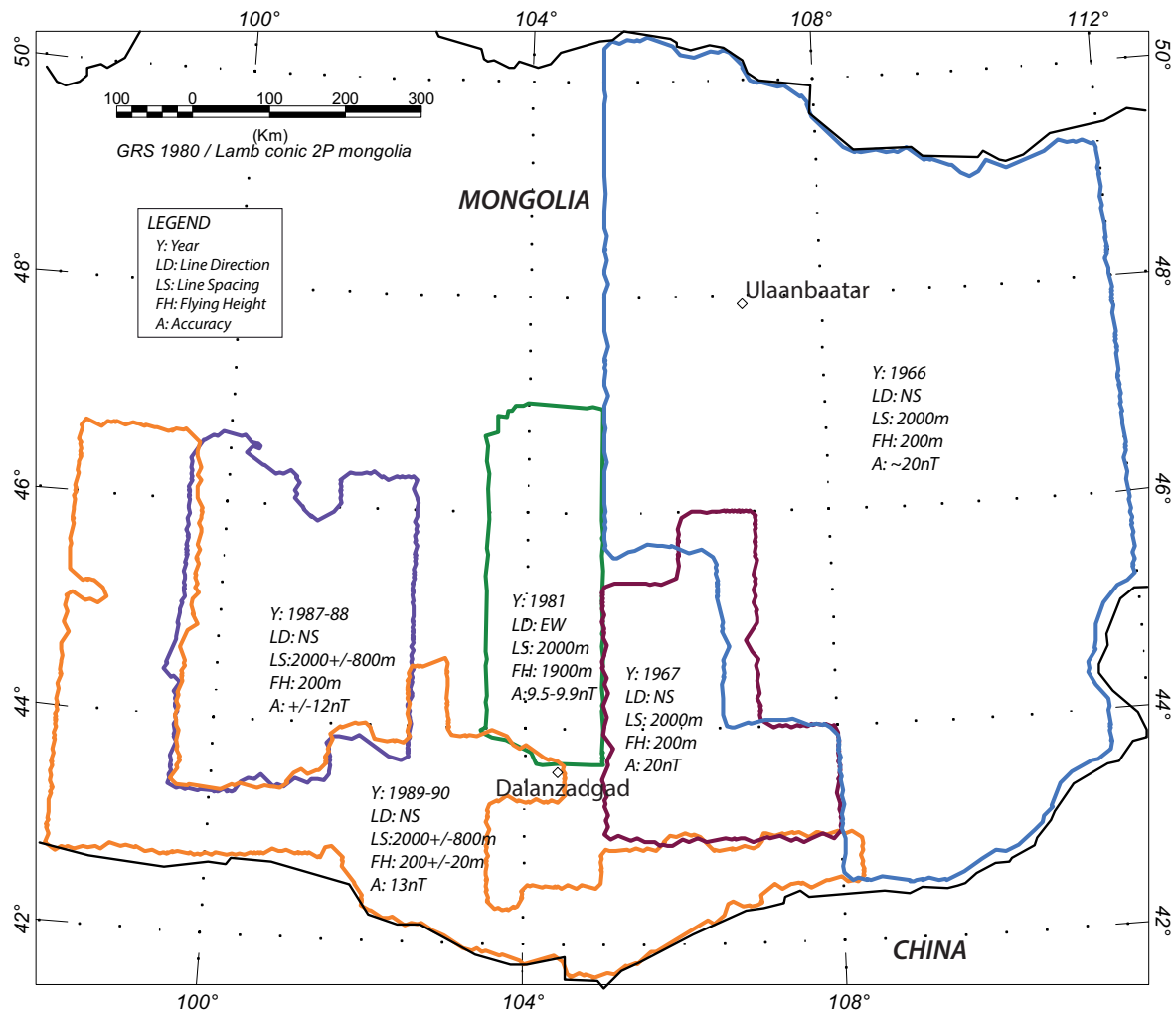


Figure 9: Location of magnetic grids and characteristics of survey.

After the digitizing process, the data were reprojected from the Gauss-Kruger projection using Krasovsky spheroid (the original projection of aeromagnetic maps) to the Lambert conic projection in order to create a coherent set of aeromagnetic grids. As for the gravity data, the qualitative and quantitative evaluation of the magnetic data is difficult.

The gravimetric and magnetic datasets can lead to many controversies. However, it is unfortunately the only datasets available and determining the uncertainties of each grid is very difficult as the acquisition modes and the treatments processes remain ambiguous.

4. Traitements et outils d'interprétation des données de méthodes potentielles

Cette partie, en français, est un résumé non exhaustif des méthodes de traitements des grilles de méthodes potentielles utilisées pour ce travail de thèse.

4.1. Traitements et outils d'interprétation pour les données gravimétriques

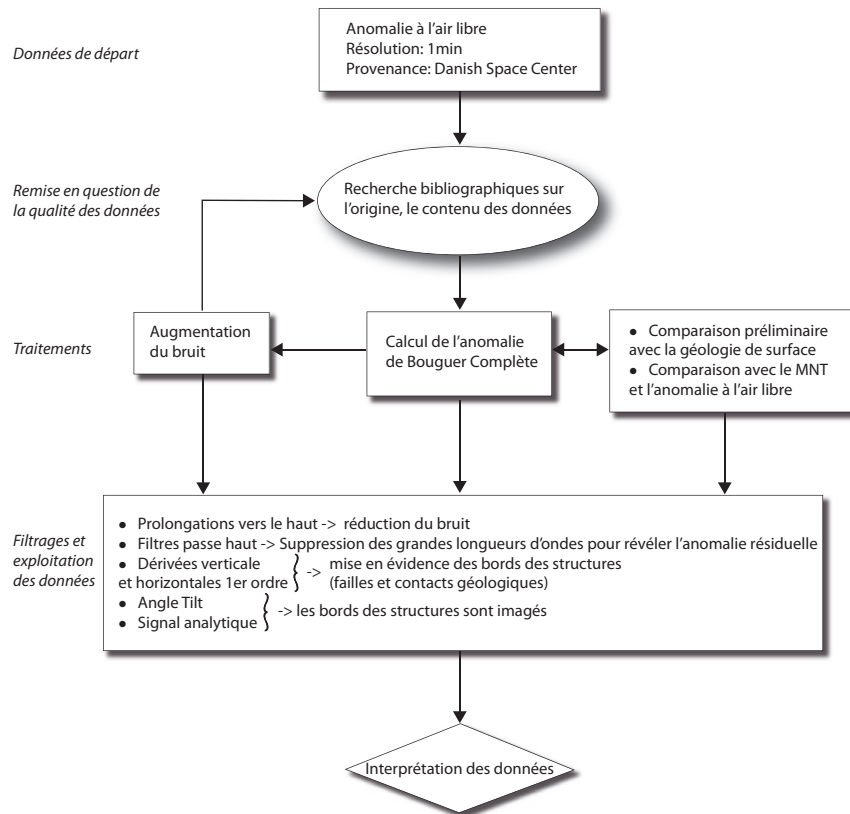


Figure 10: Workflow de l'exploitation des données gravimétriques.

Figure 10: Workflow of the gravity data processes.

4.1.1. Traitement qualitatif des données gravimétriques : calcul de l'anomalie de Bouguer

Les données d'anomalie à l'air libre existent sous la forme d'une grille présentant les variations du champ de pesanteur corrigé des effets de latitude et d'altitude. Cette grille constitue nos données de départ en gravimétrie. L'anomalie à l'air libre est fortement influencée par la topographie et a, par conséquent, une forte corrélation avec celle-ci. L'anomalie à l'air libre n'est donc qu'en partie influencée par l'effet gravitationnel des masses qui se situent entre la surface topographique et le géoïde. Ainsi, pour analyser et mettre en évidence les hétérogénéités de masse et l'ensemble des corps présents sous la surface topographique, l'anomalie de Bouguer doit être calculée.

La correction de Bouguer peut être scindée en trois étapes : (1) l'anomalie de Bouguer simple aussi appelé Bullard A (Fig. 12) qui est la différence entre la valeur mesurée à une altitude h et la valeur théorique corrigée de la correction à l'air libre et de la correction de plateau ; (2) la correction du rayon de courbure (ou Bullard B) qui prend en compte l'effet gravimétrique de la courbure de la calotte sphérique (LaFehr, 1991b) ; et (3) l'anomalie de Bouguer complète à laquelle est ajoutée, en plus des corrections précédentes, la correction de terrain, également nommée Bullard C (Nowell, 1999 ; Fulla et al., 2008).

La méthode de Nettleton a été utilisée le long d'un profil traversant les quatre zones lithotectoniques (Fig. 11) afin de déterminer au mieux la densité de référence à utiliser pour le calcul de l'anomalie de Bouguer. Il en résulte que le choix de la densité de référence pour le calcul de l'anomalie de Bouguer n'est pas aisé à déterminer puisque la méthode de Nettleton (1939) est difficilement utilisable sur une vaste zone comme la notre (Fig. 11). En effet, Nettleton (1939) a appliqué le principe le long d'un profil traversant une vallée et son haut relief adjacent sur une distance n'excédant pas les 2 km de long. A titre de comparaison, notre région pour laquelle l'anomalie de Bouguer doit être calculée fait environ 600x400 km. N'ayant donc aucune contrainte particulière possible, nous prenons la valeur habituelle de densité utilisée pour le calcul de l'anomalie de Bouguer, à savoir 2,67.

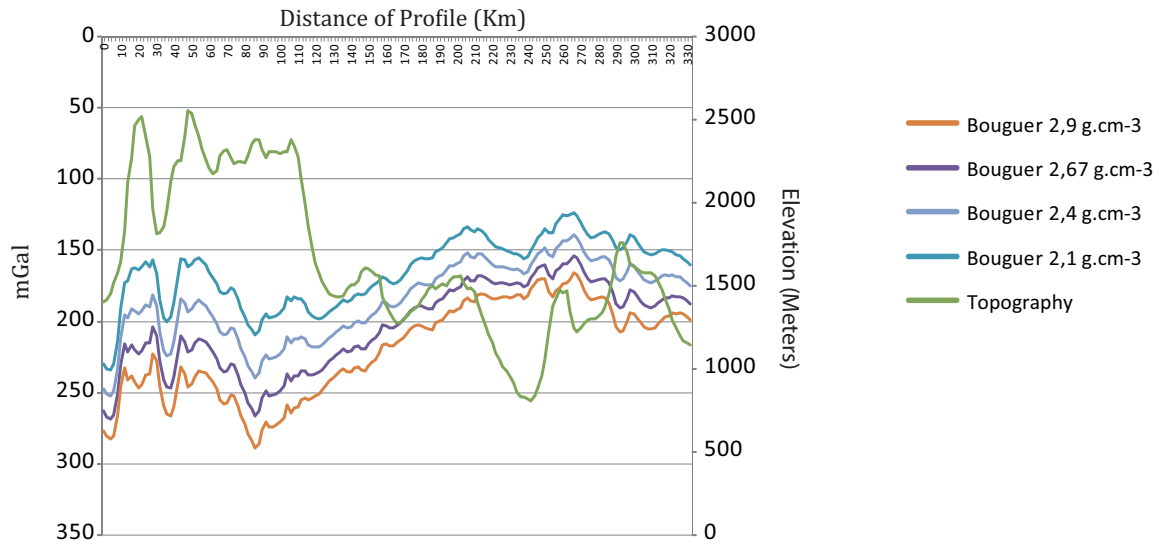


Figure 11: Méthode de Nettleton (1939) appliquée le long d'un profil traversant les quatre zones lithotectoniques
Figure 11: Method of Nettleton (1939) along a profile cross-cutting the four lithotectonic zones.

Equation de l'anomalie de Bouguer simple (Bullard A) :

$$GA = g_m \pm (g_t - \Delta g_{CAI} + \Delta g_{CP}) = g_m \pm (g_t - \frac{2g_t}{R} * h + 2\pi G \rho h)$$

unité : [mGal]

$$= \text{Anomalie à l'air libre} - 2\pi G \rho h$$

Où g_m la gravité mesurée

g_t la valeur théorique de la gravité

Δg_{CAI} la correction à l'air libre (0.3086h)

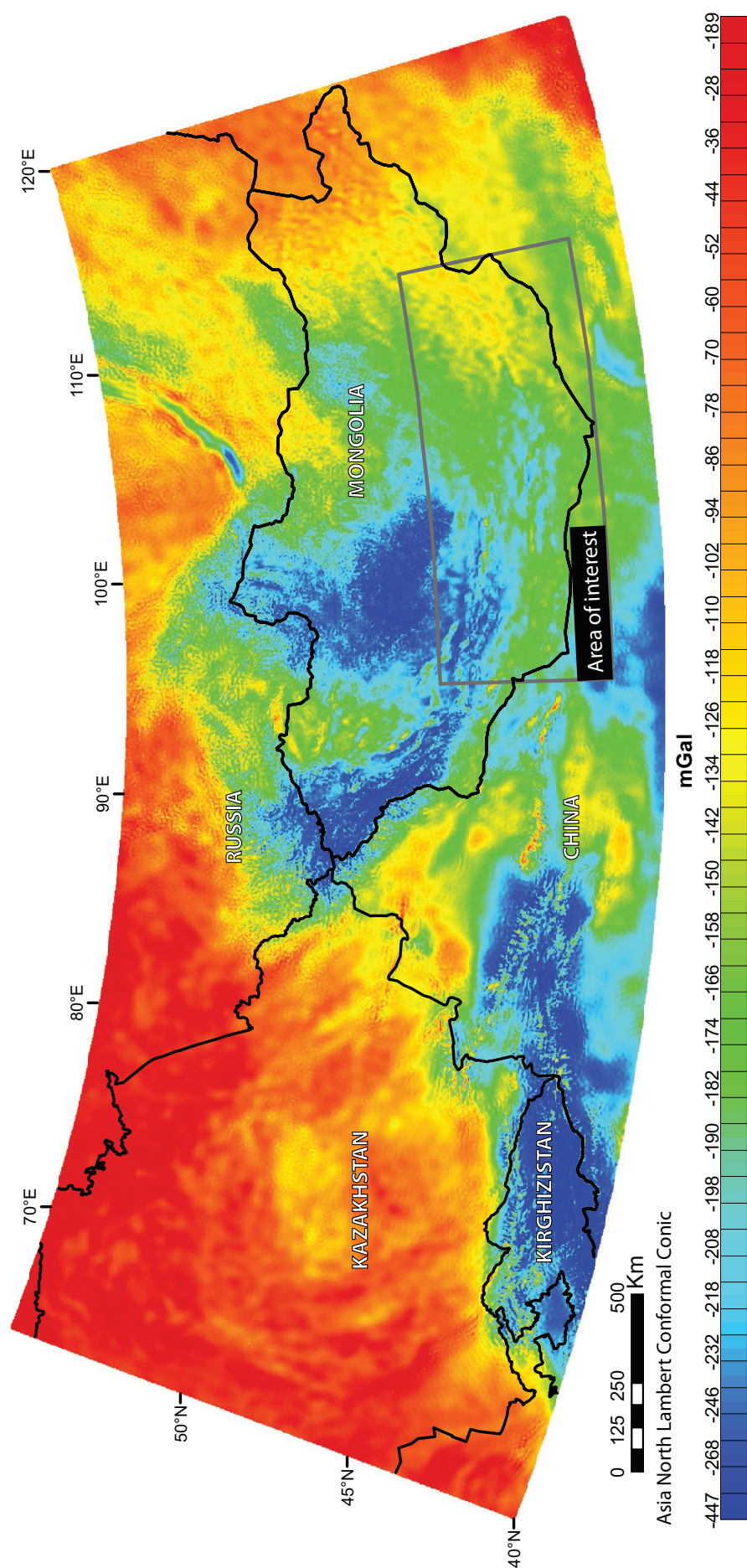
Δg_{CP} la correction de plateau

R le rayon moyen de la Terre

h l'altitude de la station en mètre

G la constante de gravitation universelle

ρ la densité de référence



Equation de la correction du rayon de courbure de la correction de plateau dans l'anomalie de Bouguer simple :

$$GB \approx 2\pi G \rho h \left(\frac{\alpha}{2} - \eta \left[1 + \frac{1}{2\alpha} \right] \right)$$

Où $\alpha = \frac{S}{R_o}$ S étant le rayon de la zone de Hayford-Bowie (166.735 km)

$\eta = \frac{h}{R_o + h}$ R0 le rayon de la Terre (~6371 km)

Equation de l'anomalie de Bouguer complète :

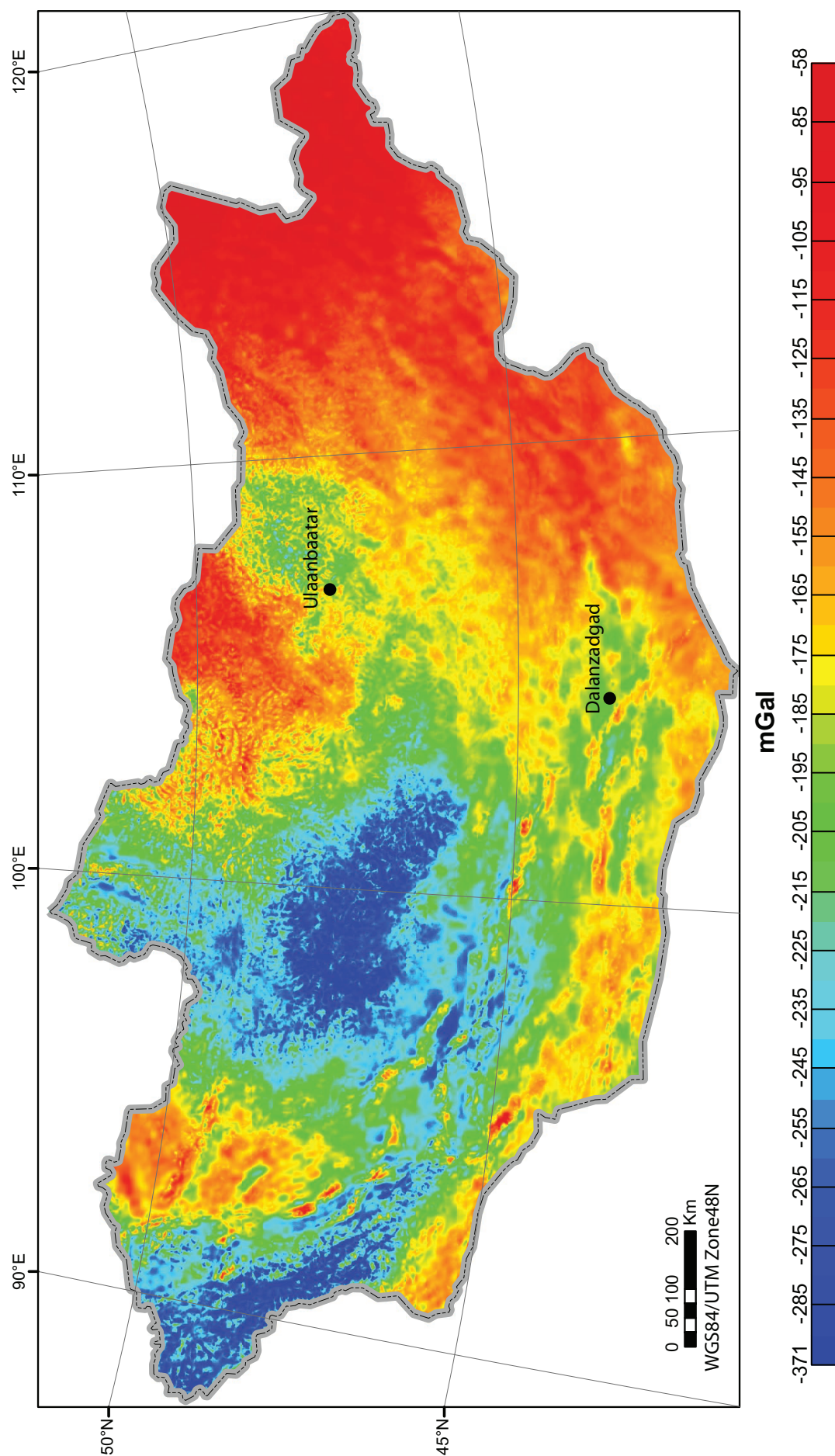
$$A_{Bc} = g_m \pm (g_t - \Delta g_{Cal} + \Delta g_{CP} - \rho T) \quad \text{unité : [mGal]}$$

Où Δg_{CP} contient la correction Bullard B

T est la correction de terrain qui prend en compte l'effet de la topographie environnante de la station de mesure à l'aide d'une intégrale.

L'anomalie de Bouguer complète a été calculée à l'aide du logiciel Oasismontaj avec la densité de référence pour la croûte de 2,67 (Fig. 12). En plus des autres corrections, la correction de la courbure de la Terre selon LaFehr (1991a) pour convertir le plateau supposé infini en un plateau sphérique a été prise en compte. La correction de terrain a été calculée au préalable et indépendamment du processus de calcul de l'anomalie de Bouguer, en appliquant le modèle numérique de terrain ETOPO1 (Amante et Eakins, 2009) à 1 min de résolution, et en utilisant la combinaison des méthodes de Nagy (1966) et Kane (1962). Il est à préciser que le calcul de la correction de terrain requiert une puissance de calcul informatique non négligeable. Ainsi, il n'a donc pas été possible de calculer l'anomalie de Bouguer complète à l'échelle de la Ceinture Orogénique d'Asie Centrale, mais seulement à l'échelle de la Mongolie.

Figure 12: Anomalie de Bouguer simple calculée à partir de l'anomalie à l'air libre fournie par DTU.
Figure 12: Simple Bouguer anomaly computed from the free air anomaly provided by DTU.



4.1.2. Anomalie à l'air libre, MNT et anomalie de Bouguer : Clivages et similitudes

La figure 14 compare l'anomalie à l'air libre, l'anomalie de Bouguer simple, l'anomalie de Bouguer complète et la géologie sur une partie du sud de la Mongolie afin d'identifier les différences et les analogies entre les différents traitements gravimétriques, la géologie de surface et la topographie.

L'anomalie à l'air libre (Fig. 14c) est ainsi fortement corrélée à la topographie (Fig. 14b) comme nous l'avons déjà vu. Les anomalies de Bouguer simple (Bullard A et B) et complète (Fig. 14d et e) sont négatives. Ceci est dû au fait que la correction de Bouguer permet d'enlever l'effet de la croûte continentale mais sans supprimer les effets des masses à grandes profondeurs à l'origine des anomalies isostatiques de cette même croûte continentale. De plus, les corrélations entre la topographie et les anomalies de Bouguer simple et complète sont globalement atténuées par rapport à celles qui existent entre la topographie et l'anomalie à l'air libre. Cependant, il est à noter que l'anomalie de Bouguer simple et l'anomalie de Bouguer complète présentent une composante régionale inversement proportionnelle aux grandes longueurs d'ondes de la topographie. La différence entre l'anomalie de Bouguer simple et l'anomalie de Bouguer complète est la correction de terrain qui est sensée supprimer entièrement l'effet topographique dans le signal gravimétrique. Toutefois, les différences de valeurs entre l'anomalie de Bouguer simple et l'anomalie de Bouguer complète sont faibles.

Figure 13: Anomalie de Bouguer complète sur la Mongolie.

Figure 13: Complete Bouguer anomaly over Mongolia.

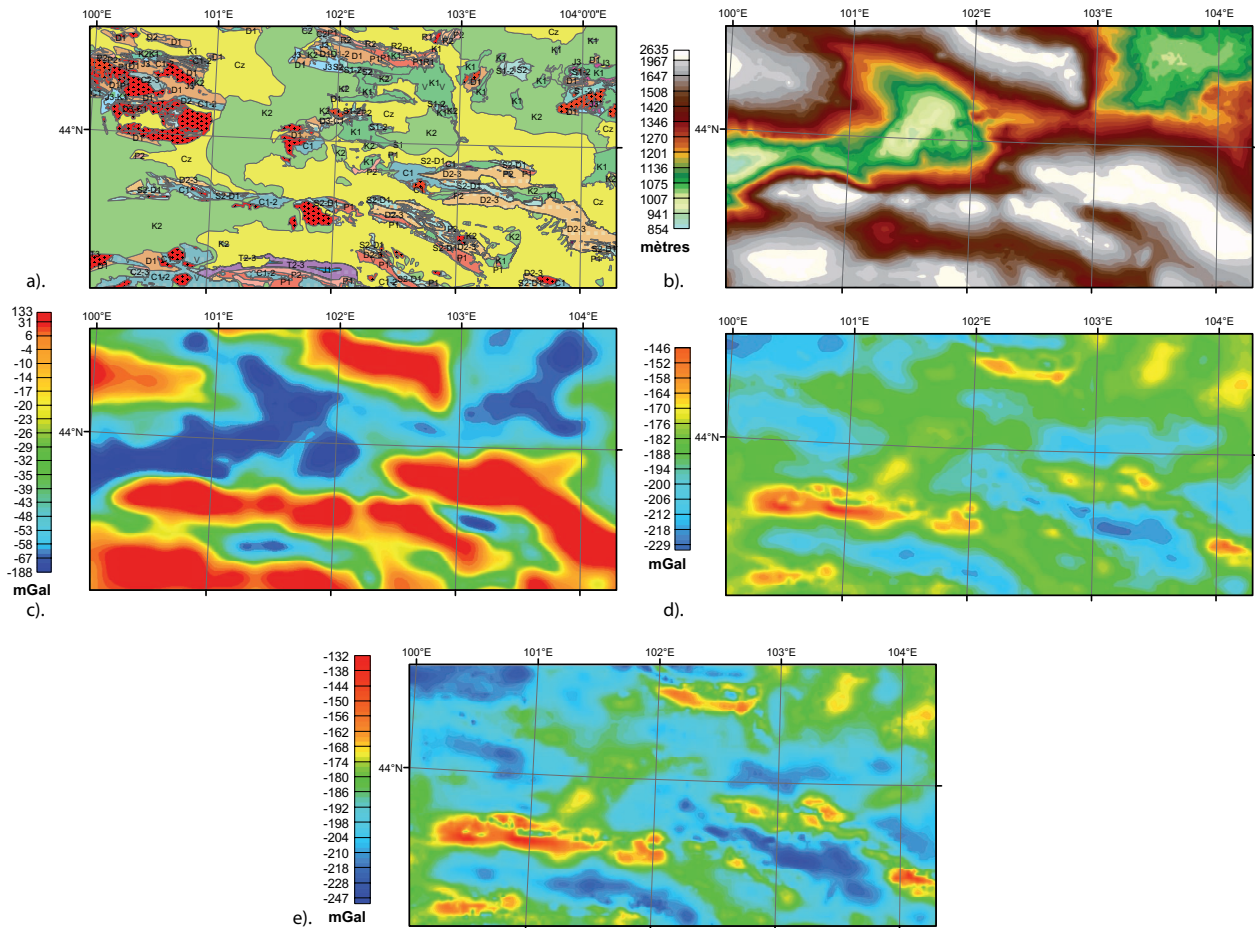


Figure 14: Comparaisons des corrections effectuées sur les anomalies gravimétriques sur une zone de la Mongolie. a). Géologie de la zone ; b). Topographie de la zone ; c). Anomalie à l'air libre ; d). Anomalie de Bouguer simple ; e). Anomalie de Bouguer complète.

Figure 14: Comparison of the different gravity corrections on a restricted area. a). Geological map; b). Topography; c). Free air anomaly ; d). Simple Bouguer anomaly ; e). Complete Bouguer anomaly.

4.1.3. Opérateurs de traitements et mise en valeur des données gravimétriques

Toutes les opérations de traitements suivants ont été effectuées à l'aide du logiciel Oasimontaj. Les opérateurs se définissent dans le domaine des fréquences en utilisant la transformée de Fourier, puis l'inverse de la transformée de Fourier pour revenir dans le domaine spatial.

4.1.3.1. Prolongement vers le haut

Le signal de la grille de l'anomalie de Bouguer complète obtenue semble contenir du bruit. Cela n'est finalement pas très surprenant étant donné que la grille d'anomalie à l'air libre serait une compilation de plusieurs sources d'acquisition différentes. Le prolongement vers le haut atténue les hautes fréquences du signal par rapport aux basses fréquences en ramenant le signal gravimétrique sur un même plan tout en l'éloignant des sources (Fig. 15a). Les contours de l'anomalie gravimétrique sont alors lissés (Fig. 15 b) ce qui réduit les petits artefacts dus au

bruit. L'opérateur de prolongement vers le haut dans le domaine spectral s'écrit :

$$e^{-\sqrt{u^2+v^2}z} \text{ où } u \text{ et } v \text{ sont respectivement les pulsations associées à } x \text{ et } y.$$

z est l'altitude du prolongement.

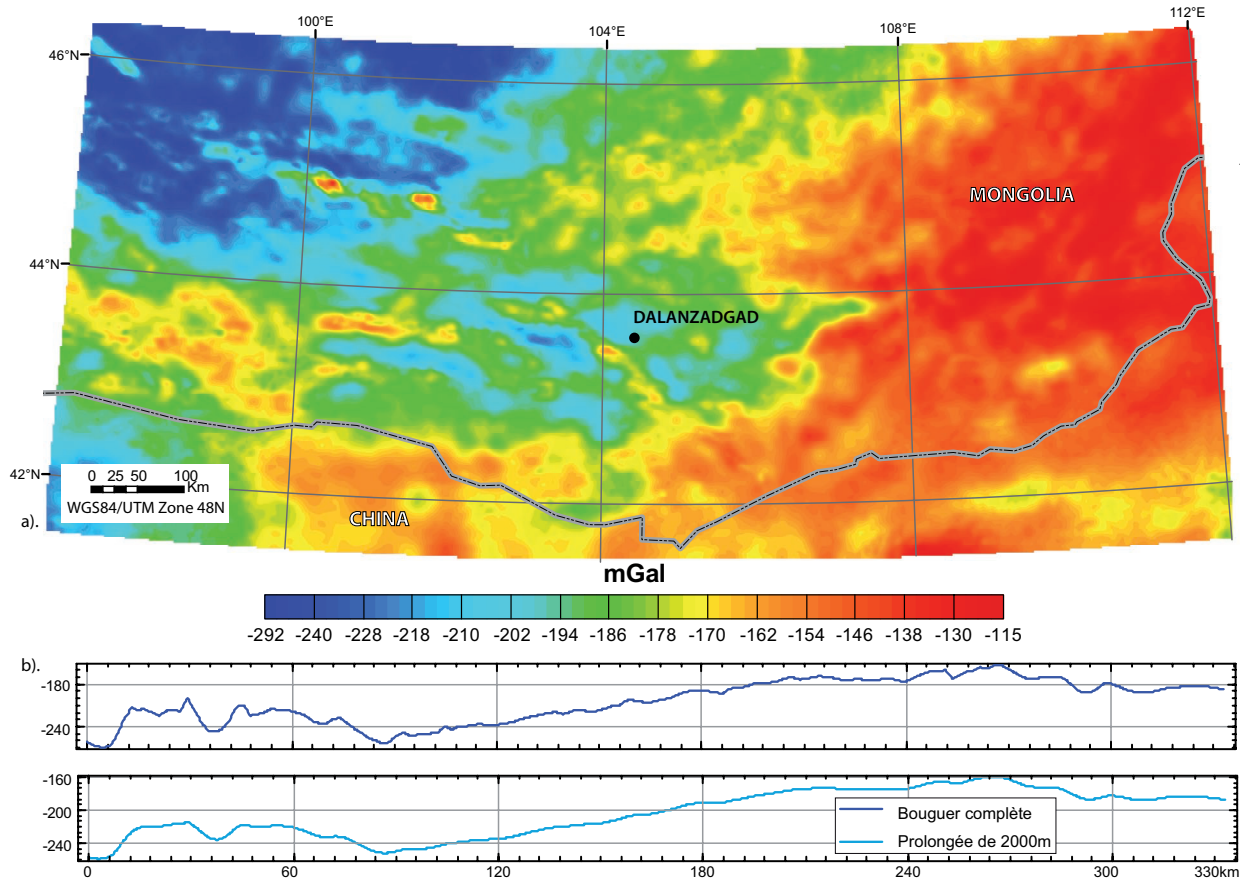


Figure 15: a). Grille de l'anomalie de Bouguer complète sur la partie sud de la Mongolie prolongée de 2000 m vers le haut ; b). Extraction des valeurs de l'anomalie de Bouguer complète et de l'anomalie de Bouguer complète prolongée de 2000 m vers le haut.

Figure 15: a). Upward continuation of 2000 m of the complete Bouguer anomaly over the south of Mongolia; b). Comparison of the tendency along one profile between the complete Bouguer anomaly and the one upward continued.

Les petits artefacts attribués au bruit du signal étaient encore visibles à 1000 m de prolongement vers le haut mais semblent être suffisamment atténués à 2000 m (Fig. 15a). Au-delà de 2000 m de prolongement vers le haut, le signal est trop lissé pour mener l'interprétation qui nous intéresse.

4.1.3.2. Filtre passe-haut

L'anomalie de Bouguer peut être décomposée en anomalies de grandes, moyennes et courtes longueurs d'onde. D'une part, le signal contenant les variations gravimétriques de grandes longueurs d'ondes, ces variations forment l'anomalie régionale. Elle est essentielle pour évaluer l'influence sur le signal des structures à grandes échelles telles les grands bassins sédimentaires,

les chaînes volcaniques/plutoniques généralement associés à des variations topographiques du Moho. D'autres parts, superposée à l'anomalie régionale, l'anomalie résiduelle représente les courtes et moyennes longueurs d'ondes du signal gravimétrique. Les courtes longueurs d'ondes sont produites par des contrastes de densités localisés préférentiellement dans les parties supérieures de la croûte.

Une des méthodes retenues pour obtenir l'anomalie résiduelle est le filtre passe-haut: toutes les longueurs d'ondes, qui sont inférieures à la fréquence de coupure déterminée, sont supprimées. Le but étant d'éliminer les grandes longueurs d'ondes supposées être dues aux variations du Moho voire à l'hétérogénéité du manteau ainsi que l'influence des grandes structures tectoniques. Les tests de filtre passe-haut ont été faits pour différentes fréquences de coupures. La figure 16 est la grille obtenue avec une fréquence de coupure de 100 km.

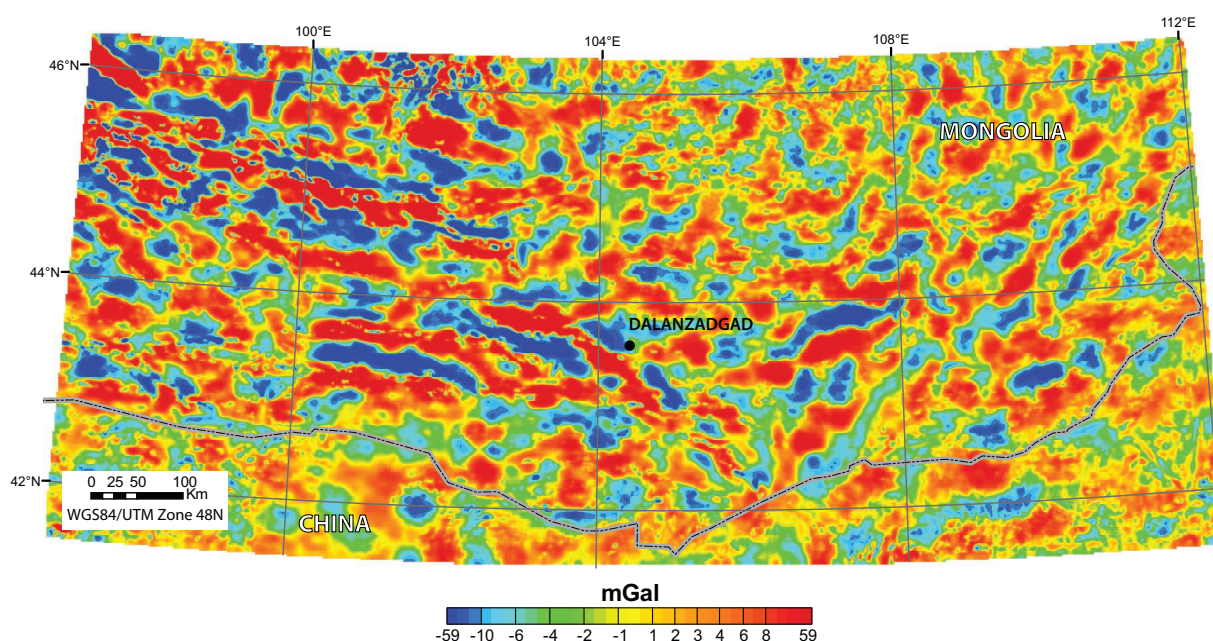


Figure 16: Filtre passe-haut de fréquence de coupure de 100 km appliqué à l'anomalie de Bouguer complète sur la partie sud de la Mongolie.

Figure 16: High-pass filter of a cutoff of 100 km of the complete Bouguer anomaly over the south of Mongolia.

4.1.3.3. Dérivée verticale

La dérivée verticale permet de séparer les anomalies et de localiser les limites des structures. Le gradient est maximum à l'aplomb des limites des structures lorsque celles-ci sont subverticales. Comme ce filtre réduit la longueur d'onde, le bruit du signal a tendance à augmenter (Fig. 17), il faut donc ensuite souvent y appliquer un filtre pour atténuer le bruit du signal obtenu. La dérivée verticale (selon z) au 1er ordre a été appliquée à l'anomalie de Bouguer, puis prolongée vers le haut pour atténuer le bruit induit (Fig. 17).

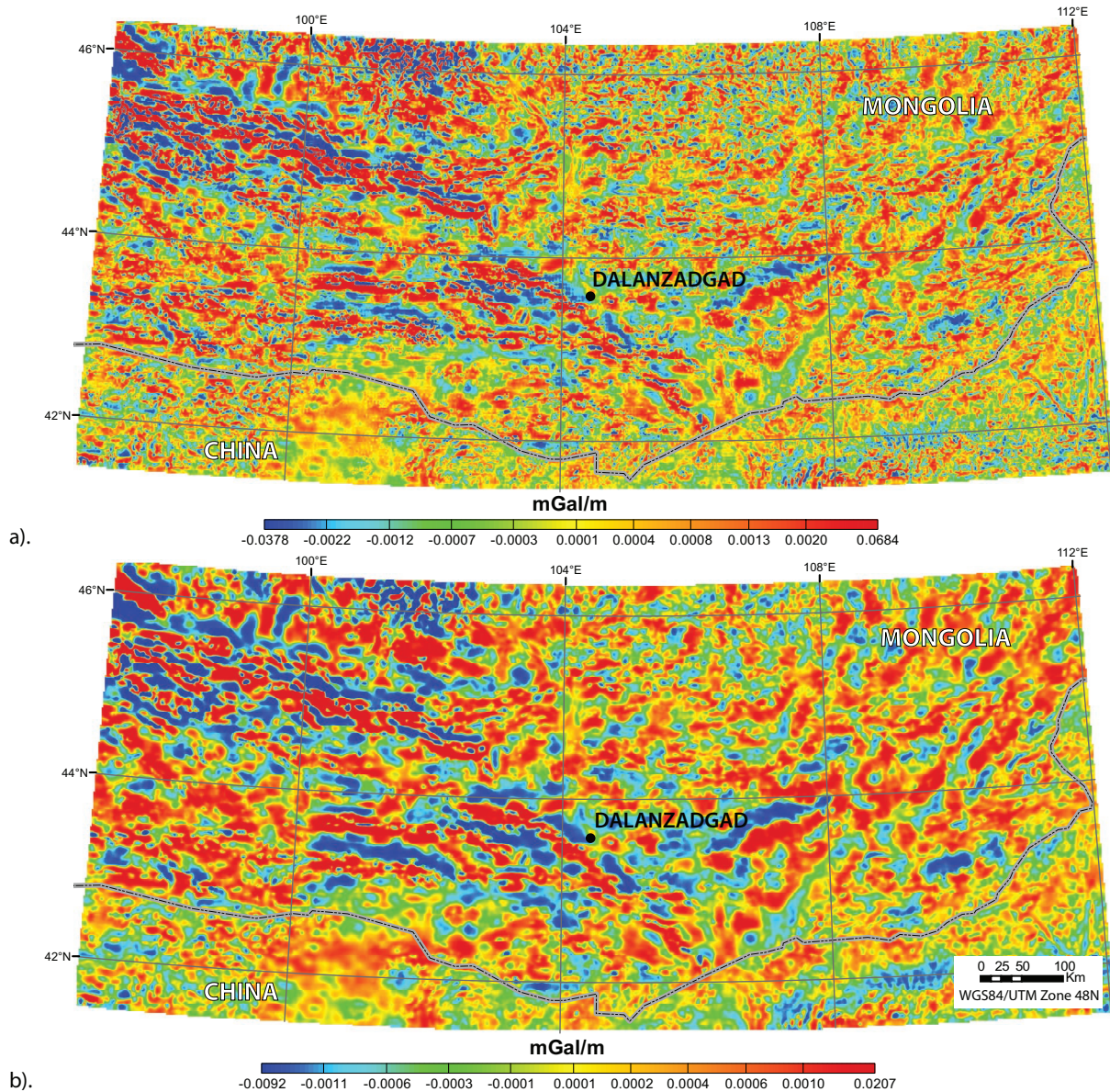


Figure 17: Dérivée verticale au 1er ordre de l'anomalie de Bouguer complète. a). Dérivée verticale au 1er ordre brute révélant le bruit du signal ; b). Dérivée verticale au 1er ordre prolongée vers le haut de 2000m afin de réduire le bruit du signal.

Figure 17: First verticale derivative of the complete Bouguer anomaly. a). raw verticale derivative with signal noise; b). upward continuation of 2000 m of the first vertical derivative to remove the signal noise.

4.2. Traitements et outils d'interprétation pour les données magnétiques

Les traitements de la grille magnétique ont été effectués à l'aide du logiciel Oasimontaj. De même qu'en gravimétrie, les opérateurs se définissent dans le domaine des fréquences en utilisant la transformée de Fourier, puis l'inverse de la transformée de Fourier pour revenir dans le domaine spatial.

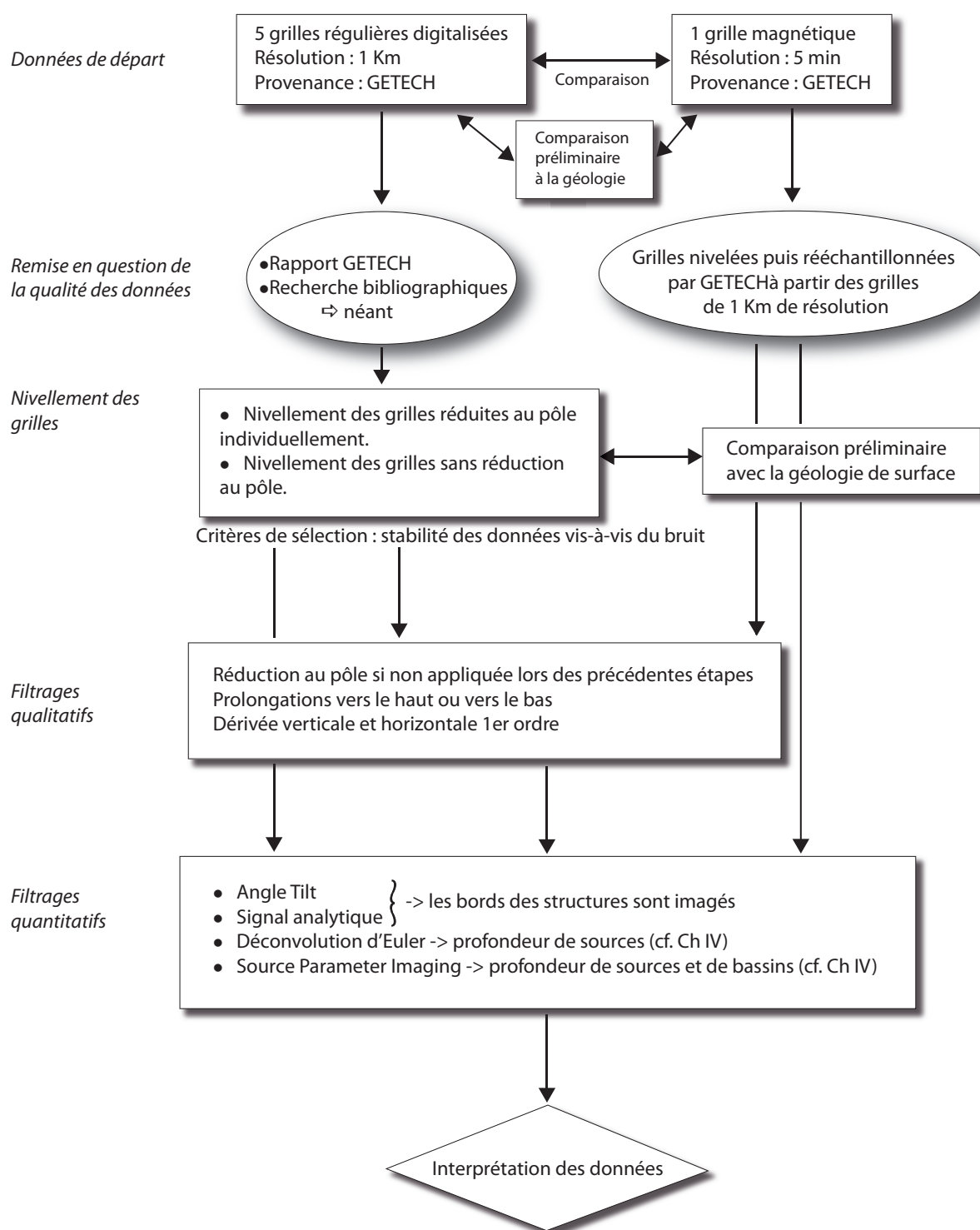


Figure 18: Workflow de l'exploitation des données magnétiques.

Figure 18: Workflow of the magnetic data processes.

4.2.1. Nivellement des grilles

Deux jeux de données magnétiques sont à notre disposition : le premier, qui a 5 min de résolution, est composé des grilles de 1 km de résolution ré-échantillonnées et est déjà nivelé ; le second qui est composé des 5 grilles individuelles de relevés magnétiques doit être corrigé en

partie puis nivelé avant d'être fusionné pour obtenir une grille unique afin de faire une analyse à grande échelle. En effet, le mode d'acquisition des 5 grilles n'est pas homogène (Fig. 9) et pour relier les grilles entre elles, quelques corrections préliminaires s'imposent.

4.2.1.1. Réduction au pôle

La réduction au pôle est la transformation du signal permettant de ramener la direction du champ magnétique régional à la verticale comme ce serait le cas du champ magnétique régional situé aux pôles. Pour appliquer une réduction au pôle, il faut connaître la direction du champ magnétique régional de la zone mesurée au moment de l'acquisition des données. Chaque grille ayant été relevée à une époque différente, il nous faut déterminer les paramètres du champ régional (Tableau 2) correspondant à la date d'acquisition grâce au modèle IGRF (International Geomagnetic Reference Field).

Tableau 2 : Valeurs IGRF correspondantes aux années de relevés magnétiques. F, champ régional; I, Inclinaison; D, Déclinaison.

Table 2: International Geomagnetic Reference Fields used to reduce to the pole each different survey. F, magnitude of the regional magnetic field; I, the inclination; D, the declination.

Grille ID	Année de relevé	IGRF correspondant	F [nT]	I [°]	D [°]
contours verts	1981	1980	58009,8	66,6	-2,4
contours oranges	1989-90	1990	57371,4	64,7	-0,7
contours violets	1987-88	1990	57683,5	65,1	-0,5
contours marrons	1967	1965	58502,7	62,5	-4
contours bleu	1966	1965	60853,2	65	-5,2

La réduction au pôle est également appliquée dans le domaine de Fourier où l'opérateur de changement de direction pour une réduction au pôle du champ régionale et de l'aimantation supposée induite est :

$$\left(\frac{(\pm \sqrt{(u^2 + v^2)})}{\left(iu\alpha_x + iv\alpha_y \pm \alpha_z \sqrt{(u^2 + v^2)} \right)} \right)^2$$

Où α_x , α_y et α_z sont respectivement les composantes du vecteur unitaire dans la direction du champ magnétique régional.

Plusieurs options s'offrent à nous :

- Réduire au pôle chaque grille magnétique en fonction du modèle IGRF correspondant avant de niveler les grilles entre elles ;
- Ne pas réduire au pôle avant le nivellement ;

- Appliquer la réduction au pôle après le nivellement des grilles, le modèle IGRF étant alors choisi d'une manière arbitraire compte tenu de l'hétérogénéité des relevés ;

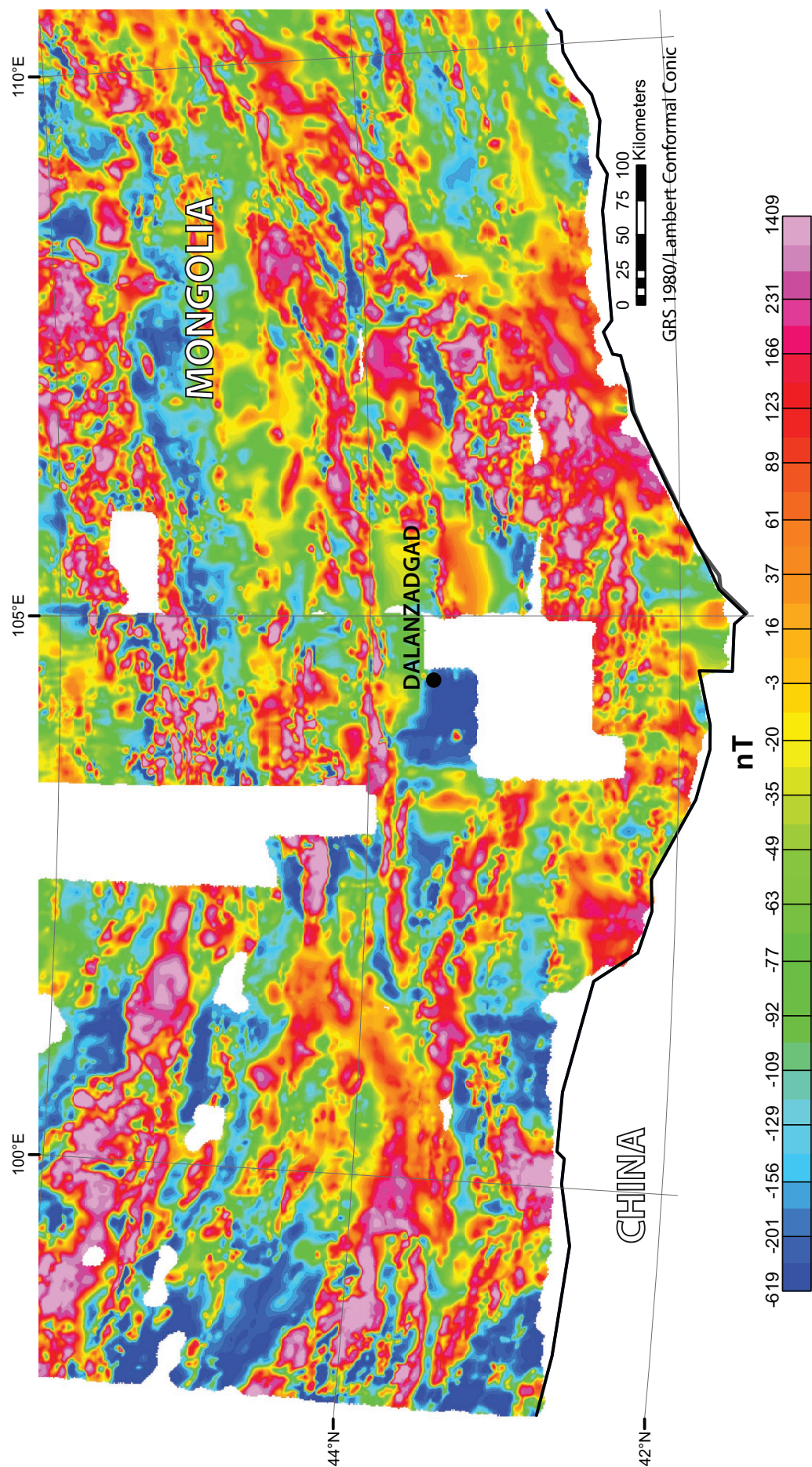
La dernière option est la plus mauvaise et n'a pas été retenue étant donné qu'à ces traitements suivra une interprétation des grilles magnétiques afin d'avoir un à priori sur les structures de la croûte. Les deux premières options ont été mises en oeuvre donnant lieu à deux grilles rassemblant les 5 grilles.

4.2.1.2. Prolongement vers le haut

La dernière étape avant le nivellement est de ramener chaque grille à une même altitude avant de les fusionner entre elles. Le prolongement vers le haut ou le bas, suivant les cas, est l'opérateur qui a été retenu. Son expression est identique à l'opérateur de prolongement en gravimétrie (cf. partie 4.1.3.1.). Ainsi toutes les grilles ont été amenées à une altitude d'acquisition de 1000 m. Toutes les grilles ont été levées en théorie à 200 m d'altitude, exceptée la grille levée en 1981 qui a été levée à 1900 m. C'est pourquoi l'altitude moyenne de 1000m nous a semblé la plus appropriée. Ainsi les 4 grilles levées à 200 m ont été prolongée vers le haut de 800m et la grille levée à 1900 m a été prolongée vers le bas de 900 m.

Une fois les grilles réduites au pôle ou non, les prolongements adéquats effectués, les grilles peuvent être fusionnées (Fig. 19).

Figure 19: Grille nivelée et fusionnée de l'anomalie magnétique du Sud de la Mongolie sans réduction au pôle.
Figure 19: Magnetic anomaly grid leveled and merge over the south of Mongolia without reducing to the pole.



4.2.2. Traitements qualitatifs de l'anomalie magnétique

4.2.2.1. Dérivée verticale

La dérivée verticale de l'anomalie magnétique permet de mieux individualiser les sources proches de la surface en renforçant les hautes fréquences. L'opérateur de dérivation met en évidence les bords des structures (Fig. 20).

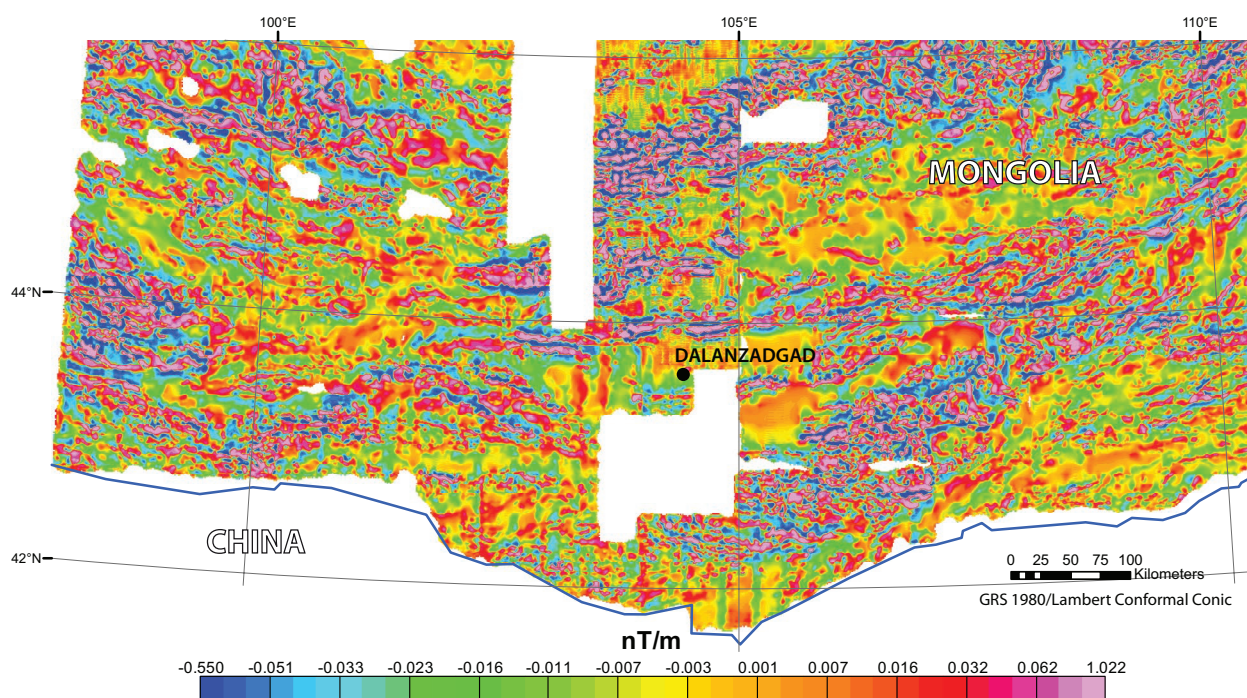


Figure 20: Dérivée verticale au premier ordre de l'anomalie magnétique.

Figure 20: First verticale derivative of the magnetic anomaly.

4.2.2.2. Dérivées horizontales

Les dérivées de l'anomalie du champ magnétique en X (généralement dirigé vers le nord) et en Y (vers l'Est) permettent aussi de mettre en évidence les contacts majeurs (par exemple les failles) car les gradients sont situés à l'aplomb de ces contacts par les mêmes procédés que la dérivée verticale (Fig. 21).

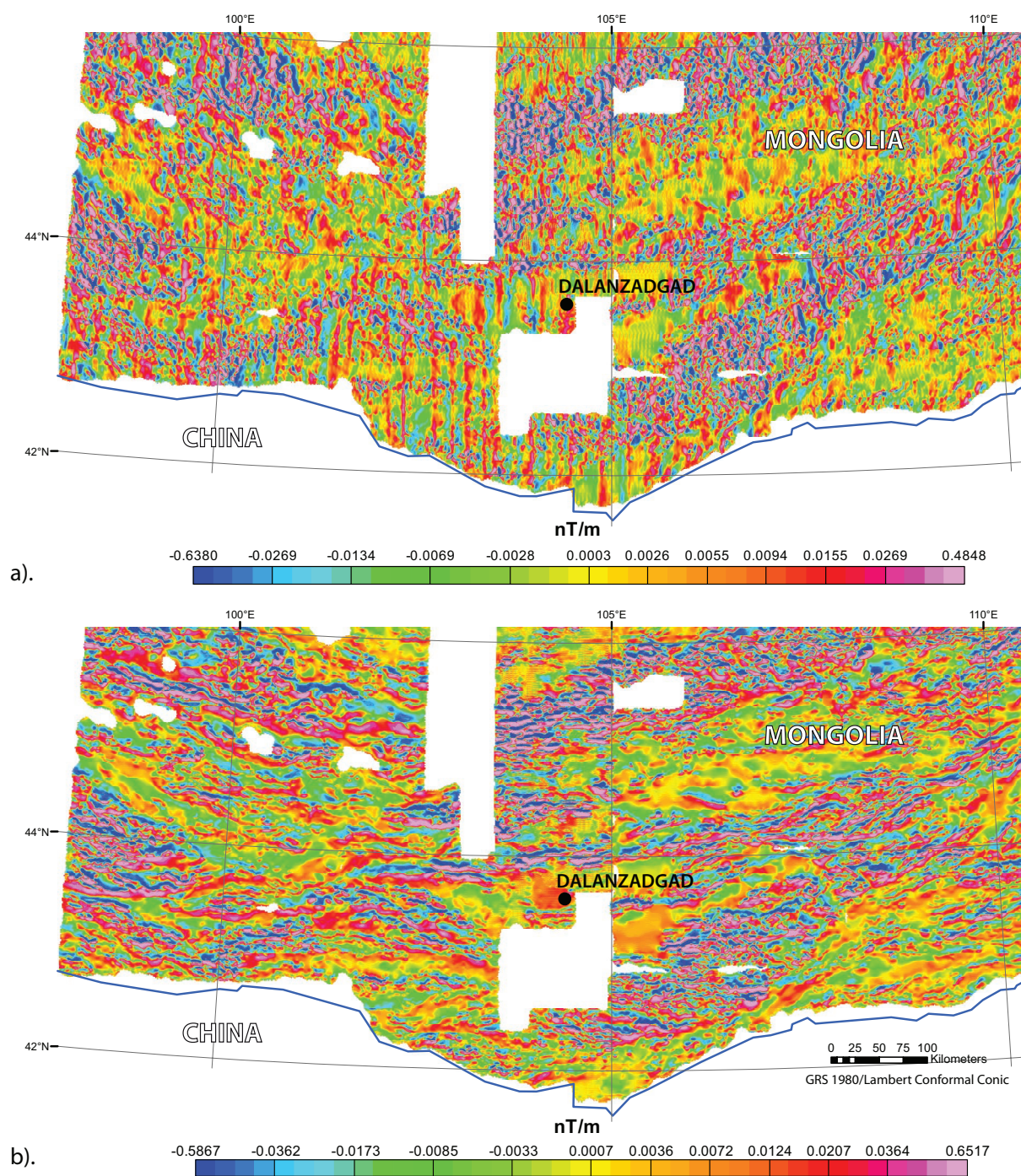


Figure 21: Dérivées horizontale au premier ordre de l'anomalie magnétique. a). Dérivée selon la direction X ; b). Dérivée selon la direction Y.

Figure 21: First horizontal derivatives of the magnetic anomaly. a). Horizontale derivative in X direction; b). Horizontale derivative in Y direction.

4.2.3. Traitements quantitatifs : estimation des profondeurs de sources

4.2.3.1. Angle tilt

Les traitements dits de « l'angle tilt » peuvent permettre de caractériser la source du signal magnétique. L'angle tilt (Miller et Singh, 1994) permet de localiser le bord des structures

ainsi qu'une profondeur de source relative. Il s'exprime par la relation mathématique suivante :

$$TILT = \arctan \left(\frac{\frac{\partial M}{\partial z}}{\sqrt{\left(\frac{\partial M}{\partial x}\right)^2 + \left(\frac{\partial M}{\partial y}\right)^2}} \right) \quad M \text{ étant l'anomalie magnétique}$$

L'angle tilt a plusieurs propriétés : (1) grâce à la nature de la fonction trigonométrique arctangente, toutes les valeurs du tilt sont comprises entre $-\frac{\pi}{2}$ et $\frac{\pi}{2}$ quelque soit l'amplitude de la dérivée verticale $\frac{\partial M}{\partial z}$ ou de la valeur absolue du gradient horizontal total $\sqrt{\left(\frac{\partial M}{\partial x}\right)^2 + \left(\frac{\partial M}{\partial y}\right)^2}$; (2) il est théoriquement possible d'avoir un à priori sur la profondeur des structures en plus de la localisation de ses bords (angle nul) en approximant ces structures au cas simple d'un contact vertical (Fig. 21a). Ainsi la distance h observée le long du profil de l'angle tilt entre l'intersection de la courbe de valeur du tilt et 0° d'une part, et l'intersection de la courbe et 45° d'autre part, est égale à la profondeur z du contact verticale (Salem et al., 2007). Le contact vertical se situe au niveau de 0° de l'angle tilt. Bien évidemment, le contact vertical entre deux structures aux aimantations différentes est une approximation pouvant être abusive selon le cas. Cependant, l'application de cette méthode de détermination de la profondeur des structures en faisant l'hypothèse préliminaire de contacts verticaux (Fig. 22b), peut constituer un point de départ à l'interprétation des structures de la croûte.

Figure 22: Angle tilt appliqué à l'anomalie magnétique. a). Théorie de détermination de la profondeur du contact (modifié d'après Salem et al., 2007) ; b). Grille de l'angle tilt obtenu avec la mise en évidence des isocontours pour les valeurs du tilt 0° à l'aplomb du contact théorique et des isocontours pour les valeurs du tilt 45° , ce qui permet une évaluation des profondeurs des structures (plus la distance entre l'isocontour 0° et 45° est grand plus la structure sera située en profondeur, et vice versa).

Figure 22: Tilt angle of the magnetic anomaly. a). Theory to evaluate the depth of the contact (modified after Salem et al., 2007); b). Isolines of 0° and 45° of tilt angle values superimposed on the tilt angle gravity grid. The 0° tilt angle value corresponds to the theoretical contact. The distance between the 0° and 45° tilt angle values allow evaluating the depth of the contact.



4.2.3.2. Signal analytique

Les maxima du signal analytique (Nabighian, 1972, 1974) se situent à l'aplomb des limites des structures (Fig. 23). Dans le cas du modèle de Nabighian (1972, 1974), la forme du signal analytique (en cloche) donne la profondeur étant donné que la largeur de la courbe en cloche à mi-hauteur équivaut, en théorie, à la profondeur de la source. Le signal analytique peut s'écrire de la forme suivante :

$$|SA| = \sqrt{\left(\frac{\partial M}{\partial x}\right)^2 + \left(\frac{\partial M}{\partial y}\right)^2 + \left(\frac{\partial M}{\partial z}\right)^2} \text{ où } M \text{ est l'anomalie du champ magnétique}$$

These gravity and magnetic qualitative and quantitative treatments provide only a first estimation of the source parameters; but they are an essential step to determine the geophysical characteristics of the area and to evaluate the correlation between the geophysical signal and the geology.

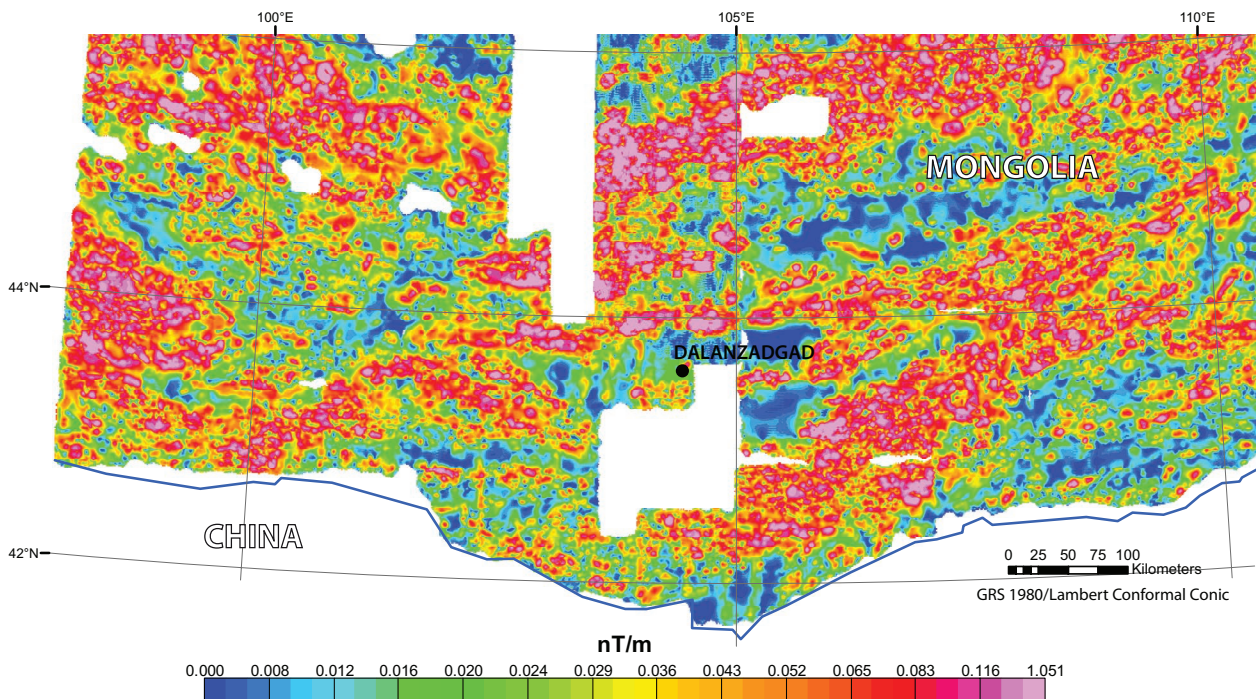


Figure 23: Signal analytique de l'anomalie magnétique.

Figure 23: Analytic signal of the magnetic anomaly.

5. Geophysical patterns of southern Mongolia and comparison with the surface geology

5.1. Potential field maps

The potential field data may allow inferring the origin of anomaly sources when correlating different set of data, like surface geology or the tectonic setting. Basically, the anomalies with large wavelengths (hundreds of kilometers) are induced by sources located in the lower crust or even more in the upper mantle. However, we have to keep in mind that a wide, shallow and thin source with low dipping edges can also produce a large wavelength anomaly. On the contrary, the anomalies with short-wavelengths are induced by sources located at shallow level of the crust. The processing of the gravity and magnetic anomaly grids are used to enhance the effects of density and susceptibilities contrasts and thus to highlight the boundaries.

5.1.1. Magnetic anomaly map

The magnetic anomaly map (Fig. 24.1.c.) presented here is the result of the merge of five different surveys, individually reduced to the pole according to the characteristics of the IGRF (International Geomagnetic Reference Field) for each survey. As the magnetic field attenuates faster with the distance to the source than the gravity field, the magnetic anomalies enhance the upper and mid-crustal features of the crust. The computed isolines of the vertical derivative are superimposed on the magnetic anomaly map in order to illustrate the lateral contrasts. This map displays an alternation of magnetic highs and lows allowing correlations with the surface geology as well. However, the sedimentary basins (mainly Cretaceous and Cenozoic) distributed all over our area of interest can attenuate the relics of highly magnetic Palaeozoic arcs, calc-alkaline granitoids or ophiolites. In an other hand, it can be also the high magnetic signal of volcano-sedimentary basins (few small examples sporadically distributed) superimposed and thus, this high magnetic signal masks the deep magnetic anomalies. These concealed geological structures can be partially deduced from an analysis of processing magnetic anomaly map correlated with the tectonic framework of the area.

5.1.2. Residual Bouguer anomaly map

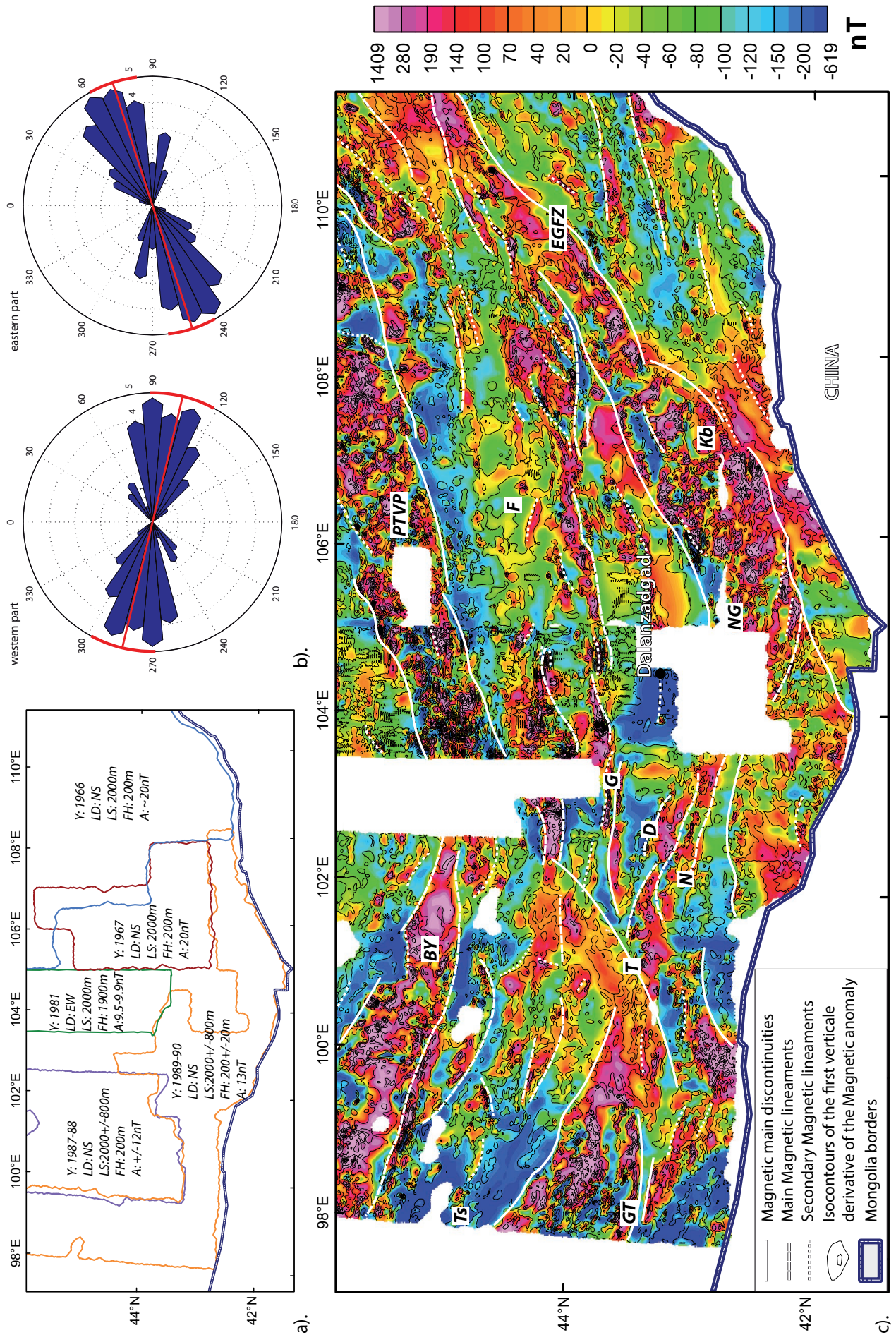
A map of residual Bouguer anomaly displays short- to intermediate-wavelengths (Fig.

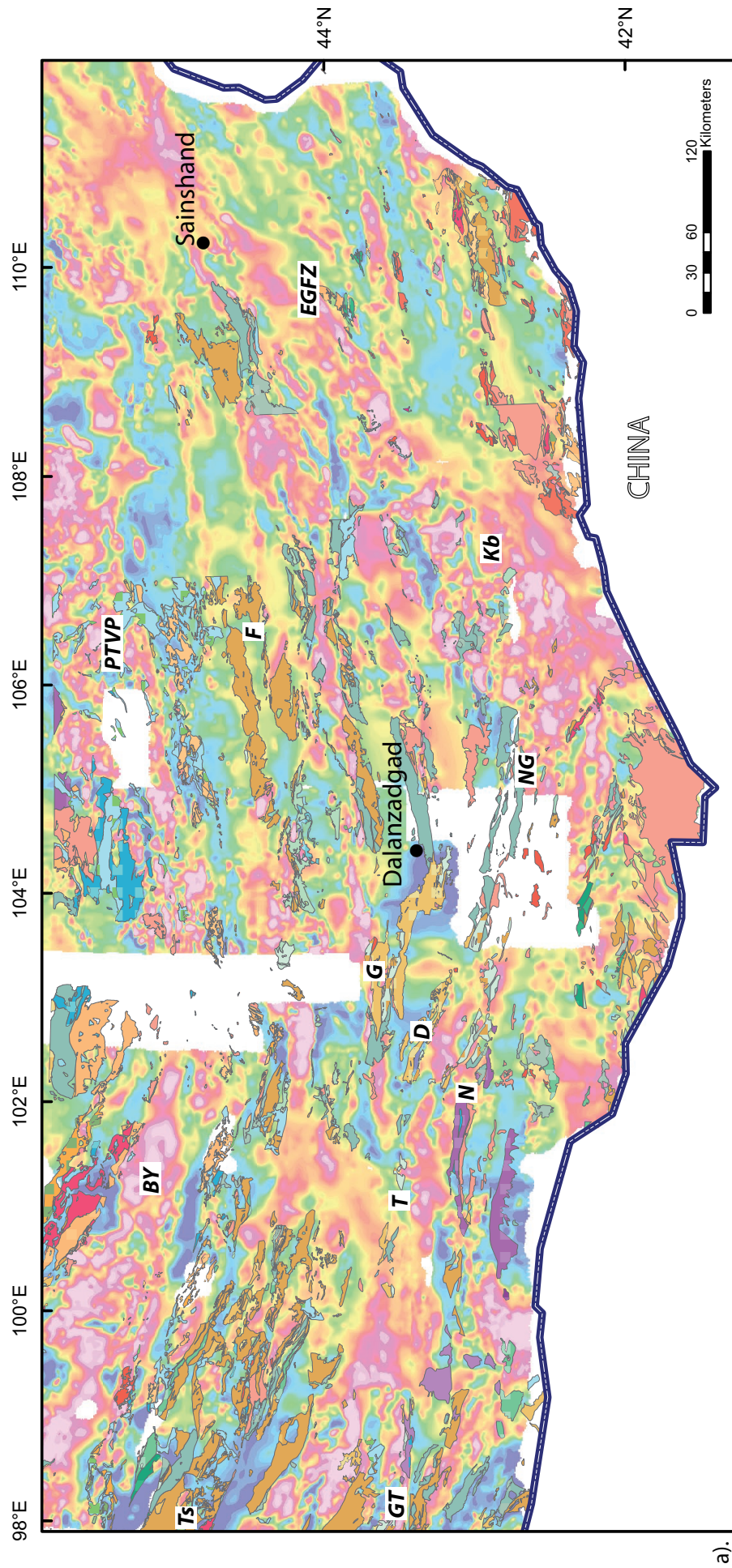
25.1.c.). Our residual Bouguer anomaly map is obtained after applying a cutoff of 100 km which corresponds to a compromise between the half wavelength associated with the Hangay dome and the high Bouguer anomaly area to the east of Mongolia (Fig. 25.1.a.). This process removes long-wavelengths anomalies induced by sources in the deep crust or in the upper mantle, and should remove the effect of the Moho topography. Therefore, the map in figure 25.1.c. shows the density contrasts in the upper crust. In addition, the isolines of the vertical derivative of the complete Bouguer anomaly are superimposed on this residual Bouguer anomaly map in order to highlight the boundaries of gravimetric bodies making the gradients stronger. This map displays an alternation of gravity highs and lows allowing correlations with the surface geology. However, at the present time shallow crustal rocks cannot explain all of the gravity anomalies observed.

5.2. Magnetic structures analysis

The magnetic anomaly map of the south Mongolia ranges from -619 nT to 1409 nT (Fig. 24.1.c.). The interpretation of magnetic features is depicted by lineaments in figure 24.1.c.: magnetic discontinuities are delineated as solid lines and are defined by strong and elongated gradients; and dotted lines trace magnetic highs. Thus, the magnetic lineaments mostly strike WNW-ESE to the western part and ENE-WSW to the eastern part (Fig. 24.1.b.). The analysis of the magnetic anomaly lineaments (Fig. 24.1.b.) reveals a major change in orientation of the lineament trends. The inflexion of the lineament trend is approximately located at 104° of longitude. The sharp magnetic contrasts are often correlated with major fault traces, which are sometimes only inferred on the basis of their weak surface expression. With the magnetic signal, these fault traces can be clearly delineated. Three major faults can be delineated by markedly discontinuities of the magnetic anomaly: the Gobi-Tianshan fault zone (GT), the Tost fault (T) and the East Gobi fault zone (EGFZ). Several minor faults can also be delineated by strong magnetic anomaly gradients. The high amplitude magnetic anomaly province to the northwestern part corresponds to the Baydrag block (BY) and Figure 24.2.e. shows that the basement is obscured by Cenozoic sediments. The Permian-Trias volcanic-plutonic belt (PTVP) also displays high amplitudes which correlate with the granitoids of early Permian in age (Fig. 24.2.c.). South of the BY, the Tseel area (Ts) and its surrounds globally expose a low

Figure 24.1.: Magnetic anomaly analysis. a). Location of the surveys and their characteristics; b). Rose diagrams of the preferred orientation of the magnetic lineaments; c). Magnetic anomaly map reduced to the pole according to each surveys. The isocontours of the first vertical derivative is superimposed on the map. The white lines are the lineaments. The color scale is in equal area distribution. BY: Baydrag microcontinent; Ts: Tseel terrane; GT: Gobi-Tianshan fault zone; T: Tost fault; G: Gurvansaykhan range; D: Dzolen range; N: Noyon area; F: Flyshoid basin; NG: Nomgon area; Kb: Khan Bogd granite; EGFZ: East Gobi Fault Zone.





a).

Figure 24.2.a.: Sedimentary rocks superimposed on the magnetic anomaly map.

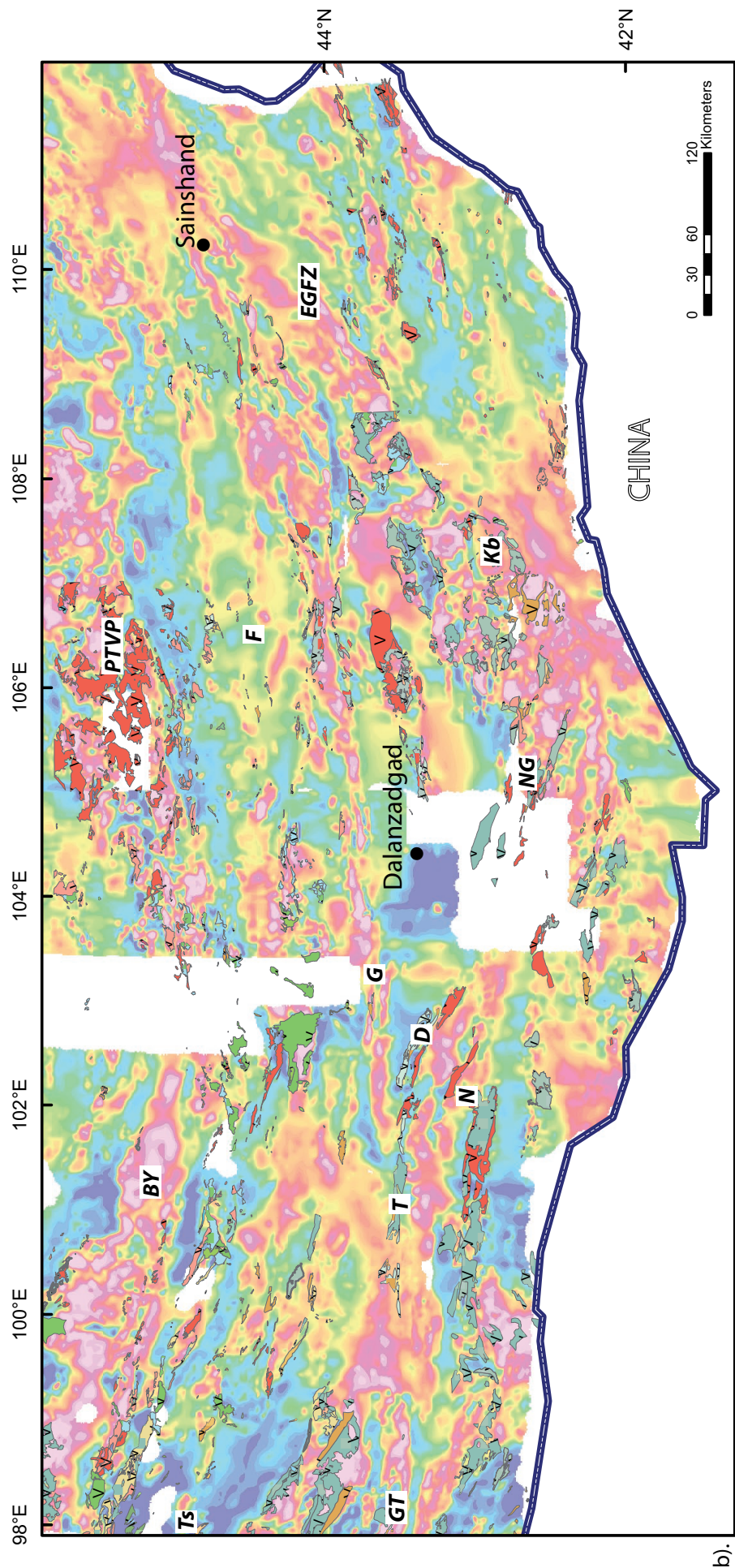


Figure 24.2.b.: Volcanic rocks superimposed on the magnetic anomaly map.

amplitude magnetic anomaly province mostly correlated with Palaeozoic sedimentary rocks (Fig. 24.2.a.), punctuated by magnetic highs due to presence of ultramafic rocks (Fig. 24.2.d.) and volcanic rocks of Devonian, Devonian-Carboniferous and early Permian in ages. To the north of the GT, the magnetic highs correlate with the Devonian and Carboniferous volcanic rocks essentially basalts and basaltic andesites (Markova, 1975). Similarly, to the south of the GT, the Carboniferous volcanic rocks (basalts and andesites) associated with granitoids of early to middle Carboniferous age correspond to magnetic highs (Fig. 24.2.b.). The Gurvansaykhan range (G) shows two parallel highly magnetic ribbons which correspond to the late Silurian-early Devonian sedimentary rocks containing slivers of ultramafic rocks. To the east of the G and north of Dalanzadgad, until nearly the EGFZ, an elongated high amplitude magnetic anomaly is observed, which apparently has no correlation with the geological surface composed mostly of Cretaceous and Cenozoic basins, and some scarce Devonian and Carboniferous sediments. This zone may correspond to a major shear zone described by Blight et al., (2010). To the north of this discontinuity, the flyschoid basin (F) defined by Zaitsev et al. (1970) presents intermediate to low amplitudes magnetic anomalies. The Dzolen range (D), south of the G, displays unexpected magnetic low despite presence of ultramafic rocks and late Silurian-early Devonian and Carboniferous volcanic rocks. Only, blurred magnetic high is located below the Cenozoic basin which can correspond to Dzolen type lithologies in this area. To the south of the D, the Noyon Uul Mesozoic syncline and its Carboniferous and Permian volcanic rocks are correlated with a magnetic low. In the Nomgon area, the magnetic highs correlate partly with the Carboniferous volcanic rocks (essentially basaltic and andesitic) associated with granitoids of various age (Fig. 24.2.b. and c.), but the Cenozoic basins cover the magnetic highs (Fig. 24.2.e.). The early Permian Khan Bogd pluton (Kb) shows a high amplitude magnetic anomaly and is surrounded by middle to late Devonian granitoid associated with early Devonian and Carboniferous volcanic rocks that are also highly magnetic. To the north of the EGFZ, high amplitude magnetic anomalies are covered by Cretaceous sedimentary basins indicating that the magnetic sources are buried underneath sediments. To the south of the EGFZ, the magnetic highs are most probably due to ridges formed by late Carboniferous granites.

In summary, there is a major change of orientation of magnetic lineament from WNW-ESE to ENE-WSW oriented belts, which is correlated with common geological trends. Among the rock units exposed in southern Mongolia, the Palaeozoic sedimentary rocks correlate with low amplitude magnetic anomaly. On the contrary, the volcanic rocks (Devonian, late Carboniferous-early Permian, Permian, late Jurassic-early Cretaceous, and Cretaceous) display a positive magnetic anomalies, except for several early Carboniferous and early Permian volcanic rocks particularly in the Noyon area. The early Permian alkaline granitoids are

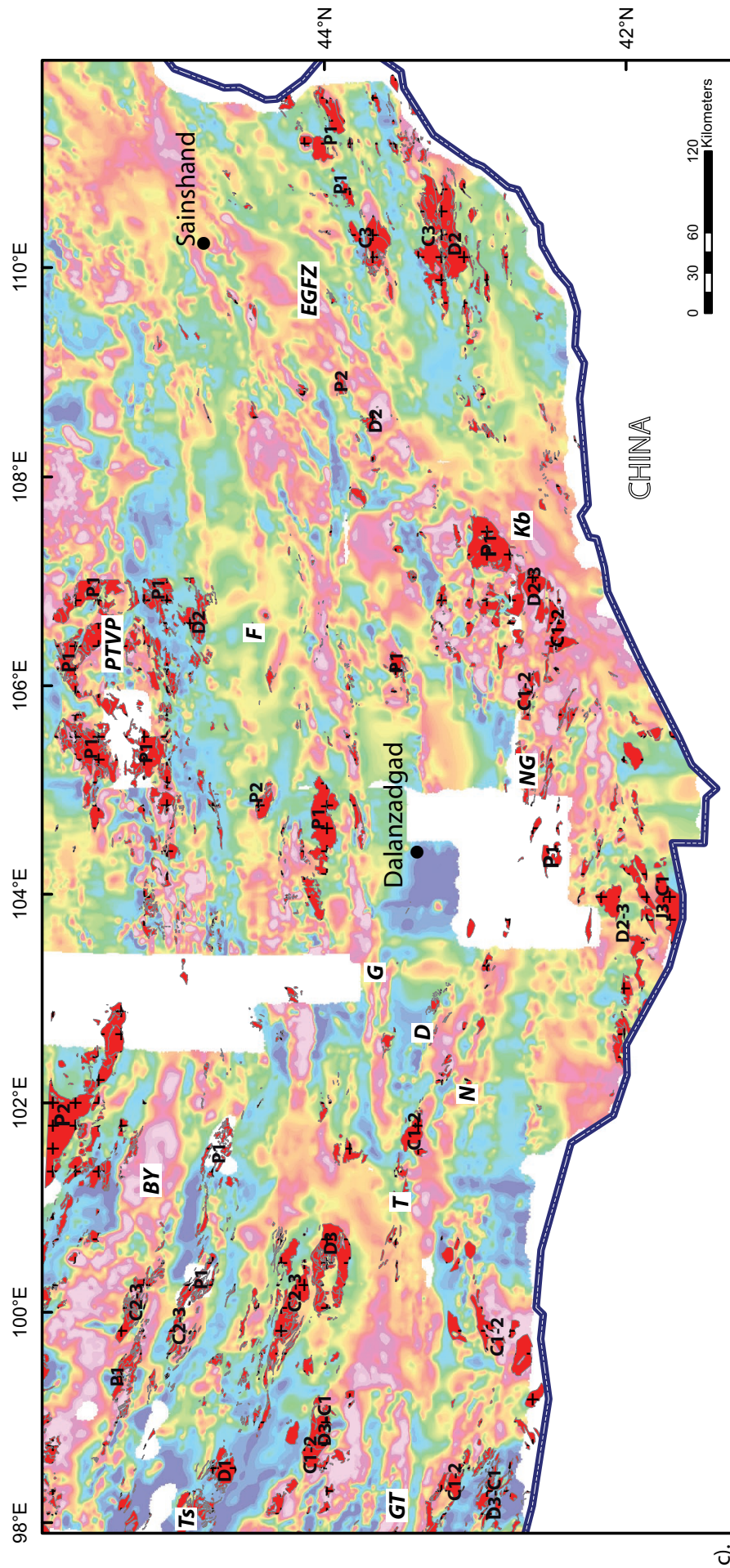


Figure 24.2.c.: Granitoids superimposed on the magnetic anomaly map.

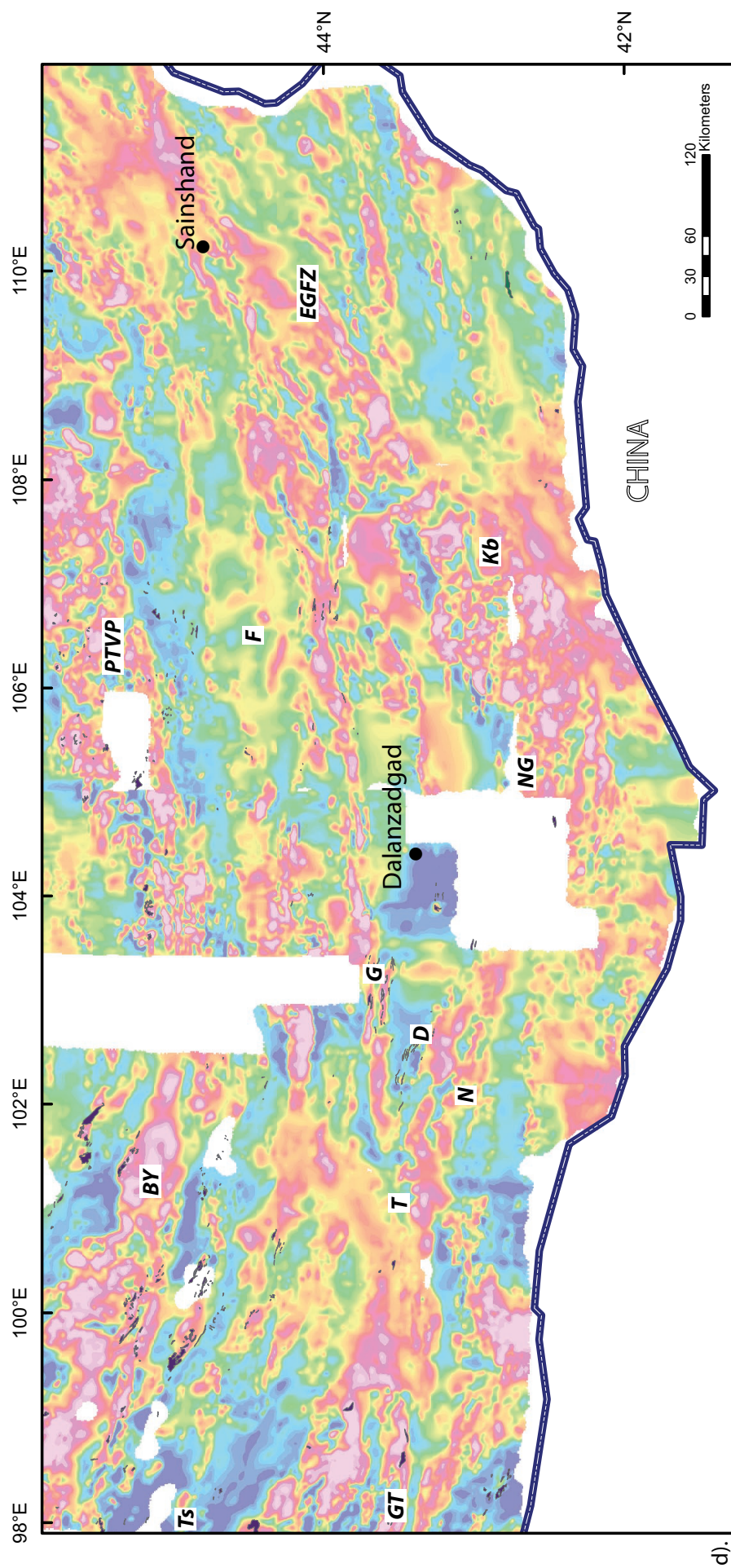


Figure 24.2.d.: Ultramafic rocks superimposed on the magnetic anomaly map.

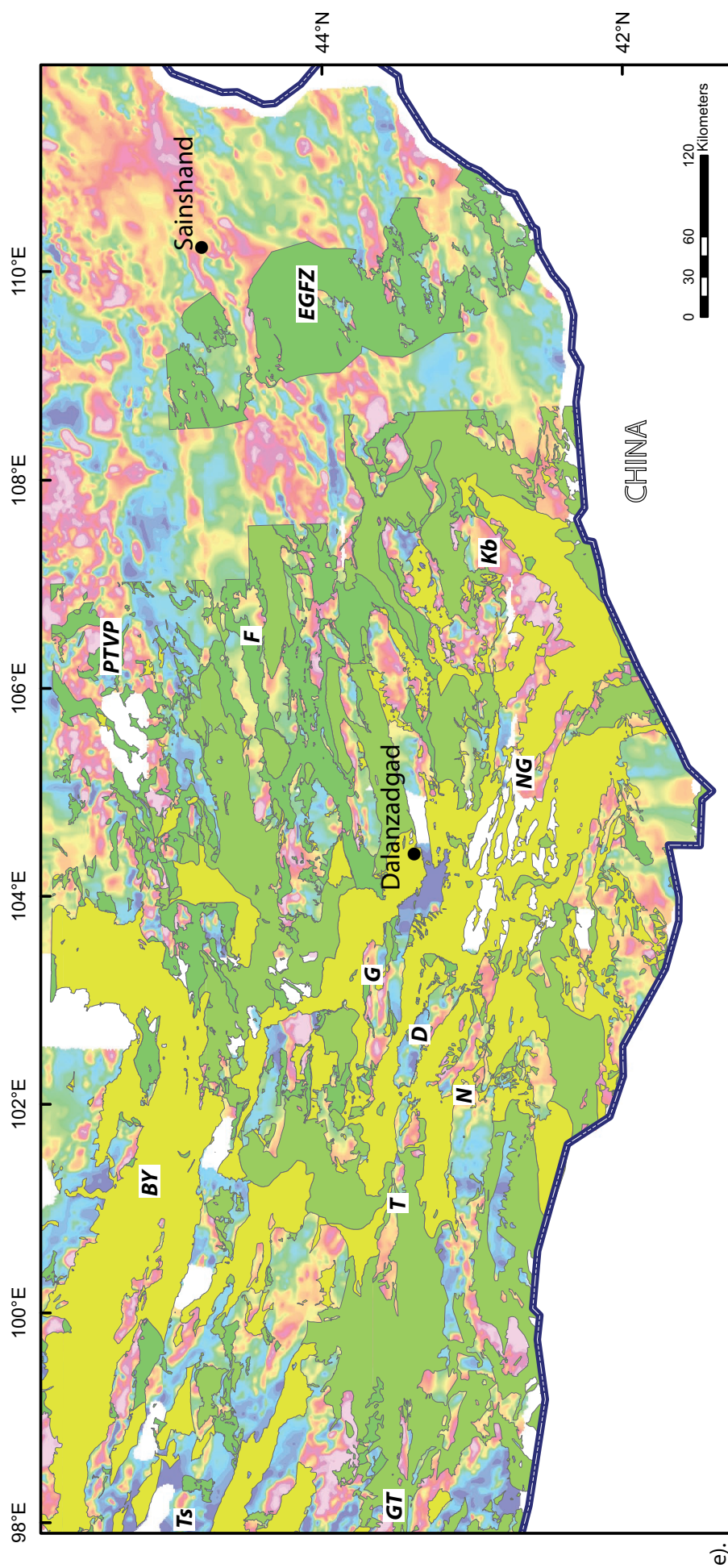


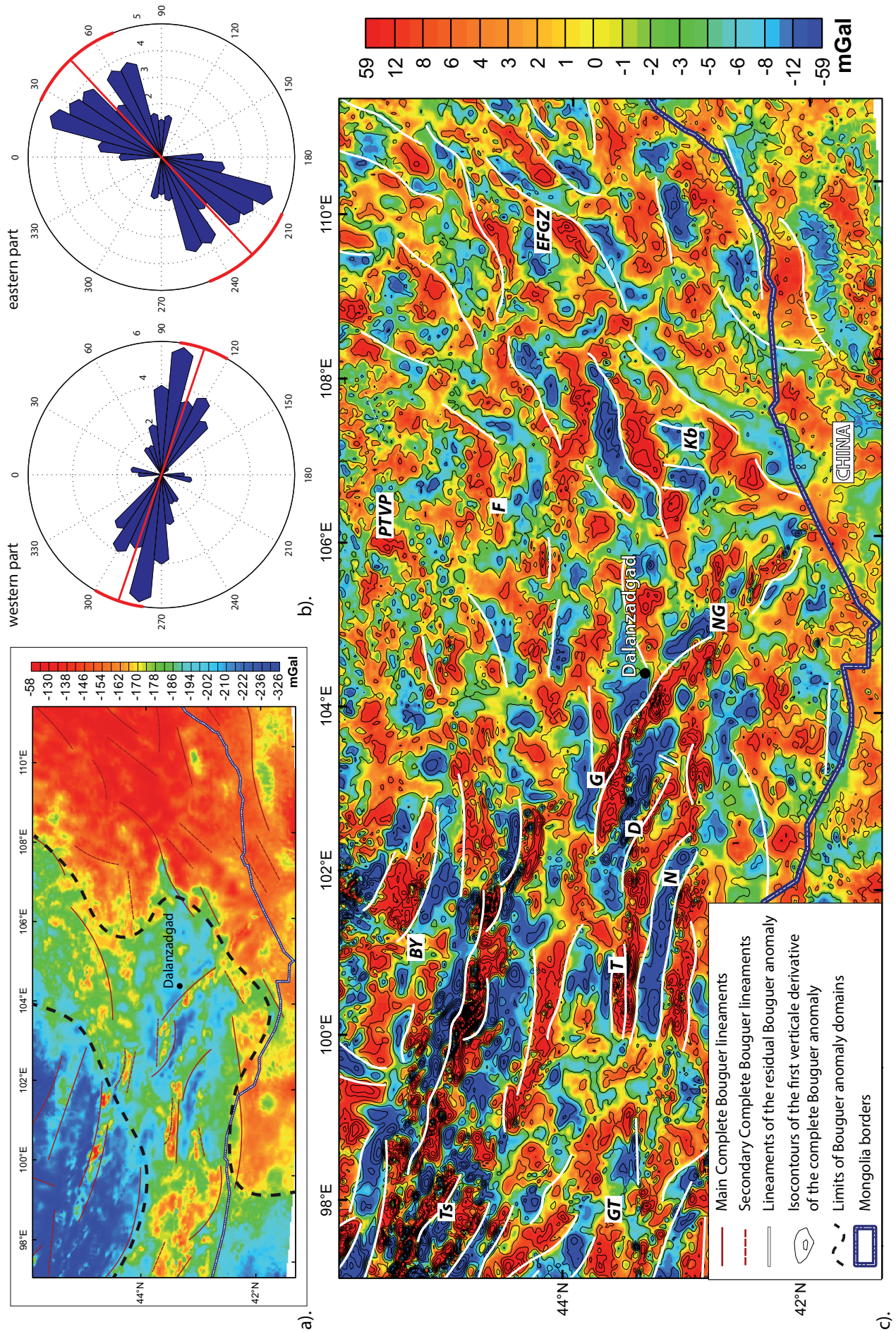
Figure 24.2.e.: Mesozoic and Cenozoic basins superimposed on the magnetic anomaly map.

strongly magnetic together with calco alkaline Carboniferous granitoids and ultramafic rocks. The Cretaceous and Cenozoic basins sometimes display high amplitude magnetic anomaly provinces although their gradients are rather scattered indicating that the magnetic sources are located in depth. These high amplitude magnetic trends in the basins do not often coincide with the surface geology but seem to be the continuation of the Palaeozoic outcrops which are in the borders of the basins. Globally, the large magnetic anomalies are correlated with the limits of tectonic provinces, such as microcontinents, magmatic arcs or crustal scale shear zones.

5.3. Gravity structures analysis

The Bouguer anomaly map ranges from -326 mGal to -58 mGal (Fig. 25.1.a.) and three principal zones can be distinguished trending approximately NE-SW. The highest Bouguer anomalies are located to the south-east of Mongolia, characterized by alternating metamorphic core complexes and sedimentary basins related to the Cretaceous extension (Cunningham et al., 2005; Daoudene et al., 2012). To the north-west of southern Mongolia, the lowest Bouguer anomalies are associated with the overprint of the Hangay dome, a mountain bulge, combining flexural effects with an anomalous asthenosphere mantle upwelling with a low density lower crust or uppermost mantle (Petit et al., 2002). This lithospheric template is marked by an important Bouguer anomaly low over the Hangay dome. Between the south-east Bouguer anomaly high and the north-west Bouguer anomaly low, the intermediate NE-SW oriented Bouguer anomalies reveal high gravity short wavelengths. These anomalies mostly correspond to the Palaeozoic mountain ranges. However, the Bouguer anomaly map conceals the majority of short wavelengths of the gravity signal whereas the residual Bouguer anomaly enhances them. Hence, the high-pass filter of a cutoff of 100 km removes these long-wavelengths. The interpretation of the residual Bouguer anomaly features (Fig. 25.1.c.) shows that the lineaments mainly strike WNW-ESE to the western part and NE-SW to the eastern part (Fig. 25.1.b.). The analysis of the residual anomalies reveal the same change in orientation of the lineament trends as observed in magnetic anomalies. In addition, the Cretaceous extension could explain the significant difference we can observe between the western part of the residual Bouguer anomaly map marked by sharp and strong amplitudes and frequencies of the gravity signal and

Figure 25.1.: Bouguer anomaly analysis. a). The complete Bouguer anomaly map with the main lineaments superimposed; b). Rose diagrams of the preferred orientation of the gravity lineaments; c). The residual complete Bouguer anomaly map with the isocontours of the first vertical derivative and the lineaments superimposed. The color scales are in equal area distribution. BY: Baydrag microcontinent; Ts: Tseel terrane; GT: Gobi-Tianshan fault zone; T: Tost fault; G: Gurvansaykhan range; D: Dzolen range; N: Noyon area; F: Flyshoid basin; NG: Nomgon area; Kb: Khan Bogd granite; EGFZ: East Gobi Fault Zone.



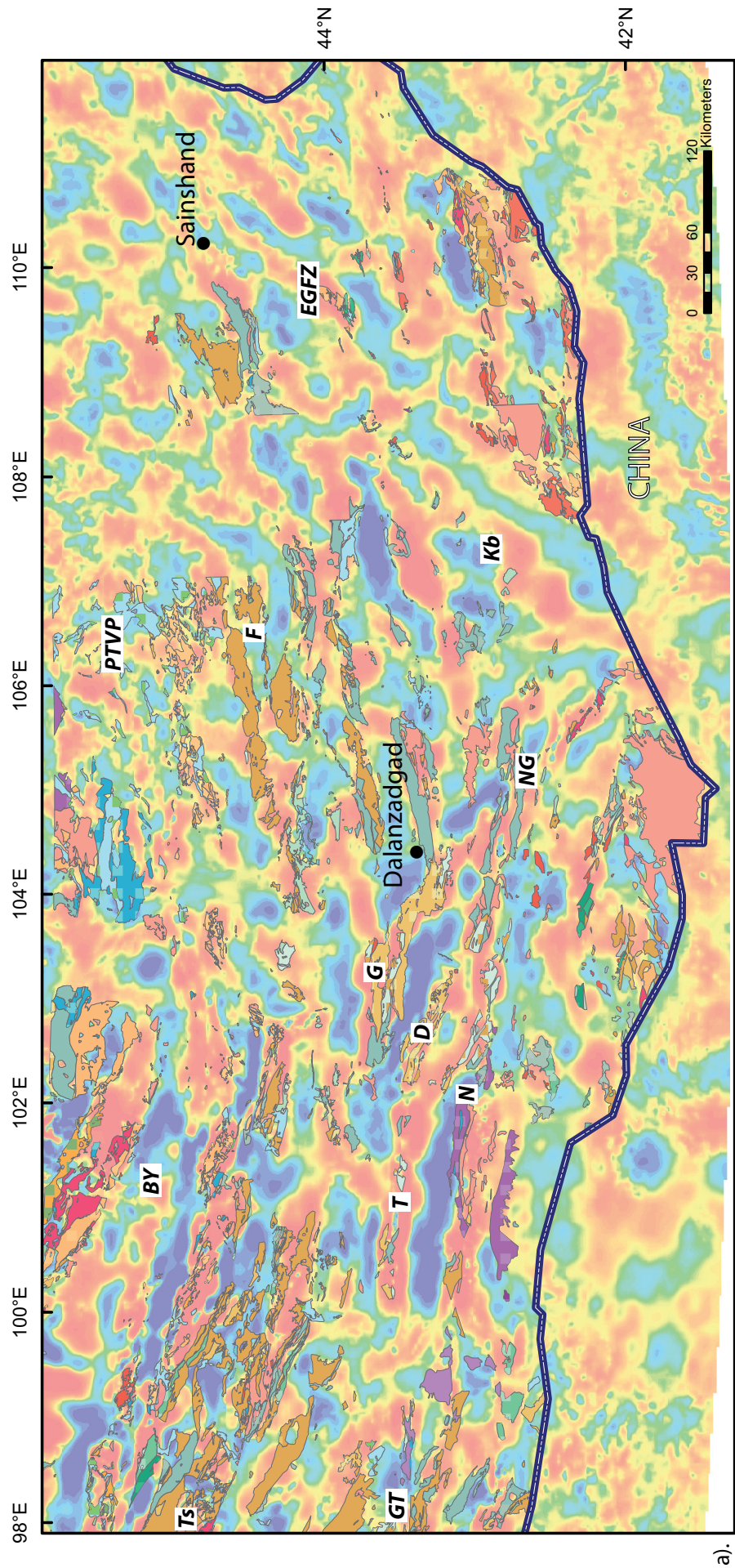


Figure 25.2.a.: Sedimentary rocks superimposed on the residual Bouguer anomaly map.

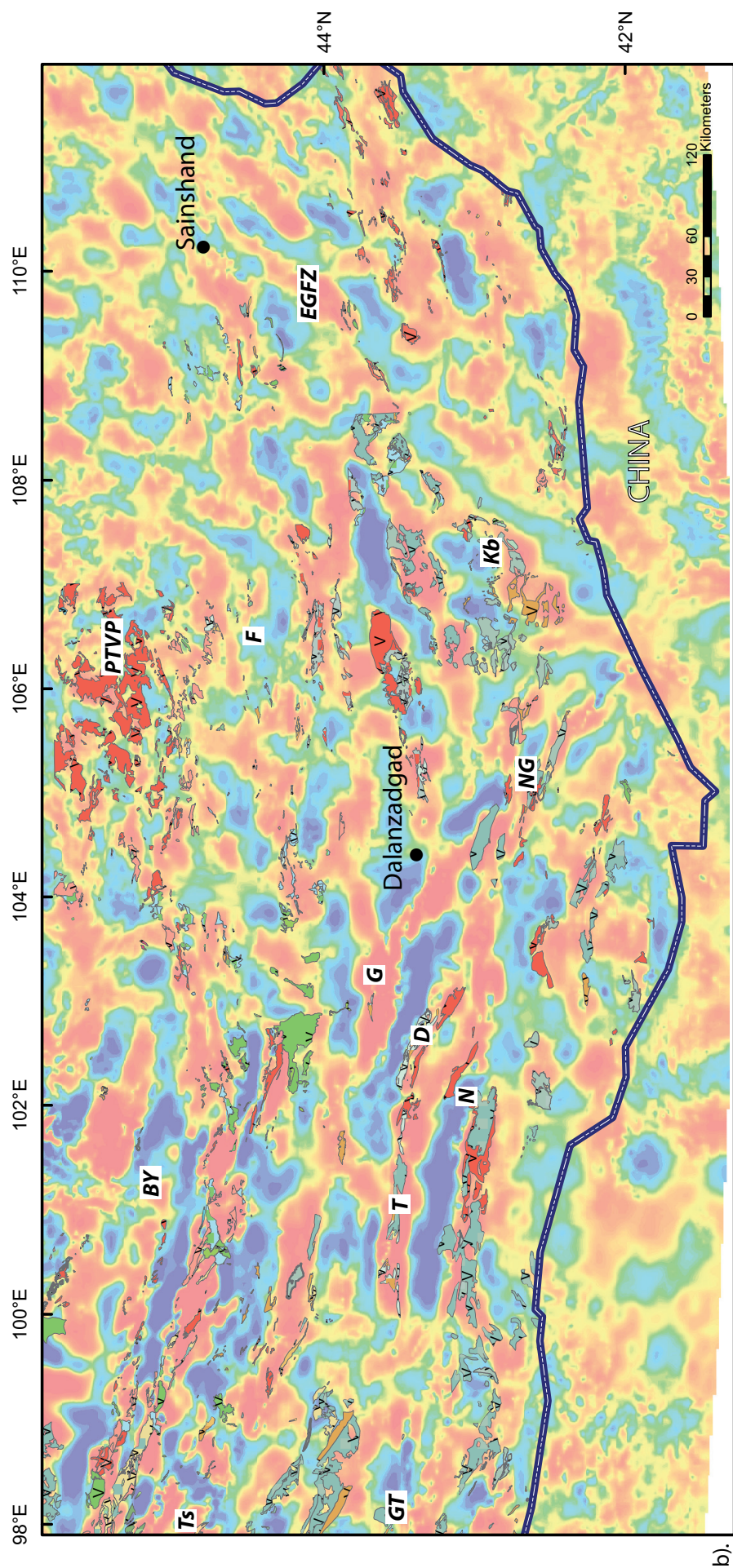
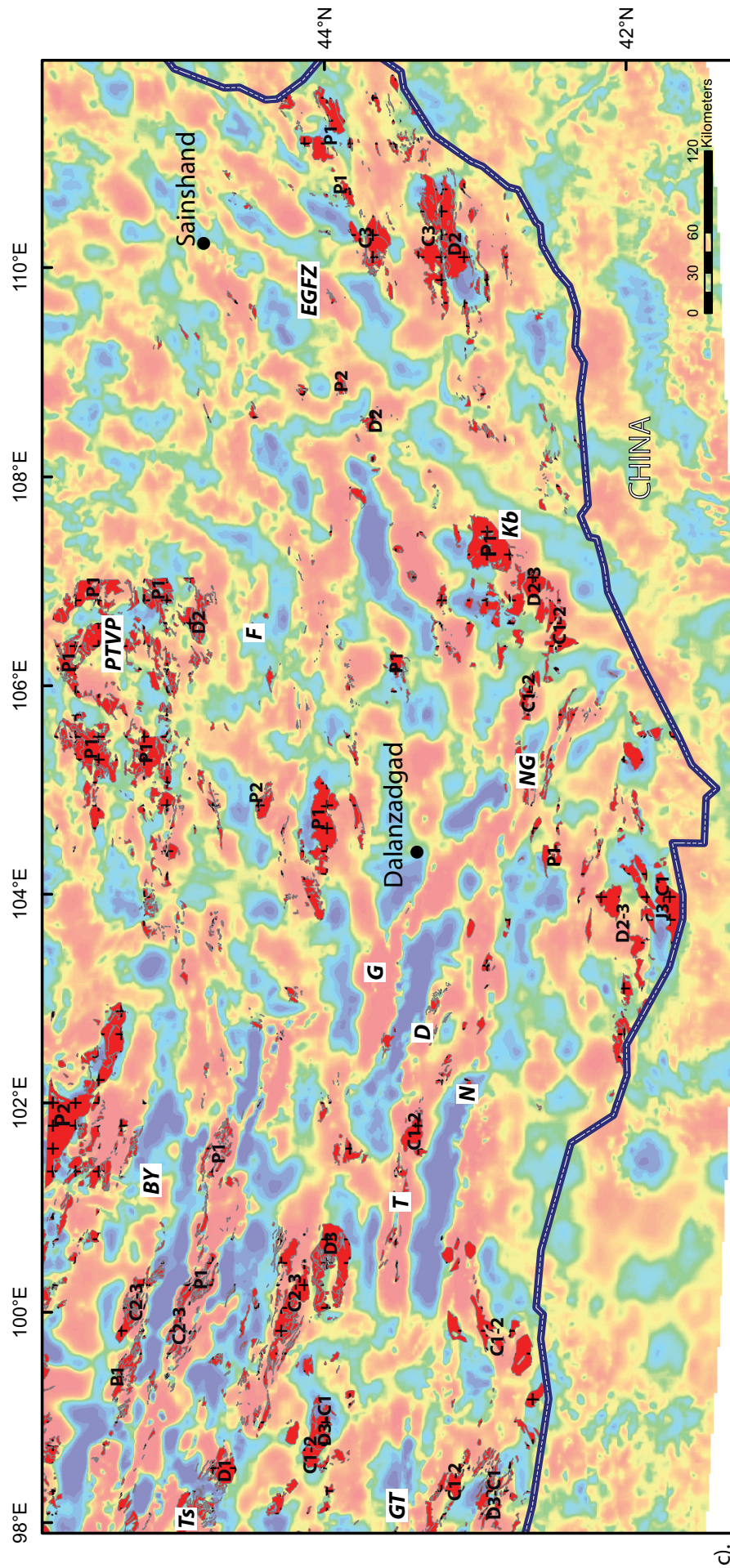


Figure 25.2.b.: Volcanic rocks superimposed on the residual Bouguer anomaly map.

the eastern part marked by a signal which is marked by intermediate contrast intensities and blurred shapes of anomalies. Indeed, the Cretaceous extension may have completely reworked the Palaeozoic orogenic fabric in depth as well as in the shallower part of the crust.

Except for the EGFZ, the GT and T the faults can hardly be associated with distinct residual Bouguer discontinuities. However at some places, several gravity gradients correlate with minor faults. The BY province is characterized by an alternation of gravity lows and highs but it does not display a homogeneous gravity signal over the entire province as it is the case for magnetic anomaly. The high amplitudes observed in the Permian-Trias volcanic-plutonic belt (PTVP) correlate with the early Permian volcanic rocks and granitoids (Fig. 25.2. b. and c.). South of the BY, the high amplitude residual anomalies surrounding the Ts are mainly due to middle to late Carboniferous and early Permian granitoids associated with ultramafic rocks (Fig. 25.2. c. and d.). Although the volcanic and sedimentary rocks in this area are largely distributed, it is considered that they may have a minor effect on the gravity signal (Fig. 25.2. a. and b.). The late Devonian and early to middle Carboniferous granitoids in this area display a low amplitude signal whereas all the other early to middle Carboniferous granitoids in southern Mongolia show a high amplitude signal (Fig. 25.2.c.). To the north of the GT the residual Bouguer anomaly highs correlate with the early to middle Carboniferous volcanic rocks while to the south of the GT the gravity highs are due to the early to middle Carboniferous granitoids. At the Gurvansaykhan range, the residual anomaly high corresponds to the presence of ultramafic rocks. The elongated E-W trending high amplitude magnetic anomaly east of the G and reaching the EGFZ is also observed in the gravity signal. However, the gravity high is broader and less continuous compared to the magnetic one. To the south of G, the D reveals high amplitude gravity anomaly due to the presence of ubiquitous ultramafic rocks associated with late Silurian-early Devonian and early Permian volcanics. The gravity high continues into the Cenozoic basin to the south of the D. Concerning the N, the Mesozoic syncline is clearly associated with a low amplitude gravity area, while the Carboniferous and Permian volcanic rocks are correlated with high amplitude residual anomalies. To the NG, the gravity highs are due to the presence of the early Carboniferous and early Permian volcanic rocks associated with the early to middle Carboniferous granitoids (Fig. 25.2. b. and c.). The Khan Bogd pluton (Kb) is associated with a gravity low signal whereas the middle to late Devonian and the early to middle Carboniferous granitoids display a high amplitude signal. To the north of the EGFZ, high amplitude gravity anomalies are correlated with early Devonian, early Carboniferous and early Permian volcanic rocks. South of the EGFZ, the gravity highs correspond to the surface Permian volcanic rocks combined with the late Carboniferous and early Permian granitoids while to the south dykes of gabbro together with early to middle



c).

Figure 25.2.c.: Granitoids superimposed on the residual Bouguer anomaly map.

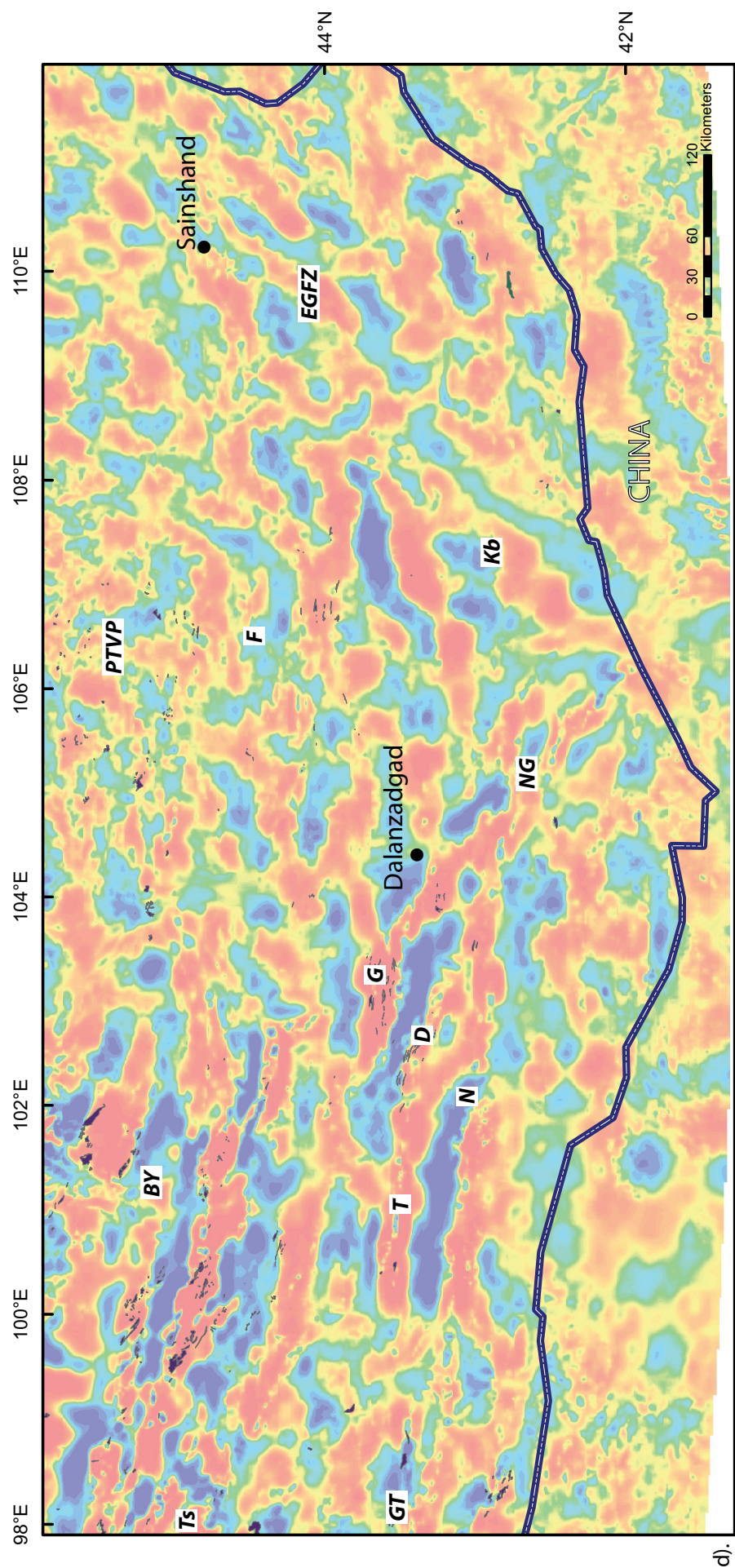


Figure 25.2.d.: Ultramafic rocks superimposed on the residual Bouguer anomaly map.

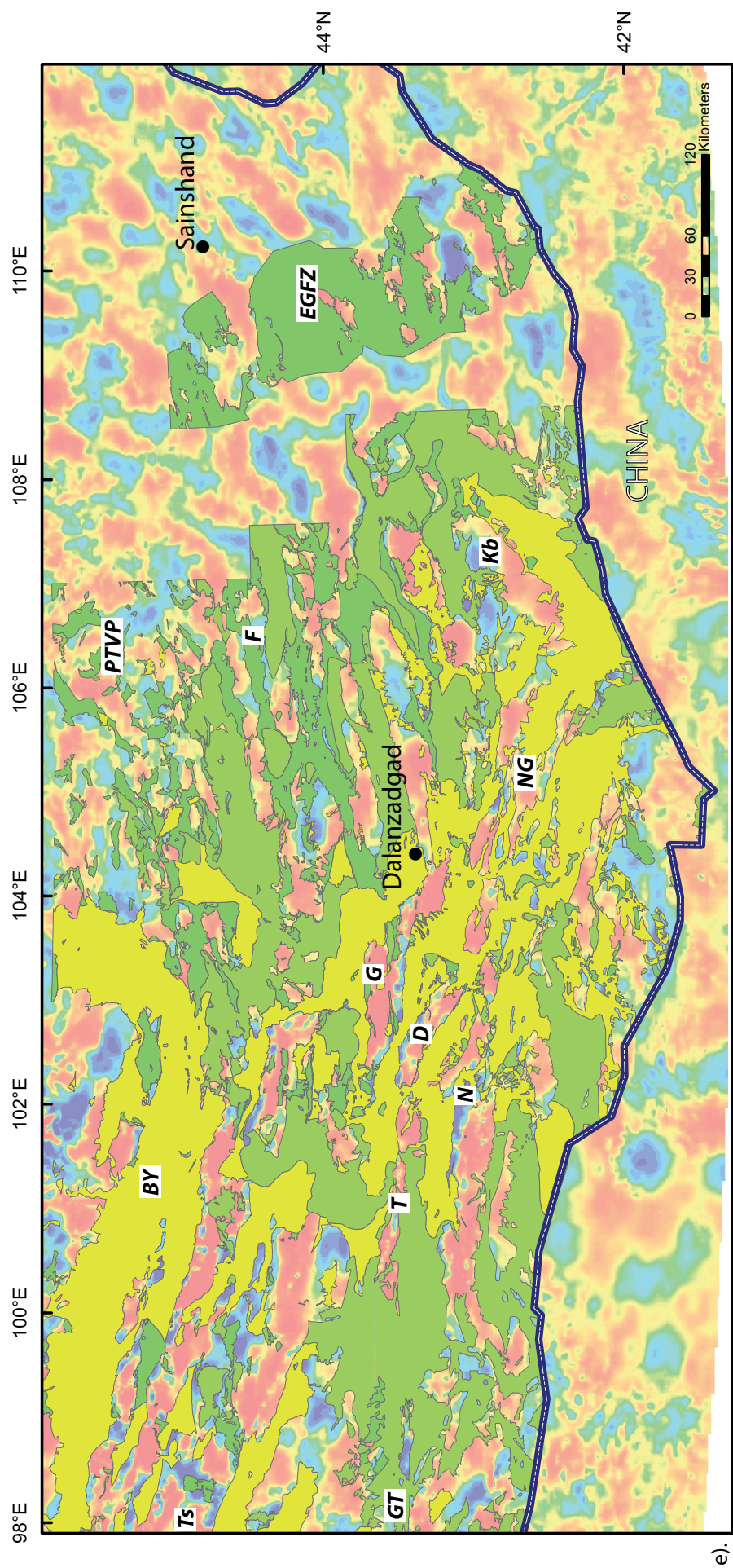


Figure 25.2.e.: Mesozoic and Cenozoic basins superimposed on the residual Bouguer anomaly map.

Devonian and Permian sediments displays a high amplitude anomaly. Compared to the magnetic anomaly map, the Cretaceous and Cenozoic basins often display gravity highs which correlate with positive magnetic anomalies (Fig. 25.2.e.). These gravity and magnetic highs have gentle gradients and thus the sources of these anomalies are located in the depth, corresponding most probably to the Palaeozoic rocks buried under the Cretaceous and Cenozoic sediments.

In summary, the same change in the orientation of the gravity lineaments from WNW–ESE to the west to NE–SW to the east is observed in gravity and magnetic anomaly maps. It appears that the Cretaceous extension makes the gravity signal intermediate to blurred in the eastern part of the map. The volcanic rocks of any age correlate with gravity highs, except for several early Carboniferous outcrops. The middle to late Carboniferous and early Permian calc-alkaline granitoids display a high amplitude residual anomaly as well as the ultramafic rocks. Similarly to the magnetic anomaly map, several highly gravity sources are located underneath the Cretaceous and Cenozoic basins and we can assume that in most of the areas, the anomalies correspond to buried Palaeozoic rocks, which outcrop along margins of the corresponding basins.

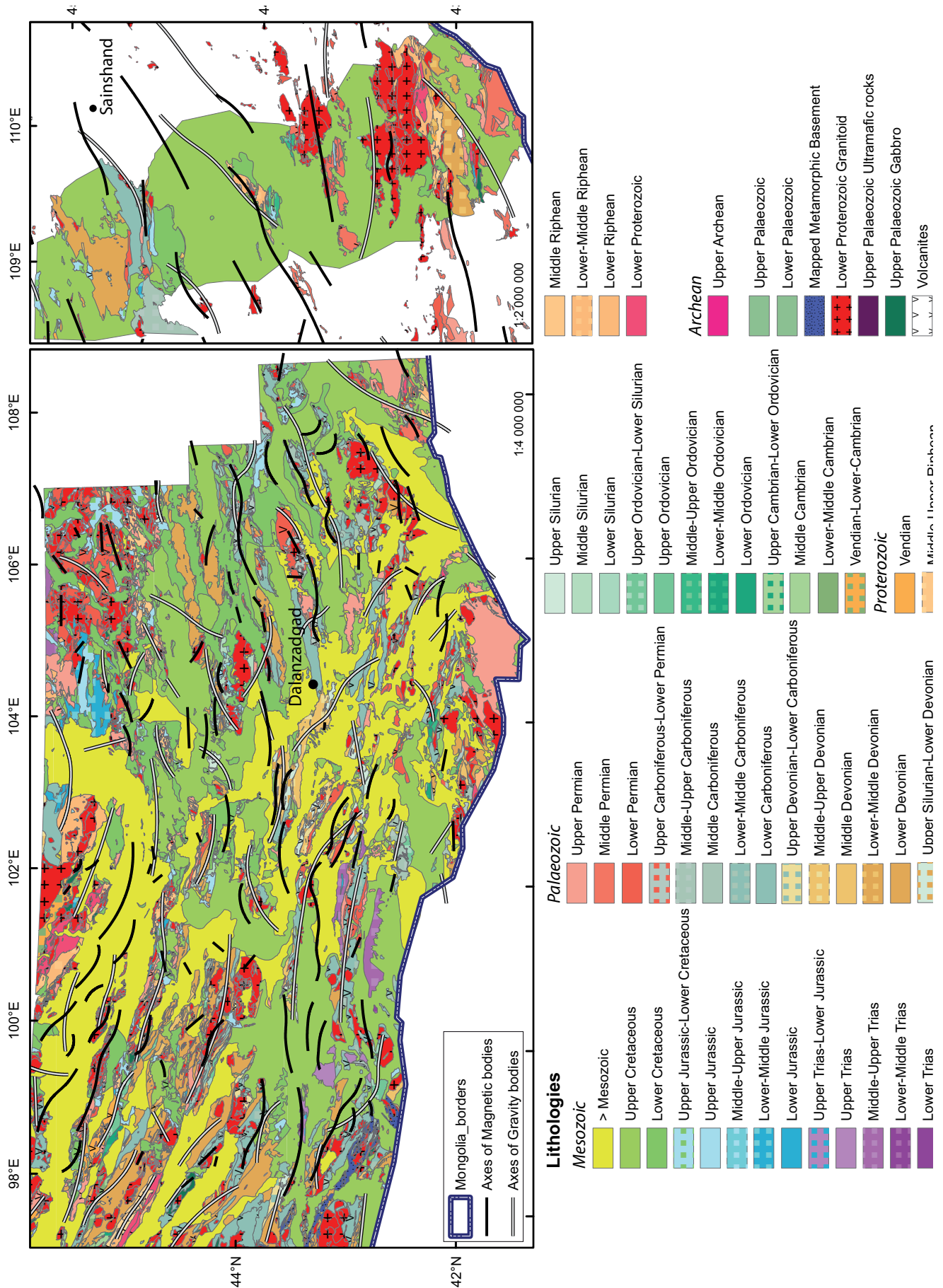
6. Discussion: Review of tectonic boundaries according to the synthesis of potential field and geological data

The aim of this work is to relate geophysical domains to their geological counterparts. The analysis of the geophysical signatures in south Mongolia could help to understand the relation between the different geological domains and to solve the characteristics of the transitions between the domains. The criteria defining a geophysical domain are: (1) the amplitude and frequency trends of the geophysical signals in contrast to surrounding areas; (2) the nature of anomalies (their gradients, their structural features such as contacts and faults) in the crust, which are not obviously correlated with the outcrops. In summary, a region of common geology, tectonic, or magmatic history, should reveal the same geophysical pattern. A terrane is this kind of region.

The south of Mongolia was divided by Badarch et al. (2002) into several volcanic arc, back-arc and fore-arc, accretionary wedge, ophiolites and microcontinents called terranes. They proposed north-directed accretion of terranes, followed in the late Palaeozoic by their imbrication along huge shear zones. Therefore, the Central Asian Orogenic Belt in Mongolia is supposed to grow as a result of accretion of terranes above a series of parallel subduction zones (Badarch et al., 2002; Windley et al., 2007; Xiao et al., 2009). In addition, if we look at

the lithostratigraphic columns (Fig. 7) of the individualized so-called terranes, or lithotectonic zonation (Kröner et al., 2010), the differences between each one are rather clearly noticeable as the Lake Zone is composed of metamorphic rocks with no sedimentary or volcanic events from the Upper Cambrian to the Permian; the Gobi-Altai Zone only displays sedimentary rocks deposited during Palaeozoic times. Although the differences between the Trans-Altai Zone and the South Gobi Zone are not as distinct as for the Lake Zone and the Gobi-Altai Zone, the Trans-Altai Zone shows typical oceanic sequences whereas the South Gobi Zone displays the sequences typical for a passive continental margin developed later into continental magmatic arc associated with volcanism and sedimentation of products of volcanic activity. In theory, almost all the orogeny contains distinct terranes originated not only from continental fragments or magmatic arcs involved in the collision but also from exotic blocks. However, Şengör and Dewey (1990) pointed out the problems which can arise when using the term of “terrane” to explain tectonic processes, because this concept is less objective due to lack of accurate definitions. Therefore, could we really call the Lake, Gobi-Altai, Trans-Altai and South Gobi zones “terranes” just because their lithologies and stratigraphies are different? Could we assert that a continental crust, bordered by a margin (passive or active), bordered by an oceanic crust clearly constitute three distinct terranes? The history of this margin, continental and oceanic crusts are definitely linked and not independent. The interpretation of geological units and their structures according to the geophysical signals without any complementary information has also to be made with caution. However, a geophysical domain is defined by its crustal rock properties (density and susceptibility contrasts) and therefore has to display a characteristic signal as it is observed for instance in Alaska (Glen et al., 2007a), Tasmanides (Burton, 2010), European Variscan belt (Edel and Weber, 1995) or Iberian branch of the Variscan belt (Martinez Catalan and Jose, 2012).

The main results of the gravity and magnetic data analysis are summarized in the figure 26. They show that southern Mongolia is characterized by a WNW-ESE trending geophysical fabric to the western part and by a NE-SW trending geophysical fabric to the eastern part. This is the best reflected in a series of bands of magnetic highs (Fig. 27a) that have been used here to refine the extent of major lithotectonic units. However, the same correlation cannot be clearly established in the case of the gravity anomaly highs (Fig. 27b). Globally the magnetic anomalies show a clear correlation between the rock types and the magnetic highs and lows. Moreover, several high amplitude magnetic areas display a significant trend of the signal and thus, several delineations can be established at large scale (Fig. 27a): (1) the Baydrag microcontinent is mainly covered by a wide Cenozoic basin, which correlates to a high amplitude magnetic anomaly area assuming to be a magmatic province; (2) the late Devonian-early Carboniferous

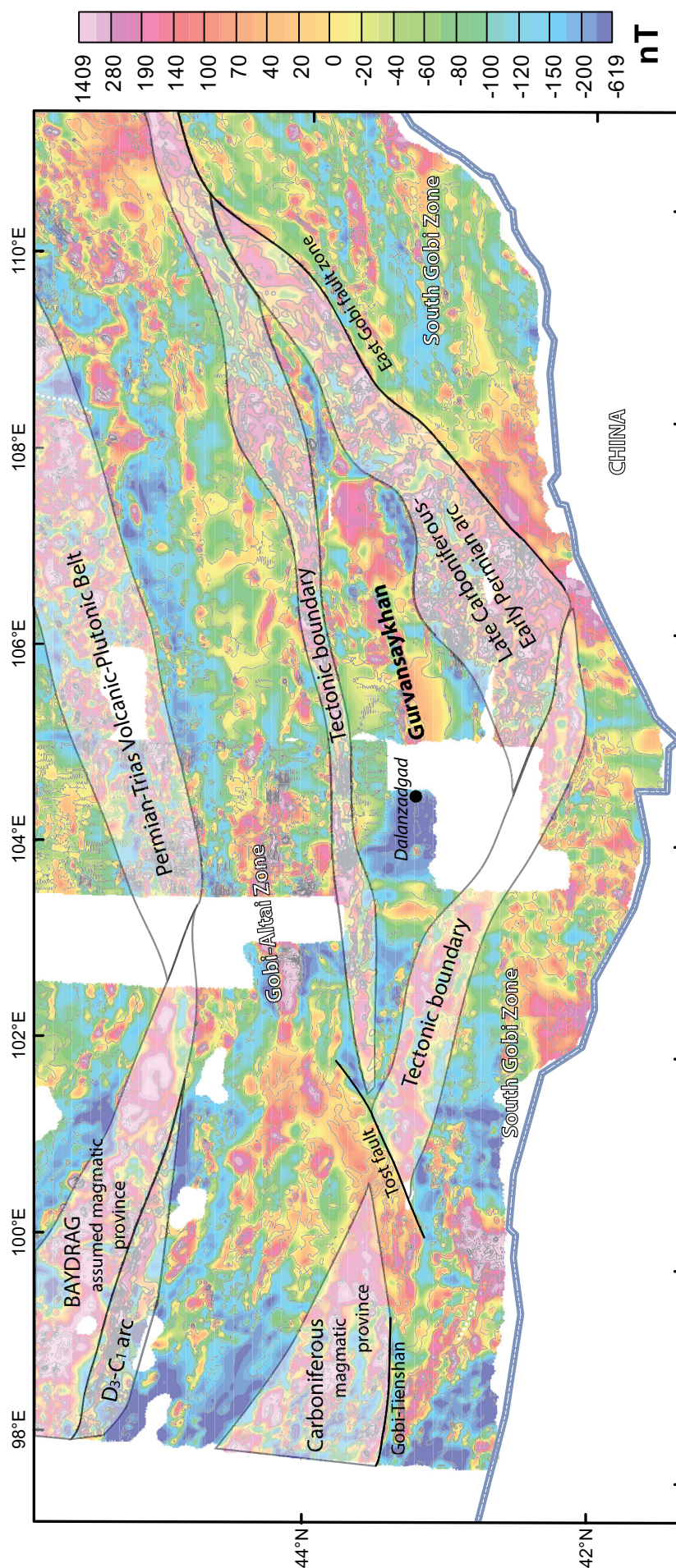


magmatic arc; (3) the Permian-Trias volcanic-plutonic province also can be clearly delineated with strong magnetic contrasts; (4) the Carboniferous magmatic province in the west; (5) the late Carboniferous-early Permian arc to the south-east partly coinciding with that defined by Kovalenko et al. (2004 and 2006). Two high amplitude magnetic areas are interpreted to reflect main tectonic boundaries as their geological characteristics are complex, and the correlation between geological and geophysical fabrics is unclear.

The magnetic anomaly map shows good correlations with the rock types at a small scale and therefore several provinces with a common signal can be identified (Fig. 27a). However, at a large scale a systematic correspondence between the high/low amplitude magnetic provinces cannot be established and does not correspond to major terranes defined by lithostratigraphic analysis. Indeed, the South-Gobi, Gobi-Altai and to a certain extent the Trans-Altai zones do not display a characteristic signal tendency which could be attributed to a typical region of specific geophysical character. Therefore, these magnetic contrasts are related to the subsurface-upper crustal structures and they do not attest the existence of terranes. The magnetic signal does not have a source in the depth and therefore is not characteristic for the whole crustal thickness as it is the case in accreted terranes in Alaska (Glen et al., 2007a) or in Tasmanides (Burton, 2010). Indeed, in Alaska which formed by an assemblage of different terranes, the correlation between the magnetic anomalies and the lithostratigraphic terranes is very good. Here the areas of high amplitude magnetic anomaly (i.e. strong magnetization) coincide with specific terranes (containing usually oceanic material) while the areas of intermediate to low amplitude magnetic anomalies coincide with other terranes (containing usually continental material). In south-central Alaska, each terrane has a characteristic geophysical signature (Glen et al, 2007a) marked also by variations in the gravity signal which is relevant to deeper parts of the crust. However, in Mongolia the gravity anomaly analysis shows no obvious correlation between the presumed terranes and the signal (Fig. 27b) both for long or for short wavelengths. In addition, we observe that the magnetic contrast tendencies are not necessarily correlated with the residual Bouguer anomaly tendencies and certainly not with the regional Bouguer anomaly. Therefore, at the scale of southern Mongolia, most of the geophysical signal trends do not correspond to tectonostratigraphic terranes previously identified by Badarch et al. (2002).

In order to understand current crustal structure of the Central Asian Orogenic Belt, we attempted to evaluate the influence of the Cretaceous extension on the potential field signals. The objective of this analysis is to understand as whether the Cretaceous extensional tectonics interferes with the signal of the Palaeozoic collisional structure and thus could be a possible explanation of the

Figure 26: Comparison of gravity and magnetic axe bodies with the geological map



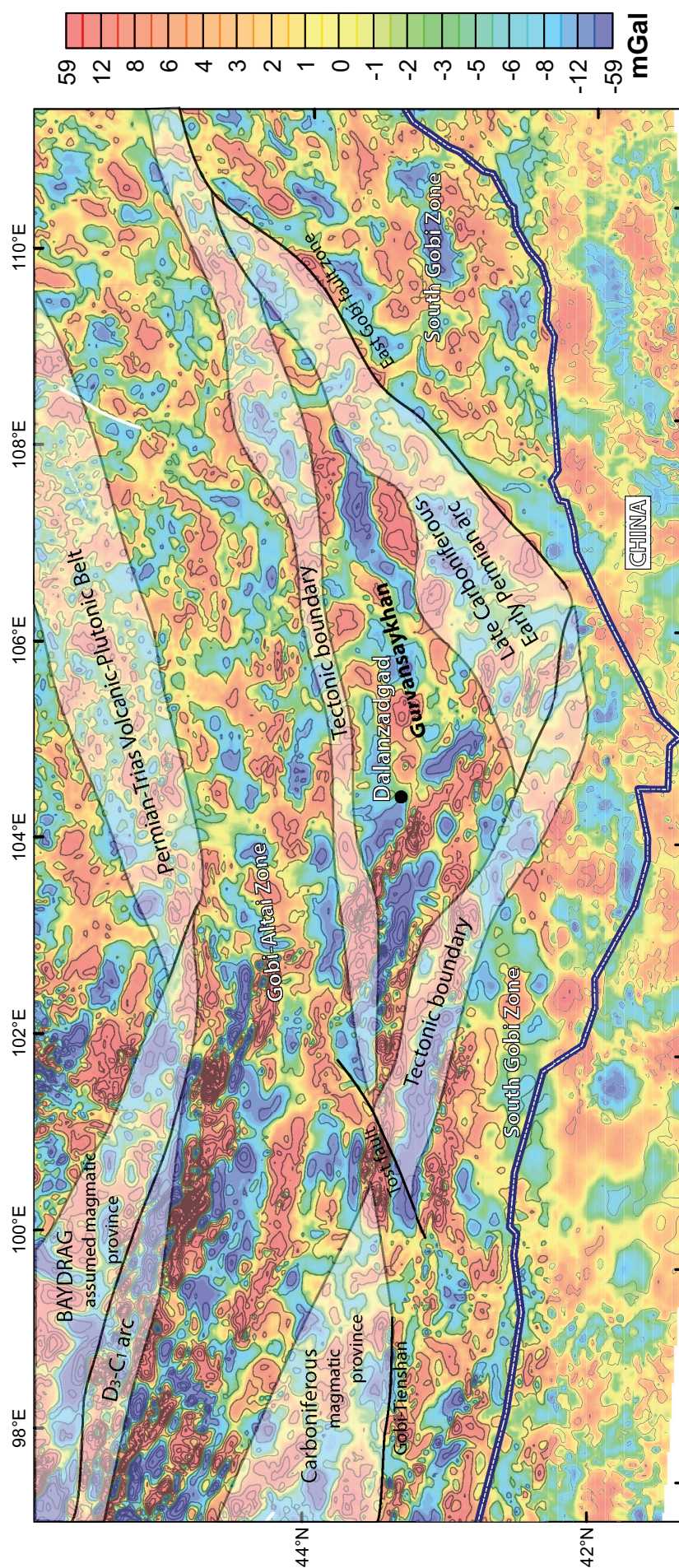


Figure 27: a). Interpretative scheme of the magnetic anomaly defined areas ; b). Interpretative scheme of the gravity anomaly defined areas.

uncorrelated tendency between geophysical signal and terrane boundaries. This extension affected the eastern part of the south Mongolia significantly more than the western part (Daoudene et al., 2012) which correlates with a slight difference of gravity signal tendency from west to east. In the east, the gravity signal seems to be more blurred compared to the west where we can identify sharp gradients. On the other hand, there is not a significant difference in trends of the magnetic signal from west to east. Figure 28 quantitatively compare the contours of Cretaceous and Cenozoic basins with the trends of geophysical anomalies. We observe that the three basins exhibit the same trend which does not match the magnetic fabric. However, the gravity signal trends may have a slight correlation with the contours of sedimentary basin. Therefore, no really clear correlation can be made between the basin geometry and the geophysical signatures apart for the gravity signal, which may indicate that the Mesozoic extension affects deeper crust than supracrustal levels.

As discussed above, the geophysical domains do not entirely correspond to tectonostratigraphic terranes as defined by Badarch et al. (2002). These geological domains do not show distinct geophysical responses suggesting that the compartmentalization of the Central Asian Orogenic Belt into terranes for this area can be questioned. Approximately half of the terranes boundaries defined by structural analysis and stratigraphic studies cannot be confirmed by geophysical analysis. Even more, looking at the magnetic anomalies, it appears that there are following tendencies: (1) a north-south fragmentation of southern Mongolia as the signal in the Lake Zone and the Gobi-Altai Zone displays a specific contrast delineating two magnetic domains. In contrast, the magnetic anomalies in the Trans-Altai and South Gobi Zones seem not to be related to any major zone although several tectonic boundaries are documented at the surface. (2) The second tendency is a west-east fragmentation of the signal corresponding to the variations in the strike of the gravity and magnetic lineaments.

At the light of all these observations, the models of multiple-subduction systems (Windley et al., 2007) responsible for the accretion of the Central Asian Orogenic Belt should be regarded with caution. Indeed, a suture zone between two terranes should be clearly visible because it forms a prominent deep-seated crustal discontinuity present at all the crustal levels as it is the case of the European Variscan belt where the subduction of the Saxothuringian plate is magnetically and gravimetrically defined (e.g. Edel and Schulmann, 2009; Guy et al., 2011). In southern Mongolia, these geophysical markers apparently do not exist and the ophiolitic slivers cannot be the only argument for existence of suture. We assume that the Gurbansaykhan range and surroundings correspond to a crustal scale zone of deformation affecting the Trans-Altai Zone which may correspond to large scale shear zone as imaged in the Tasmanides (Burton,

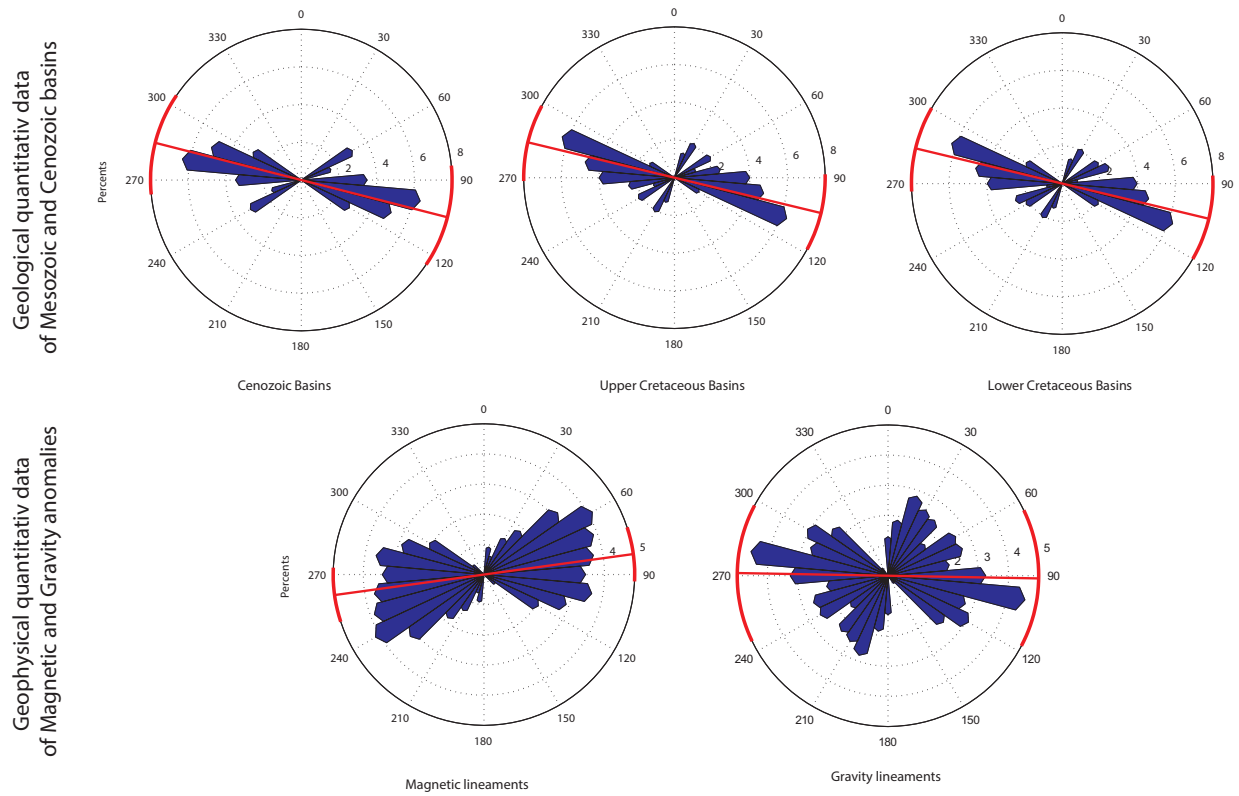


Figure 28: Rose diagrams showing the preferred orientation of the three different major basins and the preferred orientation of the lineaments of the magnetic and gravity anomalies.

2010) or can correspond to large scale fold (Peschler et al., 2007). However, this region cannot be interpreted as a major suture zone between the two terranes (Gobi-Altai Zone to the north and Trans-Altai Zone to the south). Moreover, the seismic tomography study (Kulakov, 2008) over Mongolia does not attest the existence of lithosphere scale structure such as a remnant of subduction plate in the mantle. The oceanic crust of the southern Mongolia is characterized by the absence of suture. Wilhem et al. (2012) suggest the context of small oceanic basins called “small pockets of ocean relics” and these small basins closed without the occurrence of subduction zones. This hypothesize might be a starting explanation of the lack of clear geological and geophysical markers of suture zones in southern Mongolia.

Conclusion of the compartmentalization into terranes of the Central Asian Orogenic Belt

The complete Bouguer and magnetic anomaly analysis, combined with stratigraphic and structural information, provide new insights into the crustal structure beneath the south of Mongolia. The gravity and magnetic lineations have been identified at a regional scale revealing the change in orientation from WNW–ESE striking (to the west) to NE–SW striking (to the east). These lineaments mostly correlate to the trends of main different Palaeozoic rock types of southern Mongolia. However, at a large scale, the geophysical signatures of the gravity and magnetic anomalies globally do not display an accurate correlation with the tectonostratigraphic terranes which are assumed to constitute the Central Asian Orogenic Belt. To the north of our studied area, there are several zones defining by internally uniform geophysical fabrics, well-defined geophysical gradients at their borders, and prominent narrow magnetic anomalies. However, at the southern part of Baydrag microcontinent and the Permian-Triassic volcanic-plutonic belt, the magnetic signal cannot be attributed to wide provinces. Supposing that the exotic terranes really exist, their potential field data should be characterized by major tendencies and by sharp location and good orientation of terrane bounding structures (Glen et al, 2007a; Burton, 2010). However in the Central Asian Orogenic Belt and unlike in terranes with well defined geophysical fabric (Tasmanides, Alaska terrane collage), the analysis and interpretations of combined gravity and magnetic data combined with the surface geology suggest that the compartmentalization into terranes should be reconsidered. It is suggested that the delineation of the terranes should be re-examined taking into account the geophysical data available. For these reasons, the quasi-exclusive use of terranes is not a useful and objective method of regional tectonic analysis for the basement geology of Mongolia.

Chapter IV:

Crustal structure of southern Mongolia inferred from
geophysical forward modelling along four transects

Chapter IV:

Crustal structure of southern Mongolia inferred from geophysical forward modelling along four transects

In the previous chapter we compared gravity and magnetic maps with the geological map and proposed a review of terrane boundaries. The present work examines the orogenic crustal structures and the segmentation of the Central Asian Orogenic Belt in southern Mongolia on the basis of magnetic and gravity modelling. Evaluation of geometry of the bodies responsible of these anomalies can contribute to our additional understanding of the tectonic evolution. Four gravity and magnetic profiles have been modelled to see as whether the existing terrane subdivision can be confirmed. Even though the 2D forward modelling can be regarded a preliminary thanks to the lack of high resolution geophysical data, the integration of the available gravity, magnetic, structural, petrophysical and geological data along the four profiles can contribute to better locate the possible terranes boundaries, and to the visualisation of large scale geological structures like folds, dykes or intrusions of granitoids. In the following, we first present the collection of datasets used for the modelling. Afterward, we analyze the correlation of the geological and geophysical data for each profile area. Finally, we present the results and the interpretation of the magnetic and gravity modelling along the profiles.

1. Geophysical datasets used for modelling

1.1. Magnetic data

The magnetic data used are from GETECH Company in collaboration with the Mongolian Geological and Geophysical Exploration Company (MGGEC). The magnetic data analyzed in this study have been digitized from maps of a number of airborne surveys performed over several years, which were converted to five individual grids (Fig. 1). Each magnetic grid is a 1x1 km grid and is reprocessed according to the aim of the modelling. Elevation of the grids is 200 m and theoretically corresponds to the original flying elevation of 200 m terrain clearance. The flight lines were spaced at 2000 m \pm 800 m and flown with a north-south orientation. Except for the grid in the upper central part (delineated by green line) where the elevation is 1900 m and the flight lines were spaced at 2000 m and flown with an east-west orientation.

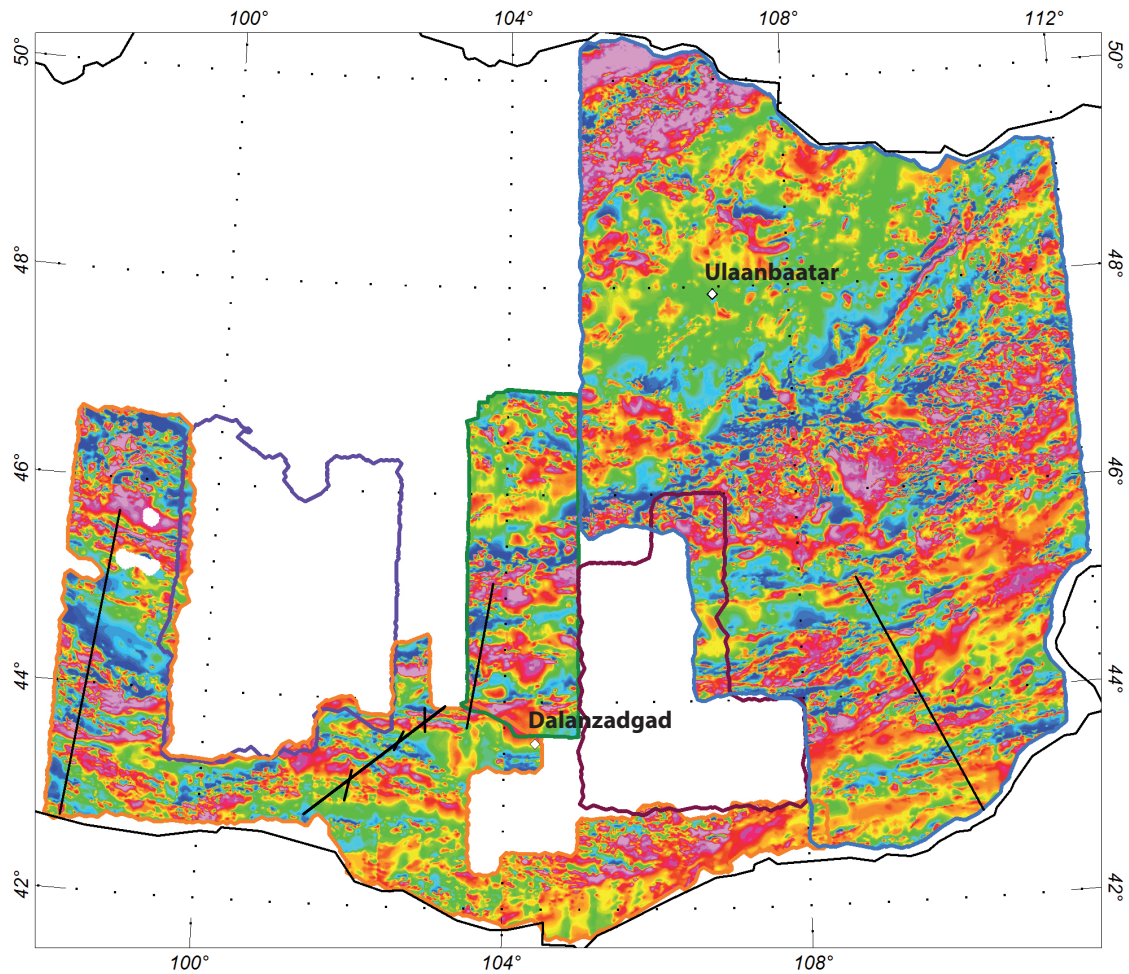


Figure 1: The location and the limits of the magnetic grids used for the modelling. Straight black lines: the four profiles.

1.2. Gravity grid and Bouguer anomaly

The free air gravity data used are available from the model DNSC08 of DTU (Andersen and Knudsen, 2009) and have 1'x1' resolution. The relatively poor quality of these gravity data must be taken into account when modelling the data. The complete Bouguer anomaly (Fig. 2) has been calculated from the free air anomalies using a reference density of 2.67. The topographic corrections were calculated using a digital elevation model based on ETOPO1 with a grid spacing of 1 min.

On one hand, the complete Bouguer anomaly corrections require a crustal reference density whereas it is obvious that the density is not homogeneous over the entire area of the grid. Thus, it can be considered that there is an error in the Bouguer anomaly data. On the other hand, the free air anomaly contains the topography effects and does not need any assumption on a homogeneous density value. Thus, we could use the free air anomaly to model the gravity data putting topography in the model. However, the gravity profile is extracted from a grid. Considering the free air anomaly and its signal at a determined point coordinate in a valley, the

value on the extracted profile can be laterally influence by a high mountain in the neighborhood of the station. The Bouguer anomaly should remove these lateral effects. Therefore, we used the complete Bouguer anomaly and not the free air anomaly to model the geological structures in the crust.

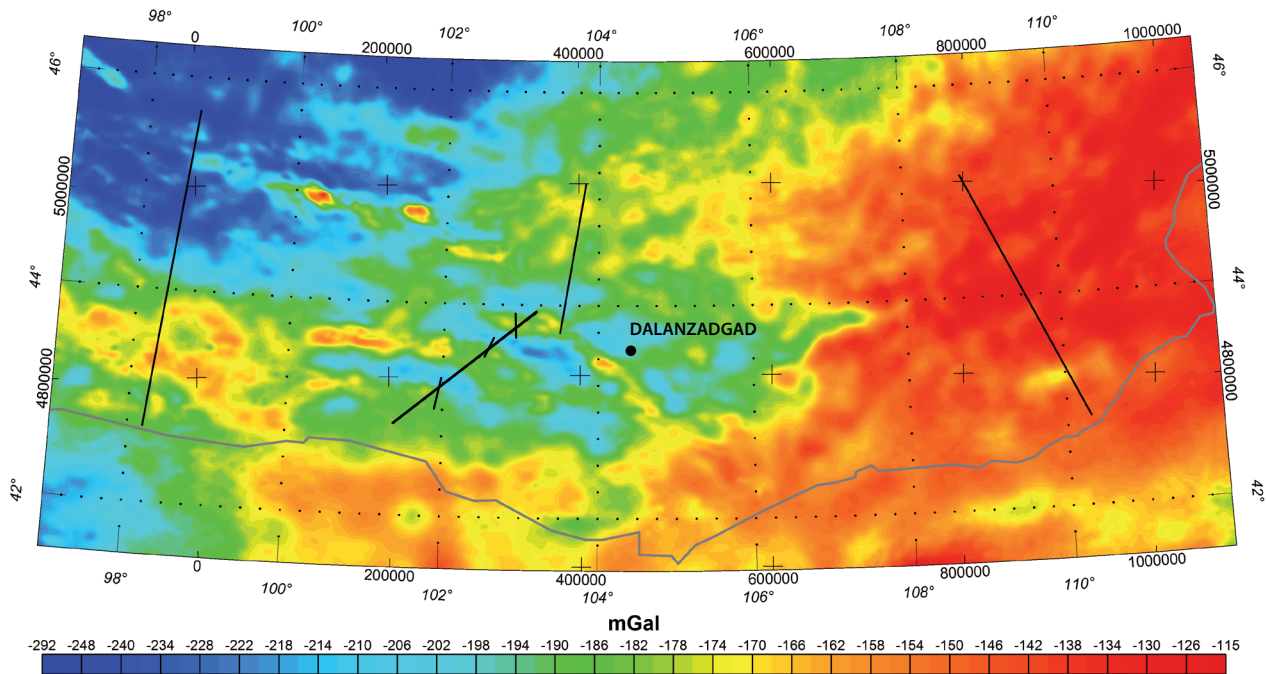


Figure 2: Bouguer anomaly grid upward 2000m

1.3. Seismic data

The seismic data available for Mongolia are scarce, often confidential and they do not exactly concern our area of interest located in southern Mongolia. The seismic data presented here (Fig. 3) come from the literature. For this study, we used the interpreted seismic lines P-to-S receiver function inversion, oriented NW-SE from the PASSCAL 1991-1992 projects and the other oriented NE-SW from the MOBAL_2003 project (respectively Mordvinova et al. 2007; Mordvinova and Artemyev, 2010). They presented seismic profiles using P-to-S receiver function inversion. These profiles start approximately in the south Baikal Lake area, end to 45° of latitude and are 900 to 1000 km long. However, these profiles stop to the north of southern Mongolia region (Fig. 3).

Some information may be found in seismic tomography results of Kulakov (2008) and Lebedev (personal communication). However, their models and profiles extracted from their seismic data are usually focused on the mantle and not exactly on the crustal issues.

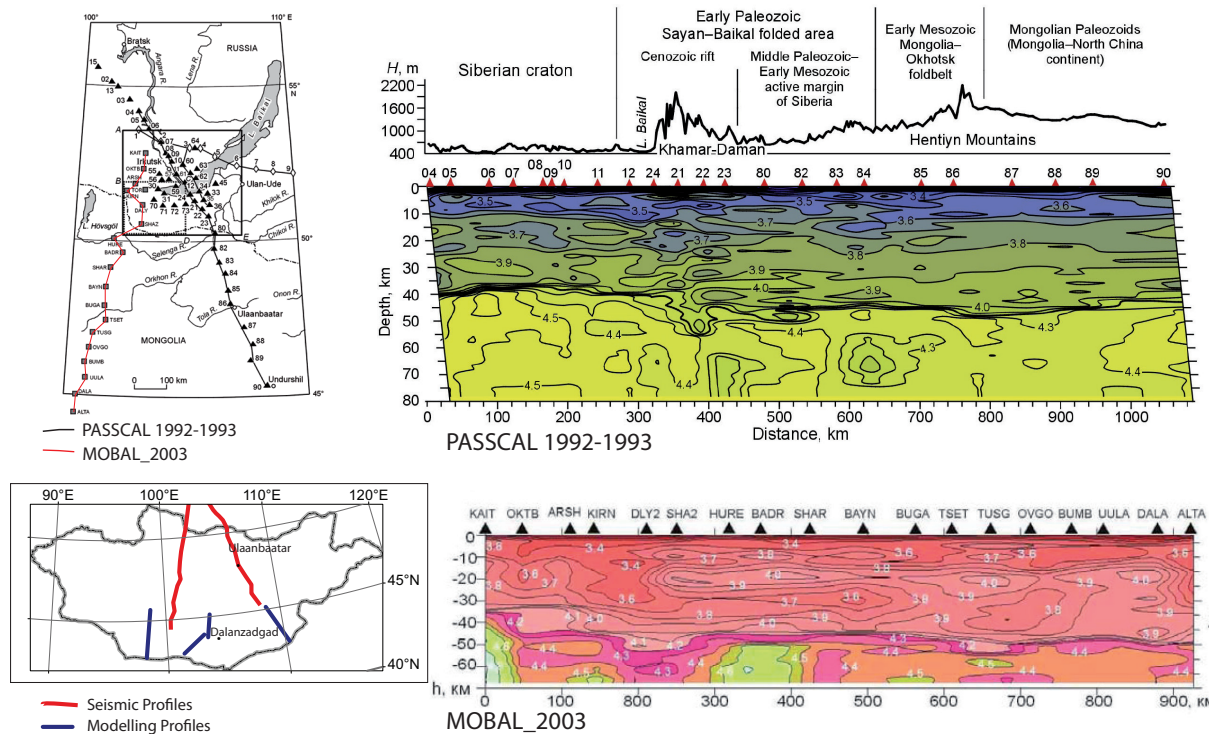


Figure 3: Seismic refraction profiles of the projects PASSCAL 1992-1993 (Mordvinova et al. 2007) and MOBAL 2003 (Mordvinova and Artemyev, 2010) over Mongolia.

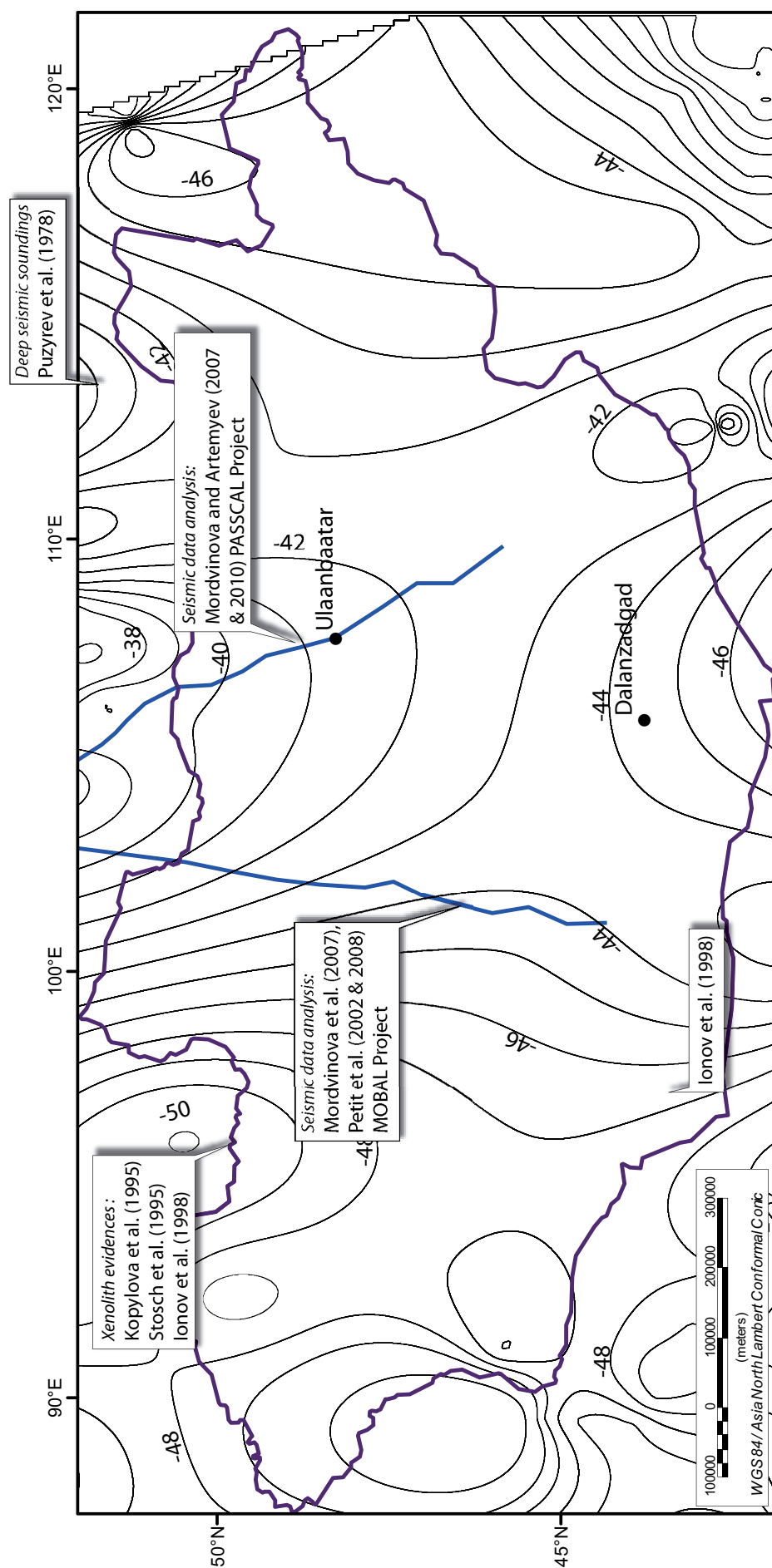
1.4. Moho depth

The Moho depth has been modified after the model CRUST 2.0, a $2^\circ \times 2^\circ$ grid (Bassin et al., 2000). Starting with the different raw data provided directly by the model CRUST 2.0 team, I created a grid by interpolating the database in order to slightly refine the Moho depth grid. Then, I compared the interpolated grid (Fig. 4) modified from the model CRUST 2.0 with some localized petrological and geophysical data available in the literature in order to check the similarities or the discrepancies between the grid obtained and these data.

The Moho depth displayed in the two transects studied by Mordvinova et al. (2007) and Mordvinova and Artemyev (2010) is located between 40 and 45 km in depth. These depths given by seismic receiver function method confirm the Moho depth obtained with the interpolation of the CRUST 2.0 model.

Kopylova et al. (1995), Stosch et al. (1995) and Ionov (1998) used thermobarometric and petrological studies of xenoliths to show that the mean depth of the Moho in the southwestern part of Mongolia is 46 km depth and approximately 50 km to the northern Hangai area. The

Figure 4: Moho depth grid with contours displayed modified after the model CRUST 2.0. The blue lines are the location of the seismic profiles PASSCAL 1991-1992 (east) and MOBAL 2003 (west).



In global agreement with Zorin (1999) and Zorin et al. (1990) except for the Hangai area.

model of the Moho depth we obtained is in agreement with these assertions.

The only discrepancy between the model and the other datasets concerns the crustal thickness model of Zorin et al., 1990 in the region of the Hangai dome where the authors established the Moho at 60 km depth below the Hangai dome. This value has no longer been confirmed by any new seismic studies, in particularly by the MOBAL 2003 experiment (Petit et al., 2002 and 2008). It should be noticed that the calculation of the crustal thickness of Zorin et al. (1990) was realized with the isostatic calculation and not with seismic methodology.

Although the Moho data we have to our disposal over Mongolia are scarce and the seismic studies do not cover the whole country, we can assume that the Moho under Mongolia is most probably between 39 and 52 km depth with a global average of 44.6 km. It is difficult, if not impossible, to determine the uncertainties in Moho depth for such a grid as it is based on a model compiled by combination of several methods like receiver functions, gravity and petrological data.

2. Profile locations

The location of the four profiles is established taking into account the geology versus the geophysical gravity and magnetic signals in order to model the evolution of the crustal structure.

Table 1: Geographic coordinate points of profiles.

	<i>Northern point</i>		<i>Southern point</i>	
	Longitude	Latitude	Longitude	Latitude
<i>SW Profile</i>	98°39'41,758"E	45°40'49,962"N	98°11'34,34"E	42°42'43,431"N
<i>Noyon area Profile</i>	103°11'40,072"E	43°55'56,711"N	101°23'1,844"E	42°51'39,409"N
<i>Gurvansaykhan range Profile</i>	103°49'34,024"E	45°8'13,708"N	103°30'7,559"E	43°44'30,212"N
<i>SE Profile</i>	108°46'17,183"E	45°8'58,404"N	110°18'5,244"E	42°50'9,972"N

The four profiles (Fig. 5) were selected for following reasons:

(1) The profiles cross the four main lithotectonic zones, covering principal lithologies such as continental, accretionary wedge and oceanic domains. The contacts between these domains are sharply delineated in the field and will be suitable for modelling.

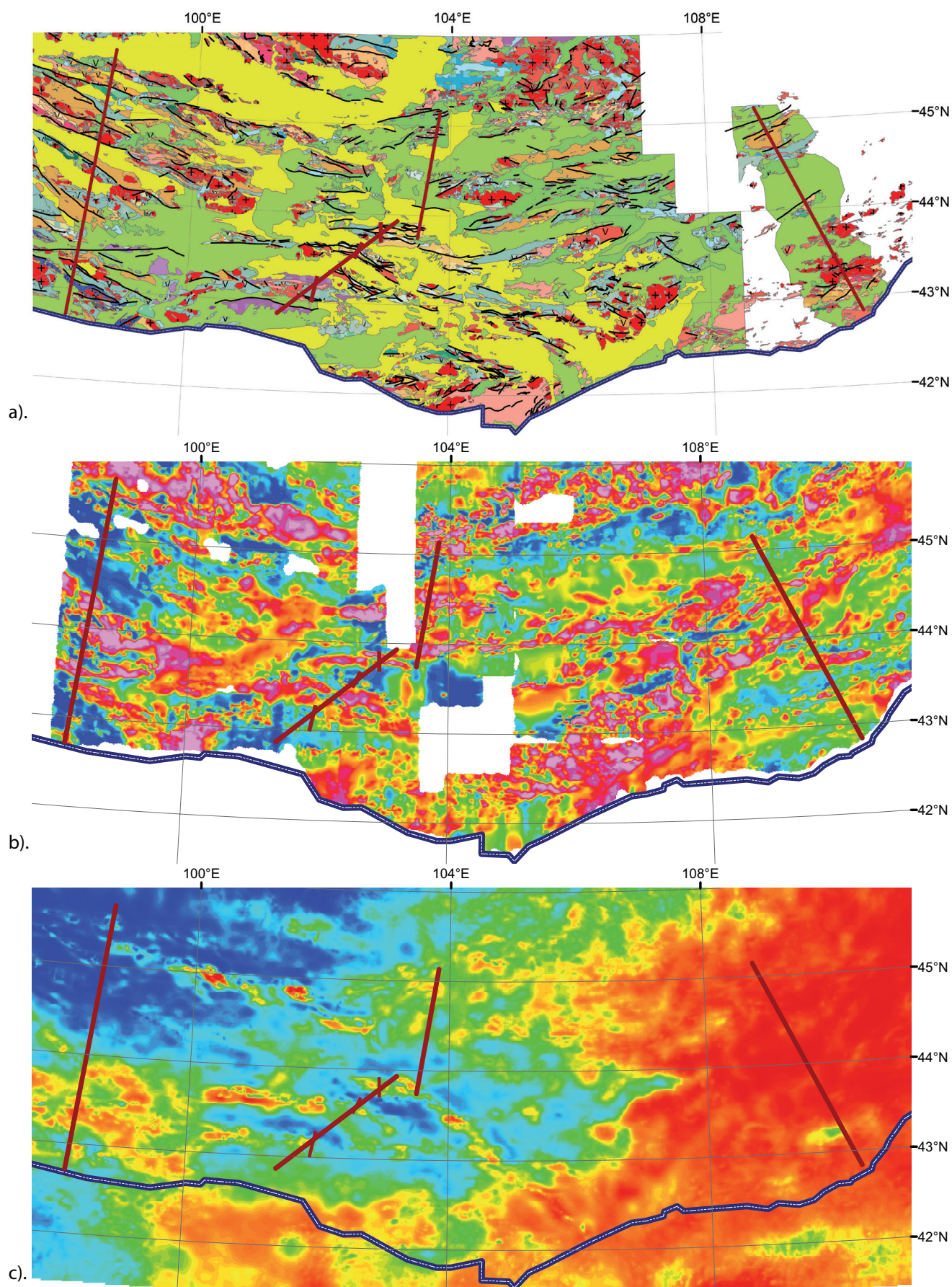


Figure 5: a). Geological map with the modelling profiles superimposed; b). Magnetic anomaly map; c). Complete Bouguer anomaly map.

(2) The profile intersects major mapped geological contacts and the gravity and magnetic contours at nearly 90° , except for the so-called Noyon profile.

(3) The correlations between the Bouguer anomaly, the magnetic anomaly and the surface geology are not necessarily obvious in most of the investigated areas.

(4) The profiles cover different regions allowing contrasting the geological structures in the western region poorly affected by the Mesozoic extension, to the geological structures in the eastern region highly affected by the Mesozoic extension (Daoudene et al., 2012; Cunningham et al., 2009).

The western profile is 331 km long, reaches 46 km in depth and is oriented at azimuth 5° in order to maintain orthogonality of the strike of geological fabrics and geophysical profile. The southern profile was divided into two smaller profiles of approximately 160-180 km long and reaches 45 km in depth in order to cross the major units and to avoid the lack of magnetic data in the area (Fig. 5). Therefore, the southernmost profile is not perpendicular to the geological boundaries. Finally, the southeastern profile is 280 km long, reaches 45 km in depth and is oriented in azimuth -5° .

3. Geophysical and geological correlations for each profile area

3.1. South-west of Mongolia

The profile is located in the south-west of Mongolia and crosses the four main lithotectonic zones, from north to south: the Lake Zone, the Gobi Altai Zone, the Trans-Altai Zone and the South Gobi Zone (Fig. 6).

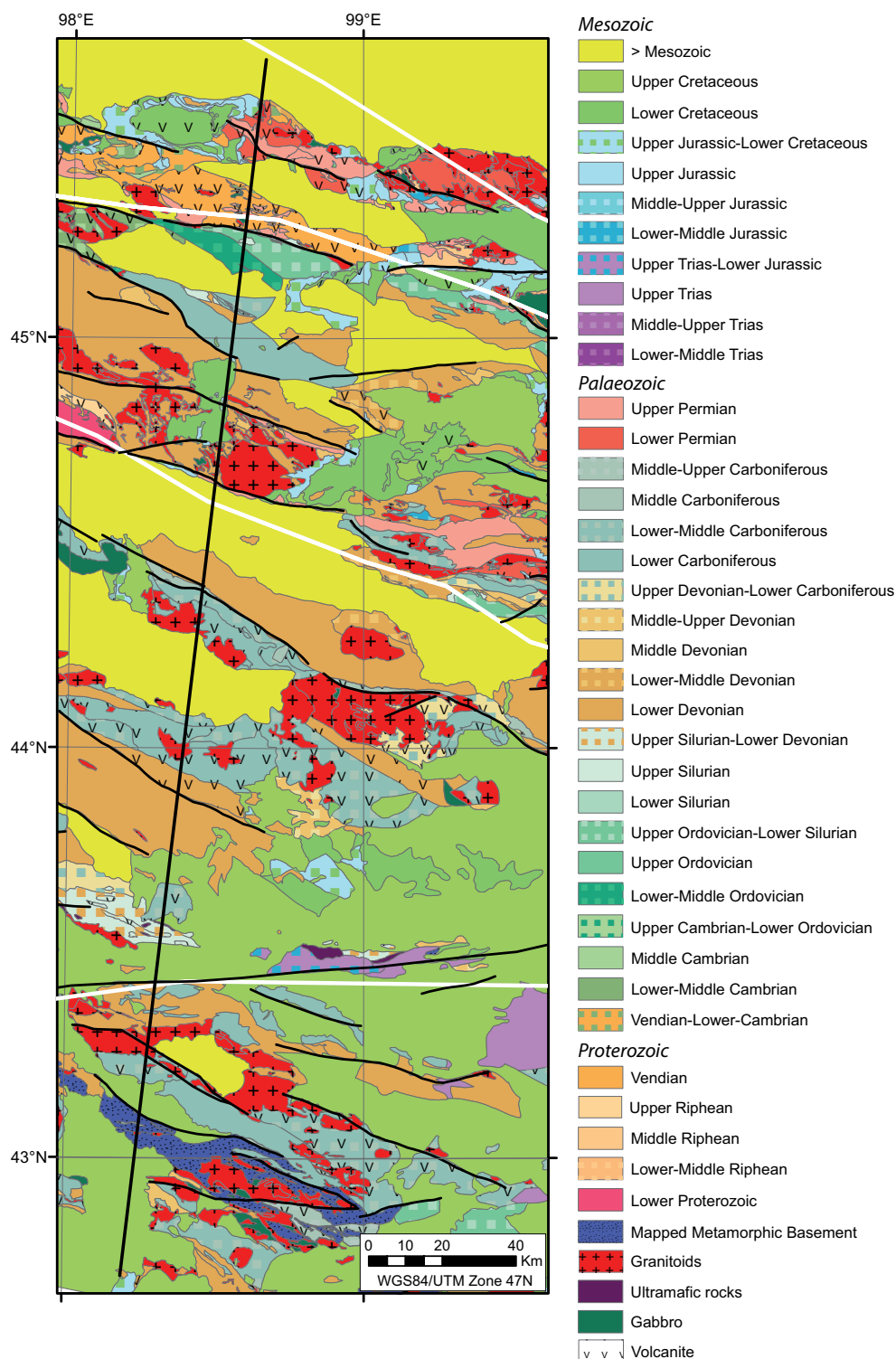


Figure 6: Geological map of the region of the profile located in the south-west of Mongolia. The white lines are the limits of the lithotectonic units and the black lines are faults.

3.1.1. Magnetic correlation

The magnetic anomalies range from -619 to 1384 nT (Fig. 7). The amplitude and frequency trends of magnetic anomalies vary according to the lithotectonic zones. Thus, the magnetic anomaly over the Lake Zone is of rather high amplitude and high frequency (Fig. 7). The Lake Zone is interpreted as the proximal passive margin of the Baydrag and Dzabkhan microcontinents to the north (Kroener et al., 2010). The lithologies consist of Vendian to Cambrian metamorphic rocks overlain unconformably by Permian continental deposits (Fig. 6) which can attest the existence of an emerged continental crust. The magnetic anomaly over the Gobi Altai Zone is monotonous with a low frequency and amplitude signal. The Gobi Altai Zone is an Ordovician to Early Devonian passive margin with thick sedimentary covers of clastic and turbiditic sequences derived from the nearby continent. Several granitic massifs most probably of middle Permian age intruded the early Devonian sedimentary sequences. These granites do not display a high amplitude magnetic anomaly trend whereas the middle Devonian granite to the west of the profile is marked by distinct magnetic high (Figs. 6 and 7). The magnetic anomaly over the Trans-Altai Zone is high frequency and high amplitude for the area of the profile which correlates with Carboniferous volcanic rocks. Finally, the magnetic anomalies are marked by mean frequency and amplitude to the south area of the profile in the region of the South Gobi Zone. The analysis of the surface geology tends to assume an alternation of synclines and anticlines of approximately 70 km wavelength over the Trans-Altai and the South Gobi Zones. According to Daoudene et al. (2012), the Cretaceous extension did not affect this area.

In summary, the magnetic anomalies correlate well the surface geology but not really the limits of the different lithotectonic zones.

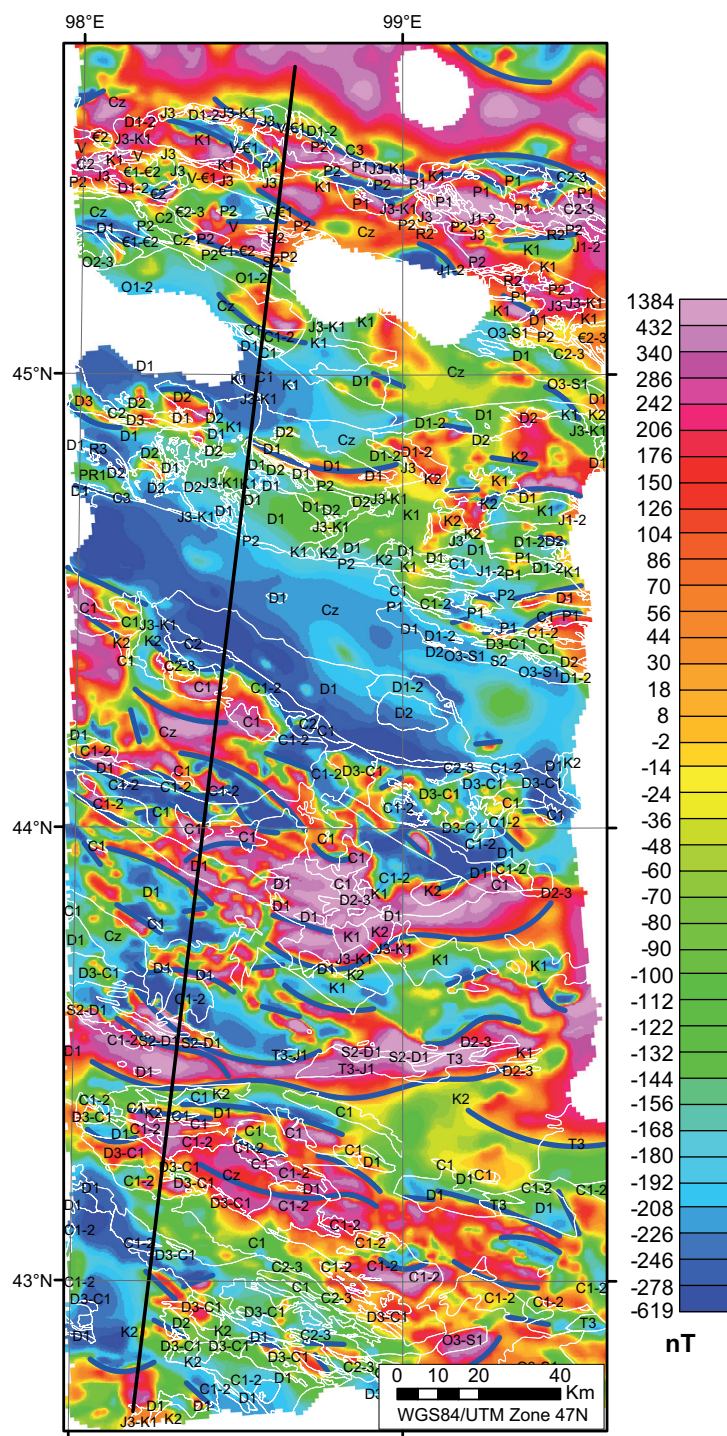


Figure 7: Magnetic anomaly map of the profile located in the south-west of Mongolia. The white curves are the geological contours. The blue curves are the lineaments of the Magnetic anomaly.

3.1.2. Gravity correlation

The Complete Bouguer anomalies range from -291 to -156 mGal in the area of the SW profile (Fig. 8). Two principal anomaly trends can be identified: (1) the northern half part of the area displays a gravity low but it is most probably due to the overprint of the very low amplitude gravity signature of the Hangai dome located to the north of this area. Therefore, in this area it is more relevant to analyze the residual Bouguer anomaly map which removes the long wavelengths of the gravity signal. (2) The southern half part of the area is associated with high amplitude gravity anomalies.

The residual Bouguer anomaly map of the Lake Zone shows gravity highs associated with the volcanic rocks whereas in the Gobi Altai Zone this correlation between high gravity and volcanic rocks is not confirmed. High amplitude gravity anomalies also correlate with Permian granites. The Trans-Altai Zone reveals no obvious correlation between the gravity signal and the surface geology. Finally, in the South Gobi Zone, most of the granites display significant gravity anomalies. In the southernmost part of the profile area, we can infer from continuity of gravity anomalies that the Carboniferous granite and the Devonian volcanic rocks surrounding the Cretaceous basin continue underneath the basin sequences.

In summary, for the south-west profile, the correlation between Bouguer anomalies and rock types is difficult to establish. According to the gravity signature, there is no convincing evidence, at this scale, that it exists four different tectonic domains with contrasting geophysical signature. Therefore, the correlation between the gravity signal trends and the lithotectonic zones is not clearly developed.

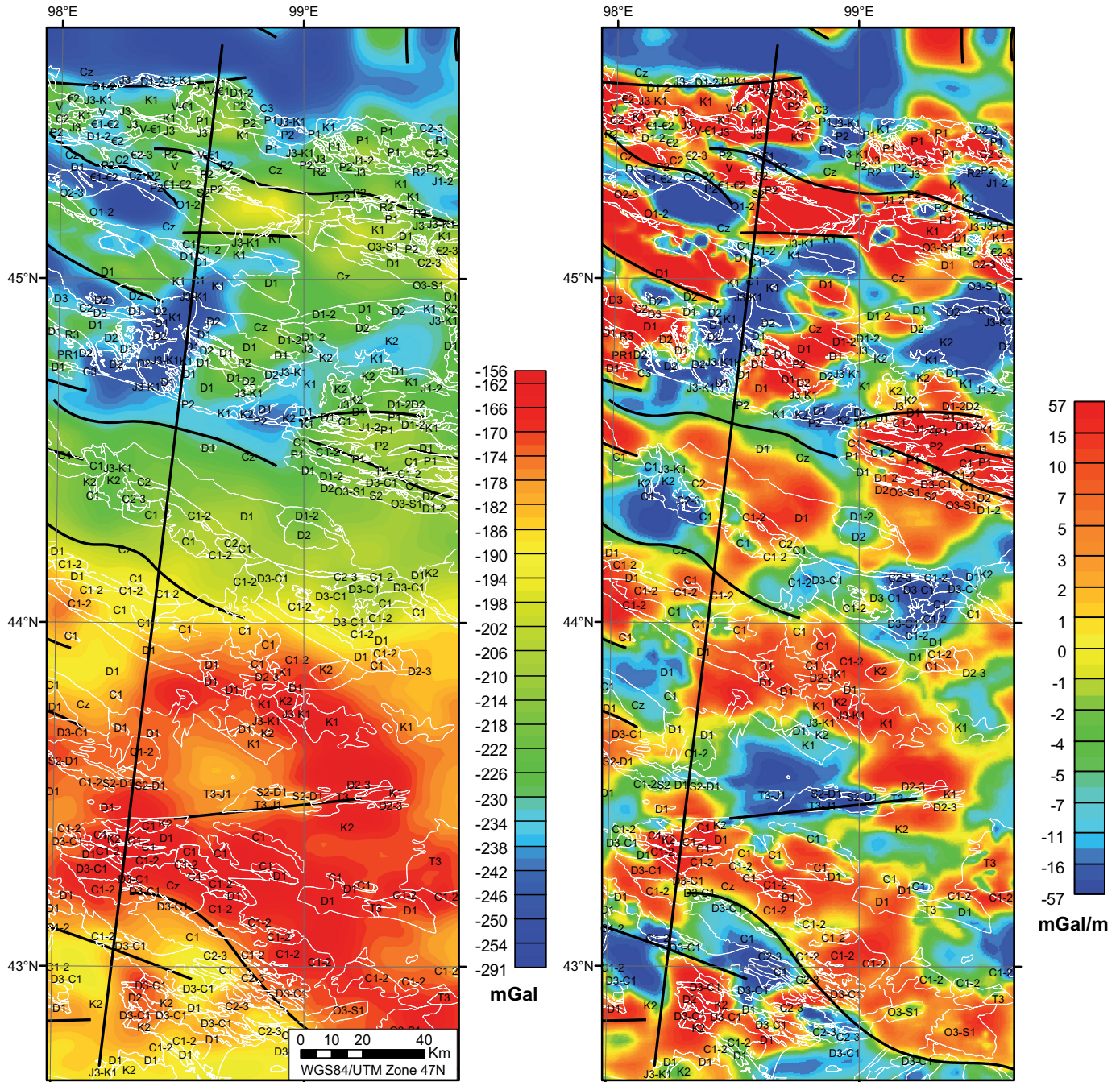


Figure 8: Bouguer anomaly map of the profile located in the south-west of Mongolia. The white curves are the geological contours. The black curves are the lineaments of the Bouguer anomaly.

3.2. Central south of Mongolia

3.2.1. North of Gurvansaykhan Range

The profile is located in the central part of the south of Mongolia and in the north of the Gurvansaykhan range. It crosses the Lake Zone and the Gobi-Altai Zone over the Cretaceous basins and some localized Palaeozoic rocks.

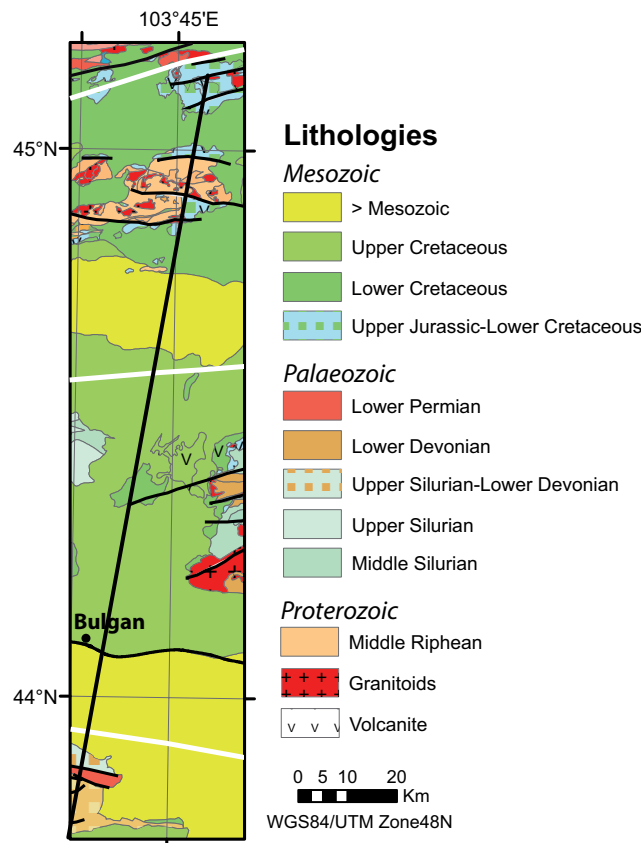


Figure 9: Geological map of the region of the profile located in the north of the central part of the area of interest. The white lines are the limits of the lithotectonic units and the black lines are faults.

3.2.1.1. Magnetic correlation

The magnetic anomalies range from -329 to 121 nT (Fig. 9). A correlation between the Cretaceous volcanic rocks and the high amplitude magnetic anomaly signals is observed and it is in harmony with the model of the Cretaceous extensional deformation affecting the area (Daoudene et al., 2012). The high amplitude magnetic anomalies over the sedimentary basins in this area show mean gradients and are not often correlated with the surface geology, indicating that the sources must be located deeper within the crust. Thus, we assume that important amount of highly magnetic rocks buried underneath the Cretaceous basins display substantial susceptibility contrasts with the sedimentary rocks of these basins. These ring-shaped high amplitude magnetic anomalies are located in the sedimentary Cretaceous basins

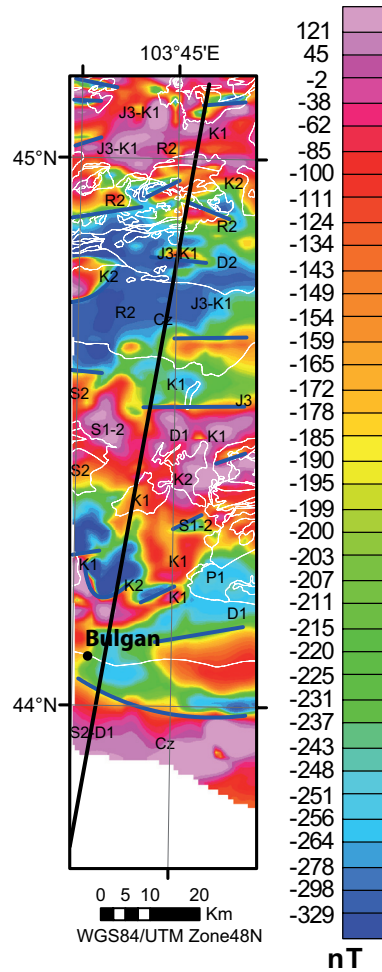


Figure 10: Magnetic anomaly map of the profile located in the north of the central part of the area of interest. The white curves are the geological contours. The blue curves are the lineaments of the Magnetic anomaly.

regardless lithotectonic zones, e.g. the same signature is observed in the continental (Lake Zone) or the passive margin (Gobi Altai Zone) tectonic context. Therefore, it is assumed that the rocks responsible of these high amplitude magnetic anomalies covered by the basinal sequences formed after the amalgamation of these two zones. Moreover, these high amplitude magnetic anomalies are often in the close vicinity of the late Jurassic-early Cretaceous and early Cretaceous volcanic rocks at the surface. Thus, we assume that the volcanic rocks of late Jurassic to early Cretaceous in age are the magnetic sources located in depth and covered by Cretaceous and Cenozoic sedimentary sequences (Fig. 8 and 9) in the area of the North Gurbansaykhan profile.

The low magnetic anomalies are generally correlated to the Palaeozoic rocks at the northern part of the profile in the Lake Zone. In contrary, to the south of the profile at the beginning of the Gurbansaykhan range, there is a high amplitude magnetic anomaly continuing underneath the Cenozoic basins that is most probably related to the late Silurian-early Devonian rocks containing lenses of ultramafic rocks. No real correlation can be established between the

granitic rocks in this area and magnetic anomaly tendencies.

In summary, there is a poor correlation between the magnetic signal and the surface geology. We assume that the majority of the magnetic sources are late Jurassic-early Cretaceous volcanic rocks buried in the Cretaceous and Cenozoic sedimentary basin.

3.2.1.2. Gravity correlation

Globally, the Palaeozoic and the Jurassic rocks have a high gravity anomaly comparing to the Cretaceous basin. However, there is no distinct correlation between the gravity anomalies and the surface geology (Fig. 11) except for the southernmost part of the profile, which displays a high density contrast in comparison to the rest of the profile.

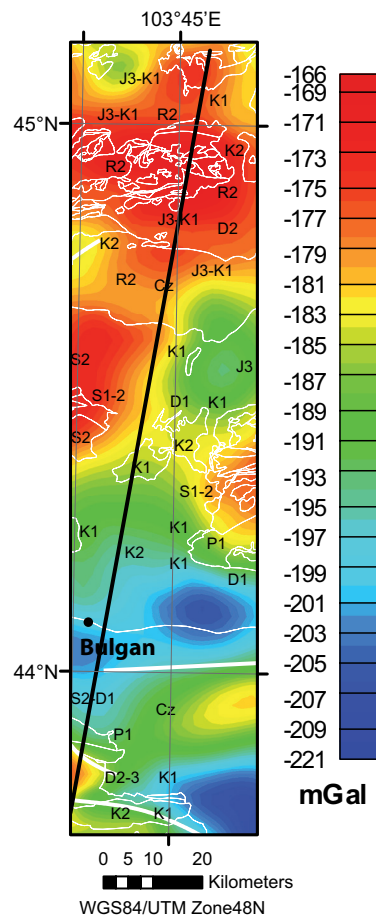


Figure 11: Bouguer anomaly map of the profile located in the north of the central part of the area of interest. The white curves are the geological contours. The thick white curves are the lineaments of the Bouguer anomaly.

3.2.2. In between Gurvansaykhan Range to Noyon Uul syncline

The profile covers the area in between the Gurvansaykhan Range to the Noyon Uul syncline through the Trans-Altai and the South Gobi Zones (Fig. 12).

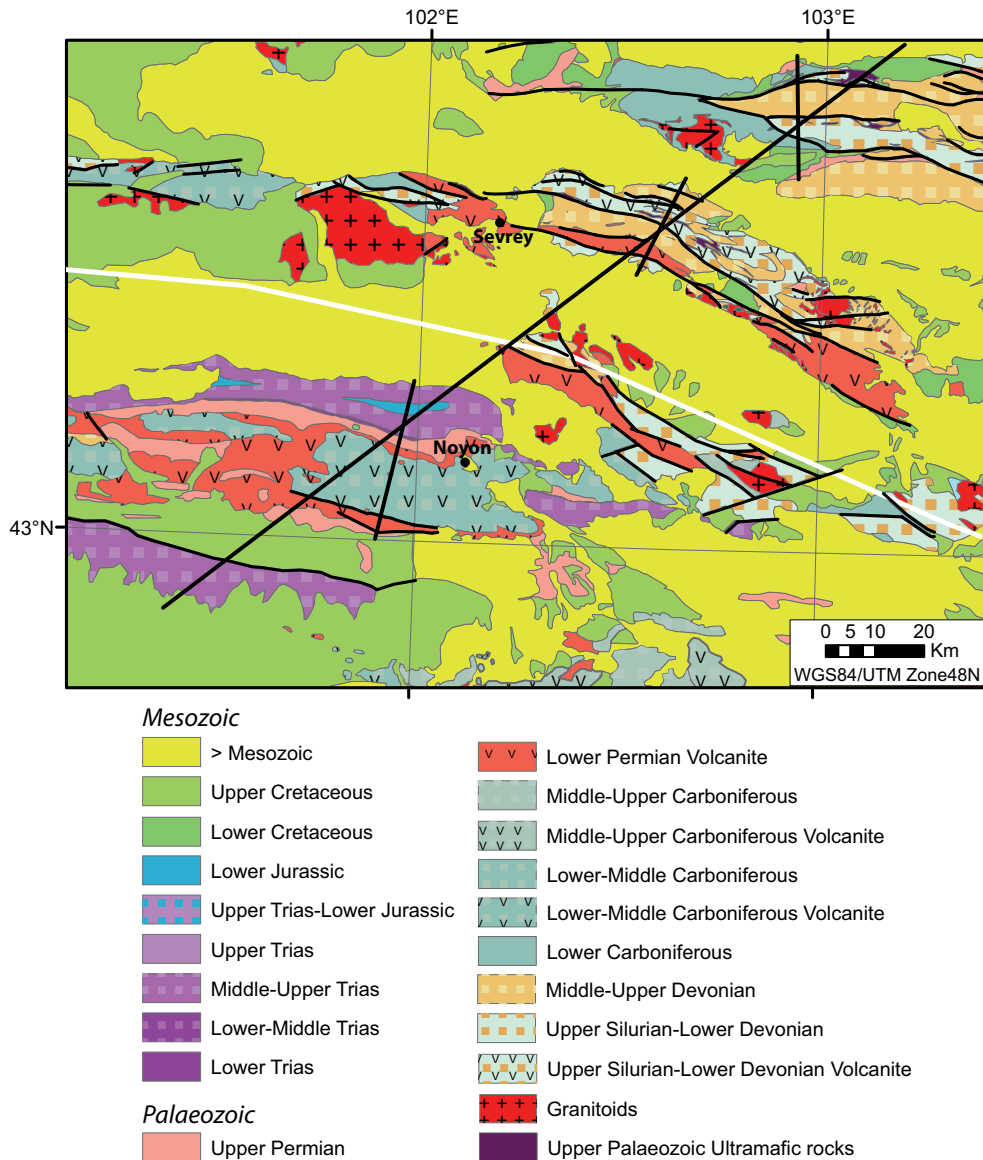


Figure 12: Geological map of the region of the profile crossing the Gurvansaykhan range and the Noyon syncline. The white lines are the limits of the lithotectonic units and the black lines are faults.

3.2.2.1. Magnetic correlation

According to Daoudene et al. (2012), the profile is located in an area not affected by the Cretaceous extension. On one hand, there are good correlations between the surface geology and the magnetic anomalies in some regions of the profile, on the other hand the correlation is difficult in some areas, as, for example, in the Cretaceous basin between the Dzolen Range and the Noyon Uul syncline where high amplitude magnetic anomalies with low gradients are

amplitude magnetic anomaly. To the south of Sevrey, the high amplitude magnetic anomalies have smooth gradients which indicates a deep-seated magnetic source or a magnetic body with low dip and wide borders. Starting from the Noyon Uul syncline, the magnetic signal is marked by lower frequencies and amplitudes. Over the Noyon Uul syncline, there is a quite high but scattered magnetic anomaly. Considering the lithology of this synclinal composed of Mesozoic sedimentary rocks, these rocks cannot be responsible for this high amplitude magnetic anomaly observed. Thus, the magnetic source is most probably due to Palaeozoic rocks located astride underneath the syncline and the Cenozoic basin. In the south of the Noyon Uul syncline, the Carboniferous-Permian volcanic rocks reveal a heterogeneous magnetization marked by low gradients suggesting that the magnetic source is most probably located in depth. In the southernmost part of the profile, the magnetic anomaly is low with low frequencies and amplitudes corresponding to sedimentary sequences.

In summary, there is a good correlation between the magnetic anomalies and the lithologies. However, the magnetic anomaly does not yield strong evidence for two distinguished tectonic zones separated by a major fault, shear or suture zone.

3.2.2.2. Gravity correlation

The Bouguer anomalies range from -224 to -157 mGal (Fig.14). Comparing the gravity and the magnetic signals, the correlation between them in this area is rather good. Indeed, the Gurvansaykhan range displays both high amplitude magnetic anomaly and a high Bouguer anomaly. The basins in this area reveal a relatively low amplitude gravity anomaly (Fig. 14) whereas the rocks at high topography display a higher amplitude gravity anomaly. To the north of the Noyon Uul syncline, the gravity anomaly over the Cenozoic basin is low whereas the magnetic anomaly is high. The sediments in the southernmost part of the profile show a high gravity anomaly but a low magnetic anomaly. However, although the magnetic and gravity signals are opposite, their limits are well correlated.

Regarding the high-pass Bouguer anomaly, there is a good correlation between this map and the Bouguer anomaly map which could mean that this area is poorly affected by the regional gravity anomaly.

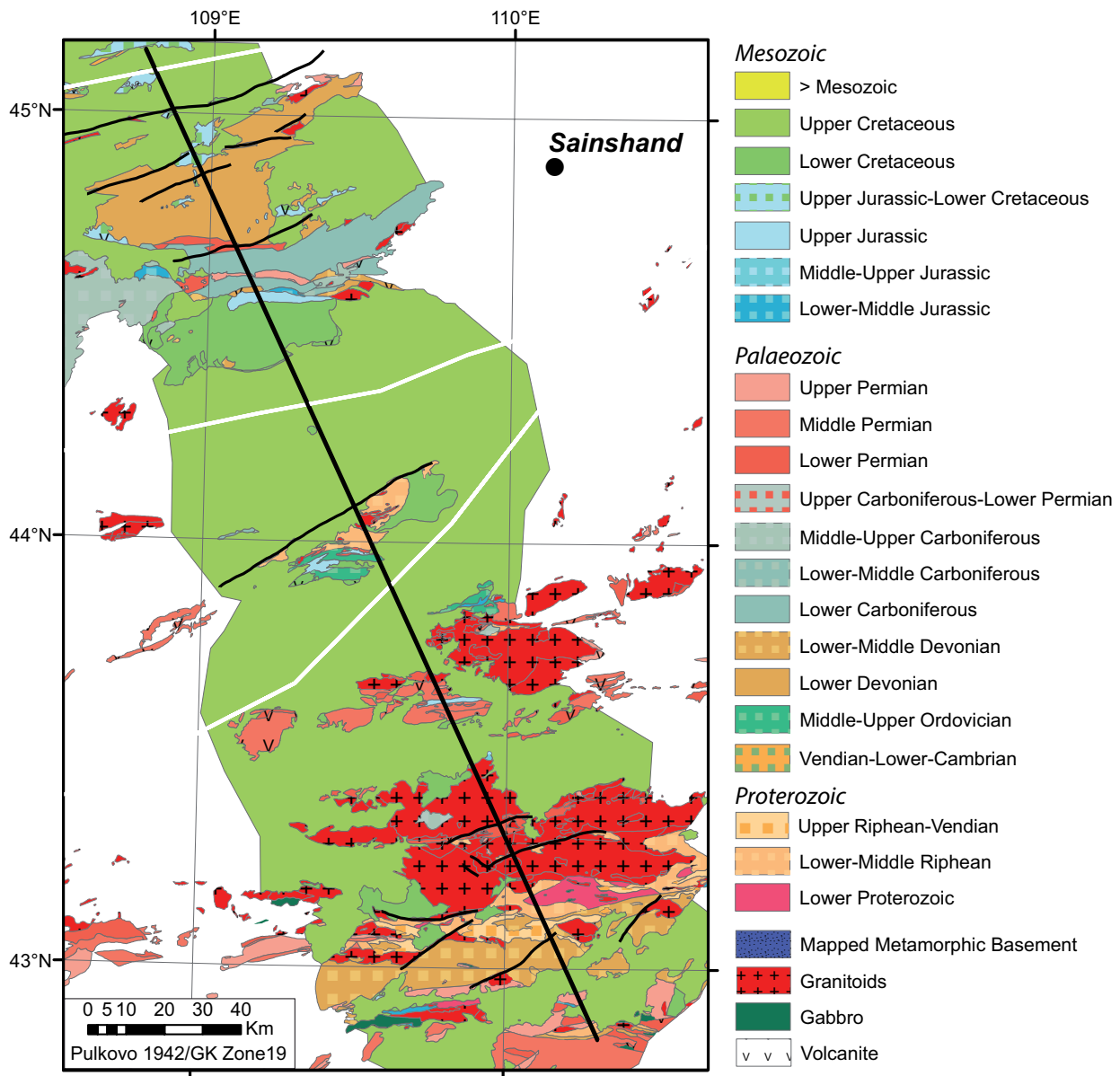


Figure 15: Geological map of the region of the profile located in the south-east of Mongolia. The white lines are the limits of the lithotectonic units and the black lines are faults.

3.3.1. Magnetic correlation

The magnetic anomalies extend from -394 to 1308 nT (Fig. 16). The correlation between the magnetic signal and the surface geology is poor for this part of Mongolia as well as there is no variation of the signal in frequencies and amplitudes which can be correlated with the lithotectonic zones. According to Daoudene et al. (2012) this area is affected by the Cretaceous extension. The East Gobi Fault Zone (EFGZ) is clearly delineated by a sharp magnetic contrast oriented NE–SW. To the east of the fault, there are major E–W oriented lineaments which are correlated to late Carboniferous granite. In the northwest quarter of the profile, high to intermediate frequencies and amplitudes of the magnetic signal followed by an area of low frequency and low amplitude is observed. This low magnetic anomaly corresponds to the

The frequency and amplitude of the magnetic signal trends change from the north to the south of the EGFZ. To the south of the fault zone, the frequency and the amplitude of the magnetic signal is rather mean. Comparing the surface geology, the sources of these magnetic anomalies are located in depth underneath the Zuunbayan Cretaceous subbasin as the gradients are smooth. To the south of the EGFZ, the surface geology displays Proterozoic to Palaeozoic rocks mostly correlated with positive but low amplitude magnetic signal. Therefore, either the magnetic sources have low and wide dips with small thickness or the magnetic sources are deep-seated. There is not a global correlation between the Cretaceous basins and the magnetic anomalies.

3.3.2. Gravity correlation

The Bouguer anomalies range from -174 to -115 mGal (Fig. 17). When looking at the regional Bouguer anomaly distribution (Fig. 2), this area has the lowest amplitude of the gravity signal and the highest Bouguer anomaly of southern Mongolia. The Bouguer anomaly is high and displays higher gravity contrast over the EGFZ. The low amplitude Bouguer anomaly to the south of the profile corresponds to Proterozoic to Palaeozoic granitic rocks (Fig. 17). Globally, the Devonian and Carboniferous granites have a low Bouguer anomaly whereas the Permian granites display a higher Bouguer anomaly.

along four selected profiles, but the results are definitely not enough reliable to be used without caution. The Oasismontaj software was used for these data treatments.

4.1. Source parameter ImagingTM (SPITM)

The SPI method (Thurston and Smith, 1997) is used to convert the gridded magnetic data to depth. This method particularly gets valuable results in the case of sedimentary basins where the depth to the basement has to be estimated (Smith et al., 1998). The SPI method is independent of the remanent magnetization, the magnetic inclination and declination, therefore the reduction to the pole does not need to be calculated.

The computation of the SPI starts with the first order derivatives of the total magnetic field anomaly in x, y and z directions. Then, the tilt derivative (A) is computed:

$$A = \arctan \left[\frac{\frac{dM}{dz}}{\sqrt{\left(\frac{dM}{dx}\right)^2 + \left(\frac{dM}{dy}\right)^2}} \right] \quad \text{where M is the total magnetic field anomaly grid}$$

Following by the calculation of the local wavenumber K:

$$K = \sqrt{\left(\frac{dA}{dx}\right)^2 + \left(\frac{dA}{dy}\right)^2}$$

Finally, the depth of the source is the opposite of the peak value Kmax of the local wavenumber K.

$$\text{DepthOfTheSource} = \frac{1}{K_{\max}}$$

where Kmax is the peak value of the local wavenumber over the magnetic source.

The peak values Kmax are evaluated using the Blakely and Simpson locating ridge method (1986). This method consists on analyzing each grid cell in order to compare its value with the eight surrounding grid cells in the four directions: x, y and both diagonals (Fig. 18).

$$g_{i-1,j-1} < g_{i,j} > g_{i+1,j+1}$$

$$g_{i-1,j} < g_{i,j} > g_{i+1,j}$$

$$g_{i-1,j+1} < g_{i,j} > g_{i+1,j-1}$$

$$g_{i,j-1} < g_{i,j} > g_{i,j+1}$$

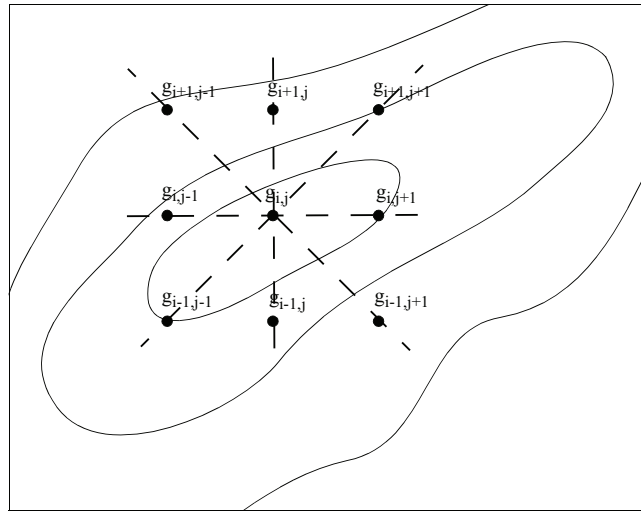


Figure 18: Method of Blakely and Simpson (1986), determination of the maxima from the gridded values. Curves are schematic magnetic gradients. Dotted straight lines are the direction of the test to find the maxima.

Then, it is possible to determine four levels to filter and refine the results of SPI. (1) One can only keep the grid cells which have the highest value in the eight surroundings (so in the four directions); (2) or only in three or two directions; (3) finally, in order to detect ridges, one can use the option which keeps all the values in any one direction. As we used this method to have an idea on the depth of the sedimentary basins, we choose the first option (values in all adjacent grid cells are lower).

We calculated the SPI independently for each profile area with the peak level of four, three, two and any directions and for different cutoff levels. For example, figure 19 shows the SPI grids obtained for the SW and SE profiles with the peak level evaluated in four directions. These solutions show an approximation of the depth of some basins. However, these results should be used with caution as we have not seismic lines directly on the profile areas to make a leveling of the SPI results and to have a critical view on the results. Except for the Zuunbayan basin having few seismic lines in the area, which display a sedimentary basin of -3000 m in depth (Webb et al., 2006) whereas the SPI method calculates a depth to basement at more than -4000m in depth, thus it seems that there is a shift of ~1000 m.

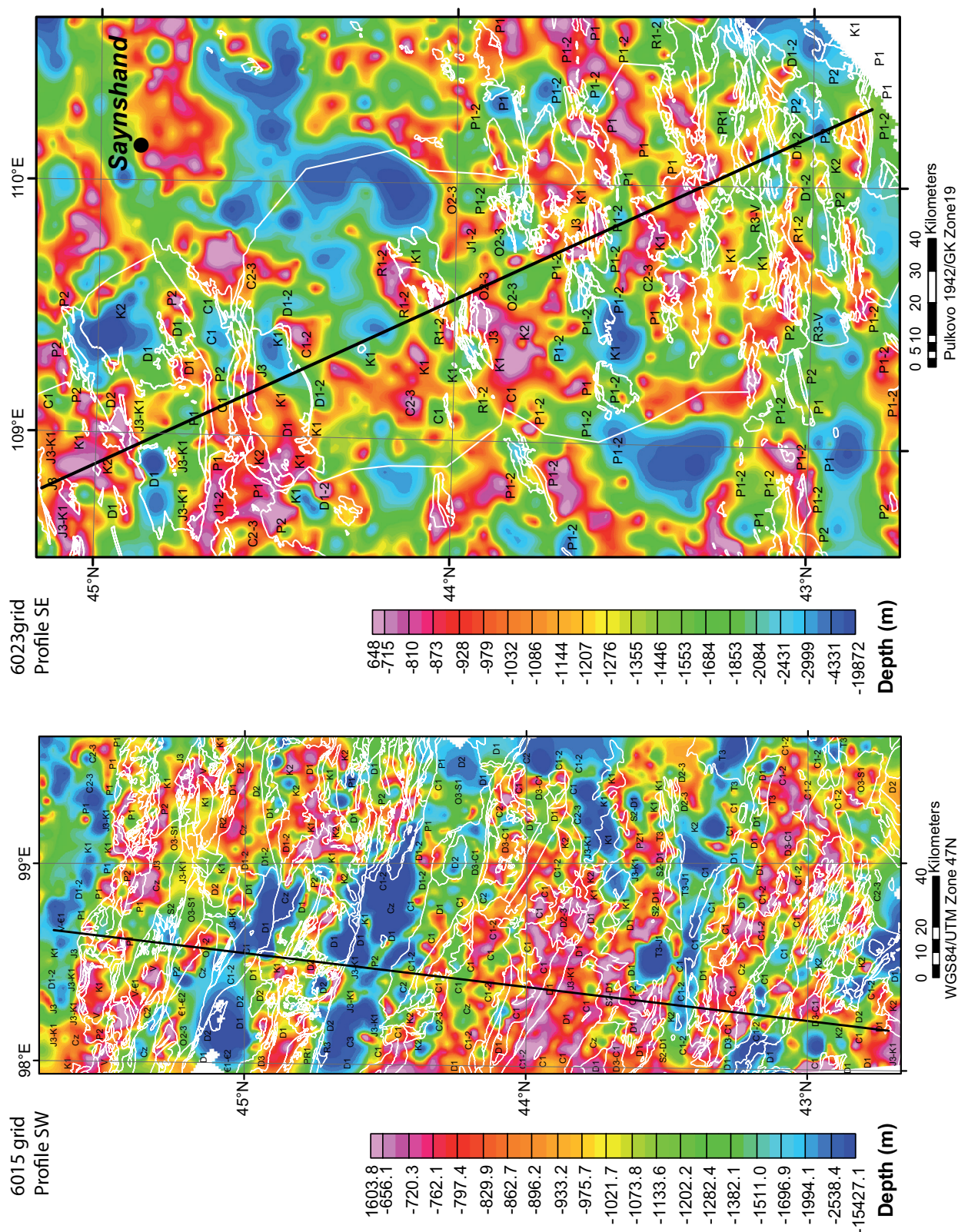


Figure 19: Source parameter imaging (SPI) grids. The white curves are the geological contours.

4.2. Euler deconvolution over the grids and along profile

The Euler deconvolution is based on the Euler's homogeneity equation:

$$(x - x_0) \frac{\partial M}{\partial x} + (y - y_0) \frac{\partial M}{\partial y} + (z - z_0) \frac{\partial M}{\partial z} = N(B - M)$$

Where (x_0, y_0, z_0) is the position of the magnetic source and (x, y, z) is the position of the center of the window.

M is the magnetic anomaly field

B is the regional magnetic field

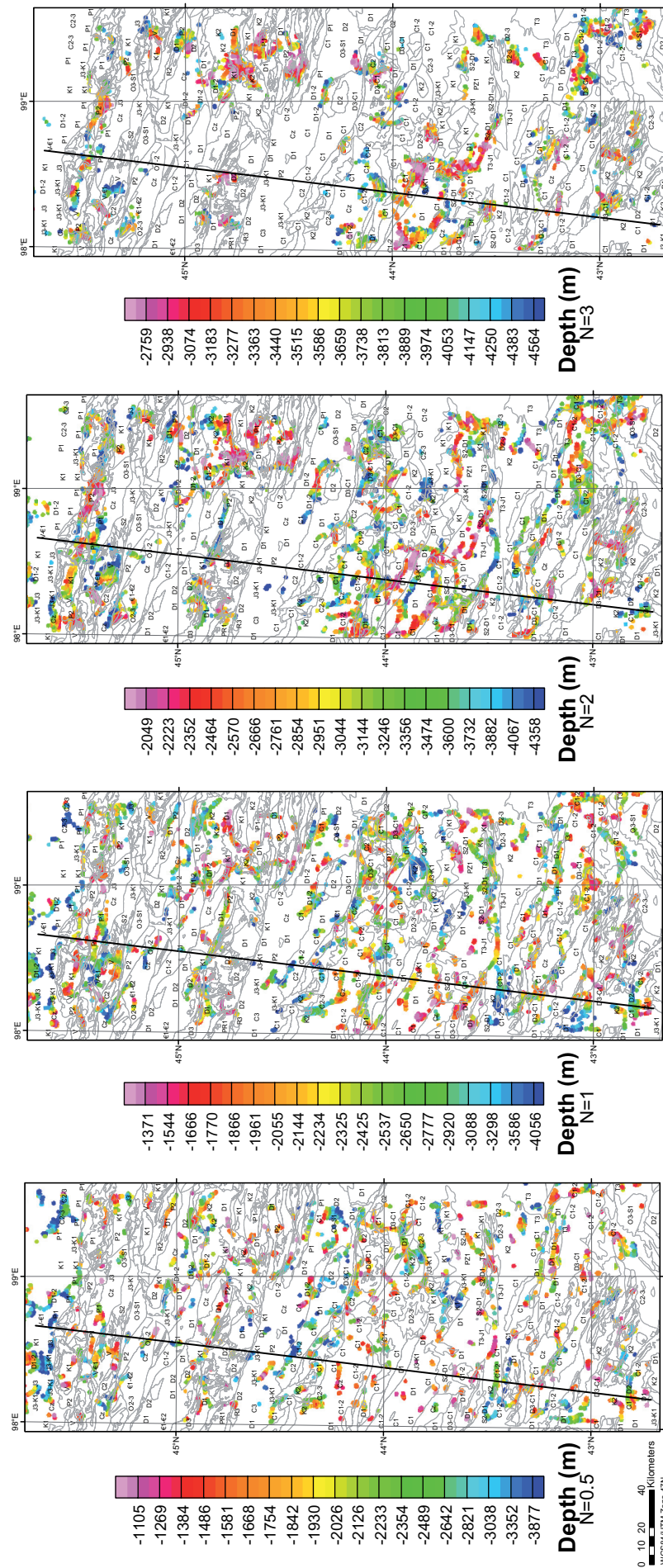
The degree of homogeneity is expressed as the structural index N. Commonly, for Euler deconvolution computation on magnetic data, N is:

- N=0 for the contact and fault
- N=1 for the dyke or the sill
- N=2 for the cylinder and pipe
- N=3 for the sphere

The structural index describes the attenuation rate of the magnetic anomaly with the distance of the field. The N value is related to the structure of the source (Thompson, 1982). This process was applied to determinate the location of the source of a magnetic anomaly for gridded data (Reid et al., 1990).

The pole reduction is unnecessary before applying Euler deconvolution as this process is independent of magnetic remanence and inclination effects. Before processing the Euler deconvolution, a square window size must be specified as well as the N appropriate value according to the magnetic source we would like to highlight. The size of the window has to be chosen in order that the window is large enough to include each solution location, but not too much large to include any adjacent anomaly. The amount of results of source points can be filtered by statistical criteria to obtain the most reliable results. The criteria we used are the minimum standard deviation (Thompson, 1982), the reasonable percentage depth uncertainty ($dZ < 15\%$) (Cooper, 2004) and the location uncertainty ($dX < 30\%$).

Figure 20: Euler deconvolution results for different structural index. The grey curves are the geological contours.



For the study area, we computed the Euler deconvolution with $N=0, 0.5, 1, 2$ or 3 and after several tests, the window size of 10 km seems to be the most appropriate for the data. Figure 20 show the results of the Euler deconvolution for the SW area profile. We display the $N=0.5$ solutions instead of the $N=0$ solutions as, according to the magnetic data and the results obtained, it is more reliable than $N=0$ as Thompson (1982) and Reid et al. (1990) demonstrate. Because there are no seismic lines available in this area, it is difficult to verify the relevance of these results. However, concerning the south-east profile, the results we obtained with the Euler deconvolution are homogeneous with the SPI methods and with the shift observed when compared the depth given by the few seismic lines with the results of these two methods.

Euler deconvolution is also applied to the gravity data. However, taking into account all the approximation about the quality and origins of the gravity datasets, the Euler deconvolution results would hardly be reliable and we decide to use this method only for magnetic data.

4.3. Analytic signal

The analytic signal depth solutions are a depth to basement method used on magnetic profiles. This treatment is based on the program elaborated by Phillips (1997) and this program is based on the studies of Nabighian (1972, 1974). The theory assumes that all the causative magnetic bodies (1) have a uniform magnetization; (2) extend to infinity in direction perpendicular to the profile; and, (3) are polygons of either finite or infinite depth extent. The input data is the first order horizontal derivative of the magnetic anomaly profile. The depth of these polygons is estimated by setting a window size going through the magnetic profile.

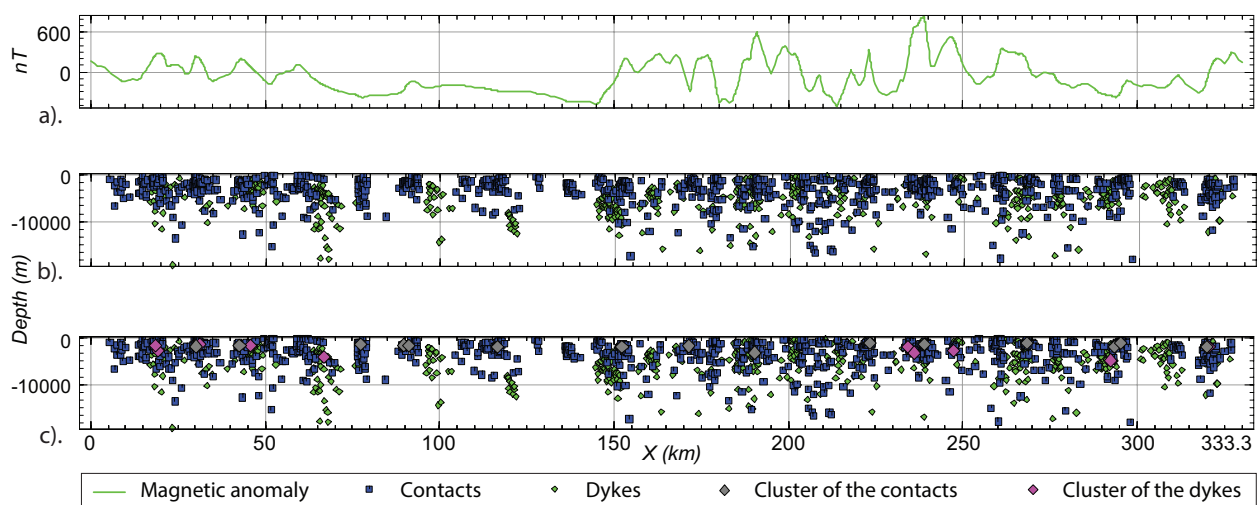


Figure 21: Example of the depth to basement source treatment along a profile. a). The magnetic anomaly curve; b). the results of the analytic signal method; c). the clustering solutions of the depth to basement treatment results.

This treatment generates a lot of scattered solutions around the real solution location (Fig. 21b) either for solutions related to dykes or for solutions related to contacts. It is then useful for the interpretation to group these multiple solutions and creates clustered solutions. The number of solutions grouped to form a cluster (Fig. 21c) will depend on the size of the window and on the number of solutions located in the area of the defined window.

Figure 21 displays one example of the different steps of the analytic signal depth solution processes along the SW profile. Some results may be linked with existing faults but the majority results apparently have not a corresponding and reliable surface geological significance according to the geological map. This method can just provide a preliminary idea on the possible structures of the crust for our case study but it cannot be completely relevant without any control data like borehole or seismic data.

5. Modelling: methodology, petrophysical data and constraints

5.1. Forward modelling

The gravity and magnetic forward modelling allows building geological cross sections of the crust at different depth by fitting the calculated potential field signal to the measured data.

Magnetic and gravity data of the profiles are extracted from the magnetic and the complete Bouguer grids respectively and imported to the GM-SYS extension of Oasismontaj software. Then, the polygons, which represent the model geological bodies along the cross section, can be elaborated. These geological bodies are truncated at a distance of 30 km perpendicular to the section line. Their surface extents are constrained by the surface geology and have to be consistent in size, shape and orientation with the outcrop features. Specific density and susceptibility properties are assigned to each polygon. Then, by iteratively adjusting both the geometry of bodies and their rock properties, we tried to fit the calculated response with the observed anomaly data. The parameters for magnetic modelling were calculated from the different IGRF models according to the year of the magnetic survey (Table 1). In the models, the depth of the Moho is set based on the interpolated Moho grid modified from the model CRUST 2.0 (Fig. 4). However, only the crust above approximately 20 to 25 km depth has been carefully modelled. A density of 3200 kg/m³ is attributed to the mantle, and the lower crust has an average of 2750 to 2870 kg/m³, which correspond to homogeneous high grade metamorphic rocks.

The four profiles are over the four major lithotectonic units described into the chapter

I. Due to the lack of complementary data like seismic relevant profiles, the starting point for the modelling of the structures of the crust is the contours of the surface geology and the interpretation of the geophysical maps according to the estimation of the density and susceptibility values of these structures.

5.2. Difficulties in determining rock properties of exposed and basement rocks

Evaluated and assigned petrophysical properties can lead to source of errors for the density and susceptibility values in depth. For example, low metamorphic grade rocks at the surface would be higher grade, and thus usually denser, in depth.

The Curie point, where the magnetic minerals lose their ferromagnetic properties, has different temperature according to the mineral. The magnetite is one of the most common magnetic mineral responsible for the magnetic susceptibility of rocks. Its Curie point is at 578°C (Clark, 1997). Thus, using an average gradient of geotherm of 30°C/km, we can consider that the crustal rocks below ~20 km in depth have very low magnetic susceptibilities.

For our study, we have only few petrophysical measurements: no density values were measured, except about thirty samples in the south-east profile area (Gine Sanchez, personal communication). Therefore, the density attributed to most of structures in our models will come from general tables of density measurements (e.g. Telford et al., 1990).

Some magnetic susceptibilities measurements were made, mostly in the south-west of Mongolia (Hanžl, personal communication), and thirty key outcrops were measured in the south-east of Mongolia (Gine Sanchez, personal communication). However, the magnetic susceptibilities of rocks having no measurements come from the literature (Clark, 1997).

5.3. Density and susceptibility constraints

Telford et al. (1990) gave the average granitic rock densities in the range of 2500 to 2810 kg/m³; sedimentary rocks in the range of 2210 to 2900 kg/m³ and metamorphic rocks in the range of 2500 to 3370 kg/m³. Then, according to the rock types, the density properties were adjusted iteratively to match the observed gravity data. The final density values assign to the geological bodies for the modelling are given in Table 2, taking into account that the densities of large and deep bodies have to been extrapolated in depth.

Table 2: Density and susceptibility of rocks used for the modelling.

Profiles	Lithologies	Densities [kg.m^{-3}]	Susceptibilities [SI]
SW			
	Late Cretaceous	2500	0
	Early Cretaceous	2300	0
	Late Jurassic-Early Cretaceous	2400-2600	0,002-0,005
	Late Permian volcanic	2700-2730	0,002
	Early Permian volcanic	2700	0,01
	Early-Middle Carboniferous	2640-2680	0
	Early-Middle Carboniferous volcanic	2750-2780	0-0,02
	Early Carboniferous	2750	0
	Early Carboniferous volcanic	2680-2770	0,005-0,03
	Late Devonian-Early Carboniferous	2450	0,01
	Early Devonian	2600	0
	Early Devonian volcanic	2780	0,04
	Late Silurian-Early Devonian	2650-2700	0-0,06
	Late Ordovician-Early Silurian	2670	0,0001
	Middle Ordovician	2790	0,015
	Early Cambrian	2710	0,0002
	Granite Early Devonian	2660	0
	Granite Early Carboniferous	2620-2780	0,01-0,07
	Granodiorite Late Devonian-Early Carboniferous	2690	0,00015
	Granodiorite Early Carboniferous	2750	0,05-0,07
	Granodiorite Early Permian	2700	0,02
	Gabbro	2750-2900	0,01-0,03
	Ultramafic rocks	2650-2850	0,05
	Metamorphic rocks	2580	0
North Gurbansaykhan			
	Cenozoic	2400	0
	Late Cretaceous	2500-2550	0
	Early Cretaceous	2500-2600	0
	Early Cretaceous volcanic	2690	0,02-0,03
	Late Jurassic-Early Cretaceous	2650	0-0,055
	Late Jurassic-Early Cretaceous volcanic	2700-2820	0,005-0,065
	Early Permian	2660	0
	Middle to Late Devonian	2790	0,001
	Late Silurian-Early Devonian	2660-2780	0,0005
	Early Riphean	2740	0,008
	Late Riphean	2710	0,008-0,01
	Granite Early Permian	2700	0,03
	Middle Devonian Monzonite	2710	0,008
	Undifferentiated rocks	2700-2750	0-0,025
Gurbansaykhan-Dzolen-Noyon			
	Early to Late Cretaceous	2670	0
	Early Jurassic	2690	0
	Middle-Late Trias	2600	0
	Early Trias	2700	0
	Late Permian	2640-2900	0
	Early Permian volcanic	2780	0,001-0,0065
	Early-Middle Carboniferous Volcanic	2750	0
	Early Carboniferous	2720	0,00025-0,01
	Middle-Late Devonian	2810	0,0001
	Late Silurian-Early Devonian	2680-2750	0,003-0,005
	Late Silurian-Early Devonian volcanic	2780	0,005
	Ultramafic rocks	2800-2900	0,06-0,1
	Granite Early Permian	2800	0,0025
	Undifferentiated rocks	2700-2870	0-0,006
SE			
	Late Cretaceous	2450-2500	0
	Early Cretaceous	2600-2690	0
	Late Jurassic-Early Cretaceous	2600-2680	0,001
	Late Jurassic-Early Cretaceous volcanic	2720	0,005-0,01
	Late Permian	2670-2720	0-0,03

Table 2. *continued*

	Middle Permian	2710-2780	0-0,007
	Middle Permian volcanic	2730-2750	0,001-0,005
	Early Permian	2700-2750	0,008-0,03
	Early Permian volcanic	2750	0,008
	Early Carboniferous	2760-2770	0,03
	Early to Middle Devonian	2740	0
	Early Devonian	2670-2690	0-0,0001
	Early Devonian volcanic	2700	0,03
	Middle-Late Ordovician	2700	0
	Early to Middle Riphean	2710-2790	0-0,0005
	Proterozoic	2690-2720	0,003-0,005
	Granodiorite Riphean	2780	0,006
	Granite Late Riphean	2620	0,01
	Granite Middle to Late Devonian	2620-2690	0,006
	Granite Late Carboniferous	2710	0,002
	Granite Late Permian	2700-2730	0,02-0,03
	Granite Early Permian	2670	0,002
	Undifferentiated rocks	2720-2760	0-0,006

The range of susceptibilities for the basement rocks depends on the composition and the metamorphic degree of the rocks, the depth and the thickness of the basement. Therefore, the average susceptibilities were taken considering the petrophysical data commonly known of basement rocks (Table 2). No attempt was made to assign remanent magnetizations to the model source bodies. The magnetic properties of model bodies were then adjust iteratively to match observed magnetic data.

6. Magnetic and gravity models

The following profiles have been modelled using both magnetic and gravity data. The starting point of the modelling is the geological surface and an attempt was made to fit the calculated with the observed curves as closely as possible. The models presented in this part are non-unique and cannot provide definitive answers to the structures of the crust. However, the models can provide several a priori solutions for the geometry of the crustal structures.

6.1. Profile south-west of Mongolia (Bayankhangor Province)

The first step of the modelling is to model the long wavelengths of the Bouguer anomaly. For the south-west profile, these anomalies can be divided into three distinct types respectively from north to south: intermediate, low and high amplitude Bouguer anomaly. The middle crust has been assigned to densities of 2800, 2750 and 2870 kg/m³ respectively in order to match the long wavelengths of the gravity profile (Fig. 22).

The second step of the modelling is to model the short wavelengths of the magnetic

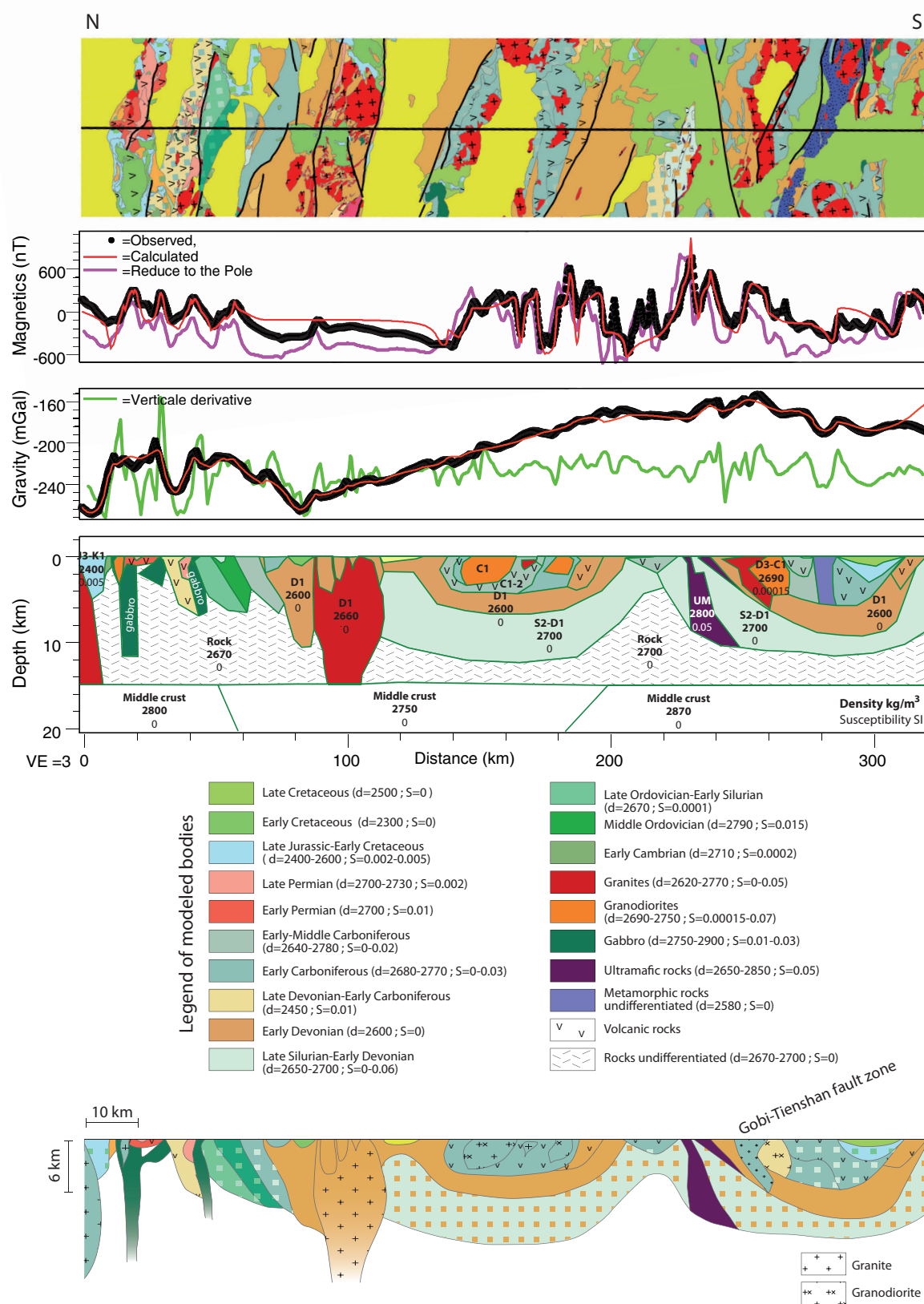


Figure 22: Gravity and magnetic potential field model along the SW profile. The surface geology is at the top. The upper panel shows observed (black circles), modelled (red solid line) and reduce to the pole (pink solid line) anomalies for magnetic field. The second panel shows observed (black circles), modelled (black solid line) and vertical derivative (green solid line) anomalies for gravity field. The third panel shows the potential field model with individual bodies colored by age of lithologies, with density (kg/m³) and magnetic susceptibility (SI) values. The last panel is the geological interpretative cross section for the SW profile. The colors attributed to the geological bodies are according to the geological map legend.

and gravity anomalies. The north of this profile starts in the Cenozoic basin of the Baydrag continent displaying high amplitude magnetic anomalies which are assumed to be due to late Palaeozoic granitoids buried into the basin. In the model, the Cenozoic cover is neglected in favour of a low density high susceptibility granitoid underneath late Jurassic-early Cretaceous sediments. In the south of the Cenozoic basin, dykes of gabbro are modelled as being located below the Permian volcanic rocks (although they do not reach the surface). This area displays high frequency and high amplitude magnetic anomalies correlated with high amplitude gravity anomalies. The composition of structures responsible of these geophysical signatures is deduced from the observation of the surface geology several kilometers on either side of the corresponding profile, where gabbros are observed (Fig. 22).

Modelling indicates that the early Devonian batholith which is the source of the dyke structures observed along the profile is most probably ~30 km wide. To obtain the low gradients and amplitudes of the magnetic and gravity signals over this area, low density and susceptibility values are required.

In the southern half of the profile, the magnetic signal is marked by high frequencies and amplitudes. The magnetic anomaly gradients are steep indicating that the sources of these anomalies reach the surface. Several Carboniferous volcanic rocks and slivers of ultramafic rocks crop out in this area and their boundaries correlate with the edge peaks of magnetic anomalies. Therefore, they are assumed to be the main sources of the magnetic and gravity short wavelength anomalies in the south of the profile.

The modelled magnetic profile has a good match with the observed profile, excluding the low amplitude and frequency magnetic anomaly in the northern half part. The modelled gravity profile is a good fit to the observed profile. The geological interpretation of the model suggests an alternation of syncline and anticline in the southern half part of the profile (Fig. 22)

6.2. Profiles south of Mongolia (Ömnogovi Province)

The profile over the south of Mongolia was first separated into two profiles due to the lack of magnetic data and the areas which are interesting to investigate: the northern profile is called “Profile north of the Gurvansaykhan Range” and the southern profile is called “Profile between the Gurvansaykhan Range and the Noyon Uul syncline”.

6.2.1. Profile north of Gurvansaykhan range

The northern part of the profile starts with a swarm of early Permian granitic intrusions intruding late Jurassic-early Cretaceous sedimentary and volcanic rocks (Fig. 23). Modelling suggests that the early Permian granite is an important batholith located ~4 km in depth. The middle Devonian monzonite is attributed a density of 2710 kg/m³ and a magnetic susceptibility of 0.008 SI to match the observed gravity and magnetic profiles. Moreover, to fit calculated gravity and magnetic curves to observed ones, a significant volume of the monzonite body is envisaged intruding the Riphean sedimentary rocks, although it only crops out in a small surface (Fig. 23).

The Cretaceous basin occupies the major central part of the profile. The long wavelengths of the intermediate to high magnetic anomalies underneath the Cretaceous basin indicate that the sources of these anomalies are deep-seated structures. According to the geological outcrop, the late Jurassic-early Cretaceous volcanic rocks might be the source of these magnetic highs. The depth of the interface between the Cretaceous sediments and the late Jurassic-early Cretaceous volcanic rocks is evaluated combining the SPI, Euler deconvolution and analytic signal depth solutions. These results give the location of the magnetic sources at approximately 5-6 km depth.

We assume the composition and origin of the early to middle Silurian rocks structure underneath the Cretaceous basin thanks to the observation of the surface geology several kilometers on either side of the corresponding profile.

The profile ends to the south in the Gurvansaykhan range. The syncline structure, which is modelled in this area, gets inspired from the existing structural cross-section (Guy et al., submitted) several kilometers to the west (cf. chapter II, Fig. 7).

The modelled magnetic profile fits the observed profile closely, expect for minor surface features such as the limits of the profile or for several anomalies over the Cretaceous basin. There is also a good fit between the observed and calculated gravity profiles, although the model fails to reproduce gravity highs to the north of the profile and the alternation of gravity high and low over the southern edge of the Cretaceous basin.

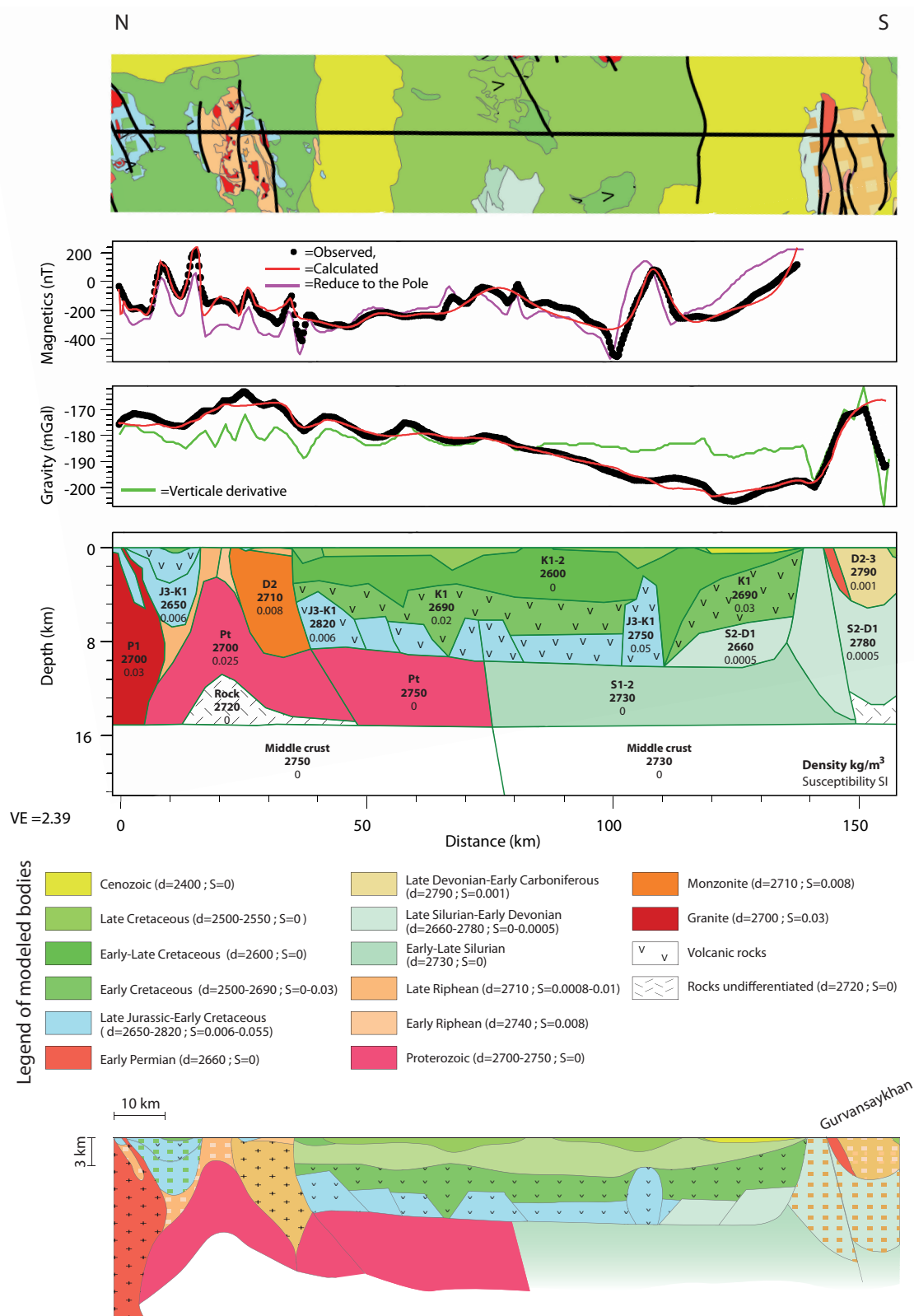


Figure 23: Gravity and magnetic potential field model along north of Gurvansaykhan profile. The surface geology is at the top. The upper panel shows observed (black circles), modelled (red solid line) and reduce to the pole (pink solid line) anomalies for magnetic field. The second panel shows observed (black circles), modelled (black solid line) and vertical derivative (green solid line) anomalies for gravity field. The third panel shows the potential field model with individual bodies colored by age of lithologies, with density (kg/m³) and magnetic susceptibility (SI) values. The last panel is the geological interpretative cross section for the north of Gurvansaykhan profile. The colors attributed to the geological bodies are according to the geological map legend.

6.2.2. Profiles between the Gurvansaykhan range and the Noyon Uul syncline

For this profile, the magnetic and gravity data were modelled dividing the profile into three segments crossing the main ranges of the region because the calculated magnetic anomalies are dependent on profile strike (Fig. 13). From north to south, the three profiles are named Gurvansaykhan range, Dzolen range and Noyon Uul syncline and surroundings, respectively. In addition, these profiles correspond to the structural cross section we present in chapter II. Therefore, we constructed the starting geometries of the geological bodies for each profile, based on the surface geology and the structural cross-sections, and then tried to evaluate the discrepancies in order to make the magnetic and gravity models fit as closely as possible in harmony with the geological structure of the area.

In the Gurvansaykhan range profile (Fig. 24), early Permian granite is modelled, which does not crop out along the profile, but it is supposed that is covered by a thin layer of Cretaceous sediments. A density of 2500 kg/m³ and a magnetic susceptibility of 0.0025 SI are attributed to this granitic body. We assume that the granite is the continuity of the early Permian granite located farther to the west of the profile. Its presence seems to be necessary to match the gravity and magnetic signatures. The mismatch at the southern end of the Gurvansaykhan range model is due to the calculated gravity that is higher than the observed one. We suggest, that the analysis of the Bouguer anomaly map seems to reveal a large error in the interpolated gravity values, most probably related to a gap in station spacing.

According to the geological map and field observations, the ultramafic bodies are located in late Silurian-early Devonian layers. The size and location of the deep-seated ultramafic rocks in the Gurvansaykhan (Fig. 24) and Dzolen ranges (Fig. 25) are determined by the steep gradients of magnetic highs combining with the limits of their outcrops. Sometimes the magnetic signal displays high but blurred amplitudes indicating that the sources of these anomalies are located in depth. Taking into account that these anomalies are localized above the late Silurian-early Devonian layers, we conclude that the most probable sources of these high amplitude magnetic anomalies are slivers of ultramafic rocks in depth. The magnetic ultramafic bodies (0.06-0.1 SI) have been assigned densities ranging from 2800 to 2900 kg/m³.

In the Noyon Uul syncline and its surrounding composed of early Permian to early Carboniferous volcanic rocks (Fig. 26), a dyke of highly magnetic and dense rock is required to fit the magnetic profile. However, the composition and origin of this dyke remain uncertain considering the geology of this region. Moreover, the model of the Noyon syncline does not provide accurate matches between the observed and calculated data for an area which provides

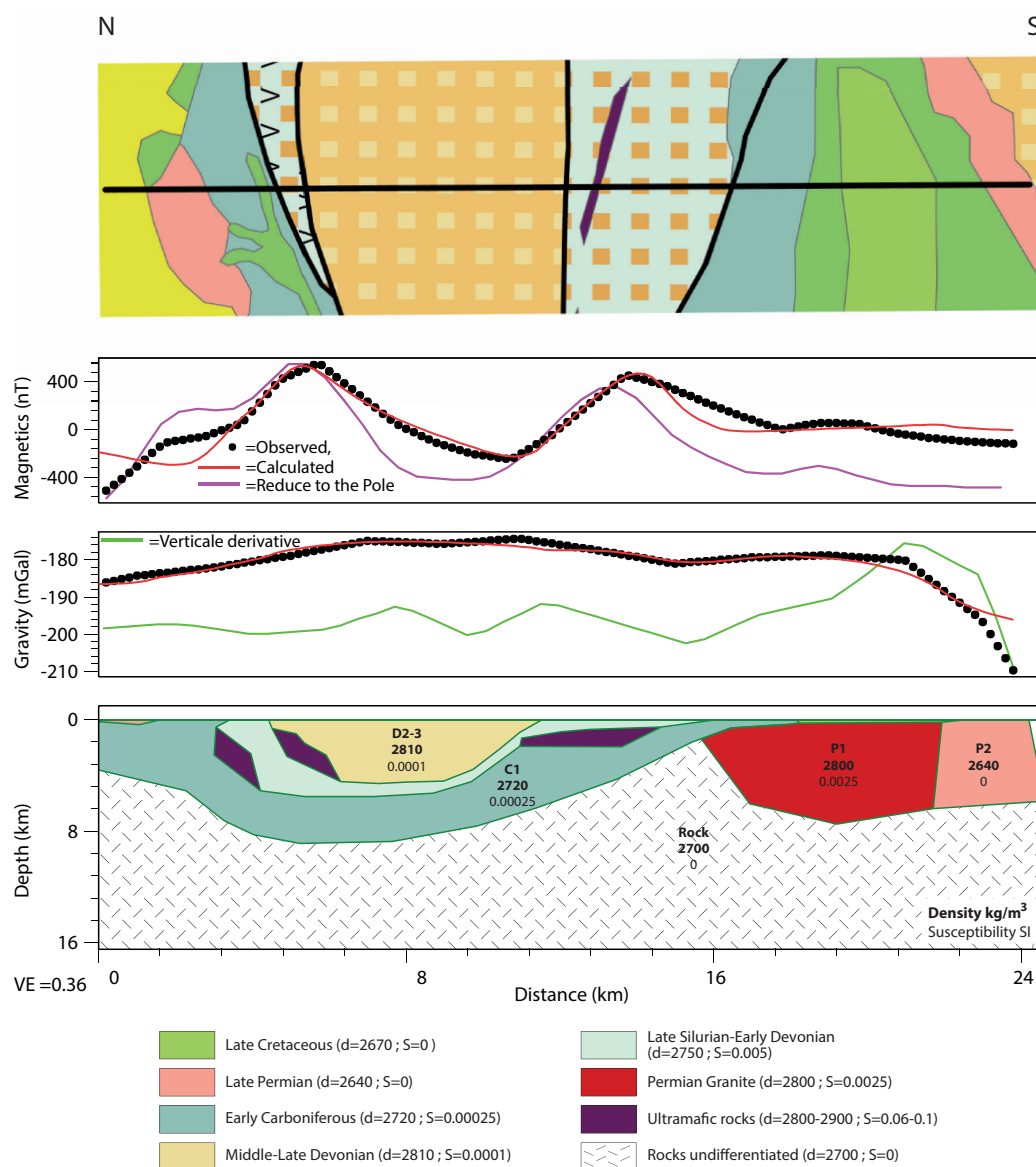


Figure 24: Gravity and magnetic potential field model along the Gurvansaykhan range. The surface geology is at the top. The upper panel shows observed (black circles), modelled (red solid line) and reduce to the pole (pink solid line) anomalies for magnetic field. The second panel shows observed (black circles), modelled (black solid line) and vertical derivative (green solid line) anomalies for gravity field. The third panel shows the potential field model with individual bodies colored by age of lithologies, with density (kg/m³) and magnetic susceptibility (SI) values.

excellent geological and structural constraints (Hendrix et al., 1996; Lamb and Badarch, 1997, 2001; Guy et al., submitted).

The alternation of anticline and syncline from the Gurvansaykhan range and the Noyon Uul syncline documented by structural geology is fairly confirmed by modelling. Consequently, a schematic geological interpretative section deduced from the modelling of the three small profiles (Fig. 27) can be elaborated.

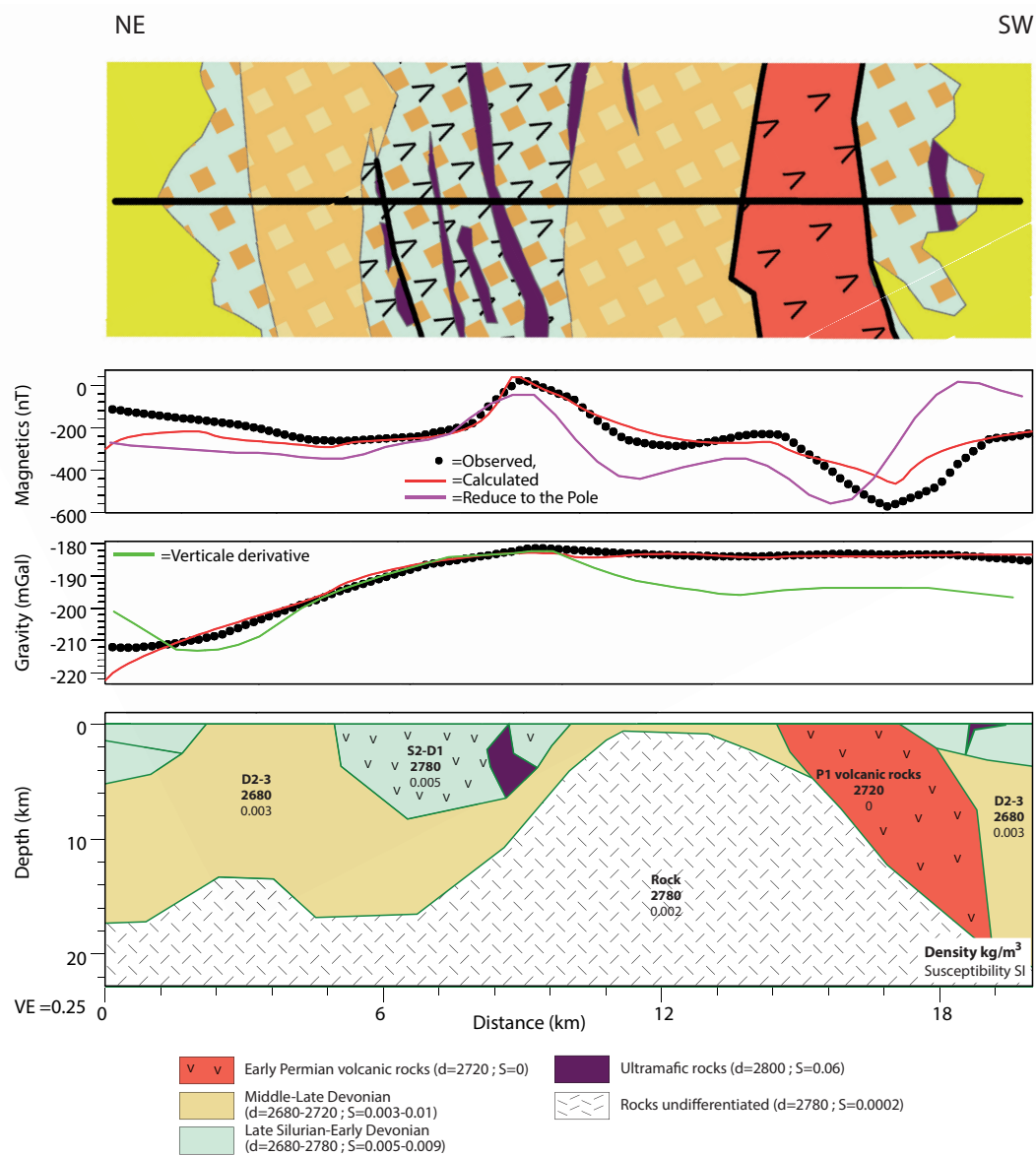


Figure 25: Gravity and magnetic potential field model along the Dzolen range. The surface geology is at the top. The upper panel shows observed (black circles), modelled (red solid line) and reduce to the pole (pink solid line) anomalies for magnetic field. The second panel shows observed (black circles), modelled (black solid line) and vertical derivative (green solid line) anomalies for gravity field. The third panel shows the potential field model with individual bodies colored by age of lithologies, with density (kg/m³) and magnetic susceptibility (SI) values.

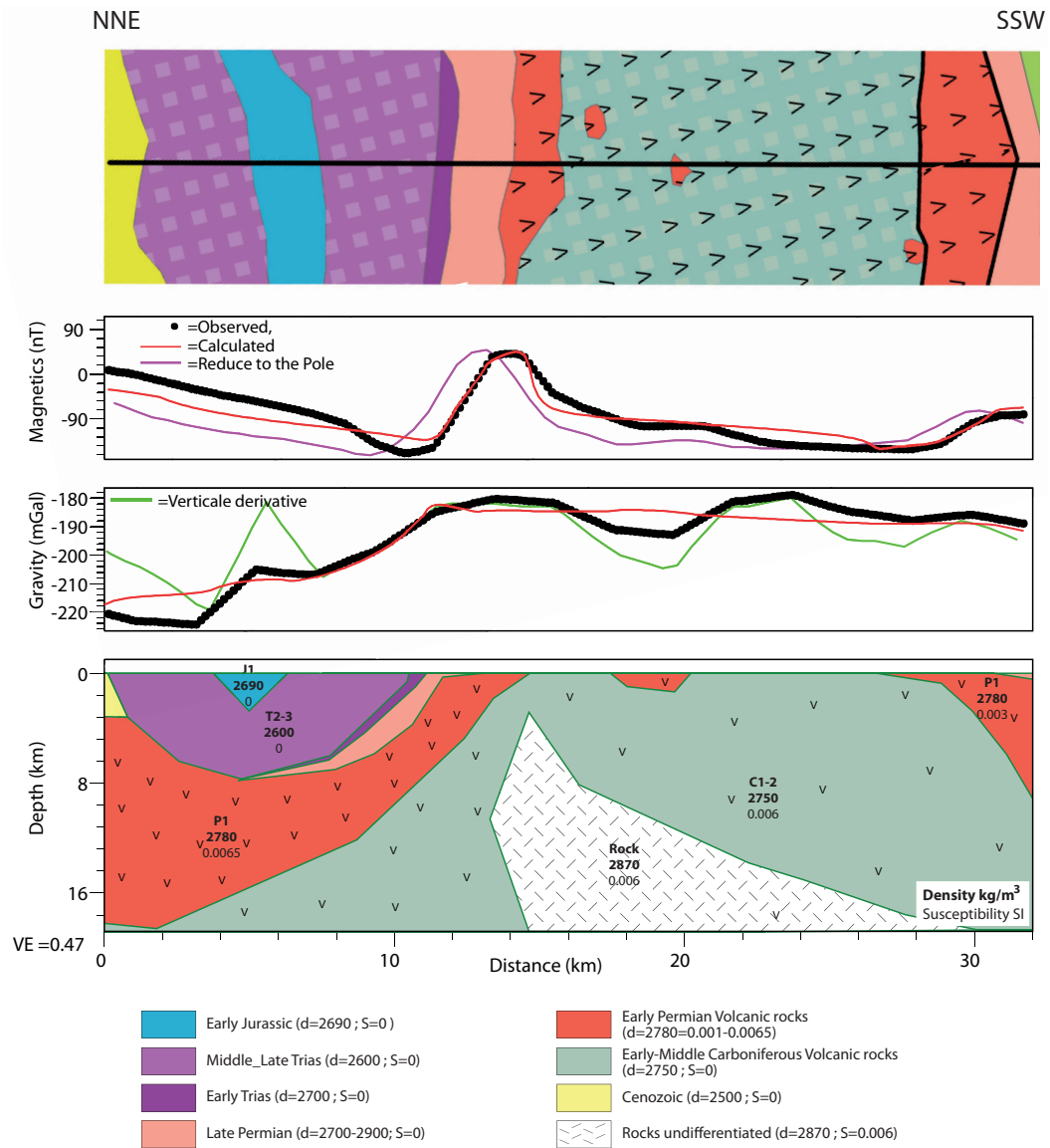


Figure 26: Gravity and magnetic potential field model along the Noyon Uul syncline and its surroundings. The surface geology is at the top. The upper panel shows observed (black circles), modelled (red solid line) and reduce to the pole (pink solid line) anomalies for magnetic field. The second panel shows observed (black circles), modelled (black solid line) and vertical derivative (green solid line) anomalies for gravity field. The third panel shows the potential field model with individual bodies colored by age of lithologies, with density (kg/m^3) and magnetic susceptibility (SI) values.

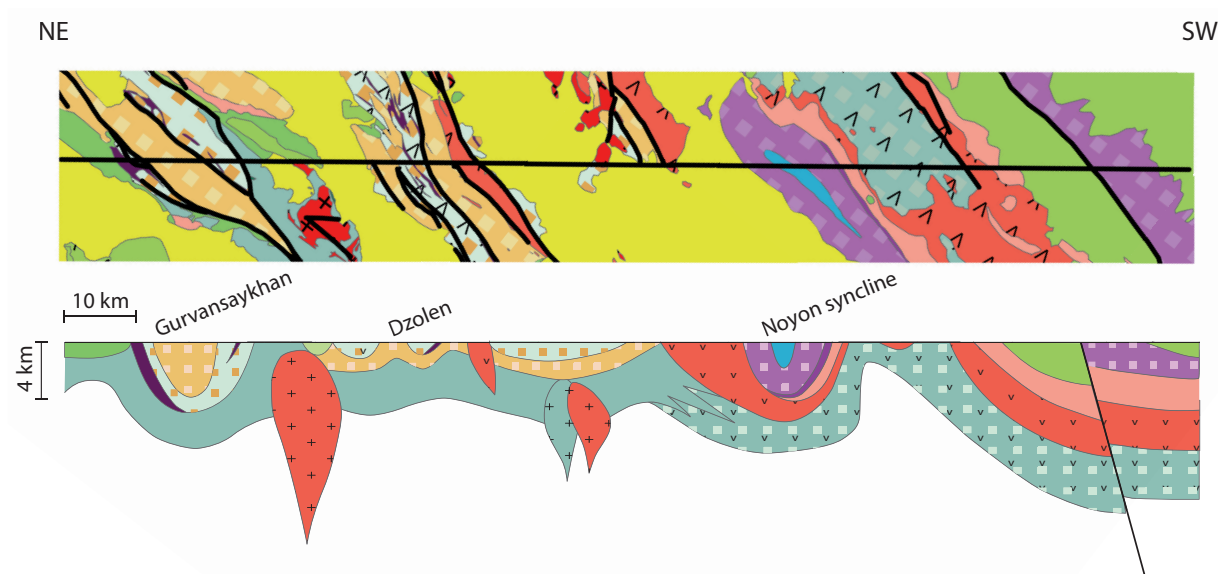


Figure 27: Geological interpretative cross section for the profile from Gurvansaykhan range to the Noyon area. The parts which have not been directly modelled are purely interpretative according to the geological surface. The colors attributed to the geological bodies are according to the geological map legend.

6.3. Profile south-east of Mongolia (Dornogovi Province)

This profile cross-cuts the East Gobi fault zone in its central part. It also crosses major Cretaceous basins often displaying high frequency and amplitude magnetic anomalies (Fig. 28). These are assumed to be partly due to the alternation of Palaeozoic horsts and grabens filled by Mesozoic sediments. The successions of geological layers in the different basins were deduced by the Carboniferous, Permian and Jurassic rock types which crop out in the region. Finally, the depths of the interfaces between the Jurassic-Cretaceous sediments and the Palaeozoic basement are evaluated combining the SPI, Euler deconvolution and analytic signal depth solutions with the seismic reflection profiles crossing the Unegt subbasin farther east of our profile. Therefore, the interfaces of the basement assuming to be the main magnetic sources are around 4-5 km depth in average.

Regarding the magnetic profile, the EGFZ displays a high amplitude magnetic anomaly peak, which also correlates with gravity high (Fig. 28). The model of these density and susceptibility contrasts requires a large Riphean granodiorite. This magnetic granodioritic body (0.006 SI) has been assigned a density of 2780 kg/m³.

The longer wavelength of the high magnetic anomaly over the Unegt subbasin indicates that the source of this anomaly is a deep-seated structure. We assume the composition and origin of the late Permian granite underneath the basin thanks to the observation of the surface geology several kilometers on either side of the corresponding profile where swarm of late Permian granites crop out. A density of 2730 kg/m³ and a magnetic susceptibility of 0.03 SI are

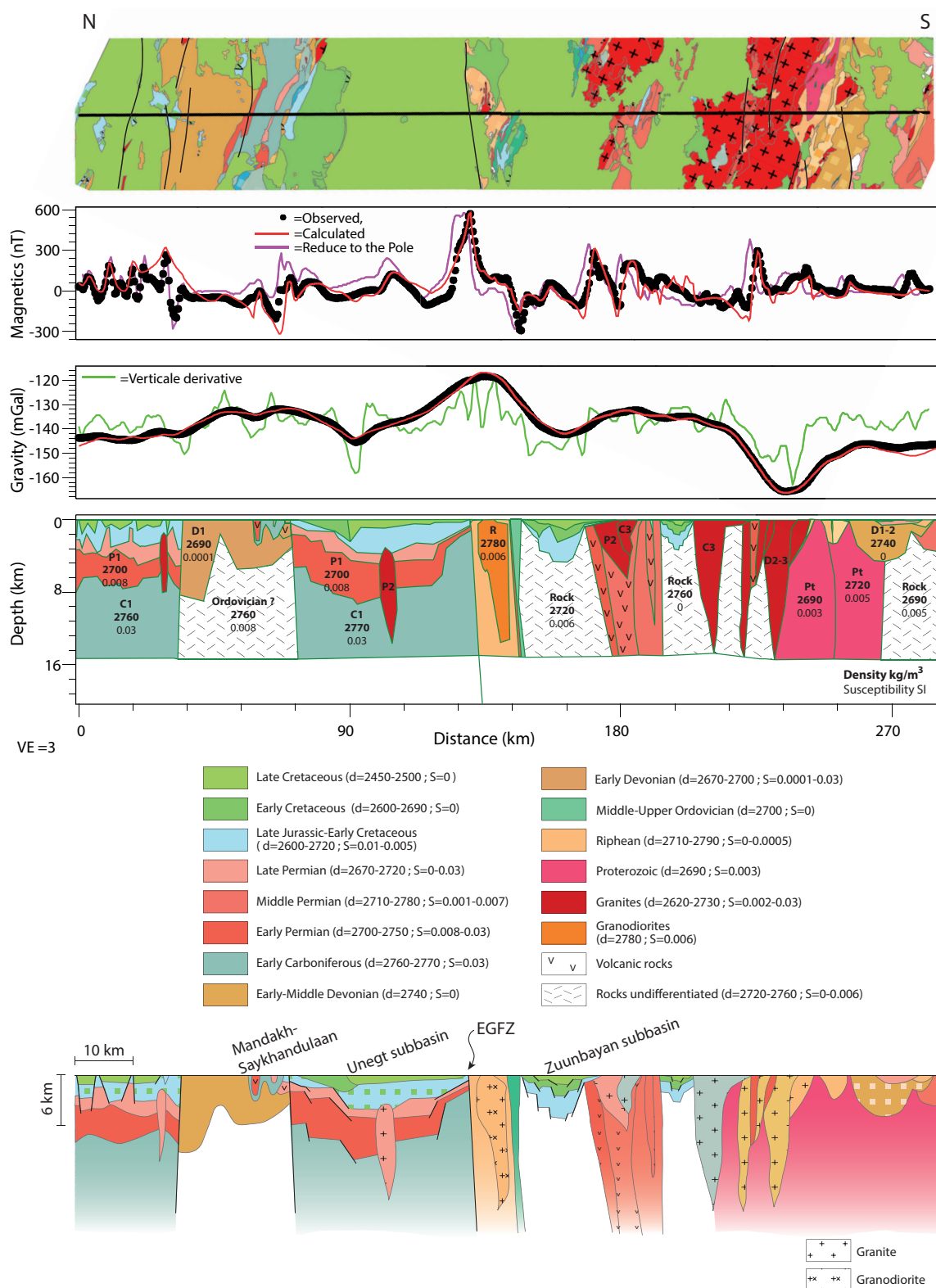


Figure 28: Gravity and magnetic potential field model along the SE profile. The surface geology is at the top. The upper panel shows observed (black circles), modelled (red solid line) and reduce to the pole (pink solid line) anomalies for magnetic field. The second panel shows observed (black circles), modelled (black solid line) and vertical derivative (green solid line) anomalies for gravity field. The third panel shows the potential field model with individual bodies colored by age of lithologies, with density (kg/m³) and magnetic susceptibility (SI) values. The last panel is the geological interpretative cross section for the SE profile. The colors attributed to the geological bodies are according to the geological map legend.

required to fit both the gravity and magnetic profiles. In contrary to the low density (2620 kg/m^3) and the low magnetic susceptibility (0.006 SI) are attributed to the middle Devonian granite which is assumed to be the source of gravity low in the south of the profile.

The modelled gravity profile has a good fit with the observed profile but the modelled magnetic signals should be improved by further field investigations as there are several areas where it does not accurately fit the observed profile (Fig. 28). For example, to the north of the profile, the high frequency and amplitude magnetic signals with strong gradients indicate that the sources of these anomalies reach the surface. However, the same area displays Cretaceous sedimentary basin where late Jurassic-early Cretaceous sedimentary and volcanic rocks sometimes crop out. That is why we assume that these high frequency and amplitude anomalies are due to the alternation of horsts and grabens of volcanic origins and fill in by the Cretaceous sedimentary rocks. However, this hypothesis does not allow to fit accurately the observed magnetic profile.

The geological interpretative section shows the envisaged structures in the area of the EGFZ and envisages the presence of Permian granitoids intruding the Cretaceous basins in south east of Mongolia (Fig. 28).

Conclusion

Actually, among the four profiles located over southern Mongolia, in the three western profiles slight changes of the signal trends are observed, which may be related to the presence of lithotectonic zones. However, the location of the changes of signal trends does not really correspond to the lithotectonic boundaries defined by the surface geology. On the other hand the changes of signal trends can not be observed for the south-east profile area. Taking into account that the major difference between the three western profiles and the south-east profile is the important EGFZ fault zone, we assume that it may disturb the magnetic signal. However, we cannot confirm as whether it is the Cretaceous extension which affects the entire magnetic signal in the area east of the EGFZ.

We used gravity and magnetic data to characterize the crustal structure of the southern Mongolia orogenic crust. Although the modelling of gravity and magnetic data are non-unique (moreover when the seismic constraints are missing), these gravity and magnetic models can provide relevant preliminary ideas on the crustal structures and its evolution, using available magnetic susceptibility measurements, reasonable density values, geologically realistic shapes

and a good fit of observed data.

These preliminary results seem to confirm the absence of sutures between the areas which display different lithologies. However, only deep seismic data would considerably increase the quality of structural interpretations of the southern Mongolia orogenic crust and provide new ideas on the geometry, the character of basement and the architecture of Cretaceous and Cenozoic basins.

Chapter V:

Geophysical model of the Variscan orogenic root (Bohemian Massif): implications for modern collisional orogens

Chapter V:

Modelling of the Bohemian Massif: THE good example Geophysical model of the Variscan orogenic root (Bohemian Massif): implications for modern collisional orogens

The Bohemian Massif is the eastern part of the European Variscan orogeny. Here, the Variscan crust is represented by a collage of the Gondwana continent (Avalonia and Armorica terrane assemblage) with Laurussia (Matte, 1991; Franke, 2000) in Paleozoic times. The Bohemian Massif has been well studied from point of view of detailed geological mapping and geophysical surveys. Therefore, the geological and geophysical data, their interpretations and thus the geodynamical models constitute a realistically constrained frame for the modelling purposes.

Introduction

The composition and structure of crustal layers forming thick orogenic roots in collisional orogens remain a matter of discussion thanks to complexity of geophysical data and derived geodynamical models (Rudnick, 1995, Rudnick and Fountain, 1995). Based on the geodynamic context and reflection seismic results, two different types of hot modern orogens are distinguished: (1) the Andean type, where oceanic crust subducts beneath a continental lithosphere. This process creates a Franciscan type accretionary wedge, a magmatic arc established on the continental crust and a large continental plateau; (2) the Tibetan type where continental crust underthrusts another continent following an oceanic subduction stage. This orogen also creates a thick continental plateau and complex metamorphic structures in front of the continental accretionary wedge. These two fundamentally different processes allow explanation of the structure of 300 km of orogen adjacent to the suture but fail to explain the orogenic fabric in more distal parts of a thick orogenic root underneath the plateau.

In the central Andes, the ANCORP'96 seismic reflection profile shows strong reflectors called "bright spots" located at 15-30 km depth underneath the surface of Altiplano which coincide with a low velocity zone of 5.9 km/s to 6.1 km/s in seismic refraction profiles (Patzwahl et al. 1999) and a zone of low resistivity located at mid-crustal depths (Oncken et al., 2003, Schilling and Partsch, 2001). The Andes are also marked by an exceptionally high negative

Bouguer anomaly underneath the plateau (~ -300 to -5 mGal) and high heat flow (~ 100 – 125 mW/m²) along the ANCORP section (Oncken et al., 2006). All these data indicate that the Altiplano middle crust coincides with a partially molten dominantly felsic zone with up to 30% distributed melt (Schilling and Partsch, 2001). This means that the important heat flow in the Andes is not associated with underplating of the root by basaltic magmas as is suggested for a range of other orogens (Götze and Kirschner, 1997; Springer, 1999).

The Tibetan Plateau shows similar geophysical features such as bright spots in reflection seismics (Nelson et al., 1996) and a low velocity and resistivity zone at mid crustal depths (Makovsky and Klemperer, 1999). Gravity surveys of the Himalaya-Tibet orogen show a large scale negative Bouguer anomaly of less than -500 mGal and elevated heat flow reaching, locally, 150 mW/m² (Hu et al., 2000). These features indicate that a partially molten mid-crustal layer similar to that proposed for the Andes also exists beneath the southern Tibetan plateau (Schilling and Partsch, 2001). However, there is no detailed study that shows the relation between the partially molten mid-crustal layer and the composition of rocks located at the bottom of the root, i.e. close to Moho depth. Some studies have suggested that the orogenic lower crustal material has to be felsic to intermediate in composition due to the high gravity potential of rocks underneath the Tibetan plateau (e.g. Le Pichon et al., 1997). In order to solve the problem of exceptionally low density felsic crust at depths of 60 km, Chemenda et al. (2000) proposed a model of underthrusting of Indian continental crust underneath the Tibetan crust, thereby replacing lithospheric mantle with felsic buoyant lower crust. By contrast, for the Andes the problem is solved by the injection of felsic lower crust from the Brazilian shield region (Lamb et al., 1997) into the central parts of the orogen. However, in general, the origin of negative gravity anomalies, the composition of orogenic lower crust and its connection to a partially molten zone at the mid-crustal depths remains unresolved.

The Bohemian Massif represents a deeply eroded section of a large high-T orogen allowing observation of the structure of fossil orogenic root similar to the Tibetan or the Altiplano plateau (Dörr and Zulauf, 2010). In the current outcrops K-feldspar-kyanite bearing granulite massifs ($18 - 20$ kbar/ $800 - 1000^\circ\text{C}$) are common, associated with felsic migmatites of Carboniferous age (O'Brien, 2008; Štípská and Powell, 2005). These HP-HT units are surrounded by middle crustal rocks represented by metagreywackes, amphibolites and subordinate metapelites ($8 - 10$ kbar, 650°C). Locally, these supra-crustal rocks are well preserved being separated from adjacent middle and lower crustal material by crustal scale normal faults (Pitra et al., 1994; Zulauf et al., 2002a, Dörr and Zulauf, 2010). In order to explain the exhumation of Saxonian HP granulites Weber & Behr (1983) proposed a model

of ‘diapiric folding’. In their model the deep granulitic layer tends to amplify and pierce through the weaker middle crust during crustal shortening, to form a large-scale steep fold bringing HP rocks to middle crustal levels. In contrast, several authors have proposed that the HP granulites and associated migmatites were exhumed to supra-crustal depths in the form of “diapiric” extrusions from the depth of the Moho (Štípská et al., 2004; Schulmann et al., 2005; Franěk et al., 2006). Indeed, based on numerical modelling, Gerya et al., (2001) showed that the exhumation of granulites and other felsic lower crustal rocks occur during gravitational redistribution processes. Therefore, it is explicitly inferred that the orogenic lower crust was felsic during Carboniferous times, forming an allochthonous body underneath the Variscan crust (Behr, 1978, 1984; Weber, 1984). Following these postulates two questions arise: where do the felsic granulites come from and; is there any correlation between the felsic granulites at the surface and the deep crustal source?

A detailed network of gravimetric data from the Bohemian Massif (Polanský and Škvor, 1975; Ibrmajer, 1981; Plaumann, 1983, 1987) shows an important negative gravimetric anomaly corresponding to the Moldanubian Zone, which is interpreted as a fossil Carboniferous orogenic root (Schulmann et al., 2009). In addition, seismic reflection and refraction studies show unexpectedly inhomogeneous lower crust with low P-wave velocities in this area. In this paper, we interpret the gravimetric data in the light of seismic sections and geological observations. An attempt is made to explain these data in terms of existence of a felsic lower crustal layer which underplated standard mafic lower crust by tectonic process. We propose a connection between this residual felsic lower crust and HP felsic granulite bodies at the surface via a gravity redistribution process which operated during the Carboniferous. Finally, it is proposed that the geophysical structure of the Moldanubian crust can provide a key insight into interpretation of modern collisional orogens such as Tibet and Andes.

1. Geology of the Bohemian Massif

The Bohemian Massif is a large Palaeozoic belt located at the eastern termination of the Variscan belt. It is generally divided into four major tectonic domains (Suess, 1926; Kossmat, 1927): the Saxothuringian, the Teplá-Barrandian, the Moldanubian and the microcontinent Bruno-Vistulian (Fig. 1). The geology of the Bohemian Massif is briefly characterized as follows:

(1) The Saxothuringian domain (Fig. 1) contains Neoproterozoic para-autochthonous rocks (~580-550 Ma) and allochthonous Late Ordovician to Devonian distal and proximal margin

sequences (Franke, 2000) containing relics of MORB-type Ordovician metabasites eclogitized during the Devonian (~395 Ma; Schmädicke et al., 1995). Later Carboniferous underthrusting of the Saxothuringian continental rocks underneath the Teplá-Barrandian domain to the east was responsible for the eclogitization of continental crust (Massonne, 2006) at ~340 Ma associated with the exhumation of deeply buried rocks in form of crustal scale nappes (Konopásek and Schulmann, 2005).

(2) The boundary between the Saxothuringian – Teplá-Barrandian is characterized by a relic Devonian oceanic suture which is well preserved in the Mariánské Lázně Complex (Kastl and Tonika, 1984, Zulauf, 1997). This complex is represented by serpentinites, amphibolites, eclogites and metagabbros of Cambrian (~540 Ma; Timmermann et al. 2004) and Ordovician (~496 Ma; Bowes and Aftalion, 1991) protolith ages metamorphosed at eclogites facies conditions during Devonian (410 and 370 Ma; Beard et al., 1995; Dallmeyer and Urban, 1998). The western boundary of the oceanic suture is marked by the presence of felsic granulites of the Egger graben (Zulauf et al., 2002b).

(3) The Teplá-Barrandian domain (Fig. 1) consists of Neoproterozoic arc-related volcano-sedimentary rocks overlain by siliceous black shales and a flyshoid sequence. The Neoproterozoic basement is unconformably overlain by Lower Cambrian clastic sediments, Upper Cambrian volcanic and sediments of the Lower Palaeozoic (Ordovician to Middle Devonian) Prague Basin (Havlíček, 1981). The whole sequence is folded by steep folds presumably of Late Devonian age (Zulauf, 2001).

(4) The Central Bohemian Plutonic Complex occurs on the boundary between the Teplá-Barrandian and the Moldanubian domains. It consists of Late Devonian (~354Ma) calc-alkaline tonalites, granodiorites, trondhjemites, quartz diorites and gabbros in the west (Janoušek et al. 2004) and Early Carboniferous (~349–346 Ma, Holub et al. 1997) high-K calc-alkaline plutonic bodies in the southeast.

(5) The Moldanubian zone (Fig. 1) consists of three major tectonostratigraphic units (Fuchs, 1976): the structurally deepest “Monotonous Group” composed of Proterozoic metasediments and numerous Late Proterozoic to Early Palaeozoic orthogneisses (e.g. Friedl et al., 2004), quartzites and amphibolites. Structurally above is the “Varied Group” composed of plagioclase-bearing paragneiss quartzites and marbles intercalated with amphibolites and leptynites. The protoliths of the varied metasediments are inferred to be Early Palaeozoic in age (Friedl et al., 1993; Janoušek et al., 2008). Both the Monotonous and Varied groups are metamorphosed under amphibolite facies conditions (8-10 kbar, 650–700 °C; Petrakakis, 1997;

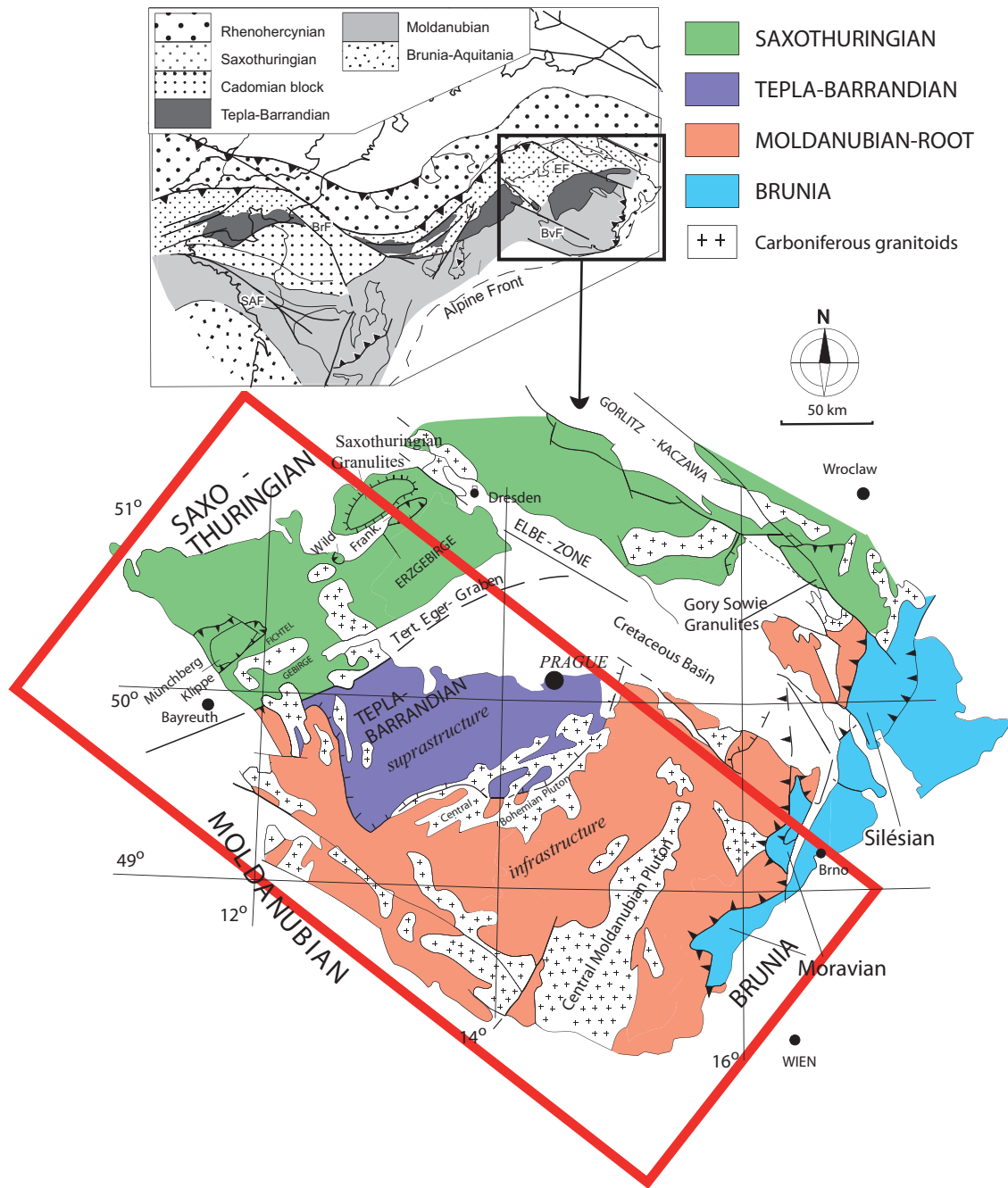


Figure 1: Simplified geological map of the Bohemian Massif (modified after Franke et al., 2000) with the main tectonic domains displayed. The upper inset shows location of the Bohemian Massif in the frame of the European Variscides (SAF: South Armoricain Front; BrF: Brie Fault; BvF: Bavarian Fault; EF: Elbe Fault; modified after Edel and Weber, (1995)). The red rectangle delimits the zone of the gravimetric modelling.

Racek et al., 2006). The structurally highest “Gföhl Unit” is composed of orthogneiss with Ordovician protolith ages (Friedl et al., 2004), amphibolitized eclogites, granulites, garnet- and spinel-bearing peridotites surrounded by felsic migmatites. Carboniferous (~350 – 340 Ma) metamorphism of the Gföhl unit is characterized by early eclogite facies (~20 kbar, 750 °C; Medaris et al., 1995) followed with granulite-facies re-equilibration (O’Brien and Vrana, 1995) and retrogression under amphibolite-facies conditions (Štípská and Powell, 2005b).

Based on existing pressure-temperature estimates, two NW-SE trending belts of high-pressure rocks (granulites, eclogites and peridotites) are distinguished, one located close to the Teplá-Barrandian – Moldanubian boundary (Finger et al., 2007) and the other rimming the eastern margin of the Bohemian Massif (Schulmann et al., 2008). These belts alternate with medium-pressure units represented by the Varied and Monotonous groups, which also form wide NW-SE trending belts. The deformation history in the Moldanubian domain reveals early (~350–340 Ma) vertical NNE-SSW trending fabrics, associated with crystallization of high-pressure mineral assemblages (Franěk et al., 2006; Tajčmanová et al., 2006). These are reworked by flat lying deformation fabrics (~335–325 Ma) that are associated with medium- to low-pressure and high-temperature mineral assemblages (e.g. Hasalová et al., 2008; Štípská et al., 2008). The Moldanubian metamorphic units were intruded by numerous and voluminous anatectic plutons loosely grouped into the Moldanubian (or South Bohemian) Plutonic Complex. These are mostly felsic–intermediate, two-mica granitic to granodioritic intrusions emplaced at 331–323 Ma (Gerdes et al., 2003).

(6) The Moldanubian – Bruno-Vistulian continental transition zone is represented by a zone of intense deformation and Barrovian style inverted metamorphism of continental Bruno-Vistulian derived rocks of the Moravo-Silesian Zone (Suess, 1926). The Moravo-Silesian Zone itself is characterized by two nappes composed of orthogneiss derived from Bruno-Vistulian at the bottom and a metapelite sequence at the top. The prograde metamorphism of the Moravian nappes is interpreted as a result of continental underthrusting and occurred at 340–325 Ma (Dallmeyer et al., 1992; Fritz et al., 1996).

(7) The Bruno-Vistulian basement domain (Fig. 1) of Dudek (1980) contains a 680 Ma old intermediate to mafic crust, intruded by 550 Ma old granites (Finger et al., 2000). This basement is unconformably overlain by shallow marine Lower Devonian quartzites and conglomerates followed by Givetian carbonate platform sediments (Kalvoda et al., 2008). From 345 till 300 Ma, a 7.5 km thick Variscan flysch (Culm facies) was deposited onto the Bruno-Vistulian foreland (Hartley and Otava, 2001).

2. Gravimetric data and the Bouguer anomaly map

The gravimetric data sets were compiled by the Czech Geological Survey and the Leibniz Institut für Angewandte Geophysik (LIAG) using previous surveys by Polanský and Škvor (1975), Ibrmajer (1981), Plaumann (1983, 1987). The resulting map is based on the average density measurements from 4–6 gravimetric stations per km². The geographic reference

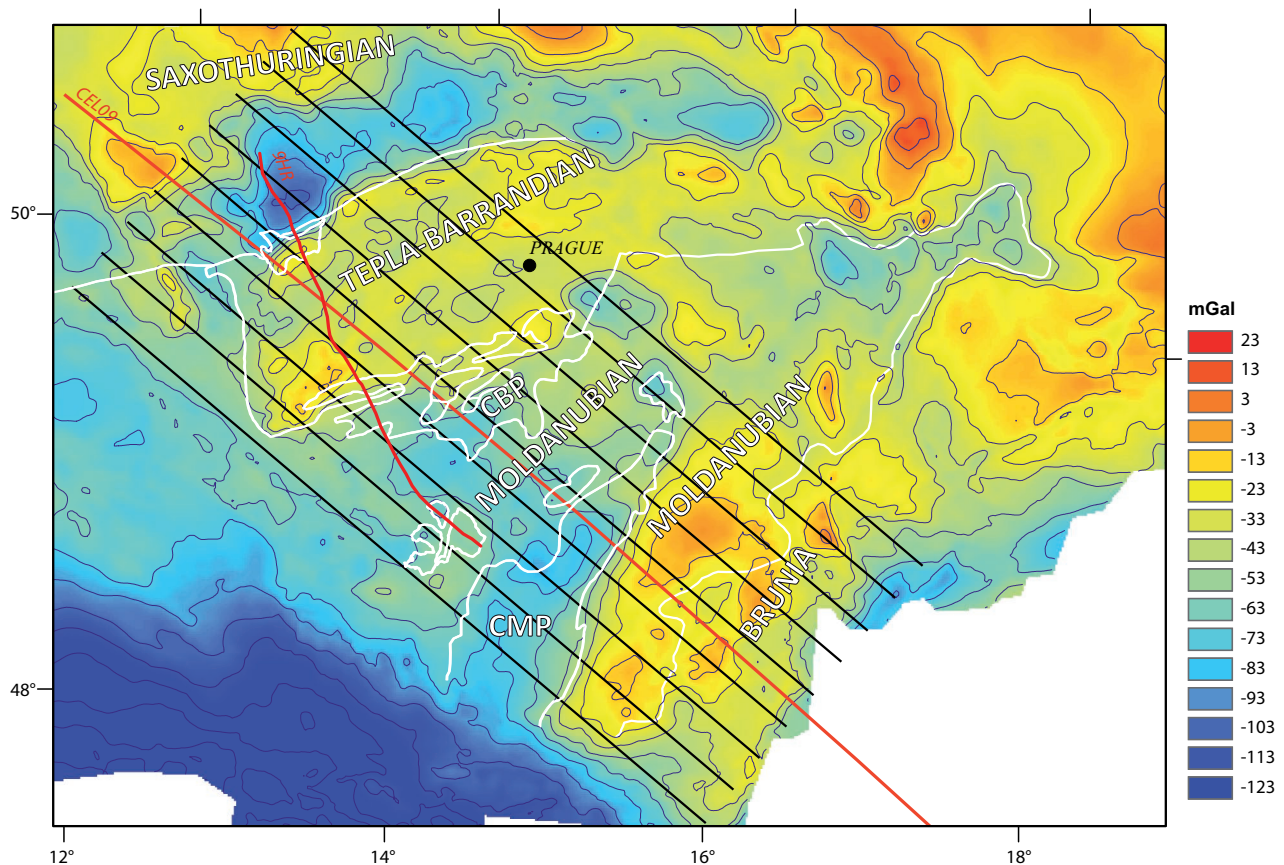


Figure 2: Bouguer anomaly map. Main lithological boundaries are represented by white lines. The nine profiles (black lines) of the gravity model cover the SW part of the Bohemian Massif (see Fig. 1). Red lines represent the seismic profiles CEL09 and 9HR. Profiles are discussed in Fig. 5 from SW to NE. CBP: Central Bohemian Pluton; CMP: Central Moldanubian Pluton. White zones in the south indicate a lack of data.

of the stations is the UTM coordinate system and the gravity is referred to the IGSN71 system (International Gravity Standardization Net 1971). The Bouguer anomaly map was obtained using a rock density of 2.67 g/cm^3 for corrections.

The Bouguer anomalies range from -123 mGal to 23 mGal (Fig. 2) and four principal SW-NE trending anomalies were identified in the Bohemian Massif: (1) In the north-west, a gravity low is associated with low density rocks identified at the surface as late Carboniferous granitic plutons and Proterozoic metagranites. This domain corresponds to the SE part of the Saxothuringian zone. (2) In the middle, the gravity high is associated with high to medium density, weakly metamorphosed Late Proterozoic and Early Palaeozoic volcanic and sedimentary rocks of the Teplá-Barrandian domain (Fig. 2). This gravity high is rimmed by a narrow belt of higher positive anomalies and high density rocks in the NW, which correspond to high pressure metabasites and ultra-mafic rocks of the Mariánské Lázně Complex. (3) South and Southeast of the Teplá-Barrandian basement, a gravity low is associated with low to medium density rocks, mainly composed of granites and high grade gneisses characteristic of the Moldanubian domain (Fig. 2); (4) Further South-East a large gravity high occurs and can be correlated with high

density rocks of the Pan-African Bruno-Vistulian basement (Dudek, 1980). The western part of the gravity high is marked by presence of migmatites and granulite facies rocks at the surface which led Schulmann et al., (2008) to propose that these Moldanubian rocks cover the high density Bruno-Vistulian basement in form of a thin nappe. The strong gravity gradient located 50 to 70 km west of the geological Moldanubian-Bruno-Vistulian boundary is interpreted as a deep crustal boundary between the Carboniferous orogenic root and Bruno-Vistulian basement promontory (Schulmann et al., 2008).

In order to image the deep structure of the Bohemian Massif, a 3D gravity model was computed. Nine, ~400 km long and 20 km spaced profiles were drawn perpendicular to the NE-SW striking gravity gradients. These lines are sub-parallel to the seismic 9HR and CEL09 profiles, which were used to constrain gravity modelling (Fig. 2). The objective of this work is to estimate the spatial distribution of major tectonic contacts and volumes of the continental crust at depth. Therefore the model is limited to a maximum depth of 45 km and the 20 km spacing between profiles exclude modelling of small anomalies.

3. Gravity modelling: constraints and methodology

The gravity modelling is constrained by a surface geological map at 1:500 000 scale (Cháb et al., 2008), density measurements (Hroudá and Chlupáčová, 1993; Chlupáčová and Švancara., 1994), reflection and refraction seismic sections (Tomek et al., 1997; Růžek et al., 2007). Due to the fact that the detailed description of 9HR seismic line is discussed elsewhere (Tomek et al., 1997, Tomek 2007), we report only major geometrical features depicted from this profile here.

3.1. Seismic constraints

The seismic reflection profile 9HR (Tomek et al., 1997) is located in the south-western part of the Bohemian Massif (Fig. 2). About 200 km long and NW-SE striking, the line starts at the southern part of the Saxothuringian domain, and crosses successively the Teplá-Barrandian domain, the Central Bohemian Pluton (CBP), high grade gneisses, migmatites and granulites of the Moldanubian domain and terminates before reaching the Central Moldanubian Pluton (CMP) (Fig. 2). The orientation of the profile differs by about 25° from the orientation of the gravity profiles which were drawn perpendicular to the mean strike of principal geological boundaries. In order to constrain the gravity modelling, we use a line drawing of a time-migrated section. Consequently, the starting model was established using the seismic line where the shape and dip

of units can be approximated by major reflective boundaries.

Two belts of southeast dipping reflectors underneath the Teplá-Barrandian domain form dominant features of the seismic section. The upper reflector crosscuts the surface in the area of the Mariánské Lázně Complex and coincides with the Devonian Teplá suture zone. The lower belt of reflectors can be followed towards northwest beneath the weakly reflective uppermost crust that consists of granites (Karlsbad and Nejdek–Eibenstock granites) and metamorphic rocks of the southern Saxothuringian domain. These reflectors correspond to Carboniferous eclogitic units that are interpreted as a trace of the Carboniferous Saxothuringian suture (Konopásek and Schulmann, 2005). Another belt of southeast-dipping reflectors has been identified in the deep crust of the northern Moldanubian domain (Fig. 3). The Teplá-Barrandian as well as the northern and central Moldanubian upper crusts are characterized by bending of highly reflective horizons with a mean wavelength of 30 km. In contrast, the southernmost part of the section, where outcrop the Moldanubian granulites are exposed, is weakly reflective.

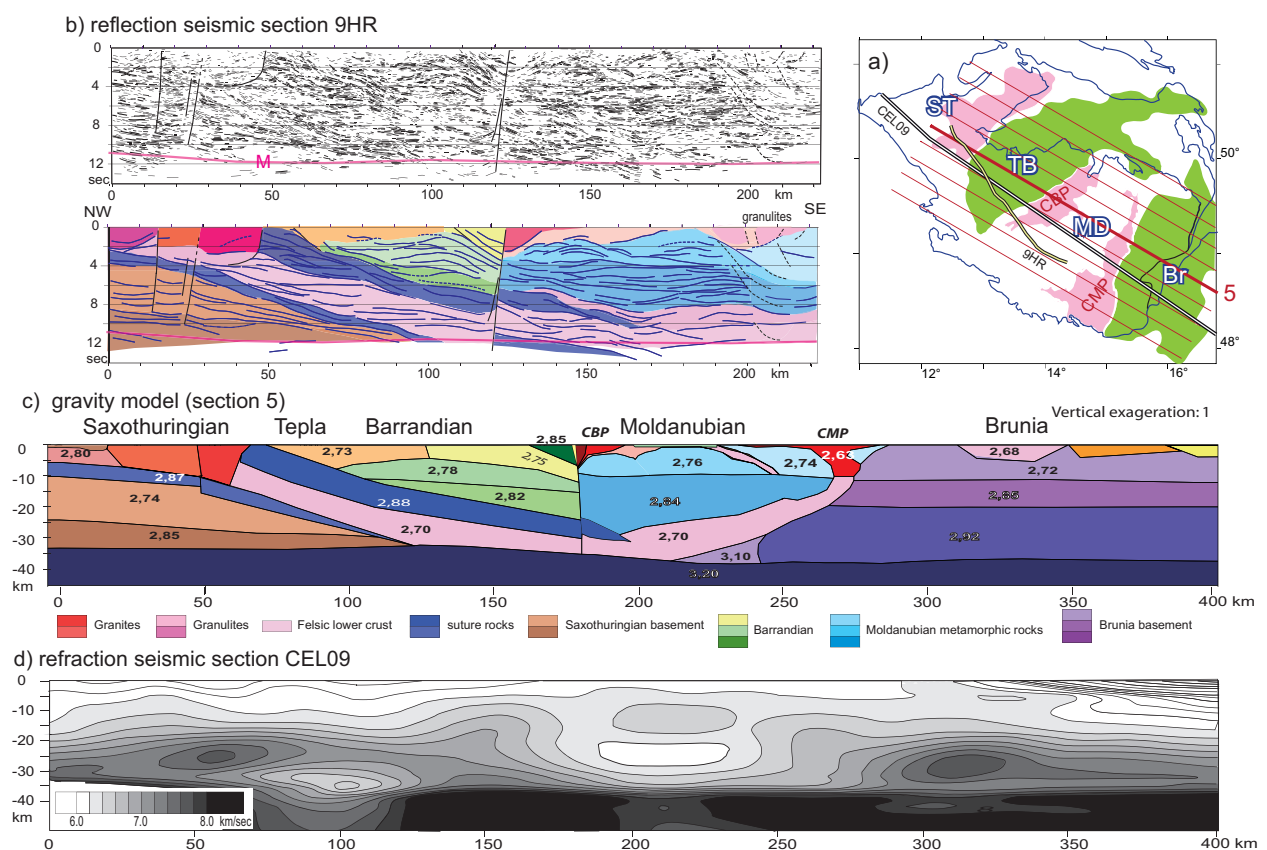


Figure 3: Comparison of the gravity model with the CEL09 seismic refraction section and the 9HR seismic reflection section. (a) Location of the nine gravimetric modelling profiles and the seismic reflection and refraction profiles. (b) Interpretation of the time migrated 9HR seismic reflection section (modified after Tomek, unpublished report), the vertical scale is in seconds. (c) Section 5 of the gravity model. (d) P-wave velocities are derived from the CEL 09 refraction section (Růžek et al., 2007), the vertical scale is in km.

Two major subvertical discontinuities bound the Teplá-Barrandian domain. In the north, the strong reflections of the Devonian suture contrast with the nearly transparent, mostly granitic Saxothuringian upper crust. In the south, the Teplá-Barrandian/Moldanubian boundary is marked by the oppositely dipping reflectors of the Teplá-Barrandian and Moldanubian domains. The reflectors bound the Central Bohemian Pluton. The fault zone, that marks the Teplá-Barrandian/Moldanubian boundary, appears to shift the highly reflective Teplá-Barrandian domain upwards by 6-7 km (Fig. 3b). This contrasts with field observations, which show a predominantly strike slip component (Scheuven and Zulauf, 2000). In the whole section but particularly in the Moldanubian part, the middle crust is characterized by subhorizontal horizons.

The 700 km long refraction section CEL09 runs nearly parallel to the gravity sections (Hrubcová et al., 2005, 2009). However, in this study we consider only the part of the reinterpreted section (Růžek et al., 2007) which coincides with the gravity sections 4 and 5 in Figs 2 and 5. The most striking feature of the P-wave velocity section is the low velocity of the lower crust of the Moldanubian domain and, to a lesser extent, of the deep crust underneath northern Teplá-Barrandian (Fig. 3). In contrast, the Saxothuringian and Bruno-Vistulian lower crust show conventional velocities in the range 7-7.5 km/s. The Moho topography shows a gentle dip towards SE from 35 to 37 km, with a slight minimum located under the Teplá-Barrandian-Moldanubian boundary (Figs 3d, 4a). Comparison of the Moho topography derived from seismic sections with the Bouguer anomalies shows a positive correlation between the gravity low and the thickened Moldanubian crust (Fig. 4). This is not valid for the Teplá-Barrandian and Bruno-Vistulian which are also characterized by a thick crust but which show gravity highs of large wavelengths. This means that the large anomalies are mainly due to density contrasts within the continental crust and not to crustal thickness variations.

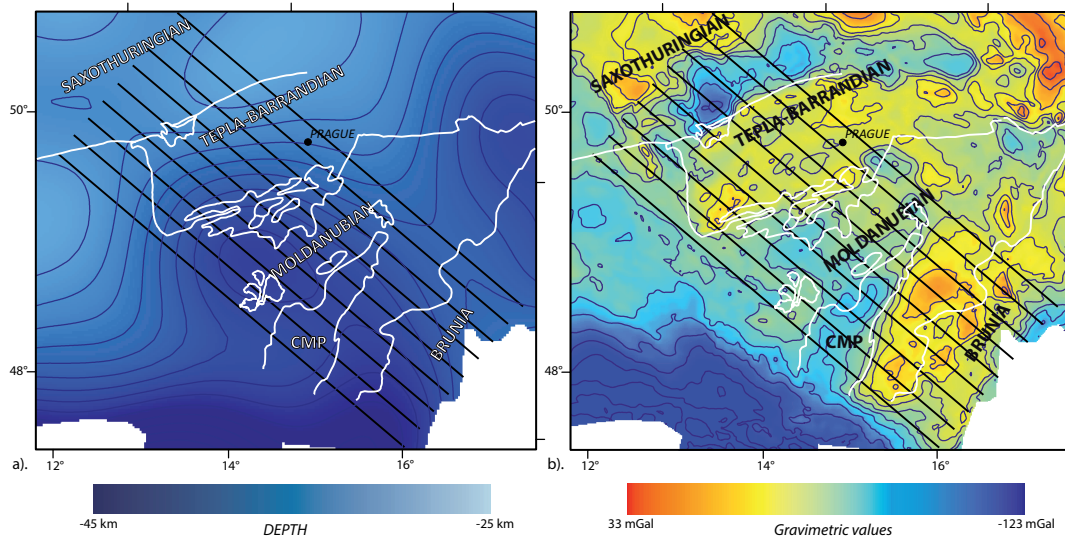


Figure 4: (a) Map of the Moho depth and (b) map of the Bouguer anomalies with contours (in white) of the main geological units.

3.2. Density constraints

In general, the density measurements on granites at the surface can be extrapolated at depth for large homogeneous bodies with a moderate error. This is impossible for lithologically heterogeneous metamorphic units because rocks of markedly different density can coexist within the same unit. For instance, it is particularly difficult to attribute a mean density to the association of banded felsic gneisses and amphibolites which are of different density. Therefore, the constraints on the densities for deep, large bodies of highly metamorphosed layered units are often poor and, seismic velocities and the geological conceptual models have to be taken into account.

The density assignments consider measurements from previous work (Table 1): Ondra and Hanák (1984), Chlupáčová and Švancara (1994). According to Ondra and Hanák (1984) the granitic rocks of the Moldanubian domain show densities in the range 2.63 to 2.70 g.cm⁻³. For paragneiss and Mg-K syenites the densities are higher, between 2.70 and 2.80 g.cm⁻³. A density of 2.66 g.cm⁻³ is attributed to the granulite rocks cropping out in the southern Moldanubian domain (Franěk, 2007). Concerning the Teplá-Barrandian and Saxothuringian domains, results of Hrouda et al. (1993) are used. The densities range from 2.62 g.cm⁻³ for granitoids and 2.88 g.cm⁻³ for metabasites of the Mariánské Lázně Complex. Density values for the Bruno-Vistulian

Table 1: Densities of rocks used for the modelling

Geological Units	Lithologies	Densities [g.cm⁻³]
Saxothuringian		
	Granite	2,62-2,68
	Felsic layer	2,72
	Mafic layer	2,8
	Basement	2,88
	Carboniferous suture	2,87
	subduction plate	2,88
Teplá-Barrandian		
	Granite	2,69
	Neoproterozoïque Layer	2,73-2,75
	Basement	2,78-2,82
	Amphibolite layer	2,85
	Central Bohemian Pluton	2,65-2,68
Moldanubian		
	Central Moldanubian Pluton	2,63
	Monotonous group and Varied Unit	2,69-2,76
	Mafic Layer-Amphibolite	2,82-2,84
	Granulite Felsic	2,66-2,70
Brunia		
	Upper crust	2,72
	Middle crust	2,85
	Lower crust	2,92
	Eclogite	3,1
Carpathian Foredeep		
	Flysch	2,53
	Sediments	2,58
Mantle		3,2

microcontinent take into account a Neoproterozoic age of this domain, outcrop geology and conceptual model of Finger et al. (2000). Consequently, we propose a stratified crustal model marked by mafic lower crust with a density of 2.92 g.cm^{-3} and a middle crust with 2.85 g.cm^{-3} .

At a crustal scale, rock densities vary for one type of rock and therefore, it is required that the density of each unit is approximated, taking into account the variations of lithology with depth. Therefore, an estimation of an average density at a kilometric scale is determined, keeping in mind that the most accurate gravity model has the lowest density contrasts from one structure to another. For example, an intermediate density between the density values of the top ($\sim 2.63 \text{ g.cm}^{-3}$) and the density values of the suture ($\sim 2.88 \text{ g.cm}^{-3}$) is taken since the middle crust is a stretched mix of the top layers and the bottom layers. The density of 2.84 g.cm^{-3} of the undefined structure in the middle crust of the Moldanubian domain is determined with this method in order to obtain the lowest density contrast. Table 1 summarizes density ranges and values approximated and used in the 3D gravimetric model.

3.3. Modelling

We used the IGMAS (Interactive Gravity and Magnetic Application System) software for the 3D gravity modelling (Götze, 1984; Götze and Lahmeyer, 1988; Schmidt and Götze, 1998; 1999). The model covers an area of $\sim 400 \text{ km} \times 160 \text{ km}$ and reaches 45 km in depth. The geological bodies are modelled in 3D by polyhedrons with triangular surfaces which connect the vertices of two successive, parallel vertical sections. The input model is established according to the orientation of main geological boundaries on the surface, the horizontal gradients of the vertical derivatives of the Bouguer anomaly map and the geometry of the main seismic units of the 9HR section (Fig. 3). A seismic unit is characterized by its reflectivity and by the dip and the shape of the reflective belts. The spacing between the profiles (20 km) and the depth of the model (45 km), exclude fine modelling of the near surface. In order to facilitate the location of the granulites in the model and the interpretation in terms of exhumation model proposed by Franěk et al., (2006), we introduced a small low density body representing the low density felsic granulites.

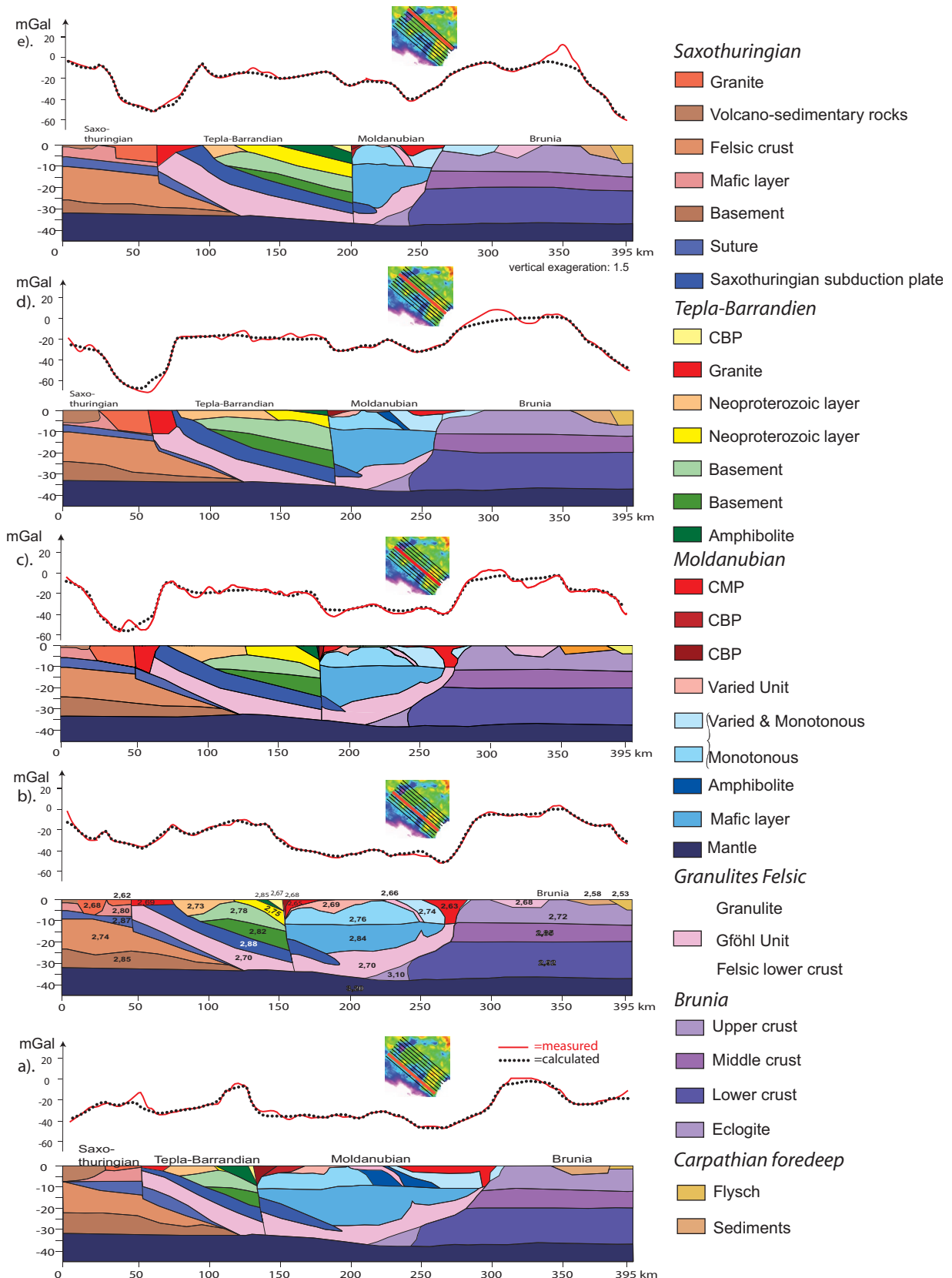


Figure 5: Selection of five of the nine modelled profiles. Details of the structures is given in the legend. The icons show the location of each profile. a). Profile N°2; b). Profile N°4; c). Profile N°5; d). Profile N°6; e). Profile N°8.

4. Results of the gravity modelling of the Bohemian Massif

Among the nine modelled profiles only five representative sections are shown in figure 5. The gravity low of the Moldanubian domain and the strong gravity gradient between Moldanubian domain and Bruno-Vistulian microcontinent are well resolved. The gravity highs on both sides of the Moldanubian gravity low are also well modelled except for few short wavelength anomalies.

The misfits between measured and calculated anomalies are explained by small near-surface mafic structures or by a sedimentary cover of small area extension (Fig. 6a). The histogram of gravity differences showing the misfit between the measured and computed anomalies of the study area reveals a correlation coefficient of 0.98, which is an acceptable average for this regional gravity model (Fig. 6b).

The necessity to attribute unconventional low densities to the lower crust is one of the most striking results of the gravity modelling. This is demonstrated in Fig. 7 in which three different models of section 4 are presented. In Fig. 7b a conventional density of 2.9 g.cm⁻³ was attributed to the Moldanubian lower crust. This classical model of crustal stratification (e.g. Hrubcová et al., 2005) shows a major misfit between modelled and measured data. Fig. 7c shows the optimized model still with a lower crust at 2.9 g.cm⁻³. This model was optimized by decreasing the density of upper crustal units in the Moldanubian domain, which is in contradiction to the presence of high density amphibolites and gneisses of the Varied and Monotonous groups at the surface. In addition, the model reveals extremely high misfit in the area of the Teplá suture because, here, the postulated dense lower crust comes to the surface. This strong positive effect can only be reduced by using unrealistically low densities values for the lower crustal rocks of the Teplá suture (Fig. 7c). In addition, the presence of a low density lower crust is supported by low seismic velocities in the range 6.0-6.4 km/s in the 20–30 km depth range revealed by the seismic refraction section beneath the Moldanubian domain (Růžek et al., 2007; Fig. 3d). Experimental studies of Christensen and Mooney (1995) shows that such low seismic velocities correspond to felsic granulites (6.25 to 6.50 km/s) in contrast to mafic, garnet-bearing granulites of common lower crust which reveal velocities in the range 6.5 to 7.25 km/s. The minimum in seismic velocities in the area of deep Saxothuringian crust and underneath the northern Saxothuringian suture zone may indicate similar low density material (Fig. 3d).

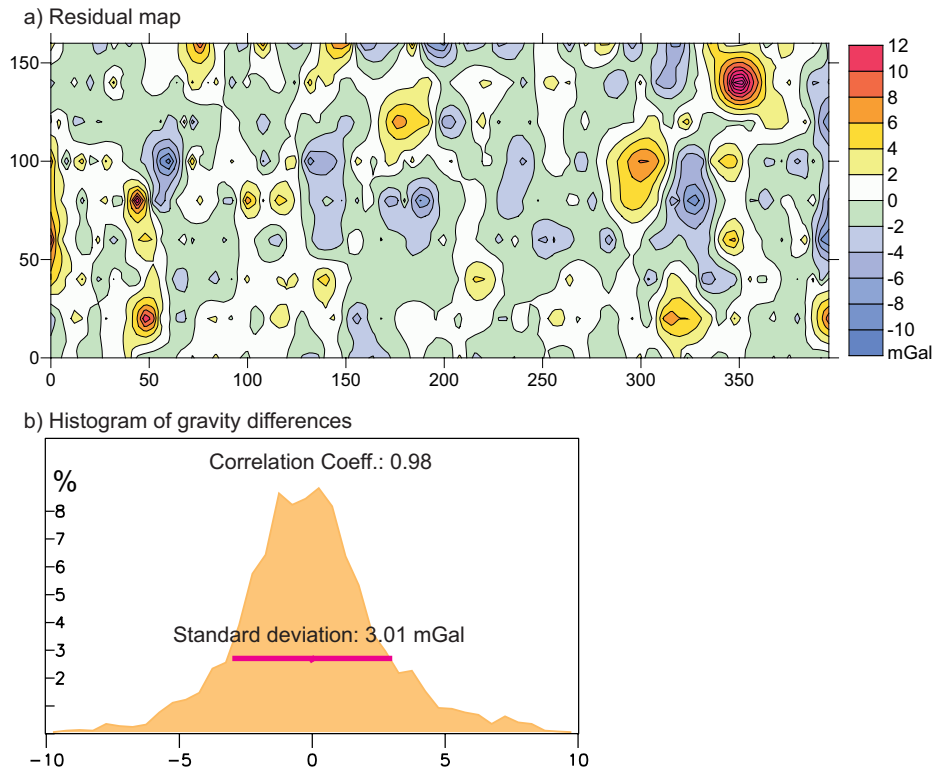


Figure 6: Statistics of the gravity model. (a) Residual map and (b) histogram of gravity differences for the whole 9 profiles (correlation coefficient 0.98).

The other main results derived from gravity modelling are as follows:

- The southern Saxothuringian upper crust is characterized by intermediate and low density rocks consisting of felsic metamorphic rocks and up to 10 km thick granitic rocks (see also previous models by Polanský, 1978; Hecht et al., 1997).
- The southeast dipping Teplá suture zone is characterized by a mean density of 2.88 g.cm⁻³ due to the association of ultramafic rocks, gabbros and eclogites.
- The Barrandian basement shows intermediate to high densities which correlate with Neoproterozoic metasedimentary and metavolcanic units.
- The southern limit of the low to intermediate density Central Bohemian Pluton dips to the NW while the northern pluton's limit is parallel to the vertical Teplá-Barrandian/Moldanubian boundary.
- The intermediate density Moldanubian upper crust corresponds to low density migmatites, while deeper rocks of Varied and Monotonous groups show higher mean density. The modelling suggests the existence of a dense layer below the Monotonous group and above the deepest low density lower crustal layer. This unit is underlain by a ~ 5–10 km thick weakly reflective and low density unit which shows similar geophysical characteristics to the granulite-

migmatite layer at the erosion surface.

- The low density (2.63 g.cm⁻³) Central Moldanubian Pluton shows a lenticular shape root parallel to the Moldanubian/Bruno-Vistulian boundary.

- In the Moldanubian granulite area, the weak gravity low is modelled with small bodies with thickness not exceeding 3 km. In contrast the small gravity highs which surround the lows require the presence of significant amounts of dense amphibolites.

- Between the Central Moldanubian Pluton and the Moldanubian/Bruno-Vistulian surface boundary, the Moldanubian low to intermediate density rocks are reduced to a thin layer (3 km max) forming a Moldanubian nappe overlying the dense Bruno-Vistulian basement rocks. The main Moldanubian/Bruno-Vistulian boundary is located beneath the Central Moldanubian Pluton. It is responsible for the prominent horizontal gradient in the gravity map (Fig. 2). This gradient results from lithological contrast between Bruno-Vistulian and Moldanubian lower crust and presence of Central Moldanubian Pluton in supracrustal level.

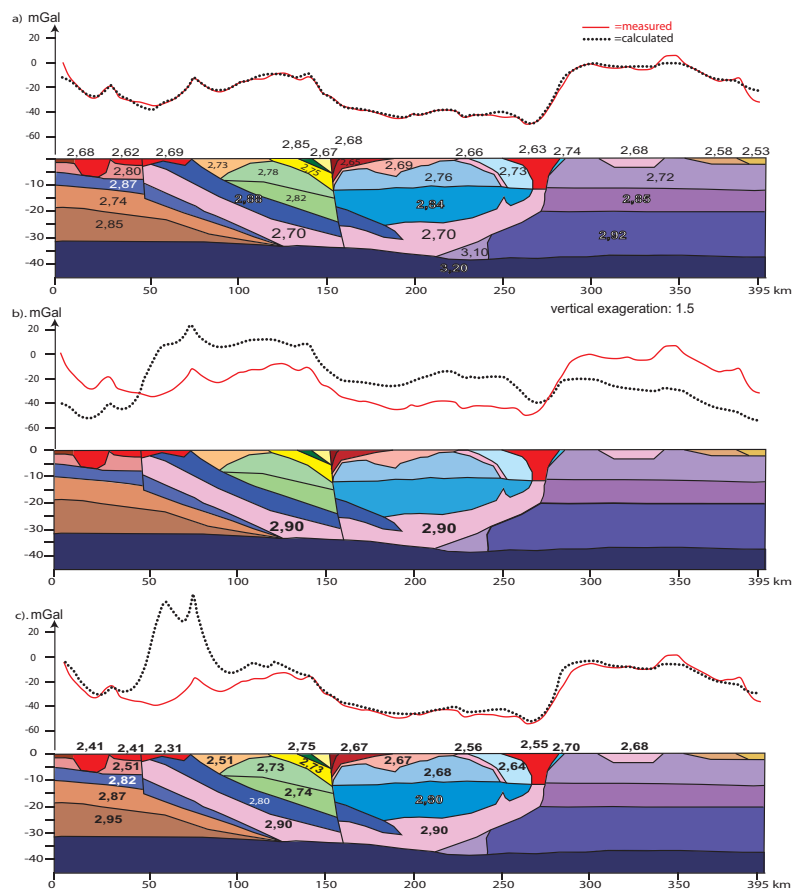


Figure 7: a). Gravimetric model for section 4; b). Gravimetric model with conventional density of 2.9 g/cm³ for the lower crust; c). Optimized model with the lower crust at 2.9g/cm³. Modelling results are clearly in favour of a light felsic lower crust.

Figure 5 shows the distribution of crustal layers thickness and shape from SW to NE. The southernmost profiles exhibit (~10 km) thick and continuous felsic lower crust in the Moldanubian domain which progressively decreases in thickness and extent towards northeast. In the north, the felsic lower crust is almost absent being replaced by thick mafic (high density) lower crust. This is consistent with the seismic refraction profile of Hrubcová et al. (2005) who reports a high velocity for the lower crust from the northern part of the Moldanubian domain, while Růžek et al. (2007) suggest a low velocity deep lower crust in the southern Moldanubian domain.

5. Geological interpretation

The geophysical structure of the Teplá-Barrandian and Saxothuringian domains is discussed elsewhere (Tomek et al., 1997, Tomek 2007; Babuska et al., 2010). Nevertheless, we define here the salient features of the gravimetric and seismic results that are necessary to understand the structure of the Moldanubian domain.

Our results allow estimation of the thickness of the Teplá-Barrandian Unit which reaches a maximum depth of 15 km to the east, confirming the values proposed by Zulauf et al., (2002; 2009). The Teplá-Barrandian basement is underlain by high density mafic and ultramafic rocks of the Devonian Teplá suture which typifies the character of lower crust in this area (Fig. 8). Importantly, the mafic lower crustal material is underlain by a low density layer of variable thickness which outcrops in the area of Eger granulite belt (Zulauf et al., 2002a). This is the crust, which directly overlies the Moho in the east, while in the west it has a form of east dipping sheet lying above heavy and intermediate rocks of Saxothuringian domain (Fig. 8). The deep structure of the Saxothuringian–Teplá-Barrandian boundary fits the model of Konopasek and Schulmann (2005) and Zulauf et al., (2002b) who suggested an outflow of a granulite channel in the area of Eger granulites. The granulite channel is structurally coherent with coevally exhumed eclogitic Saxothuringian crust during Carboniferous times.

Recent geological studies of the Moldanubian domain show systematic alternations of steep belts of deep orogenic lower crust with parallel middle crustal belts (Štípská et al., 2004; Schulmann et al., 2005). These studies suggest that the structure of the Moldanubian domain is governed by process of vertical material transfer similar to gravity overturn. In this, the structurally deepest rocks (20 kbar, 900°C peak conditions) occur in cores of NE-SW trending antiforms surrounded by NE-SW trending mid-crustal synforms (10 kbar, 650°C peak conditions). In detail, the antiforms are cored by felsic granulites and rimmed by thick mafic

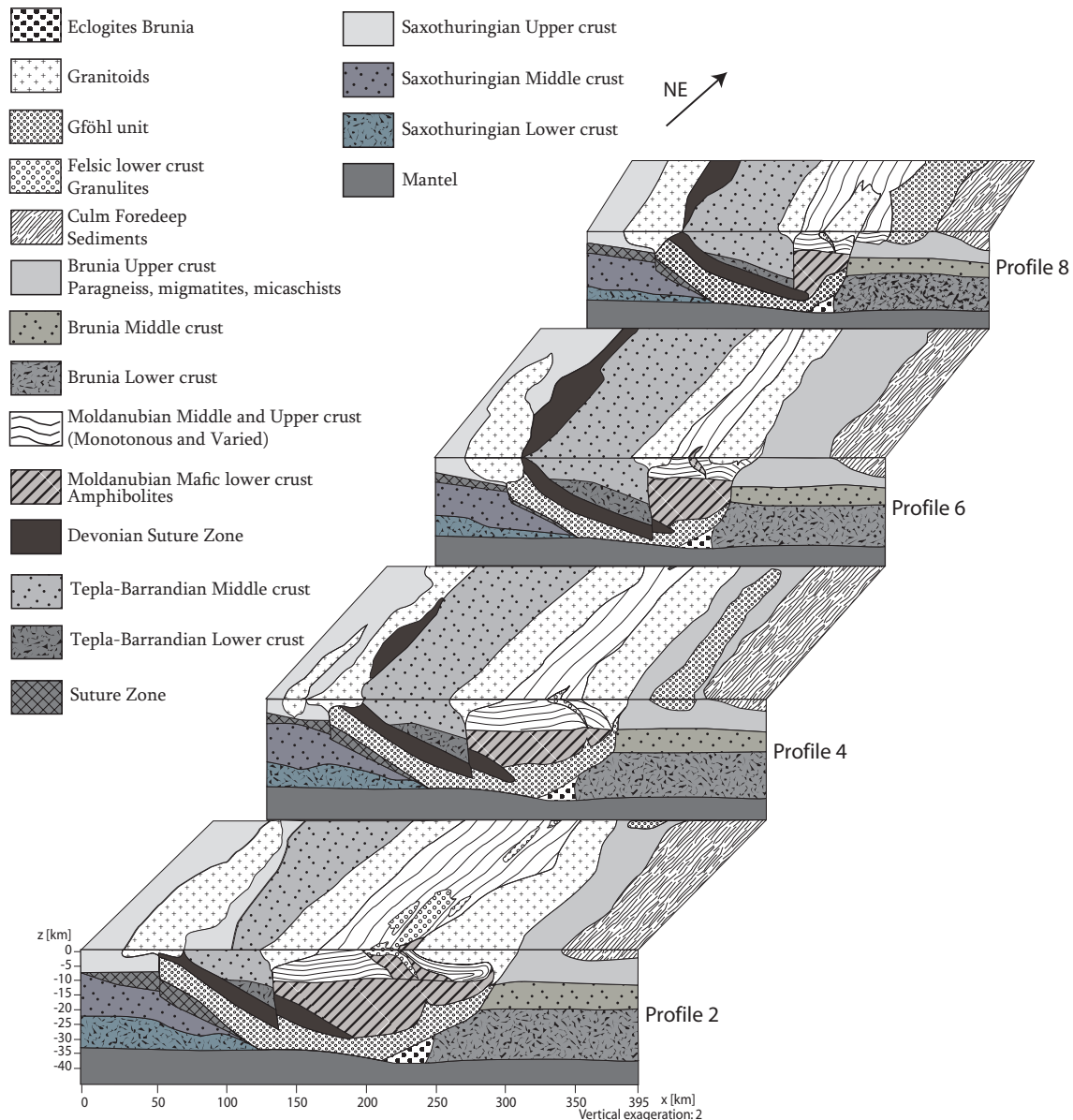


Figure 8: Geological interpretation of the modelled gravity sections from Fig. 5. Mesozoic and Cenozoic sequences are discarded so that only Palaeozoic basement and igneous units are shown.

lower crust of so called “Begleit Series” outcropping mostly in Lower Austria (Fuchs, 1976). The middle crustal synforms are cored by rocks of the Varied group surrounded by gneiss and schist of the Monotonous group. If the large-scale fold structure of the Moldanubian domain is unfolded, an original vertical stratification of Moldanubian crust can be established with felsic granulites occurring at the greatest depth, overlain by mafic “Begleit series” in the middle and Monotonous and Varied group rocks at upper crustal levels. Similar dome like structures cored by felsic HP granulites are also described in the Saxothuringian domain and Vosges (Franke, 2000; Schulmann et al., 2002) indicating a similar character of the orogenic lower crust in eastern Variscides.

The Moldanubian domain structure can also be interpreted using seismic section 9HR which shows a weakly reflective and low density layer close to the surface corresponding to the subhorizontal migmatite and granulite layer of the Gföhl Unit in south Bohemia (Franěk et al., 2006, 2010). The highly reflective and intermediate density layer located underneath the Gföhl migmatites corresponds to surface outcrops of the Varied and Monotonous groups. This geophysical structure is well consistent with the flat fabrics developed in both the migmatites and the underlying Varied and Monotonous groups at about 7 kbar conditions (Ráček et al., 2006). The high-density, high-reflectivity and high-velocity layer located beneath the Monotonous group rocks is interpreted as mafic crust, lithologically corresponding to gabbros and banded amphibolites of the “Begleit Series”. The most striking feature of the geophysical results is the existence of a low density, low velocity and low reflectivity layer which is interpreted as a deep equivalent of granulites and migmatites of the Gföhl Unit at the surface. We suggest that this vertical stratification corresponds to horizontal map structures of the Moldanubian Massif marked by alternations of orogenic middle and lower crustal rocks as defined by Schulmann et al., (2005). The geological maps show extreme reduction of mafic “Begleit Series” layer surrounding felsic granulite bodies which most likely occurred due to boudinage of this relatively competent layer during “diapiric” growth of crustal antiforms (Schulmann et al., 2009).

The seismic profile also shows reflections with moderate south-easterly dips and rather high reflectivity underlying the mafic material of the “Begleit Series” in the western part of the Moldanubian domain. We speculate that this geophysical feature may be correlated with the high-density, high-reflectivity and high-velocity features of the Teplá suture zone. Therefore, these reflectors can be tentatively interpreted as a continuation of the Teplá suture zone which is shifted upwards by the Central Bohemian shear zone, consistent with the “elevator” model of Zulauf et al. (2002a,) and Dörr and Zulauf (2010).

Recent tectonic studies of the eastern margin of the Bohemian Massif show a Bruno-Vistulian basement promontory underneath the high grade rocks of the Moldanubian nappe (Schulmann et al., 2008). These authors suggested that the deep margin of Bruno-Vistulian promontory occurs about 70 km to the west of the recent Moldanubian/Moravo-Silesian contact zone as defined by Suess (1926). From the surface geological constraints, the seismic bodies and the gravity modelling determined above, a geodynamic significance of geological units is established. Indeed, our gravity modelling closely matches the tectonic model of Schulmann et al. (2008) and confirms a high density crust close to the surface (< 3 km) to the south-eastern part of the Moldanubian domain and low density rocks corresponding to granulites and migmatites of the Gföhl Unit covering the whole area of eastern Bohemian Massif in Moravia

and Lower Austria.

This study shows that the Central Bohemian Pluton has a triangular shape controlled by the structure of the Central Bohemian Shear Zone to the west and large scale west dipping normal shear zone located to the southeast (Scheuvens and Zulauf, 2000; Žák et al., 2005). In contrast, the Central Moldanubian Pluton exhibits a diapiric shape rooted at 10 km depth in the continuity of felsic lower crustal rocks (Fig. 5). The root of the intrusion follows the steep boundary between Moldanubian root and Bruno-Vistulian promontory.

The geophysical methods do not allow the imaging of vertical structures observed in the field which are of significantly smaller scale. Nevertheless, the gravity modelling confirms vertical extrusion of lower crustal rocks predicted by geological studies (Štípská et al., 2004; Schulmann et al., 2008) along the western margin of the Bruno-Vistulian promontory. In addition, smaller scale modelling and detailed analysis of seismic fabrics in south Bohemia (Franěk et al., 2010) allowed a 20 km wide vertical paleo-channel along which deep granulites have reached the surface. Surprisingly, this geophysical study shows vertical stratification of the orogenic root preserved since Permian times.

6. Geodynamic implications

The presented geophysical model provides important constraints for the understanding of the geodynamic evolution of the Variscan internides. We highlight here several important features:

The Teplá-Barrandian unit represents an orogenic suprastructure (Zulauf, 2001, Zulauf et al., 2009) which is underlain by both rocks of the Devonian Teplá suture and those of a Carboniferous HP granulitic channel. The latter rocks overlie the Saxothuringian HP rocks, in agreement with the model of Konopásek and Schulmann et al., (2005).

The Moldanubian domain represents an eroded section of the orogenic root where the Monotonous group corresponds to a Neo-Proterozoic basement overlain by Early Palaeozoic sediments of the Varied group. The mafic layer is interpreted as a result of the Early Paleozoic magmatic underplating of gabbros during Siluro-Devonian back arc spreading (Finger and Steyrer, 1995; Schulmann et al., 2009). In addition, we cannot exclude a strong contribution of Ordovician mafic magmatism that was determined in several places of the Moldanubian system (Štípská et al., 2001). This mafic material reaches several kilometers thicknesses in Lower Austria which led some authors to propose a Siluro-Devonian break up in this region

(Finger and Steyrer, 1995). The identification of felsic lower crust forming the deepest part of the Moldanubian domain is a major result of the present work. Its existence has been anticipated by several authors for the lower crust in the root zone of the Variscan belt, being composed of K-feldspar–kyanite granulites (Behr, 1978; 1984; Weber, 1984). These authors proposed a model of “Subfluenz” tectonics which is equivalent to the deep crustal influx of continental crust into the root zone proposed by several authors for the Tibetan plateau (Chemenda et al., 2000; Avouac, 2007). In the case of the Bohemian Massif, the felsic material had to be underthrust during late Devonian (~380 Ma) Saxothuringian continental subduction and collision underneath the Teplá-Barrandian crust which is part of Armorica (Schulmann et al., 2009). The subsequent thermal weakening by changes in deformation mechanisms and melting of the Moldanubian root is responsible for rheological collapse of the orogenic root. Consequently, vertical material transfer occurred, responsible for partial exhumation of the deepest Moldanubian rocks to the surface. The exhumation mechanism is similar to diapiric ascent accompanied with intrusion of several crustal and mantle derived granitoids plutons (Franěk et al., 2006). The proposed concept is fundamentally similar to that of Perchuk (1989) and Perchuk et al. (1992) who were the first to propose gravitational redistribution model for the formation and exhumation of granulites. Thus the origin of intensely deformed felsic granulitic layer in the middle-lower crust can be related to the mechanical gravitational separation and merging of smaller scale layers of relatively felsic rocks. Numerical modelling of such merging processes was published by Perchuk et al. (1992), Weinberg and Schmeling (1992) and more recently by Gerya et al. (2004).

The presented model of the deep structure of the Moldanubian domain has important consequences for the origin of active orogens with a thick and hot root, such as in the Andes and Tibet. Attachment to the mafic crust of felsic lower crust due to the underthrusting of the Indian lithospheric crust underneath Tibet was predicted in the analogue model of Chemenda et al. (2000). In this model, the presence of high topography is explained by low density material in the root domain (Le Pichon et al., 1997). Indeed, the crust of Tibet is marked by intermediate density crust in the depth range of 0–35 km (2.7–2.8 g/cm³) and low to intermediate densities of crust in the depth range 40–60 km (2.8–2.9 g/cm³) (Hetenyi et al., 2007). It is this crustal level which is interpreted as a tectonically-underplated Indian upper crust underneath Tibetan crust (Hetenyi et al., 2007). The densities at 60–40 km depth correspond to those of granite at a temperature of 800°C and a pressure in the range of 18–20 kbar as shown by petrological modelling (LePichon et al., 1997; Goffé et al., 2003). The protolith of felsic granulites is most likely a granite and therefore the densities estimated for Tibetan lower crust correspond to granulites of granitic or granodioritic composition (Štípská and Powell, 2005a). Only rocks

in the depth range of 60–75 km show modelled densities of 3.3 g/cm³ and are interpreted as eclogitized Indian lower crust of mafic composition. Our modelling shows that high density rocks coinciding with an east dipping reflector underneath the Tepla-Barrandian domain correspond to a relic of the Saxothuringian suture zone, rich in eclogites and peridotites (Konopásek and Schulmann, 2005).

Here we show that in the Variscan belt the low density orogenic lower crust at Moho depths is still present in the Moldanubian domain and is connected with subsurface extrusions by narrow vertical channels (e.g. Franěk et al., 2006; Schulmann et al., 2008). The subsurface lateral spreading of partially molten lower crust occurred at pressures of 4 to 8 kbar (Štípská et al., 2004, 2008) which corresponds to 15–26 km depths. This crustal level of one partially molten rocks may correspond to the low resistivity and low velocity zone located underneath the Tibetan plateau and the Altiplano in the Andes as shown by geophysical surveys. The mechanism of extrusion of deep orogenic lower crust is similar to gravity overturns (Gerya et al., 2001) and may well explain emplacement of hot lower crustal material and its spreading underneath a rigid lid (Burg et al., 1994). Therefore, even if the Variscan crust shows normal thickness reduced by later extensional processes, the gravity low, P-wave velocity pattern and rock assemblage in the area of the Moldanubian domain may reflect a relic of thick orogenic root (and plateau) such as it exists today in large active collisional orogens. Finally, geological and geophysical observations reveal extrusion of high grade partially molten mass over the basement promontory in a geometry which markedly resembles to indentation of the Altiplano lower crust by crust of the Brazilian shield (Lamb et al., 1997). Therefore, the Bohemian Massif represents a unique example where deep structure of Andean and Tibetan-like plateaux can be studied and successfully modelled.

7. Model of relamination of felsic crust to early Palaeozoic mafic lower crust and gravity overturns

The relamination of the felsic lower crust has been proposed as an alternative to the model of Chemenda et al. (2000) to explain the structure of the Tibetan Plateau. The Tibetan Plateau is characterized by an exceptionally large gravity low indicating dominantly a felsic root underplated by Indian felsic crust, the density of which corresponds to felsic granulite at a pressure of 20 kbar (Hetényi et al., 2007). Indeed, Le Pichon et al. (1997) argued that the high topography of the Tibetan Plateau is due to presence of low density granulites at depth. A similar gravity low is typical of the Altiplano Plateau in central Andes, having been interpreted

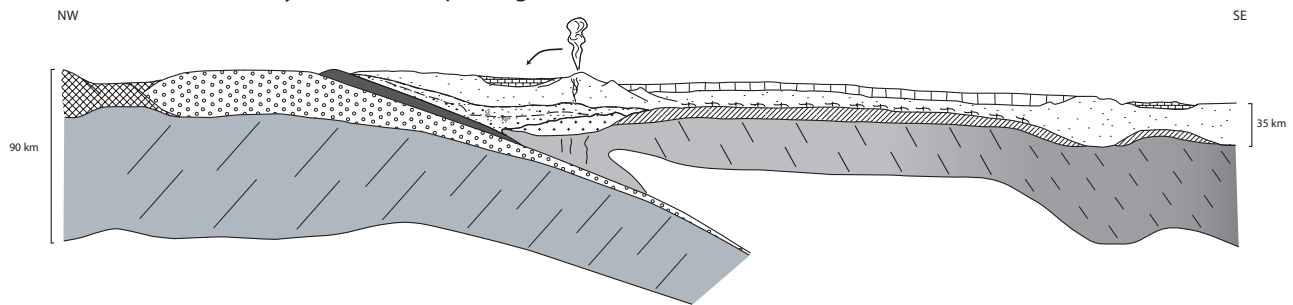
as a result of underthrusting of the Brazilian crust underneath the Andean root (Oncken et al., 2006). The gravity anomaly associated with the Moldanubian domain resembles remarkably the Tibetan and Altiplano plateaux density structure, which in this case is reduced by subsequent isostatic reequilibration (Burg et al., 1994). The common denominator of all these geophysical observations is the occurrence of felsic crust at lower crustal depths. This is explained either as continental crust underthrusting thin lithospheric mantle (Chemenda et al., 2000) or directly by influx of felsic crust into the orogenic root at Moho depth lifting the original lower crust and depressing the mantle lithosphere (Behr, 1978; Plesch & Oncken, 1999; Avouac, 2007).

In the western Bohemian Massif, the influx of ductile lower crust at granulite/eclogite facies conditions was proposed by O'Brien (2000). In Fig. 9a,b, the influx of Saxothuringian crust into the root domain is visualized in the form of a 10 km wide channel splitting the early Palaeozoic mafic lower crust from lithospheric mantle, whereas the other part of the continental crust is continuously subducted, contaminating the local mantle and sampling the mantle lithosphere. The term *relamination* (Hacker et al., 2007) is accepted as being suitable for the addition of low density crust underneath the dense root, in contrast to the term *delamination* to describe loss of heavy root material and its replacement by the asthenosphere.

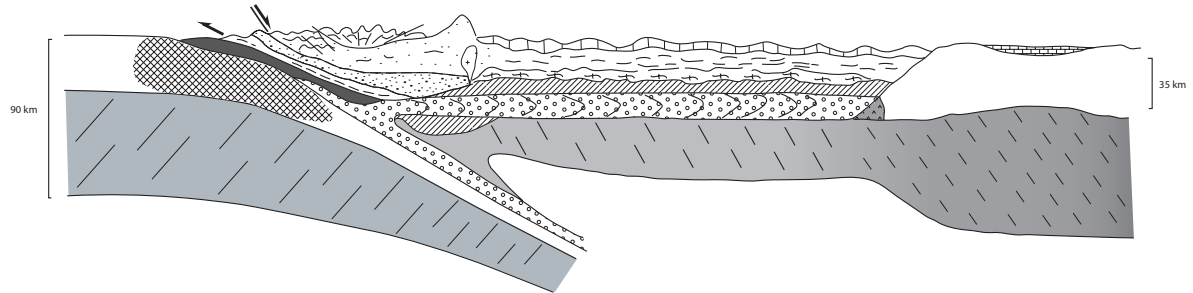
As discussed before, oceanic subduction had to have ceased by 354–346 Ma to be replaced by continental underthrusting. Incidentally, a Sm–Nd age of 354 ± 6 Ma was determined by dating of calcium-rich cores of garnet from the South Bohemian granulites indicating the onset of eclogitization of continental crust at this time (Prince et al., 2000). If true, such a scenario allows a 5–15 Ma period to c. 340 Ma, the granulite facies metamorphic climax, for the subducted continental crust to thermally incubate and elevate the orogenic geotherm (England & Thompson, 1984). Based on P–T estimates, crustal thickening had to produce a ~70-km thick crust at this time (Fig. 9c). Melting of this continental crust started at c. 345 Ma, as indicated by high-K calc-alkaline magmatism of the Blatná suite. The maximum melt production at both the base of this crust and in the underlying mantle lithosphere occurred during, or soon after, the HP metamorphic climax at c. 340 Ma, as indicated by intrusions of ultrapotassic syenites at mid- to highcrustal levels.

The scenario presented here (Fig. 9d) resembles the explanation of the formation of migmatitic domes in hot orogenic belts driven by gravitational collapse of thickened continental crust (Rey et al., 2001; Vanderhaeghe and Teyssier, 2001; Vanderhaeghe, 2009). All these conceptual models suggest partial melting of the lower crust to be a trigger mechanism for development of gravitational instability in both fossil and modern orogenic belts. The main difference of our model is in quantification of the gravitational instability, the rate of the

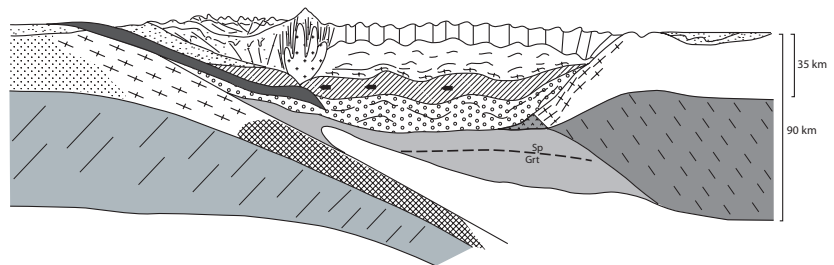
a) Oceanic Palaeotethys subduction passing to continental subduction (400-360 Ma)



b) Relamination and subduction of continental crust (360-350(?) Ma)



c) Crustal thickening
Moho at 70 km
(?)350-340 Ma)



d) Vertical extrusion stage
(340-335 Ma)

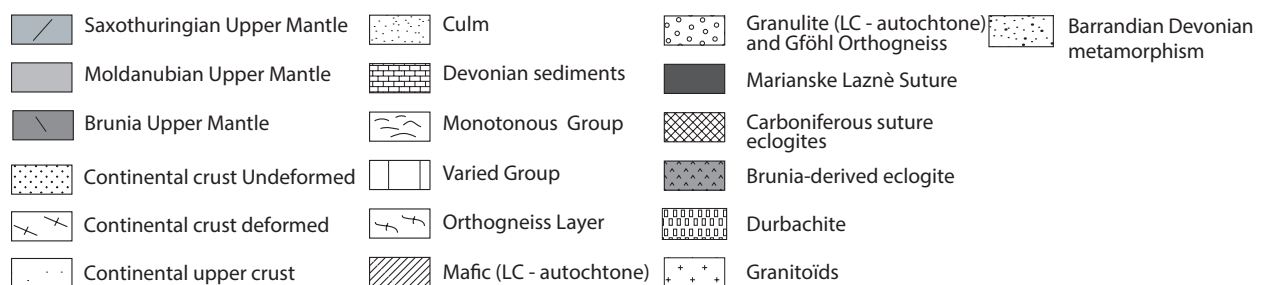
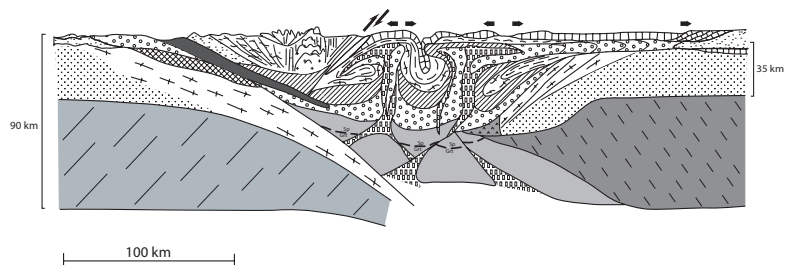


Figure 9: Model proposed for the tectonic evolution of the orogenic root domain in the Bohemian Massif. (a) Model of continental underthrusting with development of the Barrandian forearc region, CBPC magmatic arc and backarc region represents the future Moldanubian domain. The position of the Palaeotethys suture is indicated as the future Marianske Lázně Complex. (b) Relamination model with part of the allochthonous Saxothuringian crust injected between the Moho and the continental lithosphere. The other part is subducted thereby producing metasomatism of the overlying mantle. (c) Crustal thickening of the former backarc domain (Schulmann et al., 2005, 2009). (d) Vertical extrusion and gravity redistribution of relaminated Saxothuringian crust at the end of Variscan orogeny.

heating and also the rate of the development of the diapiric structures. The initial position of less dense but highly radioactive felsic material below more dense mafic lower crust seems to be the necessary prerequisite for driving the tectonic evolution of the Variscan orogeny in the Bohemian Massif.

The structural data suggest that domes are initiated by folding of the lower and mid-crustal interfaces (e.g. Štípská et al., 2004; Schulmann et al., 2005) and the linear distribution of elongate granulite belts indicates that lateral shortening was an important component (Burg et al., 2004) related to the growth of granulite domes (Fig. 9d). Therefore, the combination of gravity and laterally forced extrusion of orogenic crust may lead to a development of gravity overturns more rapidly compared with the numerical models presented herein.

Our work shows that only a model of internal heating to drive the tectonic and gravity redistribution of orogenic lower crust can satisfactorily explain the temporarily restricted orogenic event at c. 340 Ma, which is responsible for most of the Variscan tectonothermal events reported so far in the Bohemian Massif. Thus, the timing of growth of these laterally forced diapirs seems to be connected with orogenic collapse and the major plate reorganization of the whole Variscan belt (Edel et al., 2003). The co-existence of c. 340 Ma ultrapotassic plutons and extruded felsic HP granulites thus defines a key thermomechanical event, which probably signified a rheological collapse of the whole Variscan belt in Europe (e.g. Rossi et al., 2009; Rubatto et al., 2010).

Conclusion

The distribution and shape of geophysically-constrained bodies combined with modern structural, petrological and other geological data from the Bohemian Massif can be interpreted as follows:

(1) Felsic lower crust occurs underneath a thick mafic layer and the intermediate Monotonous and Varied group rocks of the Moldanubian domain. This less dense, low reflectivity felsic layer is interpreted as an allochthonous body resulting from underthrusting of Saxothuringian crust underneath the Gondwana derived continent. The process can be analogue to that proposed by Chemenda et al., (2000) for the formation of Tibetan lower crust. The overlying mafic unit is interpreted as an autochthonous sheet resulting from Early Palaeozoic basaltic underplating of rifted Proterozoic (Monotonous group) crust in sense of Finger and Steyrer (1995).

(2) The Bruno-Vistulian continent represents a deep crustal promontory replacing 70 km of weak continental root and can be compared to the Brazilian shield indenting the Andean root in the area of the eastern Cordillera. The orogenic lower crust is extruded over the Bruno-Vistulian basement promontory in the shape of a thin migmatitic nappe similar to that proposed by Beaumont et al. (2001). In the west, a similar granulite channel underneath the Teplá-Barrandian suprastructure was identified, coinciding with vertical extrusion of felsic granulites in the Eger valley (Zulauf et al., 2002a; Konopásek and Schulmann, 2005). The steep boundary between the Teplá-Barrandian and Moldanubian zone is interpreted in terms of major vertical elevation of the orogenic lower crust supporting the Dörr and Zulauf (2010) elevator tectonics model.

(3) The horizontal layer of felsic granulites and migmatites occurring at the current erosion surface is derived from the deep lower crustal felsic layer and was exhumed by mechanism similar to gravitationnal overturns. In Carboniferous times, this migmatitic layer was located at a depth corresponding to 5–8 kbar and most likely corresponded to the zone of partial melting inferred from geophysics in Andes and Tibet.

(4) The exhumation of c. 340 Ma felsic granulites in the Bohemian Massif is interpreted in terms of tectonically triggered gravity redistribution of felsic orogenic lower crust and high density mafic crust. The radioactive heat production is typical of the Ordovician felsic igneous rocks in the Fichtelgebirge (Saxothuringian domain), which are believed to have been relaminated at the bottom of thickened continental crust during the early Viséan continental underthrusting. Gravity-driven redistribution tectonics initiated by internal heating is interpreted to be the principal agent controlling the rheological collapse of the Variscan orogenic crust at c. 340 Ma.

Conclusion

The understanding of the continental growth relies on the investigation of accretionary and collisional processes and their mechanisms, respectively. This thesis presents the results of a multidisciplinary approach, which integrates geological and geophysical data in order to characterize and model the structure of a continental crust in two contrasting regions of Euro-Asian Palaeozoic orogenic system. While the European Variscan belt results mainly from collage of microcontinents, the easterly Central Asian Orogenic Belt consists of accreted island arcs, fore arcs and back arc regions with sub-ordinate volume of continental crust. Therefore, the western Variscan branch accretionary and collisional processes are dominated by continental lithospheric material while in the east these processes are dominated by mostly oceanic and passive margin lithospheres. The Palaeozoic orogens allow the observation of the entire cross section from the deepest to the shallowest parts of the orogenic system and therefore the Central Asian Orogenic Belt and the European Variscan belt (exemplified by the Bohemian Massif) represent ideal sites to investigate the structures of orogenic crust in order to better understand mechanisms of continental construction.

The study of the Central Asian Orogenic Belt was performed at different scales. Firstly, a regional-scale structural, petrological and geochronological study was conducted in two distinct oceanic and continental domains of the Ömnögovi Province (southern Mongolia). It allows identifying the succession of deformation events as well as the late Palaeozoic net crustal growth and construction of continent north of Chinese craton. Secondly, on orogen-scale study using the magnetic and Bouguer anomaly maps combined with the geological and lithostratigraphical data was carried out in South Mongolia. It allows describing and identifying the geophysical signature of the tectonic units in the southern part of the Central Asian Orogenic Belt. Finally, the magnetic, gravity and geological data are integrated in order to model the structure of the orogenic crust in the Central Asian Orogenic Belt along four key profiles distributed over southern Mongolia. In contrast, the study of the Bohemian Massif deep structure was carried out by analysis and modelling of gravity data supported by reinterpretation of refraction and reflection seismic lines.

The main results of this work can be summarized as follows:

- Two deformation phases are recognized in the Trans-Altai (oceanic domain) and South Gobi (continental domain) Zones.
- The diachronous character of the D1 deformation phase indicates that the Gobi fault zone separating the Trans-Altai oceanic zone from the South Gobi continental zone was a palaeo-transform boundary with two distinct activity peaks in the early Carboniferous and

in the late Carboniferous to early Permian.

- The strike-slip the eastern part of the Gobi Fault zone was reactivated during late Permian–Triassic N–S shortening as a zone of frontal convergence resulting from collision between North Chinese and Siberian cratons

- The magmatic petrology study combined with the structural field observation does not confirm the existence of late Carboniferous-early Permian E–W trending rift magmatism across the southern Mongolia.

- The comparison of gravity, magnetic and a new 500 000 geological maps allows reviewing terrane boundaries of the Central Asian Orogenic Belt in Mongolia. The different maps show that most of the geophysical results do not reconcile with the terrane boundaries based on tectono-stratigraphic correlations.

- The preliminary magnetic and gravity modelling confirm the ambiguous definition of terrane boundaries which were defined uniquely on the basis of surface geology data. The modelling performed along four transects allows to propose modified model structure of the orogenic crust of the Central Asian Orogenic Belt.

- The 3D gravity modelling of the Bohemian Massif suggests that the lower orogenic crust corresponds to an allochthonous felsic lower crustal fragment underplated beneath an autochthonous mafic layer. The allochthonous lower crust reflects the underthrusting of the Saxothuringian crust below Gondwana-derived continent.

- The modelling of the Bohemian Massif reveals several analogies: (1) between the lower crust in the Bohemian Massif and the lower crust under the Tibetan plateau concerning the behaviour of the felsic lower crust; and (2) between the Bruno-Vistulian continent and the Andean root regarding the indentation of continental fragments into the internal zones of orogens.

- The role of the gravity redistribution of the felsic orogenic lower crust with the high density mafic crust in the Bohemian Massif is also highlighted by the modelling.

Bibliographie

Allen, M.B., MacDonald, D.I.M., Xun, Z., Vincent, S.J., Brouet-Menzies, C., 1998. Transtensional deformation in the evolution of the Bohai Basin, northern China. *Continental Transpressional and Transtensional Tectonics* 135, 215-229.

Amante, C., Eakins, B.W., 2009. ETOPO1 1 Arc-Minute Global Relief Model: Procedures, Data Sources and Analysis, NOAA Technical Memorandum NESDIS NGDC, p. 19

Andersen, O.B., Knudsen, P., 2009. DNSC08 mean sea surface and mean dynamic topography models. *Journal of Geophysical Research-Oceans* 114.

Avouac, J.P., 2007. Dynamic processes in extensional and compressional settings-Mountain building: From earthquakes to geological deformation. *Treatise on Geophysics* 6, 377-439.

Babuška, V., Fiala, J., Plomerová, J., 2010. Bottom to top lithosphere structure and evolution of western Eger Rift (Central Europe). *International Journal of Earth Sciences* 99, 891-907.

Badarch, G., Cunningham, C.W., Windley, B.F., 2002. A new terrane subdivision for Mongolia: implications for the Phanerozoic crustal growth of Central Asia. *Journal of Asian Earth Sciences* 21, 87-110.

Bassin, C., Laske, G., Masters, G., 2000. The Current Limits of Resolution for Surface Wave Tomography in North America. *EOS Trans AGU* 81.

Beard, B.L., Medaris Jr, L.G., Johnson, C.M., Jelínek, E., Tonika, J., Riciputi, L.R., 1995. Geochronology and geochemistry of eclogites from the Mariánské Lázně Complex, Czech Republic: Implications for Variscan orogenesis. *Geologische Rundschau* 84, 552-567.

Beaumont, C., Jamieson, R.A., Nguyen, M.H., Lee, B., 2001. Himalayan tectonics explained by extrusion of a low-viscosity crustal channel coupled to focused surface denudation. *Nature* 414, 738-742.

Behr, H.J., 1978. Subfluenz-Prozesse im Grundgebirgs-Stockwerk Mitteleuropas. *Z. Dt. Geol. Ges* 129, 283-318.

Behr, H.J., Engel, W., Franke, W., Giese, P., Weber, K., 1984. The Variscan Belt in Central Europe: Main structures, geodynamic implications, open questions. *Tectonophysics* 109, 15-40.

Berg, H.C., Jones, D.L., and Richter, D.H., 1972. Gravina-Nutzotin Belt; tectonic significance of an upper Mesozoic sedimentary and volcanic sequence in southern and southeastern Alaska, in: Survey, U.S.G. (Ed.), *Geological survey research 1972*, pp. D1-D24.

Berg, H.C.J., D. L.; Coney, P. J., 1978. Map showing pre-Cenozoic tectonostratigraphic terranes of southeastern Alaska and adjacent areas, U.S. Geological Survey Open-File Report 78-1085, 2 sheets, scale 1:1,000,000 ed. U.S. Geological Survey.

Blakely, R.J., Simpson, R.W., 1986. Approximating edges of source bodies from magnetic or gravity anomalies. *Geophysics* 51, 1494-1498.

Blight, J.H.S., Crowley, Q.G., Petterson, M.G., Cunningham, D., 2010. Granites of the Southern Mongolia Carboniferous Arc: New geochronological and geochemical constraints. *Lithos* 116, 35-52.

Bonhomme, M., Thuizat, R., Pinault, Y., Clauer, N., Wendling, R., Winkler, R., 1975. Méthode de datation potassium-argon. Appareillage et technique, in: Strasbourg, U.L.P. (Ed.), Technical report of the Centre de Géochimie de la Surface. Université Louis Pasteur Strasbourg, Strasbourg, p. 53.

Bouchez J.L., H.D.H.W., and Stephens W.E., 1997. Granite : from segregation of melt to emplacement fabrics.

Brown G.C., T.R.S., Webb P. C., 1984. The geochemical characteristics of granitoids in contrasting arcs and comments on magma sources. *Journal of Geological Society* 141, 413-426.

Burg, J., Kaus, B., Podladchikov, Y., 2004. Gneiss Domes in Orogeny. Dome structures in collision orogens. Mechanical investigation of the gravity/compression interplay, 47-66.

Burg, J.P., Van Den Driessche, J., Brun, J.P., 1994. Syn- to post-thickening extension: mode and consequences. *Comptes Rendus - Academie des Sciences, Serie II: Sciences de la Terre et des Planetes* 319, 1019-1032.

Burton, G.R., 2010. New structural model to explain geophysical features in northwestern new south wales: Implications for the tectonic framework of the tasmanides. *Australian Journal of Earth Sciences* 57, 23-49.

Cady, J.W., 1989. Geologic implications of topographic, gravity, and aeromagnetic data in the northern Yukon-Koyukuk province and its borderlands, Alaska. *Journal of Geophysical Research* 94, 15,821-815,841.

Cawood, P.A., Buchan, C., 2007. Linking accretionary orogenesis with supercontinent assembly. *Earth-Science Reviews* 82, 217-256.

Cawood, P.A., Kröner, A., Collins, W.J., Kusky, T.M., Mooney, W.D., Windley, B.F., 2009. Accretionary orogens through Earth history, *Geological Society Special Publication*, pp. 1-36.

Cháb, J., Stráník, Z., Eliáš, M., 2008. Geological map of the Czech Republic 1/500000, in: Survey, C.G. (Ed.). *Czech Geological Survey, Praha*.

Chappell, B.W., White A.J.R., 1974. Two contrasting granite types. *Pacific Geology* 8, 173-174.

Chardon, D., Gapais, D., Cagnard, F., 2009. Flow of ultra-hot orogens: A view from the Precambrian, clues for the Phanerozoic. *Tectonophysics* 477, 105-118.

Chemenda, A.I., Burg, J.P., Mattauer, M., 2000. Evolutionary model of the Himalaya-Tibet system: Geopoem based on new modelling, geological and geophysical data. *Earth and Planetary Science Letters* 174, 397-409.

Chen, B., Jahn, B.M., Tian, W., 2009. Evolution of the Solonker suture zone: Constraints from zircon U-Pb ages, Hf isotopic ratios and whole-rock Nd-Sr isotope compositions of subduction- and collision-related magmas and forearc sediments. *Journal of Asian Earth Sciences* 34, 245.

Chlupáčová, M., Švancara, J., 1994. Hustotní model geologické stavby podél geotraverzu 9HR a nadstavbové zpracování tíhového pole západní části Českého masívu, č0 1028/02-b.

Czech Geological Survey report.

Christensen, N.I., Mooney, W.D., 1995. Seismic velocity structure and composition of the continental crust: a global view. *Journal of Geophysical Research* 100, 9761-9788.

Clark, D.A., 1997. Magnetic petrophysics and magnetic petrology: aids to geological interpretation of magnetic surveys. *Journal of Australian Geology and Geophysics* 17, 83-103.

Clauer, N., Chaudhuri, S., 1998 Isotopic dating of very low-grade metasedimentary and metavolcanic rocks: techniques and methods, in: Frey M., R.D.e. (Ed.), In: *Low-Grade Metamorphism*. Blackwell Science, Oxford, pp. 202-226.

Collins, W.J., 2002a. Nature of extensional accretionary orogens. *Tectonics* 21, art. no.-1024.

Collins, W.J., 2002b. Hot orogens, tectonic switching, and creation of continental crust. *Geology* 30, 535.

Collins, W.J., Belousova, E.A., Kemp, A.I.S., Murphy, J.B., 2011. Two contrasting Phanerozoic orogenic systems revealed by hafnium isotope data. *Nature Geoscience* 4, 333-337.

Colpron, M., Nelson, J.L., 2006. Paleozoic evolution and metallogeny of pericratonic terranes at the ancient Pacific margin of North America, Canadian and Alaskan Cordillera. *Geological Association of Canada, Special Paper* 45, 523.

Cooper, G.R.J., 2004. A semi-automatic procedure for the interpretation of geophysical data. *Explor. Geophys.* 35, 182-187.

Cunningham, D., 2001. Cenozoic normal faulting and regional doming in the southern Hangay region, Central Mongolia: implications for the origin of the Baikal rift province. *Tectonophysics* 331, 389-411.

Cunningham, D., 2005. Active intracontinental transpressional mountain building in the Mongolian Altai: Defining a new class of orogen. *Earth and Planetary Science Letters* 240, 436.

Cunningham, D., Davies, S., McLean, D., 2009. Exhumation of a Cretaceous rift complex within a Late Cenozoic restraining bend, southern Mongolia: Implications for the crustal evolution of the Gobi Altai region. *Journal of the Geological Society* 166, 321-333.

Dallmeyer, R.D., Neubauer, F., Höck, V., 1992. Chronology of late Paleozoic tectonothermal activity in the southeastern Bohemian Massif, Austria (Moldanubian and Moravo-Silesian zones): $^{40}\text{Ar}/^{39}\text{Ar}$ mineral age controls. *Tectonophysics* 210, 135-153.

Dallmeyer, R.D., Urban, M., 1998. Variscan vs Cadomian tectonothermal activity in northwestern sectors of the Teplá-Barrandian zone, Czech Republic: Constraints from $^{40}\text{Ar}/^{39}\text{Ar}$ ages. *International Journal of Earth Sciences* 87, 94-106.

Damdinjav, Delgersaikhan, 1996-98. report N°5307.

Daoudene, Y., Gapais, D., Ruffet, G., Gloaguen, E., Cocherie, A., Ledru, P., 2012. Syn-thinning pluton emplacement during Mesozoic extension in eastern Mongolia. *Tectonics* 31.

Darby, B.J., Davis, G.A., Zhang, X., Wu, F.Y., Wilde, S.A., Yang, J.H. , 2004. The newly discovered Waziyu metamorphic core complex, Yiwulij Shan, western Liaoning Province, Northwest China. *Earth Science Front* 11, 145-155.

De Boissgrollier, T., Petit, C., Fournier, M., Leturmy, P., Ringenbach, J.C., San'kov, V.A., Anisimova, S.A., Kovalenko, S.N., 2009. Palaeozoic orogeneses around the Siberian craton: Structure and evolution of the Patom belt and foredeep. *Tectonics* 28.

Dewey, J.F., 1989. Kinematics and dynamics of basin inversion. Geological Society of London, Special Publications 44, 352-352.

Dewey, J.F., Bird, J.M., 1970. Plate tectonics and geosynclines. *Tectonophysics* 10, 625-638.

Dewey, J.F., Burke, K., 1974. Hot spots and continental breakup: implications for collisional orogeny. *Geology* 2, 57-60.

Dhuime, B., Hawkesworth, C.J., Cawood, P.A., Storey, C.D., 2012. A change in the geodynamics of continental growth 3 billion years ago. *Science* 335, 1334-1336.

Dolgoplova, A., Seltmann, R., Armstrong, R., Belousova, E., Pankhurst, R.J., Kavalieris, I., 2013. Sr-Nd-Pb-Hf isotopesystematics of the Hugo Dummett Cu-Au porphyry deposit (Oyu Tolgoi, Mongolia). *Lithos*.

Dörr, W., Zulauf, G., 2010. Elevator tectonics and orogenic collapse of a tibetan-style plateau in the European variscides: The role of the Bohemian shear zone. *International Journal of Earth Sciences* 99, 299-325.

Dudek, A., 1980. The crystalline basement block of the Outer Carpathians in Moravia: Bruno-Vistulicum. *Rozpr. Čs. Akad. Věd, Ř. Mat. Přír. Věd* 90, 1-85.

Economos, R.C., Paterson, S.R., Said, L.O., Ducea, M.N., Anderson, J.L., Padilla, A.J., 2012. Gobi-Tianshan connections: Field observations and isotopes from an early Permian arc complex in southern Mongolia. *Geological Society of America Bulletin* 124, 1688-1701.

Edel, J.B., Schulmann, K., 2009. Geophysical constraints and model of the "Saxothuringian and Rhenohercynian subductions, magmatic arc system" in NE France and SW Germany. *Bulletin de la Société Géologique de France* 180, 545-558.

Edel, J.B., Schulmann, K., Holub, F.V., 2003. Anticlockwise and clockwise rotations of the Eastern Variscides accommodated by dextral lithospheric wrenching: Palaeomagnetic and structural evidence. *Journal of the Geological Society* 160, 209-218.

Edel, J.B., Weber, K., 1995. Cadomian terranes, wrench faulting and thrusting in the central Europe Variscides: geophysical and geological evidence. *Geologische Rundschau* 84, 412-432.

England, P.C., Thompson, A.B., 1984. Pressure-temperature-time paths of regional metamorphism I. heat transfer during the evolution of regions of thickened continental crust. *Journal of Petrology* 25, 894-928.

Finger, F., Gerdes, A., Janoušek, V., René, M., Riegler, G., 2007. Resolving the Variscan evolution of the Moldanubian sector of the Bohemian Massif: The significance of the Bavarian

and the Moravo-Moldanubian tectonometamorphic phases. *Journal of Geosciences* 52, 9-28.

Finger, F., Hanzl, P., Pin, C., von Quadt, A., Steyrer, H.P., 2000. The Brunovistulian: Avalonian Precambrian sequence at the eastern end of the Central European Variscides? *Geological Society Special Publication*, 103-112.

Finger, F., Steyrer, H.P., 1995. A tectonic model for the eastern Variscides: indications from a chemical study of amphibolites in the south-eastern Bohemian Massif. *Geologica Carpathica* 46, 137-150.

Franěk, J., Schulman, K., Lexa, O., 2006. Kinematic and rheological model of exhumation of high pressure granulites in the Variscan orogenic root: Example of the Blanský les granulite, Bohemian Massif, Czech Republic. *Mineralogy and Petrology* 86, 253-276.

Franěk, J., Schulmann, K., Lexa, O., Tomek, C., Edel J, B., 2010. A model of syn-convergent extrusion of orogenic lower crust in the core of the Variscan belt: implications for exhumation of HP rocks in large hot orogens. *Lithos*.

Franěk, J., Schulmann, K., Lexa, O., Tomek, C., Edel, J.B., 2007. Exhumation of HP-HT lower-crustal rocks in frame of multiple deformations in the centre of Variscan collisional orogen, South Bohemian Moldanubian domain of the Bohemian Massif Charles University and Strasbourg, Praha and Strasbourg.

Franke, W., 2000. The mid-European segment of the Variscides: Tectonostratigraphic units, terrane boundaries and plate tectonic evolution, pp. 35-56.

Friedl, G., Finger, F., Paquette, J.L., von Quadt, A., McNaughton, N.J., Fletcher, I.R., 2004. Pre-Variscan geological events in the Austrian part of the Bohemian Massif deduced from U-Pb zircon ages. *International Journal of Earth Sciences* 93, 802-823.

Friedl, G., von Quadt, A., Ochsner, A., Finger, F., 1993. Timing of the Variscan orogeny in the Southern Bohemian Massif (NE-Austria) deduced from new U-Pb zircon and monazite dating. *Terra Abstracts* 5, 235-236.

Fritz, H., Dallmeyer, R.D., Neubauer, F., 1996. Thick-skinned versus thin-skinned thrusting: Rheology controlled thrust propagation in the Variscan collisional belt (The southeastern Bohemian Massif, Czech Republic - Austria). *Tectonics* 15, 1389-1413.

Frost, B.R., Barnes, C.G., Collins, W.J., Arculus, R.J., Ellis, D.J., Frost, C.D., 2001. A geochemical classification for granitic rocks. *Journal of Petrology* 42, 2033-2048.

Fuchs, G., 1976. Zur Entwicklung der Böhmischen Masse. *Jb Geol B-A* 129, 41-49.

Fullea, J., Fernández, M., Zeyen, H., 2008. FA2BOUG-A FORTRAN 90 code to compute Bouguer gravity anomalies from gridded free-air anomalies: Application to the Atlantic-Mediterranean transition zone. *Computers and Geosciences* 34, 1665-1681.

Gerdes, A., Friedl, G., Parrish, R.R., Finger, F., 2003. High-resolution geochronology of Variscan granite emplacement - the South Bohemian Batholith. *Journal of the Czech Geological Society* 48, 53-54.

Gerya, T.V., Maresch, W.V., Willner, A.P., Van Reenen, D.D., Smit, C.A., 2001. Inherent gravitational instability of thickened continental crust with regionally developed low- To

medium-pressure granulite facies metamorphism. *Earth and Planetary Science Letters* 190, 221-235.

Gerya, T.V., Perchuk, L.L., Maresch, W.V., Willner, A.P., 2004. Inherent gravitational instability of hot continental crust: implication for doming and diapirism in granulite facies terrains. *Gneiss Domes in Orogeny* 380, 97-115.

Glen, J.M.G., Schmidt, J., Pellerin, L., McPhee, D.K., O'Neill, J.M., 2007a. Crustal structure of Wrangellia and adjacent terranes inferred from geophysical studies along a transect through the northern Talkeetna Mountains. 431, 21-41.

Glorie, S., De Grave, J., Buslov, M.M., Zhimulev, F.I., Izmer, A., Vandoorne, W., Ryabinin, A., Van den haute, P., Vanhaecke, F., Elburg, M.A., 2011. Formation and Palaeozoic evolution of the Gorny-Altai–Altai-Mongolia suture zone (South Siberia): Zircon U/Pb constraints on the igneous record. *Gondwana Research* 20, 465-484.

Goffé, B., Bousquet, R., Henry, P., Le Pichon, X., 2003. Effect of the chemical composition of the crust on the metamorphic evolution of orogenic wedges. *Journal of Metamorphic Geology* 21, 123-141.

Götze, H.J., 1984. Über den Einsatz interaktiver Computergraphik im Rahmen 3-dimensionaler Interpretationstechniken in Gravimetrie und Magnetik. . Technische Universität Clausthal., p. 121

Götze, H.J., Kirchner, A., 1997. Interpretation of gravity and geoid in the Central Andes between 20° and 29° S. *Journal of South American Earth Sciences* 10, 179-188.

Gotze, H.J., Lahmeyer, B., 1988. Application of three-dimensional interactive modelling in gravity and magnetics. *Geophysics* 53, 1096-1108.

Gray, D.R., Foster, D.A., 2004. Tectonic evolution of the Lachlan Orogen, southeast Australia: Historical review, data synthesis and modern perspectives. *Australian Journal of Earth Sciences* 51, 773-817.

Guy, A., Edel, J.B., Schulmann, K., Tomek, C., Lexa, O., 2011. A geophysical model of the Variscan orogenic root (Bohemian Massif): Implications for modern collisional orogens. *Lithos* 124, 144-157.

Guy, A., Schulmann, K., Clauer, N., Hasalova, P., Seltmann, R., Armstrong, R., Benedicto, A., Late Palaeozoic-Mesozoic tectonic evolution of the Trans-Altai and South Gobi Zones in southern Mongolia based on structural and geochronological data. *Gondwana Research*, resubmitted after revision.

Hacker, B.R., Kelemen, P.B., Behn, M.D., 2007. Continental relamination drives compositional and physical-property changes in the lower crust, *Eos Trans. AGU Fall Meeting Suppl.*, San Francisco.

Hall, R., 2009. The Eurasian SE Asian margin as a modern example of an accretionary orogen, *Geological Society Special Publication*, pp. 351-372.

Hartley, A.J., Otava, J., 2001. Sediment provenance and dispersal in a deep marine foreland basin: The Lower Carboniferous Culm Basin, Czech Republic. *Journal of the Geological Society* 158, 137-150.

Hasalová, P., Janoušek, V., Schulmann, K., Štípská, P., Erban, V., 2008. From orthogneiss to migmatite: Geochemical assessment of the melt infiltration model in the Gföhl Unit (Moldanubian Zone, Bohemian Massif). *Lithos* 102, 508-537.

Havlíček, V., 1981. Development of a linear sedimentary depression exemplified by the Prague Basin (Ordovician-Middle Devonian; Barrandian area - Central Bohemia). *Sbor. Geol. Věd, Geol.* 35, 7-48.

Hawkesworth, C.J., Dhuime, B., Pietranik, A.B., Cawood, P.A., Kemp, A.I.S., Storey, C.D., 2010. The generation and evolution of the continental crust. *Journal of the Geological Society* 167, 229-248.

Hecht, L., Vignerresse, J.L., Morteani, G., 1997. Constraints on the origin of zonation of the granite complexes in the Fichtelgebirge (Germany and Czech Republic): Evidence from a gravity and geochemical study. *International Journal of Earth Sciences* 86, S93-S109.

Hegner, E., Klemd, R., Kröner, A., Corsini, M., Alexeiev, D.V., Iaccheri, L.M., Zack, T., Dulski, P., Xia, X., Windley, B.F., 2010. Mineral ages and p-t conditions of late paleozoic high-pressure eclogite and provenance of mélange sediments from atbashi in the south tianshan orogen of kyrgyzstan. *American Journal of Science* 310, 916-950.

Helo, C., Hegner, E., Kröner, A., Badarch, G., Tomurtogoo, O., Windley, B.F., Dulski, P., 2006. Geochemical signature of Paleozoic accretionary complexes of the Central Asian Orogenic Belt in South Mongolia: Constraints on arc environments and crustal growth. *Chemical Geology* 227, 236-257.

Hendrix, M.S., Graham, S.A., Amory, J.Y., Badarch, G., 1996. Noyon Uul syncline, southern Mongolia: Lower Mesozoic sedimentary record of the tectonic amalgamation of central Asia. *Bulletin of the Geological Society of America* 108, 1256.

Hetényi, G., Cattin, R., Brunet, F., Bollinger, L., Vergne, J., Nábělek, J.L., Diament, M., 2007. Density distribution of the India plate beneath the Tibetan plateau: Geophysical and petrological constraints on the kinetics of lower-crustal eclogitization. *Earth and Planetary Science Letters* 264, 226-244.

Holub, F.V., Cocherie, A., Rossi, P., 1997. Radiometric dating of granitic rocks from the Central Bohemian Plutonic Complex (Czech Republic): Constraints on the chronology of thermal and tectonic events along the Moldanubian-Barrandian boundary. *Comptes Rendus de l'Academie de Sciences - Serie IIa: Sciences de la Terre et des Planetes* 325, 19-26.

Hrouda, F., and Chlupáčová M., 1993. Geologický model západní části Českého masívu ve vazbě na ultrahluboký VRT (KTB-1) V SRN. Czech Geological Survey report.

Hrouda, F., Chlupáčová, M., 1993. Geologický model západní části Českého masívu ve vazbě na ultrahluboký VRT (KTB-1) V SRN. Czech Geological Survey report.

Hrubcová, P., Geissler, W.H., 2009. The crust-mantle transition and the Moho beneath the Vogtland/West Bohemian region in the light of different seismic methods. *Studia Geophysica et Geodaetica* 53, 275-294.

Hrubcová, P., Šroda, P., Špičák, A., Guterch, A., Grad, M., Keller, G.R., Brueckl, E., Thybo, H., 2005. Crustal and uppermost mantle structure of the Bohemian Massif based on

CELEBRATION 2000 data. *Journal of Geophysical Research B: Solid Earth* 110, 1-21.

Ibrmajer, J., 1981. Geological interpretation of gravity maps of Czechoslovakia. *Geophysical syntheses in Czechoslovakia*, 135-148.

Ionov, D., 1998. Trace element composition of mantle-derived carbonates and coexisting phases in peridotite xenoliths from alkali basalts. *Journal of Petrology* 39, 1931-1941.

Jahn, B.M., 2004. The Central Asian Orogenic Belt and growth of the continental crust in the Phanerozoic, in: Malpas, J., Fletcher, C.J.N., Ali, J.R., Aitchison, J.C. (Ed.), *Geological Society of London*, pp. 73-100.

Jahn, B.M., Capdevila, R., Liu, D., Vernon, A., Badarch, G., 2004. Sources of Phanerozoic granitoids in the transect Bayanhongor-Ulaan Baatar, Mongolia: geochemical and Nd isotopic evidence, and implications for Phanerozoic crustal growth. *Journal of Asian Earth Sciences* 23, 629-653.

Janoušek, V., Braithwaite, C.J.R., Bowes, D.R., Gerdes, A., 2004. Magma-mixing in the genesis of Hercynian calc-alkaline granitoids: An integrated petrographic and geochemical study of the Sázava intrusion, Central Bohemian Pluton, Czech Republic. *Lithos* 78, 67-99.

Janoušek, V., Vrána, S., Erban, V., Vokurka, K., Drábek, M., 2008. Metabasic rocks in the varied group of the Moldanubian zone, southern Bohemia - Their petrology, geochemical character and possible petrogenesis. *Journal of Geosciences* 53, 31-64.

Johnston, S.T., 2001. The Great Alaskan Terrane Wreck: Reconciliation of paleomagnetic and geological data in the Northern Cordillera. *Earth and Planetary Science Letters* 193, 259.

Jones, D.L., Howell, D.G., Coney, P.J., Monger, J.W.H., 1983. Recognition, character, and analysis of tectonostratigraphic terranes in western North America. *Accretion tectonics in the circum-Pacific regions. Proc. seminar, 1981, Tomakomai*, 21-35.

Jones, D.L., Howell, D. G., Coney, P. J., Monger, J. W. H., 1983. Recognition, Character and Analysis of Tectonostratigraphic Terranes In Western North America. *Journal of Geological Education* 31, 295-303.

Jones, D.L., Silberling, N. J., Hillhouse J.W., 1977. Wrangellia—A displaced terrane in northwestern North America. *Canadian Journal of Earth Sciences* 14, 2565-2577.

Kalvoda, J., Babek, O., Fatka, O., Leichmann, J., Melichar, R., Nehyba, S., Spacek, P., 2008. Brunovistulian terrane (Bohemian Massif, Central Europe) from late Proterozoic to late Paleozoic: A review. *International Journal of Earth Sciences* 97, 497-518.

Kane, M.F., 1962. A comprehensive system of terrain corrections using a digital computer. *Geophysics* 27.

Kastl, E., Tonika, J., 1984. The Mariánské Lázně metaophiolite complex (West Bohemia). *Krystalinikum* 17, 59-76.

Khand, Y., Badamgarav, D., Ariunchimeg, Y., Barsbold, R., 2000. Cretaceous system in Mongolia and its depositional environments.

Konopásek, J., Schulmann, K., 2005. Contrasting Early Carboniferous field geotherms:

Evidence for accretion of a thickened orogenic root and subducted Saxothuringian crust (Central European Variscides). *Journal of the Geological Society* 162, 463-470.

Kopylova, M.G., O'Reilly, S.Y., Genshaft, Y.S., 1995. Thermal state of the lithosphere beneath Central Mongolia: evidence from deep-seated xenoliths from the Shavaryn-Saram volcanic centre in the Tariat depression, Hangai, Mongolia. *Lithos* 36, 243-255.

Kossmat, F., 1927. Gliederung des varistischen Gebirgsbaues. *Abh. Sächs. Geol. Landesamt* 1, 1-39.

Kovalenko, V.I., Yarmolyuk, V.V., Kovach, V.P., Kotov, A.B., Kozakov, I.K., Salnikova, E.B., Larin, A.M., 2004. Isotope provinces, mechanisms of generation and sources of the continental crust in the Central Asian mobile belt: geological and isotopic evidence. *Journal of Asian Earth Sciences* 23, 605-627.

Kovalenko, V.I., Yarmolyuk, V.V., Sal'nikova, E.B., Kozlovsky, A.M., Kotov, A.B., Kovach, V.P., Savatenkov, V.M., Vladykin, N.V., Ponomarchuk, V.A., 2006. Geology, geochronology, and geodynamics of the Khan Bogd alkali granite pluton in southern Mongolia. *Geotectonics* 40, 450-466.

Kozakov, I.K., Sal'nikova, E.B., Wang, T., Didenko, A.N., Plotkina, Y.V., Podkovyrov, V.N., 2007. Early Precambrian crystalline complexes of the Central Asian microcontinent: Age, sources, tectonic position. *Stratigraphy and Geological Correlation* 15, 121-140.

Kröner, A., Lehmann, J., Schulmann, K., Demoux, A., Lexa, O., Tomurhuu, D., Štípská, P., Otgonbator, D., Liu, D.Y., Wingate, M.T.D., 2010. Lithostratigraphic and geochronological constraints on the evolution of the Central Asian Orogenic Belt in SW Mongolia: Early Paleozoic rifting followed by late Paleozoic accretion. *American Journal of Science* 310, 523-574.

Kruk, N.N., Rudnev, S.N., Vladimirov, A.G., Shokalsky, S.P., Kovach, V.P., Serov, P.A., Volkova, N.I., 2011. Early–Middle Paleozoic granitoids in Gorny Altai, Russia: Implications for continental crust history and magma sources. *Journal of Asian Earth Sciences* 42, 928-948.

Kübler, B., Goy-Eggenberger, D., 2001. Illite crystallinity revisited: outcome of knowledge acquisition of the last thirty years. *La cristallinité de l'illite revisitée: Un bilan des connaissances acquises ces trente dernières années* 36, 143-157.

Kulakov, I.Y., 2008. Upper mantle structure beneath southern Siberia and Mongolia, from regional seismic tomography. *Russian Geology and Geophysics* 49, 187-196.

Kuzmichev, A., Kröner, A., Hegner, E., Dunyi, L., Yusheng, W., 2005. The Shishkhid ophiolite, northern Mongolia: A key to the reconstruction of a Neoproterozoic island-arc system in central Asia. *Precambrian Research* 138, 125-150.

Lafehr, T.R., 1991a. An exact solution for the gravity curvature (Bullard B) correction. *Geophysics* 56, 1179-1184.

Lafehr, T.R., 1991b. Standardization in gravity reduction. *Geophysics* 56, 1170-1178.

Lamb, M.A., Badarch, G., 1997. Paleozoic sedimentary basins and volcanic arc systems of southern Mongolia: new stratigraphic and sedimentologic constraints. *International Geology Review* 39, 542-576.

Lamb, M.A., Badarch, G., 2001. Paleozoic sedimentary basins and volcanic arc systems of southern Mongolia: New geochemical and petrographic constraints. *Memoir 194: Paleozoic and Mesozoic Tectonic Evolution of Central and Eastern Asia: From Continental Assembly to Intracontinental Deformation* 194, 117-149.

Lamb, M.A., Badarch, G., Navratil, T., Poier, R., 2008. Structural and geochronologic data from the Shin Jinst area, eastern Gobi Altai, Mongolia: Implications for Phanerozoic intracontinental deformation in Asia. *Tectonophysics* 451, 312.

Lamb, S., Hoke, L., 1997. Origin of the high plateau in the Central Andes, Bolivia, South America. *Tectonics* 16, 623-649.

Le Pichon, X., 1968. Sea-floor spreading and continental drift. *Journal of Geophysical Research* 73, 3661-3697.

Le Pichon, X., Henry, P., Goffé, B., 1997. Uplift of Tibet: From eclogites to granulites - Implications for the Andean Plateau and the Variscan belt. *Tectonophysics* 273, 57-76.

Lehmann, J., Schulmann, K., Lexa, O., Corsini, M., Kröner, A., Štípská, P., Tomurhuu, D., Otgonbator, D., 2010. Structural constraints on the evolution of the Central Asian Orogenic Belt in SW Mongolia. *American Journal of Science* 310, 575-628.

Li, J.-Y., 2006. Permian geodynamic setting of Northeast China and adjacent regions: closure of the Paleo-Asian Ocean and subduction of the Paleo-Pacific Plate. *Journal of Asian Earth Sciences* 26, 207-224.

Lin, W., Wang, Q., 2006. Late Mesozoic extensional tectonics in the North China block: a crustal response to subcontinental mantle removal? *Bulletin de la Société Géologique de France* 177, 287-297.

Lister, G.S., Forster, M.A., Rawling, T.J., 2001. Episodicity during orogenesis. *Geological Society Special Publication*, 89.

Loiselle, M.C., Wones, D.R., 1979. Characteristics and origin of anorogenic granites, *Geological Society of America Abstracts with Programs* p. 468.

Makovsky, Y., Klemperer, S.L., 1999. Measuring the seismic properties of Tibetan bright spots: Evidence for free aqueous fluids in the Tibetan middle crust. *Journal of Geophysical Research B: Solid Earth* 104, 10795-10825.

Markova, N.G., 1975. Stratigraphy of the early and Middle Paleozoic of Western Mongolia. Moscow Nauka Press.

Martinez Catalan, J.R., 2012. The Central Iberian arc, an orocline centered in the Iberian Massif and some implications for the Variscan belt. *International Journal of Earth Sciences* 101, 1299-1314.

Maruyama, S., Parkinson, C.D., 2000. Overview of the geology, petrology and tectonic framework of the high-pressure-ultrahigh-pressure metamorphic belt of the Kokchetav Massif, Kazakhstan. *Island Arc* 9, 439-455.

Massonne, H.J., 2006. Early metamorphic evolution and exhumation of felsic high-pressure granulites from the north-western Bohemian Massif. *Mineralogy and Petrology* 86,

177-202.

Matte, P., 1991. Accretionary history and crustal evolution of the Variscan belt in Western Europe. *Tectonophysics* 196, 309-337.

McKenzie, D.P., Parker, R.L., 1967. The North Pacific: An example of tectonics on a sphere. *Nature* 216, 1276-1280.

Medaris Jr, L.G., Beard, B.L., Johnson, C.M., Valley, J.W., Spicuzza, M.J., Jelínek, E., Misár, Z., 1995. Garnet pyroxenite and eclogite in the Bohemian Massif: geochemical evidence for Variscan recycling of subducted lithosphere. *Geologische Rundschau* 84, 489-505.

Meng, Q.-R., 2003. What drove late Mesozoic extension of the northern China–Mongolia tract? *Tectonophysics* 369, 155-174.

Meng, Q.-R., Hu, J.-M., Jin, J.-Q., Zhang, Y., Xu, D.-F., 2003. Tectonics of the late Mesozoic wide extensional basin system in the China–Mongolia border region. *Basin Research* 15, 397-415.

Miller, H.G., Singh, V., 1994. Potential field tilt—a new concept for location of potential field sources. *Journal of Applied Geophysics* 32, 213-217.

Monger, J.W.H., Price, R.A., Tempelmankluit, D.J., 1982. Tectonic accretion and the origin of the 2 major metamorphic and plutonic belts in the Canadian Cordillera. *Geology* 10, 70-75.

Moore, G.W., 1973. Westward Tidal Lag as the Driving Force of Plate Tectonics. *Geology* 1, 99-100.

Mordvinova, V.V., Artemyev, A.A., 2010. The three-dimensional shear velocity structure of lithosphere in the southern Baikal rift system and its surroundings. *Russian Geology and Geophysics* 51, 694-707.

Mordvinova, V.V., Deschamps, A., Dugarmaa, T., Deverchère, J., Ulziibat, M., Sankov, V.A., Artemyev, A.A., Perrot, J., 2007. Velocity structure of the lithosphere on the 2003 Mongolian-Baikal transect from SV waves. *Izvestiya, Physics of the Solid Earth* 43, 119-129.

Nabighian, M.N., 1972. The analytic signal of two-dimensional magnetic bodies with polygonal cross-section: its properties and use for automated anomaly interpretation. *Geophysics* 37, 507-517.

Nabighian, M.N., 1974. Additional comments on the analytic signal of two-dimensional magnetic bodies with polygonal cross-section. *Geophysics* 39, 85-92.

Nagy, D., 1966. The prism method for terrain corrections using digital computers. *Pure and Applied Geophysics* 63, 31-39.

Nelson, K.D., Zhao, W., Brown, L.D., Kuo, J., Che, J., Liu, X., Klemperer, S.L., Makovsky, Y., Meissner, R., Mechie, J., Kind, R., Wenzel, F., Ni, J., Nabelek, J., Chen, L., Tan, H., Wei, W., Jones, A.G., Booker, J., Unsworth, M., Kidd, W.S.F., Hauck, M., Alsdorf, D., Ross, A., Cogan, M., Wu, C., Sandvol, E., Edwards, M., 1996. Partially molten middle crust beneath southern Tibet: Synthesis of project INDEPTH results. *Science* 274, 1684-1685.

Nettleton, L.L., 1939. Determination of density for reduction of gravimeter observations. *Geophysics* 4, 176-183.

Nowell, D.A.G., 1999. Gravity terrain corrections — an overview. *Journal of Applied Geophysics* 42, 117-134.

O'Brien, P.J., 2000. Orogenic Processes: Quantification and Modelling in the Variscan Belt. The fundamental Variscan problem: high-temperature metamorphism at different depths and high-pressure metamorphism at different temperatures, 369-386.

O'Brien, P.J., 2008. Challenges in high-pressure granulite metamorphism in the era of pseudosections: Reaction textures, compositional zoning and tectonic interpretation with examples from the Bohemian Massif. *Journal of Metamorphic Geology* 26, 235-251.

O'Brien, P.J., Vrána, S., 1995. Eclogites with a short-lived granulite facies overprint in the Moldanubian Zone, Czech Republic: petrology, geochemistry and diffusion modelling of garnet zoning. *Geologische Rundschau* 84, 473-488.

Oncken, O., Hindle, D., Kley, J., Elger, K., Victor, P., Schemmann, K., 2006. Deformation of the Central Andean upper plate system - facts, fiction, and constraints for plateau models. *The Andes - Active Subduction Orogeny*, 3-27.

Oncken, O., Sobolev, S., Stiller, M., Asch, G., Haberland, C., Mechie, J., Yuan, X., Lüchen, E., Giese, P., Wigger, P., Lueth, S., Scheuber, E., Götze, H.J., Brasse, H., Buske, S., Yoon, M.K., Shapiro, S., Rietbrock, A., Chong, G., Wilke, H.G., Gonzales, G., Bravo, P., Vieytes, H., Martinez, E., Rössling, R., Ricaldi, E., 2003. Seismic imaging of a convergent continental margin and plateau in the central Andes (Andean Continental Research Project 1996 (ANCORP'96)). *Journal of Geophysical Research B: Solid Earth* 108.

Ondra, P., Hanák, J., 1984. Densities of principal rock types of the Moldanubicum on Czechoslovak territory. *Geofyzika, Casopis pro mineralogii ageologii* 29.

Parfenov, L.M., Bulgatov, A.N., Gordienko, I.V., 1995. Terranes and accretionary history of the Transbaikalian orogenic belts. *International Geology Review* 37, 736-751.

Parfenov, L.M., Khanchuk, A.I., Badarch, G., Miller, R.J., Naumova, V.V., Nokleberg, W.J., Ogasawara, M., Prokopyev, A.V., Yan, H., 2003. Preliminary Northeast Asia Geodynamics Map. U.S. Geological Survey Open-File Report 03-205.

Patzwahl, R., Mechie, J., Schulze, A., Giese, P., 1999. Two-dimensional velocity models of the Nazca plate subduction zone between 19.5° S and 25° S from wide-angle seismic measurements during the CINCA95 project. *Journal of Geophysical Research B: Solid Earth* 104, 7293-7317.

Pavlis, N., Kenyon, S., Factor, J., Holmes, S., 2008. Earth gravitational model 2008, pp. 761-763.

Perchuk, L., 1989. Evolution of Metamorphic Belts. P-T-fluid regimes of metamorphism and related magmatism with specific reference to the granulite-facies Sharyzhalgay complex of Lake Baikal, 275-292.

Perchuk, L.L., Podladchikov, Y.Y., Polyakov, A.N., 1992. Hydrodynamic modelling of some metamorphic processes. *Journal of Metamorphic Geology* 10, 311-319.

Peschler, A.P., Benn, K., Roest, W.R., 2006. Gold-bearing fault zones related to Late Archean orogenic folding of upper and middle crust in the Abitibi granite-greenstone belt, Ontario. *Precambrian Research* 151, 143-159.

Petit, C., Déverchère, J., Calais, E., San'kov, V., Fairhead, D., 2002. Deep structure and mechanical behavior of the lithosphere in the Hangai-Hövsögöl region, Mongolia: New constraints from gravity modelling. *Earth and Planetary Science Letters* 197, 133-149.

Petit, C., Tiberi, C., Deschamps, A., Déverchère, J., 2008. Teleseismic traveltimes, topography and the lithospheric structure across central Mongolia. *Geophysical Research Letters* 35.

Petrakakis, K., 1997. The eclogites in the Monotonous Series of the Moldanubian zone and the theory of thermal pulses: A discussion. *Geologische Rundschau* 86, 710-715.

Phillips, J.D., 1997. Potential-field geophysical software for the PC, version 2.2: , U.S. Geological Survey Open-File Report, pp. 97-725.

Pierce, J.A., Harris, N.W., Tindle, A.G., 1984. Trace element discrimination diagrams for the tectonic interpretation of granitic rocks. *Journal of Petrology* 25, 956-983.

Pitra, P., Burg, J.P., Schulmann, K., Ledru, P., 1994. Late orogenic extension in the Bohemian Massif: petrostructural evidence in the Hlinsko region. *Geodinamica Acta* 7, 15-30.

Plaumann, S., 1983. Die schwerekarte 1:500000 der Bundesrepublik Deutschland (Bouguer-Anomalien). *Blatt Nord. Geol. Jb.* E27, 3-16.

Plaumann, S., 1987. Karte der Bouguer-Anomalien in der Bundesrepublik Deutschland 1:1 500.000. *Geol. Jb* 40, 3-7.

Plesch, A., Oncken, O., 1999. Orogenic wedge growth during collision - constraints on mechanics of a fossil wedge from its kinematic record (Renohercynian FTB, Central Europe). *Tectonophysics* 309, 117-139.

Polanský, J., 1978. Geophysikalische Erforschung des Gebirges Slavkovský les. *Journal of Geological Sciences CSSR* 15, 7-27.

Polansky, J., Skvor, V., 1975. Strukturotektonická problematika severozápadních. *Cech. Sborník Geologický* 13, 47-64.

Prince, C.I., Kosler, J., Vance, D., Günther, D., 2000. Comparison of laser ablation ICP-MS and isotope dilution REE analyses - implications for Sm-Nd garnet geochronology. *Chemical Geology* 168, 255-274.

Qu, J.F., Xiao, W.J., Windley, B.F., Han, C.M., Mao, Q.G., Ao, S.J., Zhang, J.E., 2011. Ordovician eclogites from the Chinese Beishan: Implications for the tectonic evolution of the southern Altaids. *Journal of Metamorphic Geology* 29, 803-820.

Racek, M., Štípská, P., Pitra, P., Schulmann, K., Lexa, O., 2006. Metamorphic record of burial and exhumation of orogenic lower and middle crust: A new tectonothermal model for the Drosendorf window (Bohemian Massif, Austria). *Mineralogy and Petrology* 86, 221-251.

Reid, A.B., Allsop, J.M., Granser, H., Millett, A.J., Somerton, I.W., 1990. Magnetic

interpretation in three dimensions using Euler deconvolution. *Geophysics* 55, 80-91.

Ren, J., Tamaki, K., Li, S., Junxia, Z., 2002. Late Mesozoic and Cenozoic rifting and its dynamic setting in Eastern China and adjacent areas. *Tectonophysics* 344, 175-205.

Rey, P., Vanderhaeghe, O., Teyssier, C., 2001. Gravitational collapse of the continental crust: Definition, regimes and modes. *Tectonophysics* 342, 435-449.

Ripington, S., Cunningham, D., England, R., 2008. Structure and petrology of the Altan Uul ophiolite: New evidence for a Late carboniferous suture in the Gobi Altai, southern Mongolia. *Journal of the Geological Society* 165, 711.

Rojas-Agramonte, Y., Kröner, A., Demoux, A., Xia, X., Wang, W., Donskaya, T., Liu, D., Sun, M., 2011. Detrital and xenocrystic zircon ages from Neoproterozoic to Palaeozoic arc terranes of Mongolia: Significance for the origin of crustal fragments in the Central Asian Orogenic Belt. *Gondwana Research* 19, 751-763.

Rossi, P., Oggiano, G., Cocherie, A., 2009. A restored section of the "southern Variscan realm" across the Corsica-Sardinia microcontinent. *Comptes Rendus - Geoscience* 341, 224-238.

Rubatto, D., Ferrando, S., Compagnoni, R., Lombardo, B., 2010. Carboniferous high-pressure metamorphism of Ordovician protoliths in the Argentera Massif (Italy), Southern European Variscan belt. *Lithos* 116, 65-76.

Rudnick, R.L., 1995. Making continental crust. *Nature* 378, 571-578.

Rudnick, R.L., Fountain, D.M., 1995. Nature and composition of the continental crust: A lower crustal perspective. *Reviews of Geophysics* 33, 267-309.

Růžek, B., Hrubcová, P., Novotný, M., Špičák, A., Karousová, O., 2007. Inversion of travel times obtained during active seismic refraction experiments CELEBRATION 2000, ALP 2002 and SUDETES 2003. *Studia Geophysica et Geodaetica* 51, 141-164.

Ruzhentsev, S.V., 2001. The Variscan belt of south Mongolia and Dzungaria, in: Dergunov, A.B. (Ed.), *Tectonics, magmatism, and metallogeny of Mongolia*. Routledge, London, pp. 61-94.

Ruzhentsev, S.V., and Pospelov, I.I., 1992. The south Mongolian Variscan fold system. *Geotectonics* 26, 383-395.

Ruzhentsev, S.V., Badarch, G., Voznesenskaya, T.A., 1985. Tectonics of the Trans-Altai zone of Mongolia (Gurvansaykhan and Dzolen ranges). *Geotectonics* 19, 276-284.

Ruzhentsev, S.V., Pospelov, II, Badarch, G., 1992. The Inner-Mongolia ophiolitic sutures. *Doklady Akademii Nauk SSSR* 322, 953-958.

Safonova, I., Seltmann, E., Kröner, A., Gladkochub, D., Schulmann, K., Xiao, W., Kim, J., Komiya, T., Sun, M., 2011. A new concept of continental construction in the Central Asian Orogenic Belt: (Compared to actualistic examples from the Western Pacific). *Episodes* 34, 186-196.

Safonova, I.Y., Utsunomiya, A., Kojima, S., Nakae, S., Tomurtogoo, O., Filippov, A.N.,

Koizumi, K., 2009. Pacific superplume-related oceanic basalts hosted by accretionary complexes of Central Asia, Russian Far East and Japan. *Gondwana Research* 16, 587-608.

Salem, A., Williams, S., Fairhead, J.D., Ravat, D., Smith, R., 2007. Tilt-depth method. *The Leading Edge* 26, 1502-1505.

Schermer E.R., H., D.G., Jones, D.L., 1984. The Origin of Allochthonous Terranes: Perspectives on the Growth and Shaping of Continents. *Annual Review of Earth and Planetary Sciences* 12, 107-131.

Scheuven, D., Zulauf, G., 2000. Exhumation, strain localization, and emplacement of granitoids along the western part of the Central Bohemian shear zone(Bohemian Massif). *International Journal of Earth Sciences* 89, 627-651.

Schilling, F.R., Partzsch, G.M., 2001. Quantifying partial melt fraction in the crust beneath and Central Andes and the Tibetan Plateau. *Physics and Chemistry of the Earth, Part A: Solid Earth and Geodesy* 26, 239-246.

Schmadicke, E., Mezger, K., Cosca, M.A., Okrusch, M., 1995. Variscan Sm-Nd and Ar-Ar ages of eclogite facies rocks from the Erzgebirge, Bohemian Massif. *Journal of Metamorphic Geology* 13, 537-552.

Schmidt, S., Götze, H.J., 1998. Interactive visualization and modification of 3D-models using GIS-functions. *Physics and Chemistry of the Earth* 23, 289-295.

Schmidt, S., Götze, H.J., 1999. Integration of data constraints and potential field modelling - an example from southern lower saxony, Germany. *Physics and Chemistry of the Earth, Part A: Solid Earth and Geodesy* 24, 191-196.

Schulmann, K., Konopásek, J., Janoušek, V., Lexa, O., Lardeaux, J.M., Edel, J.B., Štípská, P., Ulrich, S., 2009. An Andean type Palaeozoic convergence in the Bohemian Massif. *Comptes Rendus - Geoscience* 341, 266-286.

Schulmann, K., Kröner, A., Hegner, E., Wendt, I., Konopásek, J., Lexa, O., Štípská, P., 2005. Chronological constraints on the pre-orogenic history, burial and exhumation of deep-seated rocks along the eastern margin of the Variscan orogen, Bohemian Massif, Czech Republic. *American Journal of Science* 305, 407-448.

Schulmann, K., Lexa, O., Štípská, P., Racek, M., Tajčmanová, L., Konopásek, J., Edel, J.B., Peschler, A., Lehmann, J., 2008. Vertical extrusion and horizontal channel flow of orogenic lower crust: Key exhumation mechanisms in large hot orogens? *Journal of Metamorphic Geology* 26, 273-297.

Schulmann, K., Paterson, S., 2011. Geodynamics: Asian continental growth. *Nature Geoscience* 4, 827-829.

Schulmann, K., Schaltegger, U., Jezek, J., Thompson, A.B., Edel, J.B., 2002. Rapid burial and exhumation during orogeny: Thickening and synconvergent exhumation of thermally weakened and thinned crust (Variscan Orogen in Western Europe). *American Journal of Science* 302, 856-879.

Seltmann, R., Armstrong, R., Dolgoplova, A., Yakubchuk, A., Konopelko, D., Creaser, R.A., Morelli, R., Zhang, X., Chen, C., 2008. Granitic magmatism and related mineralization

in the Altaids: Case study from the Tianshan mineral belt, 18th Annual V.M. Goldschmidt Conference. Supplement to *Geochimica et Cosmochimica Acta* Vancouver, Canada.

Seltmann, R., Konopelko, D., Biske, G., Divaev, F., Sergeev, S., 2011. Hercynian post-collisional magmatism in the context of Paleozoic magmatic evolution of the Tien Shan orogenic belt. *Journal of Asian Earth Sciences* 42, 821-838.

Şengör, A.M.C., Natal'in, B.A., 1996. Palaeotectonics of Asia: fragments of a synthesis, in: Rubey Colloquium, C.U.P., Cambridge (Ed.), *The Tectonic Evolution of Asia*, pp. 486-640.

Şengör, A.M.C., Natal'in, B.A., Burtman, V.S., 1993. Evolution of the Altaid tectonic collage and Paleozoic crustal growth in Eurasia. *Nature* 364, 299-307.

Sengor, A.M.C.D., J. F., 1990. Terranology: vice or virtue? *Philosophical Transactions of the Royal Society of London A* 331, 457-477.

Smith, R.S., Thurston, J.B., Dai, T-F, MacLeod, I.N., 1998. iSPITM— the improved source parameter imaging method. *Geophysical Prospecting* 46, 141-151.

Spakman, W., Hall, R., 2010. Surface deformation and slab-mantle interaction during Banda arc subduction rollback. *Nature Geoscience* 3, 562-566.

Spence, W., 1987. Slab pull and the seismotectonics of subducting lithosphere. *Rev. Geophys.* 25, 55-69.

Springer, M., 1999. Interpretation of heat-flow density in the Central Andes. *Tectonophysics* 306, 377-395.

Steiger, R.H., Jäger, E., 1977. Subcommission on geochronology: Convention on the use of decay constants in geo- and cosmochemistry. *Earth and Planetary Science Letters* 36, 359.

Štípská, P., Powell, R., 2005a. Constraining the P-T path of a MORB-type eclogite using pseudosections, garnet zoning and garnet-clinopyroxene thermometry: An example from the Bohemian Massif. *Journal of Metamorphic Geology* 23, 725-743.

Štípská, P., Powell, R., 2005b. Does ternary feldspar constrain the metamorphic conditions of high-grade meta-igneous rocks? Evidence from orthopyroxene granulites, Bohemian Massif. *Journal of Metamorphic Geology* 23, 627-647.

Štípská, P., Schulmann, K., Kröner, A., 2004. Vertical extrusion and middle crustal spreading of omphacite granulite: A model of syn-convergent exhumation (Bohemian Massif, Czech Republic). *Journal of Metamorphic Geology* 22, 179-198.

Štípská, P., Schulmann, K., Lehmann, J., Corsini, M., Lexa, O., Tomurhuu, D., 2010. Early Cambrian eclogites in SW Mongolia: Evidence that the Palaeo-Asian Ocean suture extends further east than expected. *Journal of Metamorphic Geology* 28, 915-933.

Štípská, P., Schulmann, K., Powell, R., 2008. Contrasting metamorphic histories of lenses of high-pressure rocks and host migmatites with a flat orogenic fabric (Bohemian Massif, Czech Republic): A result of tectonic mixing within horizontal crustal flow? *Journal of Metamorphic Geology* 26, 623-646.

Štípská, P., Schulmann, K., Thompson, A.B., Ježek, J., Kröner, A., 2001. Thermo-

mechanical role of a cambro-ordovician paleorift during the Variscan collision: The NE margin of the Bohemian Massif. *Tectonophysics* 332, 239-253.

Stosch, H.G., Ionov, D.A., Puchtel, I.S., Galer, S.J.G., Sharpouri, A., 1995. Lower crustal xenoliths from Mongolia and their bearing on the nature of the deep crust beneath central Asia. *Lithos* 36, 227-242.

Suess, E., 1901. *Das Antlitz der Erde*. F. Tempsky, Wien.

Suess, F.E., 1926. Intrusionstektonik und Wandertektonik im variszischen Grundgebirge. *Intrusionstektonik und Wandertektonik im Variszischen Grundgebirge*, 268.

Tajčmanová, L., Konopásek, J., schulmann, K., 2006. Thermal evolution of the orogenic lower crust during exhumation within a thickened Moldanubian root of the Variscan belt of Central Europe. *Journal of Metamorphic Geology* 24, 119-134.

Telford, W.M., Geldart, L. P., Sheriff, R. E., 1990. *Applied Geophysics* (2nd Edition). Cambridge University Press.

Thompson, D.T., 1982. EULDPH: a new technique for making computer-assisted depth estimates from magnetic data. *Geophysics* 47, 31-37.

Thurston, J.B., Smith, R.S., 1997. Automatic conversion of magnetic data to depth, dip, and susceptibility contrast using the SPI (TM) method. *Geophysics* 62, 807-813.

Togtokh, D., Gurtsoo, S., Lhundev, S., Bomboroo, G., Tooruul, I., Burentogs, J., Bator, C., Tomorchodor, C., Bilegsayhan, C., Minzhin, C., Bat-Olzy, S., 1986. Report N°3912.

Tomek, C., 2007. Central parts of the Bohemian Massif revisited: New interpretation of deep reflection seismic line 9HR in West and South Bohemia. In: Special meeting of French and Czech Geological Societies "Mechanics of Variscan Orogeny: a modern view on orogenic research", Orleans September 2007. *Géol. France* 2, 165.

Tomek, C., Dvořáková, V., Vrána, S., 1997. Geological Model of Western Bohemia Related to the KTB Borehole in Germany, in: Vrána, S., tědrá, V. (Ed.), *Geological interpretation of the 9HR and 503M seismic profiles in Western Bohemia*. *Journal of Geological Sciences, Praha*, pp. 43-50.

Tomurtogoo, O., 1997a. A new tectonic scheme of the Paleozooides in Mongolia. *Mongolian Geoscientist* 3, 12-17.

Tomurtogoo, O., 1997b. A new tectonic scheme of the Paleozooides in Mongolia, in: Zhiqin, X., Yufeng, R., Xiaping, Q. (Eds.), *30th Int'l Geol. Congr.*, pp. 75-82.

Traynor, J.J., Sladen, C., 1995. Tectonic and stratigraphic evolution of the Mongolian People's Republic and its influence on hydrocarbon geology and potential. *Marine and Petroleum Geology* 12, 35-52.

Vanderhaeghe, O., 2009. Migmatites, granites and orogeny: Flow modes of partially-molten rocks and magmas associated with melt/solid segregation in orogenic belts. *Tectonophysics* 477, 119-134.

Vanderhaeghe, O., Teyssier, C., 2001. Partial melting and flow of orogens. *Tectonophysics*

342, 451-472.

Vaughan, A.P.M., Scarrow, J.H., 2003. Ophiolite obduction pulses as a proxy indicator of superplume events? *Earth and Planetary Science Letters* 213, 407.

Volkova, N.I., Sklyarov, E.V., 2007. High-pressure complexes of Central Asian Fold Belt: geologic setting, geochemistry, and geodynamic implications. *Russian Geology and Geophysics* 48, 83-90.

Wainwright, A.J., Tosdal, R.M., Wooden, J.L., Mazdab, F.K., Friedman, R.M., 2011. U-Pb (zircon) and geochemical constraints on the age, origin, and evolution of Paleozoic arc magmas in the Oyu Tolgoi porphyry Cu-Au district, southern Mongolia. *Gondwana Research* 19, 764-787.

Watson, E.B.H.M., 1983. Zircon saturation revisited: temperature and composition effects in a variety of crustal magma types. *Earth Planet Sci Lett.* 64, 295-304.

Watson, M.P., Hayward, A.B., Parkinson, D.N., Zhang, Z.M., 1987. Plate tectonic history, basin development and petroleum source rock deposition onshore China. *Marine and Petroleum Geology* 4, 205-225.

Weber, K., 1984. Variscan events: early Palaeozoic continental rift metamorphism and late Palaeozoic crustal shortening. *Variscan tectonics of the North Atlantic region*, 3-22.

Weber, K., Behr, H.J., 1983. Geodynamic interpretation of the Mid-European Variscides. *Intracontinental Fold Belts*, 427-469.

Weinberg, R.F., Schmeling, H., 1992. Polydiapirs: multiwavelength gravity structures. *Journal of Structural Geology* 14, 425-436.

Wilhem, C., Windley, B.F., Stampfli, G.M., 2012. The Altaids of Central Asia: A tectonic and evolutionary innovative review. *Earth-Science Reviews* 113, 303-341.

Wilson, J.T., 1965. A new class of faults and their bearing on continental drift. 207, 343-347.

Wilson, J.T., 1966. Did the Atlantic close and then re-open? . *Nature* 211, 676-681.

Windley, B.F., Alexeiev, D., Xiao, W., Kröner, A., Badarch, G., 2007. Tectonic models for accretion of the Central Asian Orogenic Belt. *Journal of the Geological Society* 164, 31-47.

Xiao, W., Han, C., Yuan, C., Sun, M., Lin, S., Chen, H., Li, Z., Li, J., Sun, S., 2008. Middle Cambrian to Permian subduction-related accretionary orogenesis of Northern Xinjiang, NW China: Implications for the tectonic evolution of central Asia. *Journal of Asian Earth Sciences* 32, 102-117.

Xiao, W., Windley, B.F., Yong, Y., Yan, Z., Yuan, C., Liu, C., Li, J., 2009b. Early Paleozoic to Devonian multiple-accretionary model for the Qilian Shan, NW China. *Journal of Asian Earth Sciences* 35, 323-333.

Xiao, W.J., Windley, B.F., Yuan, C., Sun, M., Han, C.M., Lin, S.F., Chen, H.L., Yan, Q.R., Liu, D.Y., Qin, K.Z., Li, J.L., Sun, S., 2009a. Paleozoic multiple subduction-accretion processes of the southern Altaids. *Am J Sci* 309, 221-270.

Xiao, W.J., Zhang, L.C., Qin, K.Z., Sun, S., Li, J.L., 2004. Paleozoic accretionary and collisional tectonics of the Eastern Tianshan (China): Implications for the continental growth of central Asia. *American Journal of Science* 304, 370-395.

Yakubchuk, A.S., Shatov, V.V., Kirwin, D., Edwards, A., Tomurtogoo, O., Badarch, G., Buryak, V.A., 2005. Gold and Base Metal Metallogeny of the Central Asian Orogenic Supercollage. *Economic Geology 100th Anniversary Volume*, 1069–1096.

Yarmolyuk, V.V., Kovalenko, V.I., Kozlovsky, A.M., Kovach, V.P., Sal'Nikova, E.B., Kovalenko, D.V., Kotov, A.B., Kudryashova, E.A., Lebedev, V.I., Eenzhin, G., 2008. Crust-forming processes in the Hercynides of the Central Asian Foldbelt. *Petrology* 16, 679.

Zaitsev, N.S., Luwsandansan, B., Marinov, N.A., Menner, V.V., Pavlova, T.G., Peive, A.V., Timofeev, P.P., Tomurtogoo, O., Yanshin, A.L., 1970. Stratigraphy and Tectonics of the Mongolian Peoples Republic. Nauka Press, Trans. Joint Soviet-Mongolian Sci. Res. Geol. Exped., Moscow.

Zaitsev, N.S., Luwsandansan, B., Yanshin, A.L., Peive, A.V., Gerbova, V.G., Krasheninnikov, V.A., Timofeev, P.P., Tomurtogoo, O., 1980. The Lower Cambrian and Carboniferous Biostratigraphy of Mongolia.

Žák, J., Holub, F.V., Verner, K., 2005. Tectonic evolution of a continental magmatic arc from transpression in the upper crust to exhumation of mid-crustal orogenic root recorded by episodically emplaced plutons: The Central Bohemian Plutonic Complex (Bohemian Massif). *International Journal of Earth Sciences* 94, 385-400.

Zonenshain L.P., K.M.I., Natapov L.M., 1990. Geology of the USSR: a plate tectonic synthesis. *in*, L.P., 1973. The evolution of Central Asiatic geosynclines through sea-floor spreading. *Tectonophysics* 19, 213-232.

Zonenshain, L.P., Kuzmin, M.I., Kononov, M.V., 1985. Absolute reconstructions of the Paleozoic oceans. *Earth and Planetary Science Letters* 74, 103-116.

Zonenshain, L.P., Suyetenko, O.D., Jamyandamba, L., Eengin, G., 1975. Structure and the axial part of South Mongolian eugeosyncline in the Dzolen Range. *Geotectonics* 4, 28-44.

Zorin, Y.A., 1999. Geodynamics of the western part of the Mongolia-Okhotsk collisional belt, Trans-Baikal region (Russia) and Mongolia. *Tectonophysics* 306, 33.

Zorin, Y.A., Belichenko, V.G., Turutanov, E.K., Kozhevnikov, V.M., Ruzhentsev, S.V., Dergunov, A.B., Filippova, I.B., Tomurtogoo, O., Arvisbaatar, N., Bayasgalan, T., Biambaa, C., Khosbayar, P., 1993. The South Siberia-Central Mongolia transect. *Tectonophysics* 225, 361.

Zorin, Y.A., Novoselova, M.R., Turutanov, E.K., Kozhevnikov, V.M., 1990. Structure of the lithosphere of the Mongolian-Siberian mountainous province. *Journal of Geodynamics* 11, 327-342.

Zulauf, G., 1997. Constriction due to subduction: evidence for slab pull in the Marianske Lazne complex (central European Variscides). *Terra Nova* 9, 232-236.

Zulauf, G., 2001. Structural style, deformation mechanisms and paleodifferential stress along an exposed crustal section: Constraints on the rheology of quartzofeldspathic rocks at supra- and infrastructural levels (Bohemian Massif). *Tectonophysics* 332, 211-237.

Zulauf, G., Bues, C., Dörr, W., Vejnar, Z., 2002a. 10 km minimum throw along the West Bohemian shear zone: Evidence for dramatic crustal thickening and high topography in Bohemian Massif (European Variscides). *International Journal of Earth Sciences* 91, 850-864.

Zulauf, G., Dörr, W., Fiala, J., Kotková, J., Maluski, H., Valverde-Vaquero, P., 2002b. Evidence for high-temperature diffusional creep preserved by rapid cooling of lower crust (North Bohemian shear zone, Czech Republic). *Terra Nova* 14, 343-354.

Zulauf, G., Zulauf, J., Bornemann, O., Kihm, N., Peinl, M., Zanella, F., 2009. Experimental deformation of a single-layer anhydrite in halite matrix under bulk constriction. Part 1: Geometric and kinematic aspects. *Journal of Structural Geology* 31, 460-474.

Communications et publications scientifiques associées au travail de thèse

Publications de rang A :

Guy, A., Edel, J.-B., Schulmann, K., Tomek, Č. & Lexa, O., 2011. A geophysical model of lower crustal structure of the Palaeozoic crustal root (Bohemian Massif): implications for modern collisional orogens. *Lithos*, Volume 124, Issues 1-2, Pages 144-157

Lexa, O., Schulmann, K., Janoušek, V., Štípská, P., Guy, A., Racek, M., 2011. Heat sources and trigger mechanisms of exhumation of HP granulites in Variscan orogenic root. *Journal of Metamorphic Geology*, Volume 29, Pages 79–102.

Guy, A., Schulmann, K., Clauer, N., Hasalova, P., Seltnann, R., Armstrong, R., Benedicto, A., Late Paleozoic-Mesozoic tectonic evolution of Trans-Altai and South Gobi Zones in southern Mongolia based on structural and geochronological data, *Gondwana Research*, submitted.

Communications scientifiques :

Posters (5, 4 en premier auteur) depuis 2009

Guy, A., Edel, J.B., Schulmann, K., Lexa, O., 2009. Gravimetric imagery of crustal structure of the Bohemian Massif: new model of structure of crustal root. *Granulites & Granulites 2009 conference in Czech Rep.*

Guy, A., Edel, J.B., Schulmann, K., Tomek, C., Lexa, O., 2010. A geophysical model of lower crustal structure of the Palaeozoic crustal root (Bohemian Massif): implications for

modern collisional orogens. Geophysical Research Abstracts Vol. 12, EGU2010-13643, 2010. EGU General Assembly 2010 – Vienna.

Maierová, P., Guy, A., Lexa, O., Čadek, O., 2010. Application of FE software Elmer to the modelling of crustal-scale processes. Geophysical Research Abstracts Vol. 12, EGU2010-13643, 2010. EGU General Assembly 2010 – Vienna.

Guy, A., Schulmann, K., Munsch, Marc, 2010. Preliminary interpretations of geophysical data of the Central Asia Orogenic Belt. International workshop on Geodynamic Evolution, Tectonics and Magmatism of the Central Asian Orogenic Belt, Altay 2010 – Novosibirsk.

Guy, A., Schulmann, K., Munsch, Marc, Lehmann, J., 2010. Geophysical potential field data interpretations to study continental construction processes of the Central Asia Orogenic Belt, ID: 951024, AGU2010-San Francisco.

Présentations orales dans le cadre du consortium c2c (crust to core) the fate of subducted material- Marie Curie Research Training Network depuis 2009.

Guy, A., Edel, J.B., Schulmann, K., Lexa, O., 2009. Studies of the Bohemian Massif and the Central Asian Orogenic Belt in an interdisciplinary way :Geological structures, gravimetric, magnetic and numerical modelling tools. Charles' University, Prague

Guy, A., Edel, J.B., Schulmann, K., Maierová, P., Lexa, O., 2010. Gravimetric and numerical modelling of crustal structures of the southwestern part of the Bohemian Massif and Central Asia Orogenic Belt starting work. Charles' University, Prague.

Guy, A., Edel, J.B., Schulmann, K., Munsch, M., Lexa, O., 2010. Consequences of subduction:

->Significance of a felsic lower crust in orogenic context (Bohemian Massif)

->Formation of accretionary orogen in the Central Asian Orogenic Belt. C2c annual meeting, Trondheim, Norway.

Remerciements

Il y a plusieurs manières de remercier, mais que quelques mots pour l'exprimer. Cette thèse n'aurait jamais pu voir le jour sans le concours de nombreuses personnes : professionnels des géosciences ou non.

Tout d'abord, je voudrais remercier tout particulièrement mon directeur de thèse Karel Schulmann. La vie d'un chercheur est un apprentissage perpétuel et j'ai bien évidemment appris énormément à ses côtés grâce à son aide, ses nombreux conseils, son expertise et sa patience.

Je voudrais également remercier Carole Petit, Wen Jiao Xiao, Gianreto Manatschal, Thierry Baudin, Jean-Marc Mieke et Zdeněk Venera d'avoir accepté de faire partie du jury de thèse.

Tout au long de la thèse, j'ai eu l'opportunité de pouvoir collaborer avec bon nombre de professionnels. Je voudrais ainsi remercier Marc Munsch et Jean-Bernard Edel pour leurs disponibilités et leurs conseils quant à la partie géophysique de ma thèse. Les discussions avec les personnes d'Areva Mines ont été très enrichissantes et leur accueil au sein de leur équipe très chaleureuse. Un grand merci à Jean-Pierre Milesi, Jean-Marc Mieke, Antonio Benedicto, mais aussi Mickael, Anne-Laure, Elodie, Anna et Régis. J'ai également une pensée pour les personnes que j'ai eu la chance de rencontrer via le programme C2C et l'Université Charles de Prague. Je pense notamment à Lada, Hanka, Yakub et Eliska avec qui j'ai pu partager de nombreux repas et des soirées dans la capitale de République Tchèque.

Un grand merci à Petra Maierová qui après avoir eu l'extrême patience de me former aux B.A.-BA de la modélisation numérique est, aujourd'hui devenue une amie.

A l'heure des remerciements, je me souviens également des tout premiers instants de cette thèse sur le terrain, en Mongolie. Merci à Pavlina pour sa bonne humeur, son enthousiasme et d'avoir su partager ses connaissances en géologie. Un grand merci à Hoyda, pour son expérience des conditions de vie et des « chemins » dans le désert de Gobi, sans lui, la mission de terrain aurait été bien plus difficile. Merci également à Ondrej, les discussions scientifiques que nous avons eues ensemble ont malheureusement été trop peu nombreuses et trop courtes, mais à chaque fois riches en perspectives.

Merci enfin à Ole Balthazar Andersen, Ivan Koulakov et Sergei Lebedev pour les discussions, les conseils avisés et les échanges de bon procédés.

Merci à Natasha, pour son sourire, sa gentillesse et sa disponibilité lors de nos discussions et prises de tête avec le logiciel Oasismontaj et GM-SYS !

Je voudrais remercier Anne-Marie Karpoff pour son sourire, son écoute et ses conseils, tout au long de ma thèse et en particulier dans la dernière ligne droite. Un merci tout particulier aussi à Annie Bouzhegaïa pour sa gentillesse, sa disponibilité, son aide et son œil aguerrie quant à l'élaboration de certaines figures de cette thèse. Merci aussi à Betty Kieffer pour sa disponibilité et son efficacité sans faille quant à la recherche des documents scientifiques variés qu'ils soient récents ou anciens.

Un grand merci également à ceux qui ont rendu cette thèse un peu plus facile administrativement et logistiquement : Ghenima, David, Joelle et Didier.

Un merci à mes co-bureaux Anne-Sophie, Emilie et Adrien pour leur bonne humeur, à toute l'équipe des nouveaux arrivants dans le monde de la thèse : Julie, Alexis, Benoît, Isabelle, Morgane et Victor-Hugo ; et enfin au dernier arrivant dans l'équipe de choc, Emilien.

Une grosse pensée pour les thésards d'hier qui ont finalement partagé la plus grande partie des instants magiques qui font partie de la vie d'une équipe de recherche dynamique. Merci à leur humour caustique, leurs joutes verbales qui ressemblaient souvent à une partie de ping-pong tant la balle était rapidement renvoyée, je remercie Etienne, Bep et Francescou pour être tout simplement eux-mêmes... A présent partis vers de nouveaux horizons, vous m'avez beaucoup manqué dans la dernière ligne droite !

Merci aussi pour les moments partagés avec Momo, Fabien, Thomas, Flavia, Manu, Joachim et Edouard.

Il y a des amitiés qui ne se créent jamais et d'autres qui se créent d'une manière surprenante et fulgurante, et qui durent malgré la distance. Je pense ainsi à Brice Randrianasolo que j'ai rencontré à l'occasion de la conférence Granulite & Granulite en 2009. Je le remercie pour son soutien et ses précieux conseils tout au long de ma thèse alors qu'il avait bien d'autres choses à gérer ! Je pense également à Tanya Sherbanenko rencontrée à la conférence sur l'Altaï à Novossibirsk en 2010. Je n'ai échangé de visu qu'une seule fois avec chacune de ces personnes puis le contact a été maintenu uniquement grâce à une correspondance par mail.

Les derniers mais non les moindres, mes amis et ma famille.

Mes amis de toujours ou presque. C'est inouïe la chance que j'ai de les connaître et de pouvoir partager des instants de vies avec eux. Albina, Alice, Anaïs, Clément, Clémentine, Elodie, Emanuelle, Emilie, Gaëlle, Jean-Rémi, Julien, Luc, Marine, Matthieu, Stéphanie, Yannick, ils ont tous, à leur manière et sans peut-être le réaliser, amené une pierre à cet édifice.

Spécial dédicace à Alice pour le dernier gros coup de main et les encouragements apportés lors de la toute dernière ligne droite ! Je te dois une fière chandelle !

Je voudrais également remercier mon grand-père, qui m'a soutenu dès la première heure dans mon choix de faire cette thèse bien qu'il ne sache pas vraiment en quoi cela consistait ! Son conseil a été : « Va aussi loin que tu peux ! Ne te soucie de rien ! », je remercie ma grand-mère aussi, une femme adorable et au grand cœur qui a une façon toute particulière de dire aux autres ce que je fais.

Mes parents, qui ont toujours été là pour moi, contre vents et marées, c'est une chance rare et précieuse. Je remercie aussi ma sœur, ma frangine, ma jumelle, Katrina, de me connaître par cœur.

Toutes ces personnes sont mes racines, ma boussole, mon nord.

Martin, merci pour ta présence et ton soutien, merci de m'aider à regarder vers l'avenir.

En espérant n'oublier personne...

LISTE DES FIGURES

Chapter I

Figure 1: Distribution of present-day collisional and accretionary orogens.	21
Figure 2: Advancing and retreating accretionary orogens.	22
Figure 3: Relief map of central Asia.	24
Figure 4: Simplified lithotectonic map of the CAO.	26
Figure 5: Main lithotectonic units of the Central Asian Orogenic Belt in Mongolia.	27
Figure 6: Outline of tectonic and geological events.	28
Figure 7: Compilation of three conceptual geodynamic models of the CAO.	30

Chapter II

Figure 1: Geological map of the Ömnögovı province.	37
Figure 2: Stratigraphic columns for the South Gobi Zone and the Trans-Altai Zone.	39
Figure 3: Massifs of magmatic rocks and geochronological ages on a geological map.	41
Figure 4: Geochemistry plots for samples of intrusive units.	47
Figure 5: U-Pb Concordia diagrams.	49
Figure 6: Structural map and interpretative cross-section of South Gobi Zone.	53
Figure 7: Structural map and interpretative cross-section of Noyon	55
Figure 8: Field photographs showing structural features observed in the South Gobi Zone.	56
Figure 9: Structural map and interpretative cross-section of Sevrey.	58
Figure 10: Field photographs showing structural features observed in the Trans-Altai Zone.	60
Figure 11: Structural map and interpretative cross-section of Nomgon and east of Nomgon.	61
Figure 12: Summary of the lithostratigraphy combined with the tectonic events.	67
Figure 13: Stereograms representing the average poles of foliations and cleavages.	69
Figure 14: Scheme of the large scale tectonic evolution of the TAZ and the SGZ.	74

Chapter III

Figure 1: Workflow for geological mapping processes.	81
Figure 2: Geological maps scanned and rectified covering the south of Mongolia.	82
Figure 3: Catalog of Landsat imageries used to review the geological maps.	83
Figure 4: Basic topological rules to get a geological map with the accurate topology.	84
Figure 5: Geological map of 1:500 000 scale over the south of Mongolia.	85
Figure 6: Geological map of the south Mongolia with the lithotectonic zones superimposed.	88
Figure 7: Stratigraphic columns for four lithotectonic zones covering the south of Mongolia.	91
Figure 8: Free air anomaly grid of the CAO.	95

Figure 9: Location of magnetic grids and characteristics of survey.	96
Figure 10: Workflow de l'exploitation des données gravimétriques.	97
Figure 10: Workflow of the gravity data processes.	
Figure 11: Anomalie de Bouguer simple calculée à partir de l'anomalie à l'air libre.	99
Figure 11: Simple Bouguer anomaly computed from the free air anomaly.	
Figure 12: Méthode de Nettleton appliquée le long d'un profil.	100
Figure 12: Method of Nettleton along a profile cross-cutting the four lithotectonic zones.	
Figure 13: Anomalie de Bouguer complète sur la Mongolie.	102
Figure 13: Complete Bouguer anomaly over Mongolia.	
Figure 14: Comparaisons des différentes corrections des anomalies gravimétriques.	104
Figure 14: Comparison of the different gravity corrections.	
Figure 15: Prolongement vers le haut de 2000 m de l'anomalie de Bouguer complète.	105
Figure 15: Upward continuation of 2000 m of the complete Bouguer anomaly.	
Figure 16: Filtre passe-haut de fréquence de coupure de 100 km à l'anomalie de Bouguer.	106
Figure 16: High-pass filter of a cutoff of 100 km of the complete Bouguer anomaly.	
Figure 17: Dérivée verticale au 1er ordre de l'anomalie de Bouguer complète.	107
Figure 17: First verticale derivative of the complete Bouguer anomaly.	
Figure 18: Workflow de l'exploitation des données magnétiques.	108
Figure 18: Workflow of the magnetic data processes.	
Figure 19: Grille nivelée et fusionnée de l'anomalie magnétique sans réduction au pôle.	111
Figure 19: Magnetic anomaly grid leveled and merge without reducing to the pole.	
Figure 20: Dérivée verticale au premier ordre de l'anomalie magnétique.	112
Figure 20: First verticale derivative of the magnetic anomaly.	
Figure 21: Dérivées horizontale au premier ordre de l'anomalie magnétique.	113
Figure 21: First horizontale derivatives of the magnetic anomaly.	
Figure 22: Angle tilt appliqué à l'anomalie magnétique.	115
Figure 22: Tilt angle of the magnetic anomaly.	
Figure 23: Signal analytique de l'anomalie magnétique.	116
Figure 23: Analytic signal of the magnetic anomaly.	
Figure 24:	
Figure 24.1.: Magnetic anomaly analysis.	118
Figure 24.2.a.: Sedimentary rocks superimposed on the magnetic anomaly map.	120

Figure 24.2.b.: Volcanic rocks superimposed on the magnetic anomaly map.	121
Figure 24.2.c.: Granitoids superimposed on the magnetic anomaly map.	123
Figure 24.2.d.: Ultramafic rocks superimposed on the magnetic anomaly map.	124
Figure 24.2.e.: Mesozoic and Cenozoic basins superimposed on the magnetic anomaly map.	125
 Figure 25:	
Figure 25.1.: Bouguer anomaly analysis.	127
Figure 25.2.a.: Sedimentary rocks superimposed on the residual Bouguer anomaly map.	128
Figure 25.2.b.: Volcanic rocks superimposed on the residual Bouguer anomaly map.	129
Figure 25.2.c.: Granitoids superimposed on the residual Bouguer anomaly map.	131
Figure 25.2.d.: Ultramafic rocks superimposed on the residual Bouguer anomaly map.	132
Figure 25.2.e.: Mesozoic and Cenozoic basins.	133
 Figure 26: Comparison of gravity and magnetic axe bodies with the geological map.	136
Figure 27: Interpretative scheme of the magnetic anomaly and the gravity anomaly.	138
Figure 28: Rose diagrams of basins and lineaments of magnetic and gravity anomalies.	141
 Chapter IV	
Figure 1: The location and the limits of the magnetic grids used for the modelling.	148
Figure 2: Bouguer anomaly grid upward 2000m	149
Figure 3: Seismic refraction profiles of PASSCAL 1992-1993 and MOBAL 2003.	150
Figure 4: Moho depth grid with contours displayed modified after the model CRUST 2.0.	151
Figure 5: Geological, magnetic and Bouguer maps with the modelling profiles superimposed.	153
Figure 6: Geological map of the region of the profile located in the south-west of Mongolia.	155
Figure 7: Magnetic anomaly map of the profile located in the south-west of Mongolia.	157
Figure 8: Bouguer anomaly map of the profile located in the south-west of Mongolia.	159
Figure 9: Geological map of the region of the profile located in the north of the central part.	160
Figure 10: Magnetic anomaly map of the profile located in the north of the central part.	161
Figure 11: Bouguer anomaly map of the profile located in the north of the central part.	162
Figure 12: Geological map of the region of the Gurvansaykhan range and Noyon syncline.	163
Figure 13: Magnetic anomaly map of the Gurvansaykhan range and the Noyon syncline.	164
Figure 14: Bouguer anomaly map of the Gurvansaykhan range and the Noyon syncline.	166
Figure 15: Geological map of the region of the profile located in the south-east of Mongolia.	167
Figure 16: Magnetic anomaly map of the profile located in the south-east of Mongolia.	168
Figure 17: Bouguer anomaly map of the profile located in the south-east of Mongolia.	170
Figure 18: Determination of the maxima from the gridded values.	172

Figure 19: Source parameter imaging (SPI) grids.	173
Figure 20: Euler deconvolution results for different structural index.	175
Figure 21: Example of the depth to basement source treatment along a profile.	176
Figure 22: Gravity and magnetic potential field model along the SW profile.	181
Figure 23: Gravity and magnetic potential field model along north of Gurvansaykhan profile.	184
Figure 24: Gravity and magnetic potential field model along the Gurvansaykhan range.	186
Figure 25: Gravity and magnetic potential field model along the Dzolen range.	187
Figure 26: Gravity and magnetic potential field model along the Noyon Uul syncline.	188
Figure 27: Geological interpretative cross section from Gurvansaykhan range to Noyon area.	189
Figure 28: Gravity and magnetic potential field model along the SE profile.	190

Chapter V

Figure 1: Simplified geological map of the Bohemian Massif with the main tectonic domains.	201
Figure 2: Bouguer anomaly map of the Bohemian Massif.	203
Figure 3: Comparison of the gravity model with seismic refraction and seismic reflection.	205
Figure 4: Map of the Moho depth compared to map of the Bouguer anomalies.	206
Figure 5: Selection of five of the nine modelled profiles.	209
Figure 6: Residual map and histogram of gravity differences.	211
Figure 7: Counterexamples of the gravity model.	212
Figure 8: Geological interpretation of the modelled gravity sections.	214
Figure 9: Model for the tectonic evolution of the Bohemian Massif.	220

LISTE DES TABLES

Chapter I

Table 1: Summary of the main differences between collisional and accretionary orogens.	20
---	----

Chapter II

Table 1: Trace elements of 69 sample rocks.	42
Table 2: U-Pb analytical data and calculated ages.	50
Table 3: XRD mineralogical data of the studied <2 m fractions.	64
Table 4: Results of the K-Ar dating.	65

Chapter III

Table 1: Summary of the geophysical and topographical data.	93
Table 2: IGRF used to reduce to the pole each different survey.	109

Chapter IV

Table 1: Geographic coordinates of profiles.	152
Table 2: Density and susceptibility of rocks used for the modelling.	179

Chapter V

Table 1: Densities of rocks used for the modelling.	207
--	-----

TABLE DES MATIÈRES

SOMMAIRE	7
AVANT-PROPOS	9
INTRODUCTION	11
CHAPTER I - INTRODUCTION TO OROGENIC SYSTEMS - GEOLOGY OF THE CENTRAL ASIAN OROGENIC BELT	17
<i>1. Collisional vs. accretionary orogens</i>	20
1.1. Distinguishing features	20
1.2. Location of contemporaneous collisional vs. accretionary orogens	21
1.3. Definition of an accretionary orogen	21
1.4. Crustal growth and continent construction	23
<i>2. The Central Asian Orogenic Belt (CAOB)</i>	24
2.1. Global setting of the CAOB	24
2.2. Litho-tectonic zonation of the CAOB	25
2.3. Tectonic evolution of the CAOB	28
2.4. Existing geodynamic model for the CAOB	29
CHAPTER II - LATE PALAEOZOIC-MESOZOIC TECTONIC EVOLUTION OF THE TRANS-ALTAI AND SOUTH GOBI ZONES (OCEANIC VS. CONTINENTAL DOMAINS) IN SOUTHERN MONGOLIA BASED ON STRUCTURAL AND GEOCHRONOLOGICAL DATA	33
<i>1. Geological setting of the Trans-Altai and the South Gobi Zones</i>	35
1.1. Geology of Ömnögovi Province	35
1.2. Lithostratigraphy of the South Gobi Zone in the Ömnögovi Province	36
<i>1.2.1. Central part of the South Gobi Zone</i>	36
<i>1.2.2. Western part of the South Gobi Zone</i>	38
1.3. Lithostratigraphy of the Trans-Altai Zone in the Ömnögovi province	38
<i>1.3.1. Eastern part of the Trans-Altai Zone</i>	38
<i>1.3.2. Western part of the Trans-Altai Zone</i>	40
<i>2. Carboniferous and Permian intermediate to felsic intrusive magmatism</i>	41

2.1. Petrology and geochemistry of granitic rocks	46
2.2. U-Pb zircon geochronology	48
3. New observations of structural geology and tectonic evolution of the South Gobi and Trans-Altai Zones	52
3.1. The South Gobi Zone	52
3.1.1. Structural geology of the Khar Ovoo Range	52
3.1.2. Structural geology across the Noyon Uul Syncline	54
3.2. The Trans-Altai Zone	57
3.2.1. Structural geology east and north-east of the Sevrey village	57
3.2.2. Structural geology of the Nomgon district	59
3.3. The South-Gobi/Trans-Altai transition	62
4. K-Ar dating of low grade fabrics	63
4.1. Analytical procedure	63
4.2. Results	63
5. Discussion	66
5.1. Tectono-sedimentary and volcanic setting of the Trans-Altai Zone and South Gobi Zone	66
5.2. Kinematic regimes of D1 and D2 deformations	68
5.3. Timing of tectonic events	69
5.4. Interpretation of the Carboniferous to Permian magmatic evolution	70
Conclusions and geodynamic model	72
 CHAPTER III - GRAVITY AND MAGNETIC FEATURES COMBINED WITH GEOLOGICAL CONSTRAINTS IN SOUTHERN MONGOLIA: REVISION OF TERRANE BOUNDARIES	 77
Introduction	79
1. Processing of a geological map of 1:500 000 scale and a GIS database	80
1.1. Harmonization of geological maps of 1:200 000 scale	81
1.1.1. Rectification of the 1:200 000 geological maps	81
1.1.2. Harmonization of the map legends	82
1.1.3. Catalog of Landsat images	82
1.2. Digitalization and topological rules	84
1.3. Geological map at 1:500 000 scale of southern Mongolia	84
2. Geology and lithostratigraphy of the south of Mongolia	87
2.1. Distribution of major rock units	87
2.2. Simplified lithostratigraphic characterization of the four tectonic zones	88
2.2.1. Lithostratigraphy of the Lake Zone	88

2.2.2. <i>Lithostratigraphy of the Gobi Altai Zone</i>	89
2.2.3. <i>Lithostratigraphy of the Trans Altaï zone</i>	90
2.2.4. <i>Lithostratigraphy of the South Gobi Zone</i>	90
3. Datasets	93
3.1. Gravity data	93
3.2. Digital Elevation Model (DEM)	94
3.3. Magnetic data	96
4. Traitements et outils d'interprétation des données de méthodes potentielles	97
4.1. Traitements et outils d'interprétation pour les données gravimétriques	97
4.1.1. <i>Traitement qualitatif des données gravimétriques : calcul de l'anomalie de Bouguer</i>	
4.1.2. <i>Anomalie à l'air libre, MNT et anomalie de Bouguer : Clivages et similitudes</i>	98
4.1.3. <i>Opérateurs de traitements et mise en valeur des données gravimétriques</i>	103
4.1.3.1. Prolongement vers le haut	104
4.1.3.2. Filtre passe-haut	104
4.1.3.3. Dérivée verticale	105
4.2. Traitements et outils d'interprétation pour les données magnétiques	106
4.2.1. <i>Nivellement des grilles</i>	107
4.2.1.1. Réduction au pôle	108
4.2.1.2. Prolongement vers le haut	109
4.2.2. <i>Traitements qualitatifs de l'anomalie magnétique</i>	110
4.2.2.1. Dérivée verticale	112
4.2.2.2. Dérivées horizontales	112
4.2.3. <i>Traitements quantitatifs : estimation des profondeurs de sources</i>	112
4.2.3.1. Angle tilt	113
4.2.3.2. Signal analytique	113
5. Geophysical patterns of southern Mongolia and comparison with the surface geology	116
5.1. Potential field maps	117
5.1.1. <i>Magnetic anomaly map</i>	117
5.1.2. <i>Residual Bouguer anomaly map</i>	117
5.2. Magnetic structures analysis	117
5.3. Gravity structures analysis	118
6. Discussion: Review of tectonic boundaries according to the synthesis of potential field and geological data	126
Conclusion of the compartmentalization into terranes of the Central Asian Orogenic Belt	134
	142

1. Geophysical datasets used for modelling	147
1.1. Magnetic data	147
1.2. Gravity grid and Bouguer anomaly	148
1.3. Seismic data	149
1.4. Moho depth	150
2. Profile locations	152
3. Geophysical and geological correlations for each profile area	154
3.1. South-west of Mongolia	154
3.1.1. Magnetic correlation	156
3.1.2. Gravity correlation	158
3.2. Central south of Mongolia	160
3.2.1. North of Gurvansaykhan Range	160
3.2.1.1. Magnetic correlation	160
3.2.1.2. Gravity correlation	162
3.2.2. In between Gurvansaykhan Range to Noyon Uul syncline	163
3.2.2.1. Magnetic correlation	163
3.2.2.2. Gravity correlation	165
3.3. South-east of Mongolia	166
3.3.1. Magnetic correlation	167
3.3.2. Gravity correlation	169
4. Data treatments to obtain an information in depth	170
4.1. Source parameter Imaging™ (SPI™)	171
4.2. Euler deconvolution over the grids and along profile	174
4.3. Analytic signal	176
5. Modelling: methodology, petrophysical data and constraints	177
5.1. Forward modelling	177
5.2. Difficulties in determining rock properties of exposed and basement rocks	178
5.3. Density and susceptibility constraints	178
6. Magnetic and gravity models	180
6.1. Profile south-west of Mongolia (Bayankhangor Province)	180
6.2. Profiles south of Mongolia (Ömnogovi Province)	182
6.2.1. Profile north of Gurvansaykhan range	183
6.2.2. Profiles between the Gurvansaykhan range and the Noyon Uul syncline	185
6.3. Profile south-east of Mongolia (Dornogovi Province)	189

<i>Conclusion</i>	191
CHAPTER V - GEOPHYSICAL MODEL OF THE VARISCAN OROGENIC ROOT (BOHEMIAN MASSIF): IMPLICATIONS FOR MODERN COLLISIONAL OROGENS	195
<i>Introduction</i>	197
<i>1. Geology of the Bohemian Massif</i>	199
<i>2. Gravimetric data and the Bouguer anomaly map</i>	202
<i>3. Gravity modelling: constraints and methodology</i>	204
3.1. Seismic constraints	204
3.2. Density constraints	207
3.3. Modelling	208
<i>4. Results of the gravity modelling of the Bohemian Massif</i>	210
<i>5. Geological interpretation</i>	213
<i>6. Geodynamic implications</i>	218
<i>7. Model of relamination of felsic crust to early Palaeozoic mafic lower crust and gravity overturns</i>	221
<i>Conclusion</i>	
CONCLUSION	225
BIBLIOGRAPHIE	229
COMMUNICATIONS ET PUBLICATIONS SCIENTIFIQUES ASSOCIÉES AU TRAVAIL DE THÈSE	250
REMERCIEMENTS	253
LISTE DES FIGURES	257
LISTE DES TABLES	261
TABLE DES MATIÈRES	263

Caractérisation géologique et géophysique de système d'accrétion et de collision : application à la ceinture orogénique d'Asie centrale et au Massif de Bohême.

RÉSUMÉ

L'architecture crustale d'orogènes d'accrétion et de collision à grande échelle est étudiée en combinant géologie structurale, litho-stratigraphie, géochronologie et pétrologie magmatique avec les données gravimétriques, magnétiques et sismiques. Cette approche pluridisciplinaire permet de caractériser la structure et la composition de la croûte orogénique dans deux systèmes d'accrétion-collision : la Ceinture Orogénique d'Asie Centrale (CAOC) et le Massif de Bohême. La CAOC représente près d'un tiers du continent asiatique actuel. Ce système orogénique s'est construit par une accrétion continue de matériel depuis le Paléozoïque jusqu'au début du Mésozoïque, suivie par une collision durant le Mésozoïque. La comparaison des champs de potentiels avec les données géologiques met en évidence une compartimentation erronée de l'orogène en unités litho-stratigraphiques. Par rapport à la géologie, la géophysique permet une analyse directe des structures de la croûte orogénique sur toute son épaisseur. Le travail de thèse présente une compilation de données géologiques et de traitements gravimétriques et magnétiques inédits, dont la modélisation préliminaire pour contraindre l'architecture de la croûte continentale est proposée. Le Massif de Bohême possède quant à lui un catalogue de données complémentaires plus conséquent, ce qui permet une modélisation géophysique 3D plus précise. Dans cette zone, les données géophysiques mettent en évidence l'existence d'une croûte inférieure allochtone de composition felsique. Ceci indique que la croûte orogénique hercynienne est également le résultat d'une accrétion de portions crustales contrastées.

Mots clés : Orogenes d'accrétion et de collision, Ceinture Orogénique d'Asie Centrale, Massif de Bohême, Géologie structurale, Gravimétrie, Magnétique, Modélisation.

ABSTRACT

Large-scale accretionary and collisional crustal orogenic architecture is studied combining structural geology, lithostratigraphy, geochronology and magmatic petrology with gravity, magnetic and seismic data. This multidisciplinary approach allows characterizing the structure and composition of the orogenic crust in two accretionary-collisional systems. The Central Asian Orogenic Belt (CAOB) constituting one third of the Asia continent and the Bohemian Massif are two Palaeozoic orogens formed by accretion followed by collision. It is proposed that the CAOB formed by successive Paleozoic accretion of oceanic and continental fragments followed by a late Palaeozoic to early Mesozoic N-S convergence of North Chinese and Siberian Cratons. The comparison between the potential fields and the geological data reveals an incorrect compartmentalization into different lithostratigraphic terranes. In contrast to geology the geophysical approach allows the analysis of the crustal structures on a complete thickness of crustal column. This thesis presents a compilation of geological data combined with unique gravity and magnetic results which are integrated into a preliminary model for the architecture of the continental crust. Conversely, an important collection of complementary data is available for the Bohemian Massif, allow more precise 3D geophysical forward modeling. In this area, geophysical data reveal the occurrence of an allochthonous lower crustal layer with a felsic composition. This indicates that the Variscan orogenic crust actually resulted from the accretion of contrasted crustal fragments.

Keywords: accretionary and collisional orogens, Central Asian Orogenic Belt, Bohemian Massif, structural geology, gravity, magnetism, modeling.